University of North Dakota
UND Scholarly Commons

Theses and Dissertations | Theses, Dissertations, and Senior Projects

January 2014

An Experimental Investigation Of The Aerodynamic Losses For An Incident Tolerant Low Pressure Turbine Blade Over Moderate To Low Reynolds Numbers At Engine Representative Mach Numbers

Jonathan Long

Follow this and additional works at: https://commons.und.edu/theses

Recommended Citation
Long, Jonathan, "An Experimental Investigation Of The Aerodynamic Losses For An Incident Tolerant Low Pressure Turbine Blade Over Moderate To Low Reynolds Numbers At Engine Representative Mach Numbers" (2014). *Theses and Dissertations*. 1680.
https://commons.und.edu/theses/1680

This Thesis is brought to you for free and open access by the Theses, Dissertations, and Senior Projects at UND Scholarly Commons. It has been accepted for inclusion in Theses and Dissertations by an authorized administrator of UND Scholarly Commons. For more information, please contact zeineb.yousif@library.und.edu.

AN EXPERIMENTAL INVESTIGATION OF THE AERODYNAMIC LOSSES FOR AN INCIDENT TOLERANT LOW PRESSURE TURBINE BLADE OVER MODERATE TO LOW REYNOLDS NUMBERS AT ENGINE REPRESENTATIVE MACH NUMBERS

By

Jonathan Adam Long

Bachelor of Science, University of North Dakota, 2011

A thesis

Submitted to the Graduate Faculty

of the

University of North Dakota

in partial fulfillment of the requirements

for the degree of

Master of Science

Grand Forks, North Dakota

December

2014

This thesis, submitted by Jonathan Adam Long in partial fulfillment of the requirements for the degree of Master of Science from the University of North Dakota, has been read by the Faculty Advisory Committee under whom the work has been done and is hereby approved.

_____
Dr. Forrest Ames

_____
Dr. Nanak Grewal

_____
Dr. Clement Tang

This thesis is being submitted by the appointed advisory committee as having met all of the requirements of the School of Graduate Studies at the University of North Dakota and is hereby approved.

_____
Dr. Wayne Swisher
Dean, School of Graduate Studies

_____
Date

Title An Experimental Investigation of the Aerodynamic Losses for an Incident Tolerant Low Pressure Turbine Blade over Moderate to Low Reynolds Numbers at Engine Representative Mach Numbers

Department Mechanical Engineering

Degree Master of Science

In presenting this thesis in partial fulfillment of the requirements for a graduate degree from the University of North Dakota, I agree that the library of this University shall make it freely available for inspection. I further agree that permission for extensive copying for scholarly purposes may be granted by the professor who supervised my thesis work, or, in his absence, by the chairperson of the department or the dean of School of Graduate Studies. It is understood that any copying or publication or other use of this thesis or part therof for financial gain shall not be allowed without my written permission. It is also understood that due recognition shall be given to me and to the University of North Dakota in any scholarly use which may be made of any material in my thesis.

Jonathan A. Long

December 11, 2014

Table of Contents

List of Figures

List of Tables

Nomenclature

A	Surface area (m^2)
AC	Aero-combustor turbulence level
C	Chord (m)
C_p	Total pressure loss coefficient
C_f	Skin friction coefficient
i	Incidence angle (degrees)
KE	Kinetic energy loss coefficient (ζ)
K_t	Acceleration parameter
LT	Low turbulence level
M	Mach number
P	Pressure (Pa)
Re_C	Chord Reynolds number
Re_θ	Momentum thickness Reynolds number
T	Temperature (°K)
V, U	Velocity (m/s)
u’	RMS velocity component
u+	Wall velocity
y+	Near wall coordinate
X	Axial length (m)
Z	Pitchwise length (m)
Greek	
θ	Momentum thickness (m)
β_1	Inlet angle (degrees)
Ω	Total pressure loss coefficient
δ	Boundary layer thickness (m)
λ	Thwaite’s parameter
ν	Kinematic viscosity (m^2/s)
μ	Dynamic viscosity (Pa*s)
γ	Intermittency function
ρ	Density (kg/m^3)
ζ	Kinetic energy loss coefficient (KE)
Subscripts	
Avg	Averaged quantity
ex	Exit condition
s	Static condition
t,0	Total condition
∞	Free-stream condition

Acknowledgments

First and foremost I would like to thank my advisor, Dr. Forrest Ames, for his wisdom and knowledge he has passed onto me. I appreciate him taking me on as his graduate student. I want to thank my committee members, Dr. Nanak Grewal and Dr. Clement Tang, for reading through and reviewing this work. I would like to thank the University of North Dakota and the NASA CAN program for their support and assistance. I would also like to thank my good friends, Leolein Moualeu and Mitch Busche, for their diligent design work of the nozzles and cascades. I appreciate their availability for phone calls and email correspondence throughout the completion of this project. I thank Kristin Stahl for her help with the instrumentation of the cascades. I want to recognize Matthew Mihelish for his correspondence and assistance during the early phases of this project. I thank Jay Evenstead and Gary Debuque for their expertise and assistance during the design and build phase of the facility. I want to thank Teri Salwey for her administrative assistance as she went above the call of duty many times.

I want to thank my friends and family for their support and advice as I worked on this project. And lastly, but certainly not the least, I want to thank my parents, Caron and Jeff, and my sister, Teresa, for everything they have done to get me to this point.

Abstract

In the interest of reducing airport congestion in the near future, researchers at NASA Glenn Research Facility have envisioned a new civilian transport aircraft which takes off vertically and cruises horizontally at Mach 0.5 using tilt-rotor technology. The engine under development consists of a four stage low pressure (LP) turbine. Many challenges are presented as the engine transitions from 100% shaft speed at takeoff to 54% shaft speed at cruise. The blading in this engine must be designed to optimize fuel efficiency, especially at cruise. The flow conditions in the LP turbine will change significantly from a Reynolds number of about 500,000 with a nearly tenfold drop to 50,000. The low Reynolds number flow enhances the susceptibility of separation and introduces more aerodynamic losses which will act to reduce the overall efficiency of the blade design. The vastly changing shaft speeds will induce a large variation in the flow's incidence angle of about 60°. The changing Reynolds number and incidence angle increases the complexity of the flow and will have a significant effect on transition and separation phenomena along the blading.

Testing for this blade design was conducted in the University of North Dakota's high speed low Reynolds number facility. This facility is configured in a closed-circuit arrangement and allows for steady-state high speed testing at pressures well below atmospheric. The facility was configured to accommodate a six blade five full passage linear cascade to experimentally

acquire aerodynamic data concerning the inlet boundary layers, blade load distributions and total pressure losses over a wide range of Reynolds numbers and incidence angles. The Reynolds numbers under investigation were based off exit conditions and true chord and range incrementally from 50,000 to 568,000. Eight discrete inlet nozzles were fabricated for this study based of the inlet angle measured from the axial direction: -17°, -12°, -2.6°, 8°, 18°, 28°, 34.2° and 40°. These inlet angles correspond to a range of incidence angles from -51.2° to 5.8°. In addition to the Reynolds number and incidence angle effect, the effects of low and moderate turbulence intensity were also investigated. The aerodynamic losses were measured via a five-hole stinger type cone probe. The key component of this study were the mass averaged total pressure loss buckets which encompassed the range of Reynolds numbers and incidence angles under low and moderate turbulence conditions.

CHAPTER I

INTRODUCTION

The purpose of this study is to experimentally investigate the aerodynamic losses of an incident tolerant, low pressure turbine blade over a large range of Reynolds numbers with low and moderate turbulence intensities. The turbine blade in this study has been designed by Rolls-Royce for NASA's Large Civil Tilt Rotor aircraft. A linear turbine cascade facility has been configured for testing in the University of North Dakota's High Velocity Low Reynolds Number Compressible Flow Rig to perform this investigation. A wide range of incidence angles were examined to determine the aerodynamic losses for this blade design under engine representative conditions. As the engine transitions from takeoff to cruise, the blade inflow angle will vary by approximately 40-60° which results from the changing rotor speeds during the transition to level flight. In addition to the changing angles of incidence, a large range of Reynolds number conditions were investigated. The highest Reynolds numbers in this study are representative of the conditions in the forward stage of the three stage low pressure turbine during takeoff and the lowest Reynolds numbers represent the conditions in the aft stage at cruising altitude.

This study will encompass eight inlet angles ranging from +40° to -17° which are to be experimentally tested in the closed loop wind tunnel under four chord Reynolds number (Re_c) conditions, ranging incrementally from 48,000 to 568,000, at an exit Mach number of 0.72.

Additionally, two cases at Re_c of 227,500 and 568,000 were studied at an exit Mach number of 0.35 to relate to past tests performed in a transonic wind tunnel at NASA Glenn Research Center. Midspan surface static pressure measurements and wake measurements will be made for this range of Reynolds numbers for two conditions of turbulence intensity. The low turbulence level will be maintained using a flow conditioning unit and a smooth area reduction nozzle which discharges into one of eight inlet nozzles. The moderate turbulence intensity will be achieved using a mock aero-combustor in place of the smooth area reduction nozzle. Based on earlier measurements, the expected levels of turbulence intensity are approximately 0.5% and 4.5%, which depends on the incidence angle for the low and moderate turbulence conditions. Inlet boundary layer measurements will be acquired using four boundary layer rakes at 25% axial chord upstream of the leading edge of the turbine blades, in order to enhance our understanding of the flow structures in the linear cascade. The wake will be surveyed using a five-hole cone probe enclosed in a sealed traversing system that positions the probe in the pitchwise and spanwise directions. The exit surveys will span the mid-passages between Blades 1 and 2 and Blades 2 and 3 at 25% axial chord from the trailing edge of Blade 2. The surveys will investigate the effects of Reynolds number and blade incidence angle on the pressure losses and turning angles. The most critical component of this study is the mass weighted total pressure loss versus angle of incidence for a given Reynolds number condition and turbulence intensity. The loss buckets will illustrate the Reynolds number dependence over the range of incidence angles where the losses are expected to increase with decreasing Reynolds numbers.

This unique facility operates at steady state which allowing for accurate simulation of engine representative conditions. The high speed and low Reynolds number capability of this system is achieved through changing the internal pressure and velocity of the flow via a vacuum

pump and variable speed roots blower. Uniformity of the flow is maintained with a flow conditioning unit. The flow discharges into a turbulence generator and then an area contraction nozzle, which is used to accelerate and direct the flow into the turbine cascade section at specific incidence angle. The inlet static pressure is acquired at the pitchwise location of 25% axial chord upstream of the leading edge to validate the uniformity of the flow. Additionally, the exit static pressure is monitored at 25% axial chord from the trailing edge helping to monitor exit periodicity. The inlet total pressure is also measured at 25% axial chord upstream of the leading edge. The inlet turbulence intensity spectrum was acquired using a single wire hotwire anemometry system. Just aft of the test section, the wake will be surveyed using the five-hole cone probe actuated using the sealed traversing unit. The flow is then passed through a light 2-D diffuser and onto a 10 inch diameter ducting system that returns the flow to the roots blower.

Chapter II

Literature Review

In the interest of validating a new turbine blade design for the LCTR aircraft, experimental research at engine representative conditions is required. In order to quantify the efficiency and performance of this new blade design, the effects of boundary layer growth and secondary flows on the total pressure loss across the wake of the blade must be fully understood. The losses in a turbine passage are largely dependent on the exit chord Reynolds number, Mach number distribution, blade incidence angle and as well as free-stream turbulence. As will be illustrated in the proceeding section, the nature of the secondary flows and boundary layers and the turbulence intensity level will have a strong influence on the wake. For an efficient blade, it is very important to minimize the relative size of the wake which influences the total pressure losses seen in the proceeding stages. Secondary flows are inherently complicated and are difficult to predict for a given turbine design; thus the need for experimental research. The present study focuses on the wakes generated for the changing engine conditions for the 2nd stage of a four stage low pressure turbine (LPT) from takeoff to cruise. This research will supplement previous work performed at NASA Glenn Research Center.

2.1 Aerodynamic Losses

2.1.1 Boundary Layers

Aerodynamic losses can take many forms in a gas turbine which includes boundary layer flows, separated flows and secondary flows. A "loss" is defined as any flow feature which acts to reduce the efficiency of a turbine. Of these, boundary layers are the most significant source of loss in a gas turbine and are also among the most abundantly studied [1]. Hodson and Coull [2] performed flat plate experiments to simulate the profile losses along the suction surface and developed correlations for predicting trailing edge momentum thickness and shape factor. Halstead et.al [3] investigated the effects of varying Reynolds number and airfoil loading on boundary layer development for the second stage of an LP turbine. Hodson and Howell [4] studied the wake induced interactions with the suction surface boundary layer. Given that the boundary layer is laminar along much of the blade surface, the effects of passing wakes can be significant as the suction surface boundary layer contributes to the majority of the losses.

Boundary layers can be significantly affected by free-stream turbulence, local pressure gradients and Reynolds number and may have a significant effect of the flow characteristics downstream [5]. Ames and Plesniak studied the effects of elevated free-stream turbulence on a four vane cascade and found that upwards of 50% to 60% of the losses seen in turbine vane cascade can be attributed to the suction surface boundary layer [6]. Dunham found that the sensitivity of secondary flows to boundary layers increases dramatically when they are very thin [7]. Therefore, it is critical for turbine designers to examine the role of boundary layers along the endwall and blade or vane surfaces in order to optimize turbine efficiency. This is ever more important for the low pressure turbine which often operates at Reynolds numbers

near 50,000 in the aft stages where boundary layers are expected to be thicker and prone to separating [8]. The reduction in Reynolds number from the takeoff condition is due in part to the atmospheric conditions and reduced shaft speeds seen at cruising altitude [9]. Figure 1 shows an example of boundary layer development along the surface of a turbine blade. As the flow approaches the blade, it is initially laminar and undergoes a transitional flow region where it then becomes turbulent along the suction surface. Near the trailing edge on the suction surface of the figure is a region of separated flow resulting from a strong adverse pressure gradient (decelerating flow) within the turbulent boundary layer. Depending on the extent of the separation, it can significantly affect the strength of the secondary flows and pressure losses seen within the wake. A rapid separation and reattachment would be the most favorable is it would have only a small effect on the blade loading when compared a situation where the flow does not reattach. In the present study, there is potential that the boundary layer will be laminar or transitional at the point of separation.

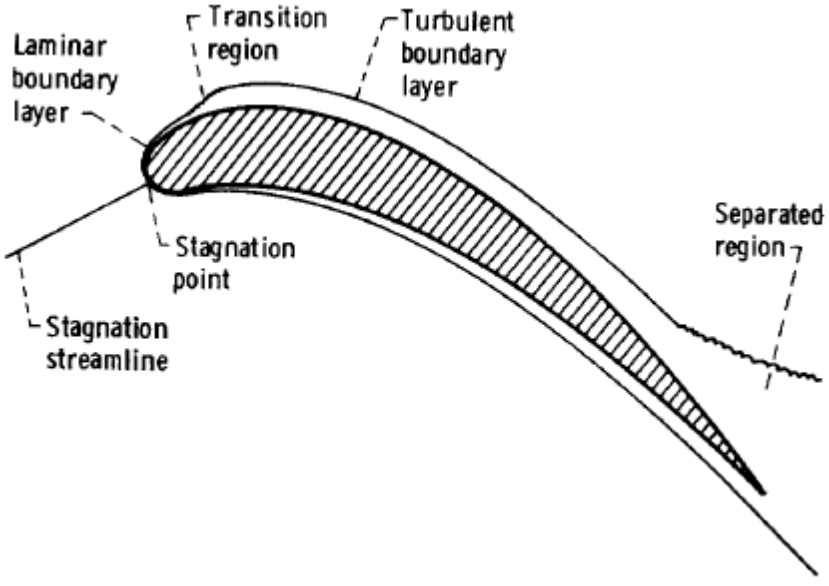

Figure 1: Boundary layer on turbine blade [1]

2.1.2 Secondary Flows and Blade Loading

Reynolds number lapse needs to be understood for efficient operation of a gas turbine given the vastly changing operating conditions. Reynolds number will tend to thicken the boundary layers as it decreases and the flow will become susceptible to separating. Higher Reynolds numbers will tend to mitigate separation vulnerabilities as the increased momentum in the fluid will suppress boundary layer growth and enhance acceleration which will act to reduce the overall total pressure losses. However this cannot be taken for granted as engine conditions at cruise significantly reduces the Reynolds number. McVetta *et al.* [10] studied the effects of Reynolds number lapse for a low pressure turbine stage using a five-hole pitch/yaw probe, but were unable to replicate low Reynolds numbers at engine representative Mach numbers due to limitations of their facility. In light of this, they found the midspan losses increased with decreasing Reynolds numbers.

Modern LP turbines used today often operate with efficiencies above 90%, making it difficult for turbine designers to make significant gains in performance [11]. An alternative solution to increasing the stage efficiency is to improve the thrust to weight ratio by decreasing the weight of the engine. This can be accomplished by reducing the blade count in the LP turbine stage. The weight savings can be significant as the LP stage accounts for approximately 33% of the weight of the entire engine [12]. However, the reduced blade count also requires an increase in loading on the blading to meet performance criterion and can be accompanied by adverse effects that will act to increase the profile losses, therefore decreasing the stage efficiency. A reduction in stage efficiency will almost directly result in an increase in specific fuel consumption [13].

Secondary flows originate from the endwall boundary layer and are highly complex and unsteady in nature. Some of the well-known components of secondary losses are horseshoe vortices, endwall vortices and corner vortices which are all interdependent of one another. It should be noted that there are many tertiary vortex systems present as well, however our understanding of these systems is limited. Langston, Sieverding, and Sharma and Butler [14, 15, 16] give comprehensive descriptions on the physics of secondary or endwall flows. Langston provides a three-dimensional representation of the boundary layer as it enters a turbine blade cascade, as seen in Figure 2. As the flow enters the cascade it encounters a stagnation region on the blade, which becomes the saddle point for forming the horseshoe vortex. In the figure below, the pressure side leg of the vortex is transported across the passage where it meets the suction surface of the adjacent blade and becomes a part of the main passage vortex [14]. The endwall flow, driven by the pitchwise pressure gradient, is largely responsible for this migration. The suction leg of the horseshoe vortex remains attached to the suction surface and rotates counter to the passage vortex. The figure also shows the suction leg of the vortex to lie just below the passage vortex, however this may not be true for every case.

Marchal and Sieverding [17] provide a detailed example on the formation of the horseshoe vortex system near the leading edge of the blade shown in Figure 3. As the flow approaches the stagnation region of the leading edge, the boundary layer fluid is decelerated by the adverse pressure gradient and causes the flow to separate at the saddle point, S1. A region of reversed circulating flow forms just ahead of the leading edge where it causes the flow to separate a second time, creating another saddle point at S2. As the upstream boundary layer fluid is transported through the recirculating zone past the leading edge, it forms the suction leg and pressure leg of the horseshoe vortex. In agreement with the model from Lansgton, the

suction leg of the horseshoe vortex remains attached to the suction surface of the blade and the pressure leg is transported across the passage and becomes a part of the passage vortex system.

The model shown in Figure 4**Error! Reference source not found.**, from Wang *et al.* [18], shows the suction leg wrapping around the passage vortex. The process seen in Figure 4 shows a little more detail of the secondary flows. In this model, the suction side leg of the horseshoe vortex is initially located just above the passage vortex near the leading edge, but it is shown to wrap around the passage vortex near the trailing edge to a final position below the passage vortex. The final location of the horseshoe vortex will vary depending on the loading and as well as free-stream turbulence. As will be seen in Section 2.3, the losses are significantly affected by periodic wake flows given the wide range of turbulence intensities induced by the upstream vanes.

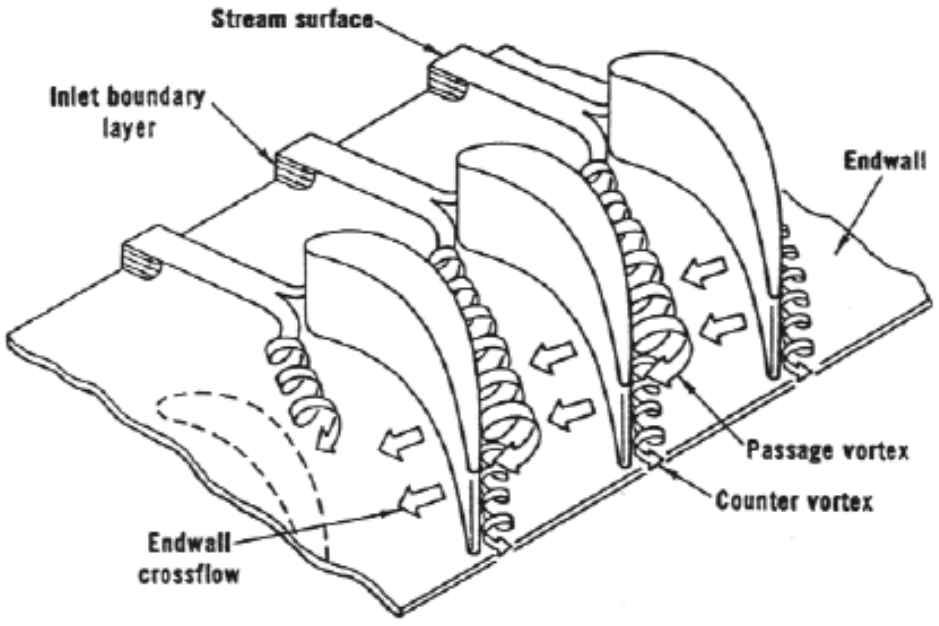

Figure 2: Three-dimensional separation of a boundary layer entering a turbine cascade [14].

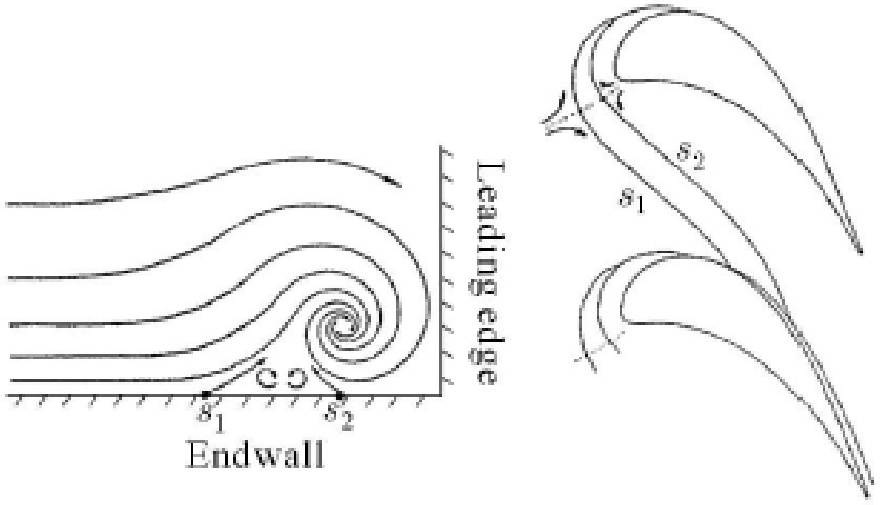

Figure 3: Horseshoe Vortex development

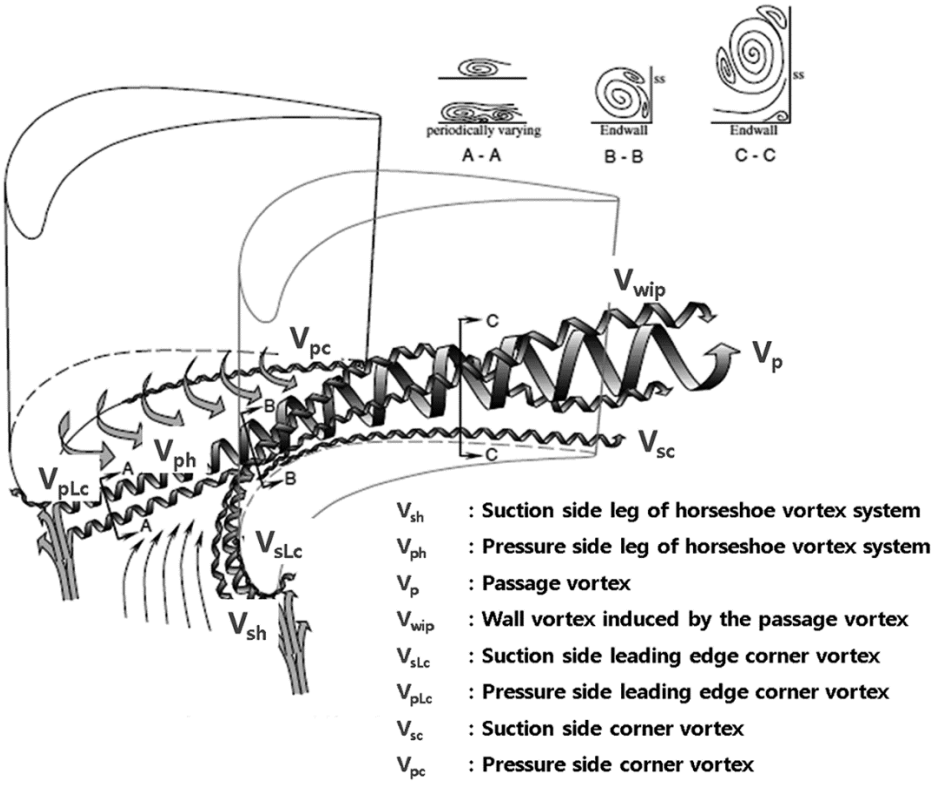

Figure 4: Endwall vortex systems from Wang *et al.* [18]

Blade loading distribution will also have an effect on the secondary flow and manipulating the pressure distribution along the surface of turbine blade or vane is one method

to control the pressure losses. Prakash *et al.* [19] studied the effects of aerodynamic loading level and distribution on LP turbine losses. They found three main mechanisms responsible for increasing the size of the suction surface separation bubble: increased loading on the blade, shifting the loading aft or by reducing the chord Reynolds number. It has been found that for blades with forward loading may exhibit reduced profile losses and the sensitivity to changing operating conditions will also be lessened. However, the forward load distribution may increase the secondary losses and therefor pressure losses. Blades with forward loaded distributions will transport the pressure leg of the horseshoe vortex to the adjacent suction surface sooner than it would for aft loaded blades [20]. In contrast, aft loaded blades allows for increased loading over the blade surface but too much loading may cause the flow along the suction surface to separate, leading to significant losses in performance. Sjolander and Corriveau [21] also studied the effects of load distribution, but for a high-pressure turbine stage, and they found the performance of the blading increased as the loading shifted aft. They noticed the performance fell off rapidly for Mach numbers above the design point. Therefore, from a design standpoint one must choose carefully which loading will be the most desirable for a given situation.

Secondary flows are also influenced by the level of free-stream turbulence intensity. Studying the effects of turbulence cannot be overstated as the interaction of turbulent vortices with the secondary flows will affect the performance of the turbine blade. Turbulent diffusion will have a tendency to mix out secondary flow features within the flow. However, Ames and Plesniak [6] found that high free-stream turbulence will act to increase the overall loss coefficients and also increase the width of the wake. Zhang *et al.* [22] found the averaged midspan loss coefficients decreased with increasing turbulence which was in agreement with

the findings of Ames and Plesniak [6]. Free-stream turbulence will also have a strong impact on the onset of transition.

2.2 Transitional Flows and Turbulence

Much work has been dedicated to investigate the physics of transitional flows on flat plates, single turbine blades, vanes and cascades. Presently, designers are moving towards low pressure turbine blading that are capable of higher loading in order to reduce the blade count as a way to cut weight and increase performance [23]. It is very important to understand how transitional flows behave under a variety of flow conditions. Their behaviors are strongly dependent on free stream turbulence and surface roughness for the flow conditions seen in gas turbines [24]. Local pressure gradients will also have an effect on transition for flows under low free-stream turbulence (Tu < 1%), where transition is to occur naturally, however natural transition is unlikely given the elevated free-stream turbulence conditions in a gas turbine. There are also tradeoffs to highly efficient and highly loaded turbine blading as the increased loading results in stronger adverse pressure gradients along the suction surface which can make the blade more susceptible to separation. The effects that a separation bubble will have on the performance of a turbine blade will depend whether it is a short bubble or long bubble. The purpose of this section is to describe the mechanisms for transitional flows.

2.2.1 Turbulent Spots

A fundamental mechanism for all turbulent flows is the presence of localized vortices and disturbances within the boundary layer, which are commonly referred to as turbulent spots. These disturbances precede the transition to turbulence in both natural transition and bypass transition. Understanding where turbulent flows originate from is an important area of interest for turbine designers where the production of turbulent spots is unavoidable. The effects of the

'spots' and their contribution to transitional flows is well documented. Some of the early investigations of turbulent spots were performed by Emmons [25] in 1951, as well as Elder [26] in 1960 and Klebanoff in 1961 [25]. Other notable studies within the last 15 years have been performed by Mayle in 1999 and by Zaki and Kyriazis in 2010 [5, 27].

Water flow experiments performed by Emmons [25] laid the groundwork for the prediction of turbulent spots. It was found that transition occurred as the random production of turbulent spots, both in time and position, coalesced downstream into fully turbulent flow. As the spots begin to form, they will extend beyond the laminar boundary layer where the resulting mixing with the free-stream will enhance the creation of spots downstream. As the spots grow, they form an irregular triangular shape whose average velocity is approximately 70% of the free-stream. Zaki *et al.* [28] found that the average velocity of the leading edge of the spot was about 50% of the free-stream and the trailing edge was approximately 90% of the free stream velocity. This velocity distribution is responsible for the elongation of the spot. Mayle [24] provides a sketch of the turbulent spot interface as seen in Figure 5. In the region that protrudes out of the boundary layer, it can be seen that the outer boundary of the spot is intermittently turbulent with the entrainment of laminar fluid from the free-stream.

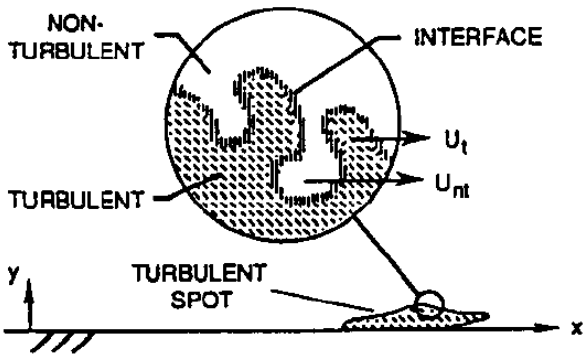

Figure 5: Sketch of the interface between non-turbulent fluid and the turbulent spot. [24]

Emmons [25] also provided a model to determine the intermittency as a means to analyze transition in turbines. Dhawan and Narishima extended the work by Emmons and used a Gaussian distribution to predict intermittency, γ, based off an arbitrary position, *x*, and the transition length, x_t. The intermittency model seen in Equation 1 represents the fraction of the flow that is turbulent for a given position in the transitional region.

$$\gamma = 1 - \exp\left(-\frac{n\sigma}{U}(x - x_t)^2\right) \quad (1)$$

Where *n* is the turbulent spot production rate per unit distance of the spanwise direction of the flow, σ is a dimensionless spot propagation parameter which was found to be about 0.27 by Schubauer and Klebanhoff [29] and U is the free-stream velocity of the flow. The important takeaway from this relationship is that intermittency increases with increasing spot production rates.

The role of free-stream turbulence intensity in the production of spots is well documented. Abu-Ghannam and Shaw, Acharya, Schubaurer and Skramstad, Kuan and Wang [30, 31, 32] have shown that the production rate of spots increases with free-stream turbulence. Higher spot production rates will tend to quicken the transition process in the boundary layer and will act to stabilize the flow from laminar separation. It is well understood that laminar boundary layers have relatively poor resistance to separation in adverse pressure gradients whereas turbulent boundary layers have better resistance due to the increased turbulence kinetic energy. The knowledge of the flow's turbulence level is important as it will affect the early stages of transition.

2.2.2 The Transition of Laminar to Turbulent Flow: Natural Transition

In order to mitigate the effects of transition in a turbine, one must have an understanding of what causes transitional flows. There are four typical paths to transition which includes natural transition, bypass transition, transition due to separation and transition due to surface roughness. White's [33] description for natural transition to turbulence on a flat plate will be used as he gives a comprehensive explanation of the process, which can be seen in Figure 6. The process of transition can be broken down into seven distinct regions: laminar stability, onset of two-dimensional Tollmein-Schlicting waves, the development of spanwise vorticity, the breakdown of three-dimensional spanwise vortices, the continuous breakdown of vortices into three-dimensional fluctuations, production of turbulent spots and the propagation of spot production into fully turbulent flow. Natural transition occurs only when the free stream turbulence levels are low, typically at levels less than 1% [27]. As flow encounters the leading edge of the flat plate in Figure 6 it is initially laminar. As the boundary layer thickens, the first signs of instability can be seen in the form of Tollmein-Schlicting (T-S) waves. Moving downstream, these T-S waves begin to fluctuate until they grow into regions of two-dimensional spanwise vortices. With the spanwise variations in the flow, the T-S waves rapidly develop into three-dimensional vortices, which are unstable by nature.

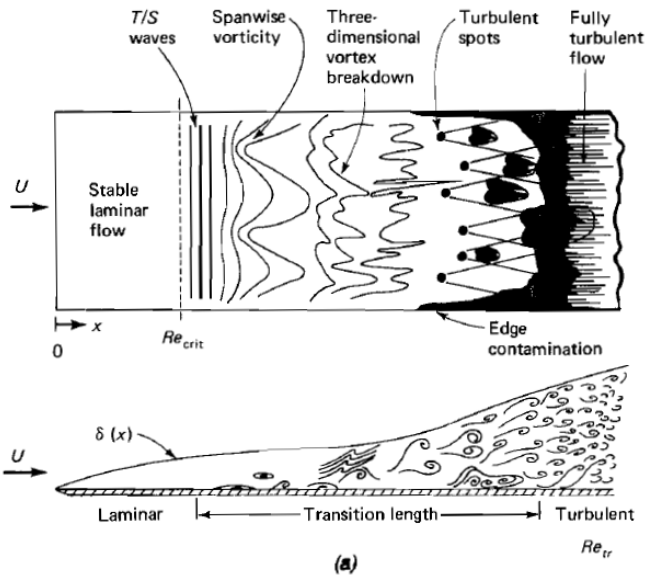

Figure 6: Boundary layer transition process on a flat plate [34]

Regions of high localized shear forms as the unstable three-dimensional T-S waves breakdown. As the vortices breakdown into smaller and smaller packets of fully three-dimensional fluctuations, turbulent bursts in the form of spots begins to form. These high intensity turbulent spots form randomly as they capture more and more of the surrounding laminar fluid. As these packets of turbulent spots propagate downstream they will eventually coalesce into fully turbulent flow. For flows in turbines, which are inherently unstable, this mode of transition is unlikely to occur where transition is mostly likely going to be caused by bypass or from a separation bubble.

2.2.3 Bypass Transition

A common mode of transition that is typically seen in a turbine is bypass transition, which occurs when there are high disturbances in the flow and the natural mode is therefore bypassed. Looking back at natural transition for a moment, it is preceded by the growth and breakdown of Tollmein-Schlicting waves, whereas bypass transition is preceded by the

formation of Klebanoff modes [27]. Klebanoff *et al.* [35] were among the first to look at the three-dimensional nature perturbations in the boundary layer using hot-wire anemometry methods in the 1960s. More recent work has been performed by Zaki *et al.* [28] where they investigated laminar-to-turbulence transition on a compressor cascade using DNS methods. They investigated the role of Klebanoff distortions in bypass transition and observed a temporary calming effect of these distortions before the formation of turbulent spots. It will become apparent that these modes play a significant role in the transition process.

Also known as perturbation streaks, Klebanoff modes consist of streamwise streaks of alternating high and low velocity fluid and whose velocity is on the order of 10-15% of the free-stream [36], [27]. Figure 7 depicts a DNS simulation from Zaki [37] and illustrates the flow phenomena of bypass transition with free-stream turbulence. Within the boundary layer there are streamwise fluctuations of fluid which coalesce into narrow bands of periodic disturbances. These disturbances are visible at approximately 50% span of the model in Figure 7 and quickly give rise to the production of turbulent spots where they subsequently coalesce into fully turbulent flow. This process of transition is known as ‘bypass transition’ as it bypasses the natural means of transition to turbulent flow and generally occurs under conditions of free-stream turbulence intensities above 1%.

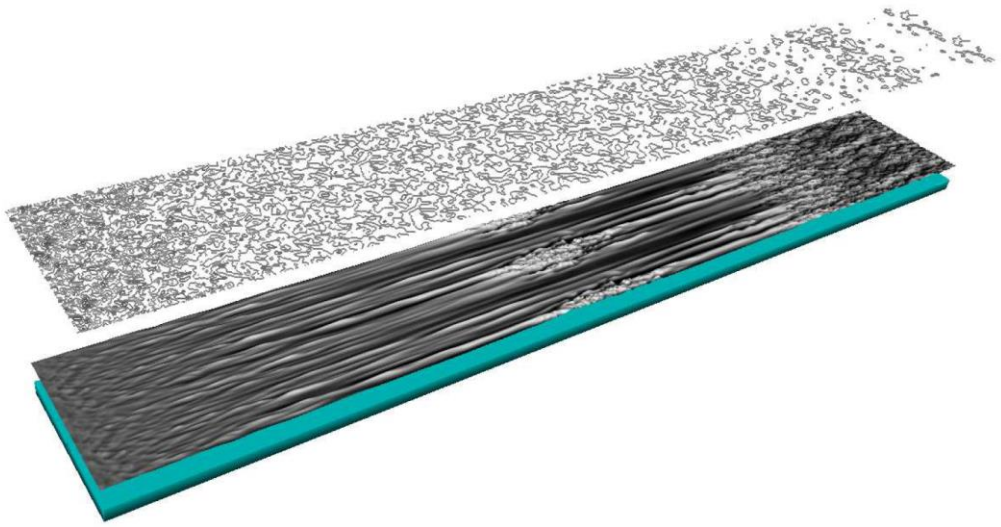

Figure 7: DNS model of bypass transition of a boundary layer due to free-stream turbulence from Zaki and Kyriazis [37].

2.2.4 Separated-Flow Transition

A third mode of transition in the boundary layer in turbines is separated flow transition but is the least studied compared to the modes described previously. Hourmouziadis [38] stated that understanding and predicting separated-flow transition through separation bubbles may be a means to improve low pressure turbine efficiency by a few points. Malkiel and Mayle [39] conducted experiments to investigate process of turbulence development in a separation bubble. They found that transition occurred within the separated shear layer. Redford and Johnson [40] developed a model based off a proven attached flow transition model and produced a model capable of predicting separated flow transition and reattachment for a flat plate. Their model predicted the separation bubble length accurately for turbulence levels above 1%, however it over predicted the separation bubble for turbulence levels below 1%. Hatman and Wang [41] provide a detailed description of the separated flow transition process. The authors point out two sources of instability, Kelvin-Helmholtz (K-H) and Tollmien-Schlichting (T-S), are responsible for transition to turbulence in separated boundary layers. The KH instability is

associated with low-speed flow in the near wall region and the separated laminar shear layer. They are known to originate at some point downstream of the initial point of separation and are associated with a region of maximum vorticity. The second mode of instability is the Tollmien-Schlichting instability. Prevalent at high Reynolds number flows with mild adverse pressure gradient, T-S instabilities will tend to induce the transition process before the flow has had a chance to separate. The T-S disturbances will advect downstream and interact with the KH instability.

The authors then go on to point out three primary modes of separated-flow transition: transitional separation, laminar separation/short bubble mode and laminar separation-long bubble mode. Transitional separation is seen at higher Reynolds numbers in the presence of a weak adverse pressure gradient. The onset of this transition process is similar to natural transition prior to boundary layer separation. Separation is induced by the interaction of T-S instabilities with the K-H instabilities and the ejected near-wall fluid. Reattachment is observed as the increased turbulent mixing between the periodic ejections and upstream flow forces the shear layer to reattach. Transition is also said to have occurred near the region of reattachment, however it is not always the case.

The next form of separation that occurs are laminar separation bubbles, which are characterized by their lengths as either short or long. Short bubbles occur at moderate Reynolds numbers in flows with mild adverse pressure gradients. Mayle [24] states that short bubbles can also be beneficial in forcing the flow to quickly transition to turbulent in order to enhance performance, however they are difficult to predict. Additionally, they only a small effect on the pressure distribution that would be seen for a scenario without separation. Transition begins downstream of the point of initial separation at an inflectional point of maximum displacement

of the shear layer [41]. This process of transition occurs rapidly due to the complex interactions between the separated shear layer and the reverse flow along the surface. In this case, the production of turbulence kinetic energy is sufficient enough to generate enough momentum to overcome the mild adverse pressure gradient and reattach.

Long bubbles are the second form of laminar separation bubbles and should generally be avoided given that they interact with the free-stream to a much greater extent. As a result, the pressure distributions will be significantly different compared to predictions without separated flows [24]. Long bubbles are prevalent in the presence of strong adverse pressure gradients at particularly low Reynolds numbers. Given the low Reynolds number, the loss of momentum in the flow allows the separation bubble to increase in length, should it reattach, or may prevent the flow from reattaching all together. The strong adverse pressure gradient acts to dampen the turbulent mixing across the boundary which will also increase the length of the separation bubble. The nature of separation bubbles may also be significantly affected by passing wakes. As the wake propagates through the rotor passage, regions of high free-stream turbulence intensity may induce earlier transition.

2.3 Wake-Induced Losses

A wake is created as flow moves past a solid body and they are comprised of regions of dampened velocity compared to the free stream. They can be seen as a culmination of history effects of the flow upstream which are dependent on free-stream turbulence, Reynolds number and as well as incidence angle. In the farfield region of the wake, the velocity profile takes on a Gaussian distribution whose velocity is proportional to the distance away from the solid body [42]. Boundary layer development on both the endwall and blade hardware can play a significant role in the formation of secondary flows and therefore strongly influences the

characteristic of the wake. A thick shear layer, prominent at the low Reynolds numbers typically seen in LP turbines, can be subjected to strong adverse pressure gradients which may force the flow to separate and cause significant increases in total pressure losses. The wake will broaden as the losses from different flow features coalesce into one another and may have an adverse impact on the performance of the proceeding stages. For this reason, designers are tasked with optimizing blade designs that minimize these losses over a wide range of operating conditions.

The reduced velocity regions within a wake result from losses of momentum from viscous interactions which will propagate downstream and broaden the wake [43]. Denton [44] identifies three primary sources of losses: profile losses, endwall losses, and leakage losses. As stated previously, these profile losses (boundary layer losses) can account for about 60% of the losses in the wake. Endwall losses are often associated with secondary flows and is sometimes referred to as secondary losses which is also used to account for losses that cannot otherwise be explained. Ames and Plesniak [6] suggested that trailing edge separation along the suction surface has been shown to account for 20 to 30% of the total losses. The final source of loss that Denton points out is tip leakage loss which arises from leakage flow over the tip of the rotor blades. There are many instances in turbomachinery where these forms of loss balance each other, however that is not always the case.

Much work has been done by turbine designers in order to understand the effects of periodic wakes in turbomachinery. Wakes are unsteady and periodic due to the interaction between the rotor and stator; therefore they have varying effects on the onset of boundary layer transition on the downstream rotors or stators. Another byproduct of passing wakes is fluctuating levels of turbulence intensity. Local turbulence levels fall off in the “quiet zone” between wakes but abruptly increases as the wake passes. As Mayle points out, transition is

predominantly controlled by free-stream turbulence intensity [24]. Ozturk *et al.* [45] experimentally investigated the effects of periodic unsteady wake flow and aerodynamic characteristics on boundary layer development, separation and re-attachment along the suction surface of a low pressure turbine blade. They used hotwire anemometry in their large scale subsonic tests and their results confirmed the damping effect of impinging wakes on the size of separation bubbles. They found that the size of the separation bubble could be reduced further with increasing the wake frequency. The higher wake frequencies will increase the turbulence kinetic energy within the boundary layer flow and will act to reverse the separation process.

Chakka and Schobeiri [46] experimentally developed a boundary layer transition model to account for the unsteadiness of periodic wake flows on a curved plate; where the periodic unsteadiness was accomplished via a wake generator. The curved plate was configured such that it simulated the pressure surface of a turbine blade and the boundary layer transition measurements were achieved with a single wire hot-wire probe. They found two primary mechanisms that expedited the onset of boundary layer transition. The first being influenced from increasing the wake frequency which induced a higher free-stream turbulence intensity. Secondly, the transition length was shown to shift towards the leading edge of the plate as the increased turbulent kinetic energy was transported into the boundary layer as the wake frequency increased [46]. Schobeiri *et al.* [47] also studied the periodic and unsteady nature of passing wakes and their interaction with boundary layer development and as well as separation bubble development on the suction surface of a LPT blade at low Reynolds numbers. In agreement with Ozturk *et al.* [45], they observed that turbulence intensity increased with increasing wake frequency which reduced the overall height of the separation bubble. The

resulting increase in turbulence kinetic energy was also responsible for energizing the boundary layer and played a role in suppressing the separation bubble, however not completely [47].

2.3.1 The Measurement of Aerodynamic Losses

Flows in turbomachines are highly unsteady due to the interactions between the rotor and stator. For gaseous-flow in turbines, the frequency spectrum of the unsteady flow fluctuations typically range from 0-50 kHz [48]. A popular choice for the measurement of aerodynamic losses is the multi-hole pressure probe. These probes offers a means to measure quantities such as Mach number, pressure and flow angle under a wide range of flow regimes. Aerodynamic probes are available in a variety of geometries and pressure port configurations which depend on the desired application. The design of the probe shape should optimize the high sensitivity to flow angle variations in steady flows while minimizing dynamic errors in unsteady flows at the same time. Other factors that should be considered in the probe design include desired frequency response, temperature sensitivity and robustness in high temperature environments with particulates in the flow [49]. To minimize flow direction measurement errors, the sensing ports should be positioned close together to minimize the pressure difference caused by the velocity gradient [50]. Cylindrical probes are typically chosen for flows where the Reynolds number is between 1,000 and 100,000 and Mach numbers between 0.2 and 0.9 as they exhibit good aerodynamic characteristics [48].

Sieverding *et al.* [49] reviews various fast response measurement techniques for turbomachinery applications. Fast response instrumentation is ideal for the measurement of the periodic unsteadiness caused by blade row interactions. To conduct the measurements, miniature semi-conductor pressure transducers on the order of 1.2 mm by 1.2 mm in size can be mounted in either tubes or flat mounted along a surface. The authors point out two commonly

used probes used in flow measurements which are single and multi-sensor probes. For flows in which high time a space resolution is necessary, the use of single-sensor probes are often preferred. These probes are specifically used to measure the time-averaged fluctuations in total pressure and may be paired with a pneumatic probe which measures the mean pressure. Multi-sensor probes are another popular choice for the measurement of aerodynamic losses, however size constraints of the probe must be taken into consideration for accurate measurement of strong pressure gradients produced by wakes or shocks. One drawback of surface mounted or tube mounted probes it that their use is limited by their environment. High temperature environments may exceed the material properties of the sensor and render it useless. Several investigators have used external sensors, or remote sensors, under extreme conditions and were able to cool the sensor housing with relative ease [51, 52].

CHAPTER III

EXPERIMENTAL SETUP

The purpose of this section is to describe in detail the procedures and apparatuses used throughout the experimentation of the incident-tolerant blade cascade. Testing was completed within a closed-circuit compressible flow facility which is unique to the University of North Dakota. This facility has the ability operate under vacuum to replicate engine representative conditions with precision. The present configuration facility has the ability to measure a wide range of information that is pertinent to turbine designers and an example can be seen in Figure 8. In this investigation aerodynamic tests were performed to measure the inlet boundary layer at ¼ axial chord upstream of the turbine blades, the inlet and exit endwall static pressures, the blade surface static pressures and as well as the wake.

3.1 Description of Compressible Flow Wind Tunnel Facility

The uniqueness of this facility cannot be overstated. Since it operates within a closed loop configuration, it has the ability replicate engine representative conditions by independently controlling the flow speed of the RGS 10-18 Roots blower, via 60 Hz Yaskawa variable frequency drive, and by controlling the internal tunnel pressure via a Torrvac 63B vacuum pump. The Roots blower directs flow through a 1.92 m^3 insulated outlet tank where it passes through a flow conditioning system as described by Mihelish [53]. The flow is then displaced through an aerodynamic test section designed specifically for the NASA RTAPS project.

This test section includes slanted nozzles that control the incidence angle, a modular LP turbine cascade quadrature as well as a sealed, two axis traversing system. From the traversing system, the flow is passed through light 2-D diffuser and a dump plate where the system transitions to 25.4 cm (10 in.) diameter ducting before it is returned to the 1.92 m^3 inlet tank containing the heat exchanger.

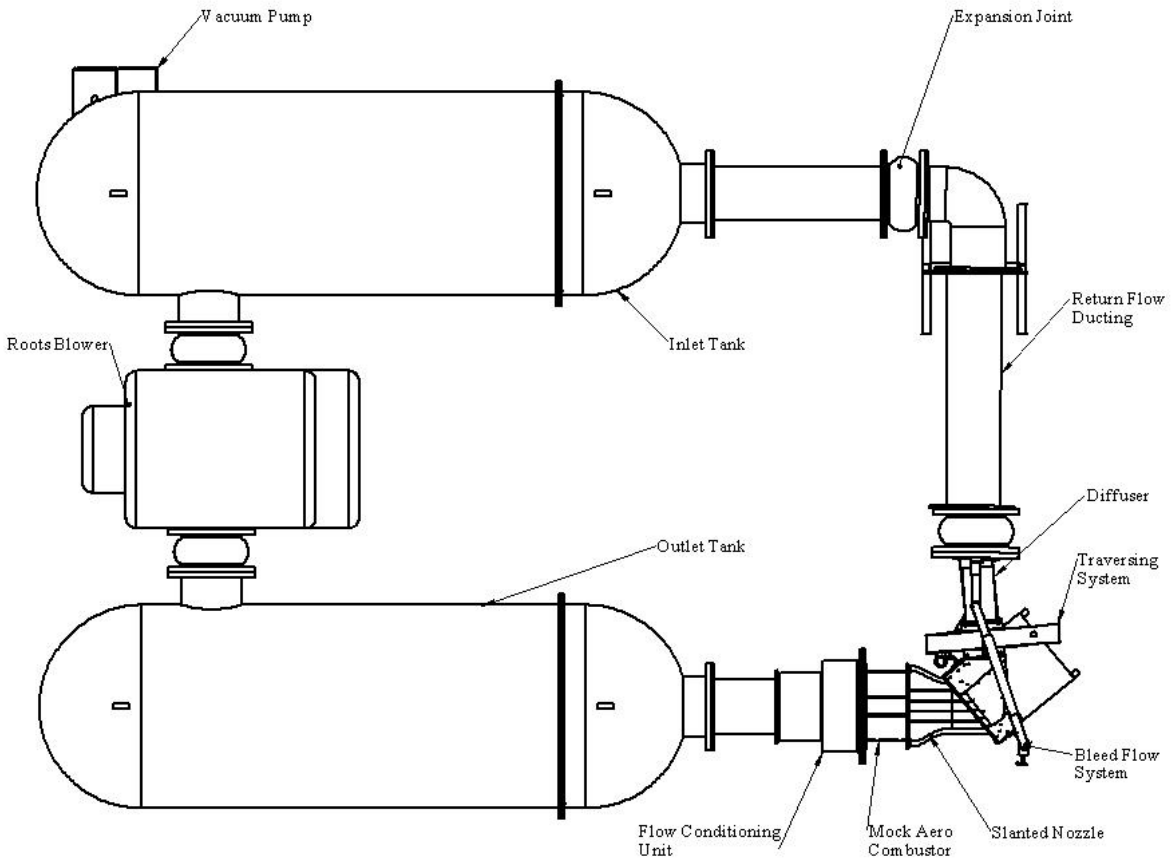

Figure 8: Schematic of the high speed, compressible flow, wind tunnel facility in the 40° configuration.

The RGS 10-18 Roots blower is a four lobe blower used to propel the air within the tunnel at a maximum rate of 227 Liters per second (L/s) or 4000 cubic feet per minute (CFM). The blower is powered through the use of a 56 KW (75 HP) electric motor. The motor is

controlled by a Yaskawa 60 Hz variable frequency driver. The driver can be controlled via the LED monitor on the unit or by a custom made controller designed to ease the operation. During operation of the facility, the LED monitor is used to monitor the power output to the electric motor to prevent overloading.

In order to achieve tunnel pressures below atmospheric within the facility, a TorrVac 63B vacuum was implemented to drop the pressure. The TV-63B vacuum pump is capable of pulling an ultimate vacuum pressure of 67 Pa at a rate of 45 GPM (2.84 L/s). The internal pressure of the system is achieved through the use of a 3.18 cm (1.25'') ball valve and 1.27 cm (0.5'') needle valve. Coarse adjustments are made with the larger ball valve while fine adjustments accomplished with the needle valve. The excess air is exhausted through an exhaust port on the vacuum pump. A polyester filtration system is used to draw in atmospheric air when needed and is capable of filtering particulates as small as 5 microns in diameter.

A system of two heat exchangers is used during operation of high speed compressible flow facility. An 11 GPM (0.69 L/s) rotameter is used to supply coolant to the shell and tube heat exchanger on the 56 KW motor to cool the lubricating oil and enhance reliability of the motor. Another heat exchanger is installed into the 1.92 m^3 inlet tank that is controlled by a 36 GPM (2.27 L/s) rotameter. The purpose of this heat exchanger is to control the air temperature within the wind tunnel as the enthalpy generated from the Roots blower can increase the tunnel temperature beyond 70°C (158°F) during a typical experiment. By controlling the air temperature within the tunnel, it enhances the ability to reach steady state at a specific Reynolds. From our definition of Reynolds number, we know that temperature influences both the viscosity and density of the fluid as seen in Equations (2) and (3). The heat exchanger not only reduces the time it takes to reach steady state, but it also serves to protect the temperature

sensitive instruments installed on the modular cascade which have an upper limit of 121 °C (250 °F).

$$\frac{\mu}{\mu_0} = \left(\frac{T}{T_0}\right)^{1.5} \left(\frac{T_0+S}{T+S}\right) \quad (2)$$

$$\rho = \frac{P}{RT} \quad (3)$$

Two 1.92 m^3 tanks are in place, one connected to the inlet and one connected to the outlet of the Roots blower and can be seen in Figure 9. The outlet tank is lined with a layer of one inch thick polyamide foam that is covered with white navy cloth to prevent degradation of the foam during testing. The foam is in place to dampen the unsteadiness from the pressure fluctuations caused by the two lobes from the Roots blower. As mentioned previously, the tank installed at the inlet contains the heat exchanger system to control the tunnel temperature and as means to remove the heat generated from the Roots blower.

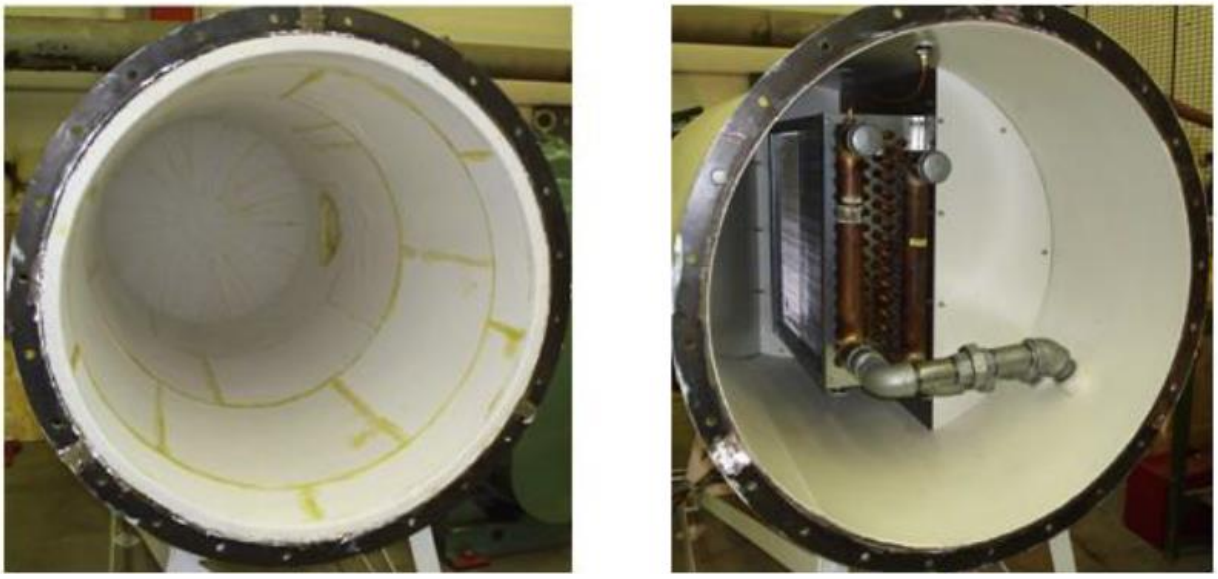

Figure 9: Internal view of outlet (left) and inlet (right) tanks.

3.2 Flow Conditioner and Turbulence Generators

To mitigate the velocity nonuniformities of the inlet flow from the Roots blower, a flow conditioning unit was use to achieve uniformity in the flow. The flow conditioner consists of a circular to rectangular flow transition as well as two perforated plates with two finely meshed screens positioned between the plates. With an exit area of 0.056 m^2 , this apparatus provides a

uniform restriction within the flow field and effectively reduces non-uniformities in the tunnel. To study the effects of turbulence in this study, two turbulence conditions were generated to simulate low and high turbulence intensity levels. A simple 2:1 reduction area ratio nozzle was used for the low free-stream turbulence case, which consisted of 0.8% background turbulence intensity and 1.7 cm length scale with a 1.35% turbulence level resulting from the periodic fluctuations in velocity form the Roots blower. The high free-stream case was accomplished with the use of a mock aero combustor, as seen in Figure 10, and produced 9.0% turbulence intensity with a 2.2 cm length scale [54]. However, these reported values of turbulence intensities were expected to change for the present study given the different inlet nozzles used in the present experiment with higher contraction ratios. Due to the increased inlet bulk velocity profiles for the redesigned inlet nozzles, the turbulence intensity decreased to nominally 0.4% and 4.0% for the low and high turbulence conditions.

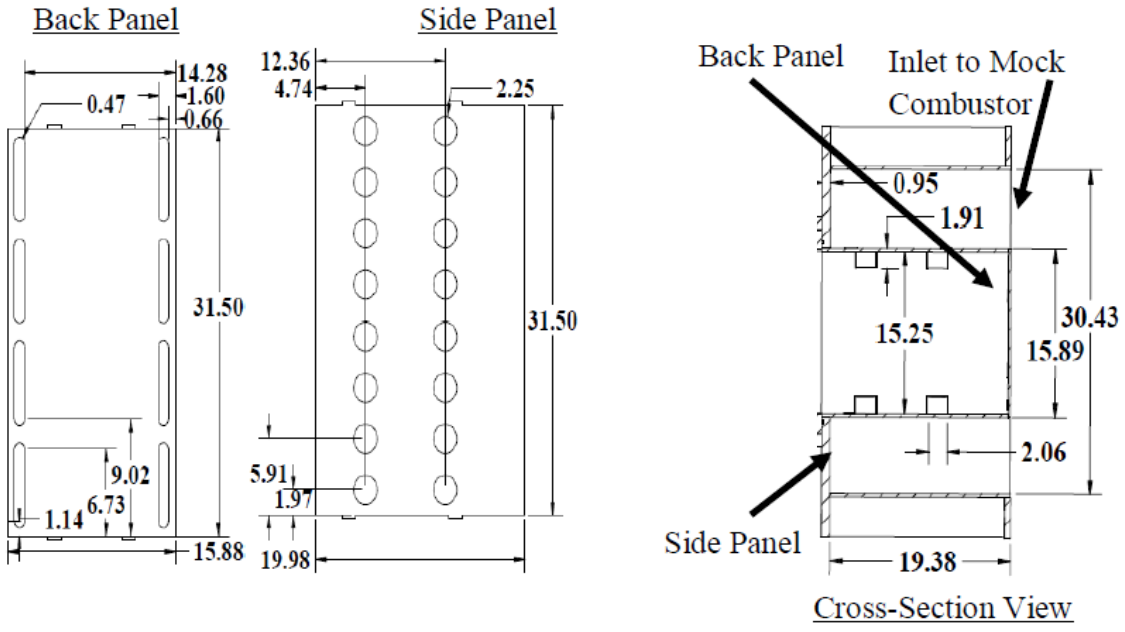

Figure 10: Schematic of the mock aero combustor.

The back panel of the mock aero combustor, shown above, consists of two rows of four oval shaped slots. The two side panels each contain two rows of eight circular holes. As a result, the slots and circular holes combine to create circulation zones within the flow field, thus augmenting the free-stream turbulence.

3.3 Variable Inlet Nozzles

A key component of this study is not only to better our understanding of Reynolds lapse on the variable speed geometry turbine blading, but also to enhance our knowledge of the effects changing blade incident angles with and without free stream turbulence. The blade incident angles are expected to change significantly, approximately 60°, as the tilt rotor aircraft transitions from vertical takeoff to level cruising conditions. The changing rotor speeds causes the flow angles to vary coming off of the guide vanes which would significantly affect the blade loading. Eight slanted nozzles with varying inlet angles of 40°, 34.2°, 28°, 18°, -2.6°, -12°, and -17° were fabricated for this experiment. Three of these inlet nozzles can be seen in Figure 11.

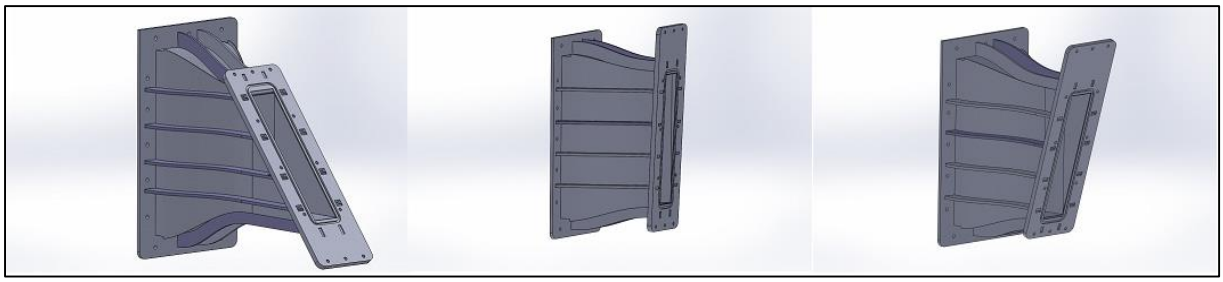

Figure 11: From left to right +40°, -2.6° and -17° inlet nozzles.

The nozzle design featured a double contraction in order to both transition and accelerate the flow from the turbulence generators to the modular blade cascade. The nozzles were contracted from a 31.54 cm by 15.24 cm inlet to 25.4 cm by 5.08 cm at the outlet where it interfaces with the modular blade cascade. The double contraction was achieved through a 6th

order polynomial which was subsequently optimized and validated with a series of 2D and 3D computational analysis in Fluent. The validation of the nozzles was achieved first with a 2D analysis placed at the midspan location of the turbine blading where the blade surface static pressure measurements were to be performed in the experiments. Several attempts were made with the 3D analysis in order to accurately replicate the blade loadings seen from the 2D case. A more comprehensive description of the CFD analysis can be found in Moualeu [55].

3.4 Modular Blade Cascade Test Section

A modular six blade cascade test section was fabricated for this investigation. Key features of this test section include: a top endwall with window, a bottom endwall, a modular blade cassette, an adjustable tail board and variable bleed flow blocks. Figure 12 shows the test section with the top plate and window removed which shows the various features of the cascade assembly. The opening of the cascade is 26.11 cm wide by 5.08 cm tall. The test section is instrumented with four custom built boundary layer rakes, endwall pressure taps, and temperature probes. In addition to the instrumentation, two removable linear turbine blade cassettes, consisting of four blades each, were fabricated using stereolithography for heat transfer and aerodynamic measurements. The turbine blades used for this experiment represent the 2nd stage of a four stage low pressure turbine. To accommodate for the wide variation in incidence angle, eight sets inlet bleed flow blocks were fabricated with pressure side and suction side geometries included into their design. The bleed flow blocks were used to redirect a portion of the flow into a collection tube system with 3.81 cm gate valves in place for pitchwise flow control. The flow is then dumped into the 25.4 cm ducting via a collection plate. Aft of the blade cassette is an adjustable tailboard positioned to control exit periodicity.

3.4.1 Endwall Pressure Taps

Built into the top plate at ¼ axial chord upstream of the blade cassette, are five tapped holes used for instrumentation which are positioned at the half passage location. These tapped holes are instrumented with four custom built boundary layer rakes with two integrating 1.57 mm diameter Kiel probes and two with total temperature probes. The center tap was plugged and unused during the experimentation. The boundary layer rakes are comprised of five 0.794 mm in diameter brass tubes. Tubes 1-4 are fixed starting from the endwall surface to 2.78 mm into the flow field. Tube #5 is positioned at 10.3 mm away from the endwall. The built in Kiel probes and temperature probes are placed at 25.4 mm away from the endwall at the halfspan location. An access slot with a 2.54 cm thick acrylic viewing window was integrated into the top plate as well. Rakes #2 and #3 were used to acquire the boundary layer measurements in this study since they were positioned closest to the inlet of Blade 2 and Blade 3. The rakes were fitted with 1.57 mm barbed fittings and clear Tygon tubing were connected to the low sides of five piezo-resistive pressure sensors and the high sides of the sensors were connected to inlet total pressure probes. A QuickBASIC program was used to help acquire the pressure differentials over the two rakes.

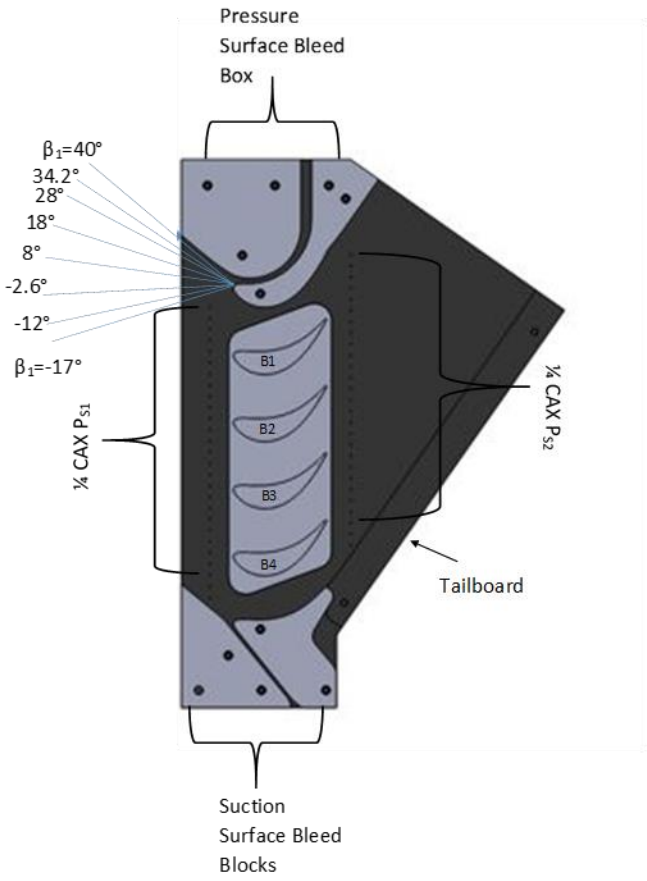

Figure 12: Modular cascade test section

The bottom endwall is instrumented with two rows of 30 static pressure taps. The inlet static pressure taps are positioned at ¼ axial chord upstream of the blade row leading edge and the exit static pressure taps are positioned at ¼ axial chord downstream of the trailing edges. This setup provided a method in analyzing the flow quality across the blade row at the inlet and outlet. The bottom endwall also included a grooved cutout section which allowed for the use of interchangeable blade cassettes for both aerodynamic and heat transfer measurements.

3.4.2 Instrumentation of Blade Insert

This two part study required blade inserts that were instrumented for and aerodynamic loss measurements and heat transfer measurements. Moualeu [55] describes the instrumentation

he used for the heat transfer portion of the overall study. The blade inserts were fabricated via stereolithography using Somos NanoTool, a proprietary material, and provided excellent surface quality and thermal resistance. Additionally, this process allowed for precise placement of internal hole geometries for the instrumented blades. The blade insert included four total blades with the two interior blades (Blades #2 and #3) instrumented for surface static pressure measurements. Blades #1 and #4 were used to ensure periodicity between the passages. The inlet metal angle for the blading was set at 34.2° with an exit metal angle of 54.88°. The pitch between the blades were 4.89 cm with a span of 5.08 cm. The leading edge and trailing edge diameters were 5.67 mm and 1.24 mm, respectively. Blade 2 is instrumented with 36 midspan surface static pressure taps positioned 2.54 cm from the endwall. The 0.79 mm diameter holes were fitted with 0.79 mm diameter brass tubes, which were epoxied in place to ensure a proper seal. 1.57 mm diameter barbed fittings were then soldered to the each pressure tap where they could be connected to the DAQ system with 1.57 mm Tygon tubing. In similar fashion, Blade 3 was instrumented with 36 surface static pressure taps but were staggered to measure both the quarterspan and midspan pressure distributions. This was done in order to examine secondary flow effects caused by the endwall.

3.5 Two-axis Traversing System

The aerodynamic losses were acquired through the use of a sealed, two axis, traversing system. The five-hole cone probe was fixed to an x-slide stepping motor system that traversed it in the spanwise (y-axis) direction and another stepper motor to traverse in the pitchwise direction (z-axis) as seen in Figure 13. Each axis is powered by a Vexta PK-245 stepping motor and was controlled by two Velmex VXM motor controllers. The 0.635 cm diameter probe was supported by two 2.54 cm by 2.54 cm aluminum rod that are held in place by adjustable bearings

that were designed to eliminate friction in the assembly. Nylon bushings were used to reduce friction on the probe's support shaft and allows for movement in the spanwise directions. Figure 14 shows a cutaway view of the traversing section passageway as viewed from the bottom. The sidewalls in the figure were contoured to account for the blockages created by the probe assembly. The contouring was determined from the streamlines around the probe and fairing. The fairing was included to reduce drag and blockages from the flow around the cylindrical shaft of the probe. The enclosure to the traversing system was constructed out of 12 gauge mild steel and featured robust flanges and internal support braces to reduce deflections during operation of the facility. Given the tight tolerances in this system, the added supports ensured a clear path for the sensitive stepping motors.

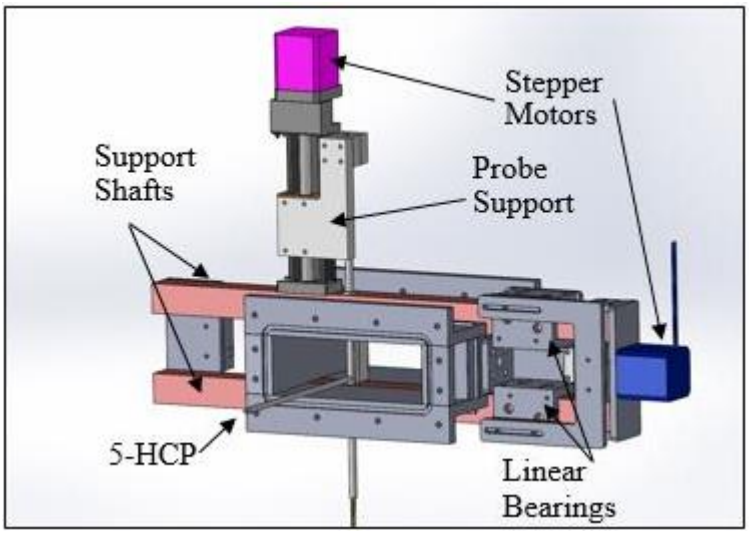

Figure 13: Two axis traversing assembly.

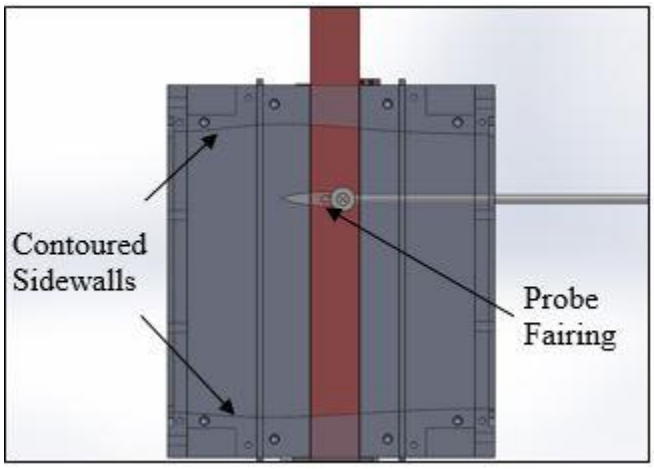

Figure 14: Cutaway of traversing section duct.

3.6 Calibration Unit and 5-Hole Cone Probe

To measure the aerodynamic losses of this turbine blade design a five-hole cone probe and a sealed traversing system were chosen to achieve this task. However, before any exit surveys could take place the five-hole cone probe had to be calibrated based on the expected operating conditions. Aerodynamic calibrations were carried out for the five-hole cone probe within a custom built calibration tunnel as described by Mihelish and Ames and Mihelish [54, 53]. This unit, pictured in Figure 15, consisted a flow conditioning unit consisting of two perforated plates and two fine meshed screens with an open area of 0.039 m^2 as well as an inlet and outlet nozzle to transition to the testing plane. A 1.67 reduction area ratio nozzle was used at the inlet and a 7.27 reduction area ratio nozzle was used to transition the flow to a final open area of 15.24 cm by 3.5 cm at the testing plane. The stinger probe was fixed into place such that stinger was normal exit plane of the transition nozzle. The 0.635 cm support shaft was held into place with a pair of 0.635 cm diameter Swagelok fittings on either end of the stinger probe. The probe was carefully aligned at the center of the exit plane with a caliper and the yaw angle was

fixed at 0° with a protractor and alignment block fixed at the top plate. This configuration provided an airtight seal while still allowing for yaw adjustments to be made during calibration.

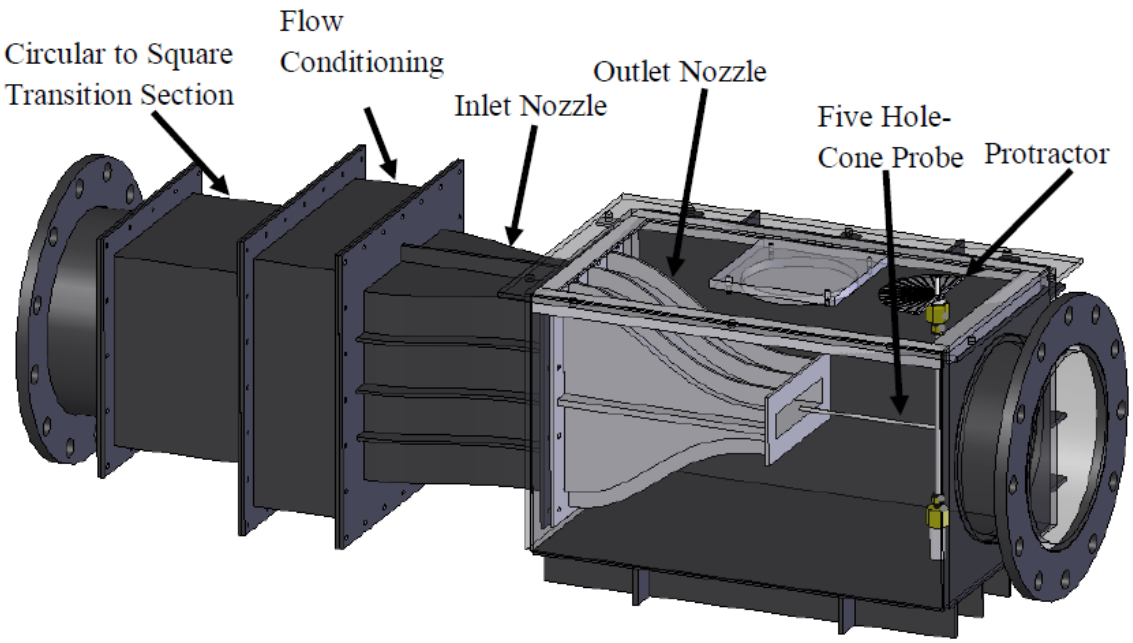

Figure 15: Schematic of calibration apparatus attached with the flow conditioning unit. [53]

A special made five-hole cone probe was used for the aerodynamic measurements in this study. The sensing end of the probe can be seen in Figure 16. It consists of a 15° included angle, with four 0.36 mm diameter pressure ports aligned at the mid-cone location, which are positioned 90° from one another, and a single 0.41 mm diameter total pressure port that is positioned at the center of the probe. The 0.317 cm sensing tube is supported by a 0.476 cm tube and is connected normal to a 0.635 supporting shaft to form a "T." This probe was used to measure the total pressure losses and measure angles of pitch and yaw from the trailing edge of the instrumented blade.

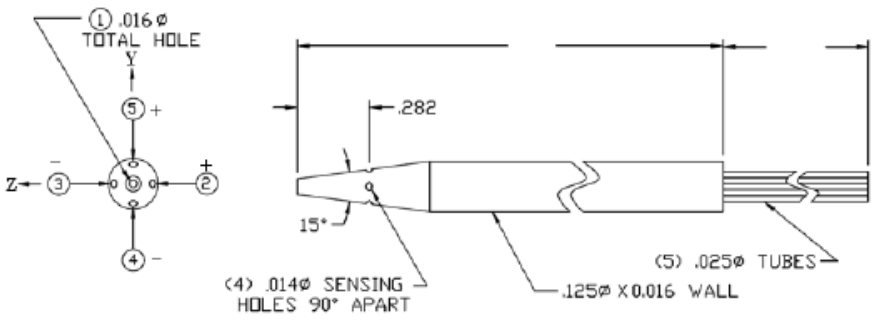

Figure 16: Two-dimensional schematic of the five-hole cone probe pressure sensing tip.

3.6.1 Data Analysis

Previous studies using this closed-circuit facility have been carried out by Mihelish and Ames [54, 56] for a first stage vane cascade. The present facility has been updated from the original configuration to accommodate the new modular blade cascade and slanted nozzles as discussed in Sections 3.3 and 3.4. A non-nulling technique, as developed by Treaster and Yocum [57], was used to calibrate the five-hole cone probe for each condition in this study; meaning that the derived relationships are determined between the pressures from the five pressure ports and the local velocity. Pressure coefficients of yaw sensitivity, pressure port sensitivity and total pressure recovery were acquired with this method. The coefficients of yaw, pitch, total pressure, and static pressure can be seen from the equations below.

$$Cp_{yaw} = \frac{P_2 - P_3}{P_T - P_s} \tag{4}$$

$$Cp_{pitch} = \frac{P_4 - P_5}{P_T - P_s} \tag{5}$$

$$Cp_{Total} = \frac{P_{Total} - P_{Ave}}{P_T - P_s} \tag{6}$$

$$Cp_{Static} = \frac{P_{Ave} - P_{Static}}{P_T - P_s} \tag{7}$$

$$P_{Ave} = \frac{P_2 + P_3 + P_4 + P_5}{4} \quad (8)$$

As presented first in Equation (6), P_1 is the pressure differential between the tunnel total pressure and the center total pressure port on the probe. P_1 is expected to recover the total pressure, completely, over a +/- 6° range of yaw. As yaw angle is increased beyond this range, the port is no longer aligned with the Kiel probe upstream and is unable to recover the total pressure. Pressures ports, P_2 through P_5 are each determined by subtracting the pressure read from the respective port from the centerline total pressure port, P_1.

3.6.2 Testing Conditions for Calibrations

Four Reynolds number conditions and two Mach number conditions have been selected by NASA Glenn Research Center (GRC) for this investigation. Since the calibration unit is separate of the cascade apparatus, the probe was calibrated at equivalent chord Reynolds numbers of 50,000, 66,000, 227,500 and 568,000 at a Mach number of 0.72 for all four cases and at Mach 0.35 for the latter two cases to validate studies performed at NASA GRC by McVetta *et al*. [10]. For the purposes of this project, the static pressure at each design condition was set and held constant throughout the range of Mach numbers tested, which ranged incrementally from 0.4, 0.5, 0.6, 0.7 and 0.8. at the exit Mach 0.72 condition. At the 0.35 exit Mach condition, the probe was calibrated for Mach numbers of 0.15, 0.2, 0.3 and 0.4. This process was chosen to enhance the accuracy of the calibrations as the static pressure is expected to remain relatively constant through the entire width of the wake, even though the Mach number within the wake may vary as much as 50% of the free stream. This approach was similar to what Mihelish and Ames [54] utilized in this facility from previous experiments, however,

their process held the Reynolds number constant throughout the range of Mach numbers that were tested.

The probe was calibrated for each chord Reynolds number condition as described above by adjusting the yaw angle +/- 22° at 2° increments. To measure the yaw angle, the probe was pivoted along the 0.635 cm support shaft. Using an alignment block and protractor, the positive angles were measured by rotating the probe in the counter-clockwise direction and the negative angles were measured by rotating in the clockwise direction. On the pressure end of the probe, Tygon tubing was fitted onto 1.5875 mm barbed fittings to connect the five piezo-resistive pressure sensors. The pressure sensors were connected to an output box, containing a five volt, 20 mA Acopian power supply. The outputs were sent to the 3497A HP data acquisition unit where it was then sent to a Quick BASIC calibration program. The program was designed to read the pressures from each port on the cone probe, the tunnel static pressure and total pressure and temperature. The static pressure was measured from a tap near the center of the transition nozzle near the exit plane. A 1.5875 mm Kiel probe was equipped to the calibration unit and was positioned to measure the total pressure inside the tunnel and a quick disconnect thermocouple probe was used to measure the temperature. From these sensors, compressible flow calculations were performed to compute the tunnel Mach number, Reynolds number, viscosity and density.

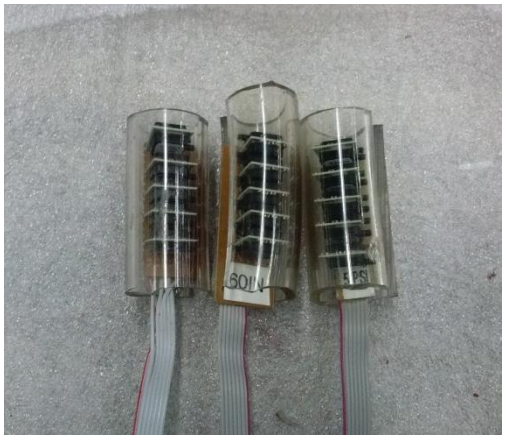

Figure 17: From left to right: 20 inWg, 60 in Wg and 5 PSI (138 inWg) sensors.

Table 1: Sensor selection for aerodynamic probe calibration and exit surveys

REYNOLDS NUMBER	**MACH NUMBER**	**SENSOR (PASCALS)**
568,000	0.72	34,376
227,500	0.72	14,944
66,000	0.72	4,981
50,000	0.72	4,981
568,000	0.35	14,944
227,500	0.35	14,944

Given the large range of Reynolds number conditions in this study, three sets of piezo-resistive mini pressure sensors were chosen in order to reduce sensitivity errors within the measurements. An image of these sensors can be seen in Figure 17. The maximum port to port pressure differentials were expected to occur at the highest chord Reynolds number condition at 568,000 at Mach 0.72. To accommodate for the pressures in the experiment, a 34,376 Pa sensor was chosen. Table 1 outlines the sensors selected for the remaining test conditions for

both the calibration and exit surveys. The pressure differentials were expected to decrease with decreasing Reynolds number and Mach number.

3.7 Aerodynamic Loss Measurement Procedure

The scope of this study required aerodynamic loss data to be experimentally measured to understand the effects of Reynolds number lapse versus incidence angle at two levels of turbulence intensity. Incidence angle was varied over a 57° range to simulate various conditions from takeoff to cruse. Mach number was held constant at 0.72 throughout the majority of this study; however the two highest Reynolds numbers at 227,000 and 568,000 were measured at Mach 0.35 and 0.72. The latter two cases at Mach 0.35 were tested in order to directly relate to tests performed at NASA Glenn's transonic linear cascade facility [10, 58]. Additionally, these particular cases were only acquired for the 40°, 34.2° and -2.6° inlet angles for brevity. Table 2 and

Table 3 outlines the inlet angles and testing conditions used throughout this study. Notable design inlet conditions include 40°, which represents the incidence angle seen at cruise, and an inlet angle of -2.6° that represents the design condition for takeoff.

To execute the exit surveys, a QuickBASIC program was written to communicate with the Velmex motor controllers linked to the sealed traversing system which jogged the five-hole cone probe to measure a 21 by 21 array of aerodynamic loss data. The plane in which the probe was traversed measured 2.81 cm in the pitchwise direction and 2.11 cm in the spanwise direction. Due to design limitations of the traversing system, the probe was set to a minimum

distance of 0.432 cm off the endwall and a maximum distance of 2.54 cm off the endwall, or the midspan location. Twenty-one equal increments of 1.397 mm were set to measure the losses in the pitchwise direction. The probe was jogged 21 times in the spanwise direction with the first 10 increments set at 0.838 mm and the final 11 increments set at 1.27 mm. The concentrated grid spacing from the endwall to quarterspan of the blade allowed for better resolution in order to improve the chances of detecting corner vortices, endwall vortices and secondary flows, such as the horseshoe vortex. The reference point for the exit surveys was held constant throughout the experiment, whose position was optimized through multiple iterations of exit surveys to guarantee the wake, in its entirety, will be captured throughout the full range of incidence angles. Therefore, any shifting in the location of the wake will be quantified within the data. Additionally, the origin of the exit surveys was referenced from the bottom plate endwall location such that the disturbances left behind the boundary layer rakes were avoided.

Table 2: Inlet angle settings, $\boldsymbol{\beta_1}$, with corresponding incidence angles, i.

Inlet Angle (β_1)	**Incidence Angle, i**
40°	5.8°
34.2°	0.0°
28.0°	-6.2°
18.0°	-16.2°
8.0°	-26.2°
-2.6°	-36.8°
-12.0°	-47.0°
-17.0°	-51.2°

Table 3: Experimental testing conditions for boundary layer and aerodynamic loss measurements

REYNOLDS NUMBER	MACH NUMBER	TURBULENCE INTENSITIES	
568,000	**0.72**	**0.5%**	**4.5%**
227,500	**0.72**	**0.5%**	**4.5%**
66,000	**0.72**	**0.5%**	**4.5%**
50,000	**0.72**	**0.5%**	**4.5%**
568,000	**0.35**	**0.5%**	**4.5%**
227,500	**0.35**	**0.5%**	**4.5%**

3.8 Experimental Uncertainties

Using the approach by Moffat [59], the experimental uncertainties for the tunnel Reynolds number was +/- 2%. The Mach number had an uncertainty value of +/- 2% as well. The uncertainties for the total pressure loss measurements under low and high turbulence were +/- 0.004 and +/- 0.005, respectively. During the setup of the five-hole cone probe, the initial probe angle had an uncertainty value of +/- 0.5° which. The nature of the initial setup procedure made it difficult to ensure a more precise setting. The flow angles due to unsteadiness and bias error had uncertainties of +/- 0.25° and +/- 0.26°, respectively.

CHAPTER IV

EXPERIMENTAL RESULTS

4.1 Endwall Static Pressure Measurements

Inlet and exit endwall static pressure measurements for each incidence angle and turbulence condition were acquired. For validation of the flow in the facility, the inlet Mach profile, in Figure 18, shows the isentropic Mach distribution over the full range of Reynolds numbers at both exit Mach conditions for the 40° inlet angle. Overall, there is good uniformity across the inlet plane of the blade cascade as seen in Figure 18. The valleys in the data, are associated with the flow decelerating as they encountered the leading edges of the blades. Increased blockages from boundary layer growth is evident at the 50,000 and 66,000 Reynolds number condition where the inlet Mach numbers have decreased from the 227,500 and 568,000 Reynolds numbers. The data acquired at the exit Mach 0.35 condition have also shown a high degree of uniformity along the inlet plane.

Endwall static pressure measurements taken at about ¼ axial chord from the exit plane of the blade row were used to formulate the isentropic Mach number distribution in Figure 19 for validation of the exit flow periodicity,. The data are very consistent across the exit plane with a slight rise in Mach number from 0.7 near Blade 4 to 0.8 near Blade 1. However, the instrumented Blades 2 and 3 show very good agreement with one another at Mach 0.72. The slight rise in Mach number could be due to blockages from the upstream bleed flow system

causing the flow to accelerate faster near Blade 1. The gradient across the cascade may also be due to curvature effects as the flow about the inside corner of the cascade, near Blade 4, will tend to accelerate, whereas the flow along the outside corner, Blade 1, will decelerate. Clear consistency across the wide range of Reynolds numbers is also present in the data, suggesting the design of the downstream traversing section is valid and is therefore not contributing to any significant increase in the losses.

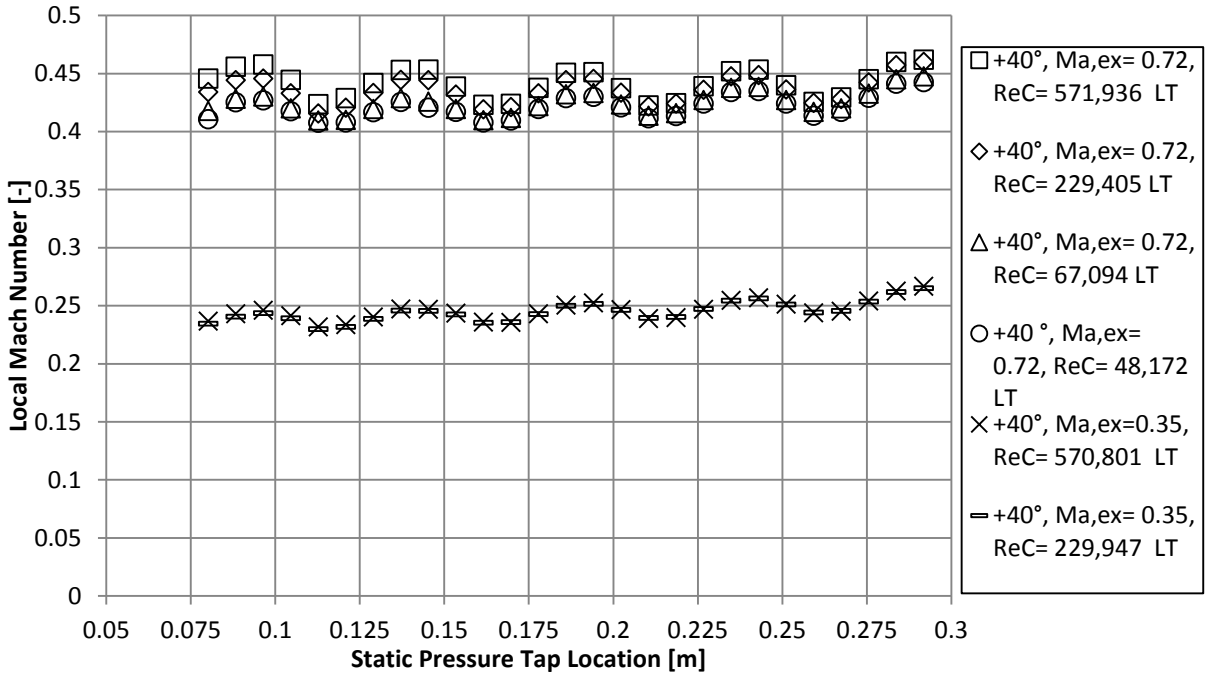

Figure 18: Inlet isentropic Mach distribution at 40° as a function of Reynolds number under low turbulence at ¼ CAX upstream of the leading edge.

The effects of incidence angle can be seen in Figure 20 where the bulk velocity at the inlet of the cascade is maximum at the 5.8° incidence (40° inlet) angle. The velocity of the flow decreases with incidence angle due to the increasing cross-sectional area at the exit plane of the inlet nozzles. The flow measured across the exit static pressure taps of the cascade was generally consistent along the span of incidence angles with minimal variation in Mach number at the high Reynolds numbers. At the low Reynolds number, incidence angle does have an effect on

the exit Mach distributions due to the effects of profile and endwall losses which can be seen in Appendix II.

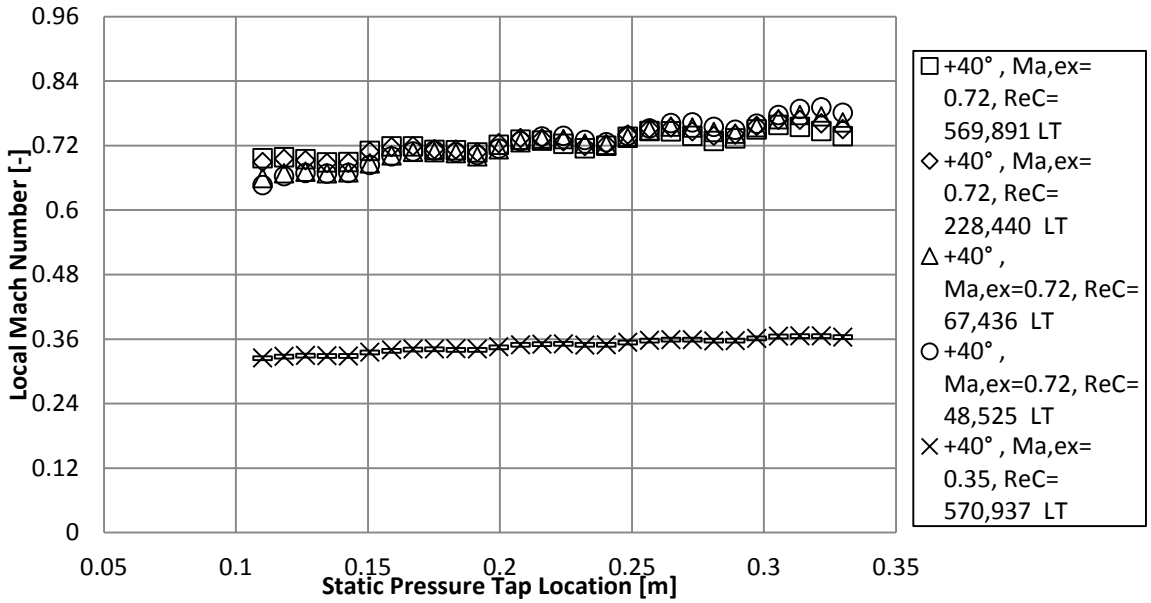

Figure 19: Exit isentropic Mach distribution at 40° as a function of Reynolds number under low turbulence at ¼ CAX downstream of the trailing edge.

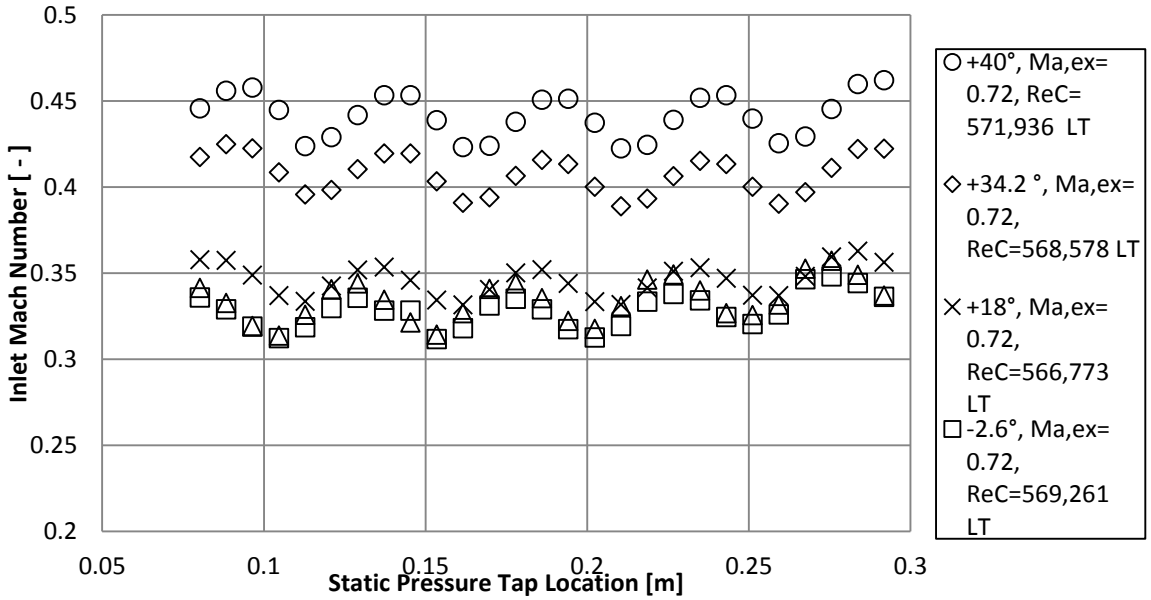

Figure 20: Inlet isentropic Mach distributions as a function of inlet angle at the 568,000 Reynolds number under low turbulence.

4.2 Quarter and Half-span Static Pressure Measurements

4.2.1 Reynolds Number Effect

Surface static pressure measurements were acquired at the midspan of Blades 2 and 3 and at the quarterspan location on Blade 3. Distributions of isentropic Mach numbers were developed from compressible flow relations for each condition. The data are presented such that positive values of normalized surface arc, s/c, are on the suction surface locations and the negative values represent the pressure surface. The local Mach number data in Figure 21 show the effects of Reynolds number at the -17° inlet angle (-51.2° incidence) at a constant exit Mach number of 0.72 under low turbulence. The flow is separated just aft of the peak velocity region on the suction surface for the lowest Reynolds number which is a direct result of the strong adverse pressure gradient seen at the high negative incidence angle. The flow is nearly supersonic just aft of the leading at the 227,500 and 568,000 Reynolds numbers and is followed by a sharp drop in Mach number towards the trailing edge; given the blockages in the flow, it is possible that the flow is nearly choked between the blades. The location of the separation bubble migrates upstream from s/c of 0.668 to 0.596 as Reynolds number is decreased from 227,500 to 50,000. A separation bubble is also present near the leading edge pressure surface for each Reynolds number with reattachment occurring near s/c= -0.666, which is followed by a moderate favorable pressure gradient.

At the -2.6° inlet angle (-36.8° incidence), as seen in Figure 22, decreasing Reynolds numbers increases the extent of the of the separation bubble on the suction surface. At the 50,000 Reynolds number condition, the onset of the separation bubble is located at s/c=0.593 but moves downstream to about 0.884 at the 227,500 Reynolds number. At the 568,000 chord Reynolds number, the adverse pressure gradient near the trailing edge is does not appear to be

strong enough to produce a separation bubble and, therefore, remains attached. In contrast, the flow is clearly separated near the trailing edge at the 50,000 and 66,000 Reynolds numbers. Reynolds number also has a strong effect on the flow characteristics on the pressure surface; the flow remains attached for the 227,500 and 568,000 Reynolds numbers but a separation bubble forms at the 50,000 and 66,000 Reynolds numbers. Aft of the reattachment zone, the flow undergoes a gradual acceleration towards the trailing edge. The losses along the blade are expected to decrease with increasing Reynolds numbers, especially given that the flow remains attached at the highest Reynolds number.

Data in Figure 23 show the isentropic Mach distributions for the low turbulence case at the 40° inlet angle (5.8° incidence). A favorable pressure gradient extends through much of suction surface with mild separation occurring near the trailing edge at the 227,500 and 568,000 Reynolds numbers. As expected, the onset of separation moved upstream for the 50,000 and 66,000 Reynolds numbers and the separation bubble has increased in length but appears to reattach near the trailing edge. Along the pressure surface, the overspeed region is more gradual than the extreme negative incidence angles. A favorable pressure gradient is gradually produced downstream towards the trailing edge; Reynolds number does not appear to have an effect on the pressure surface for this inlet angle as they share the same loading profile.

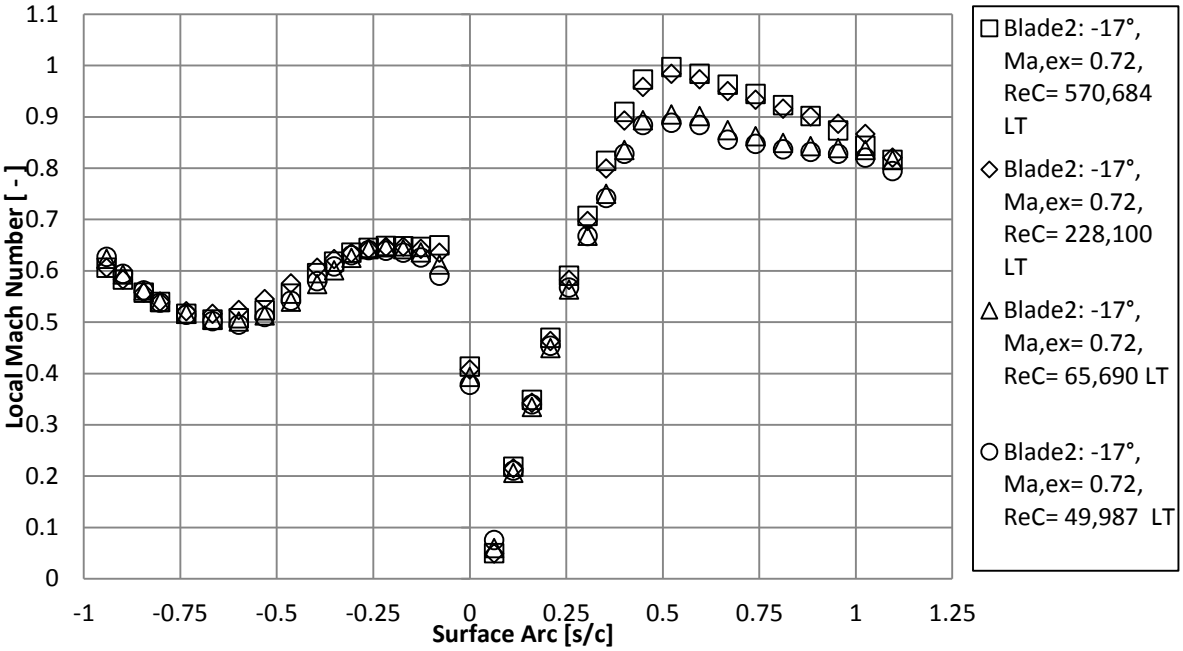

Figure 21: Low turbulence isentropic Mach distribution for Blade 2 at -51.2° incidence.

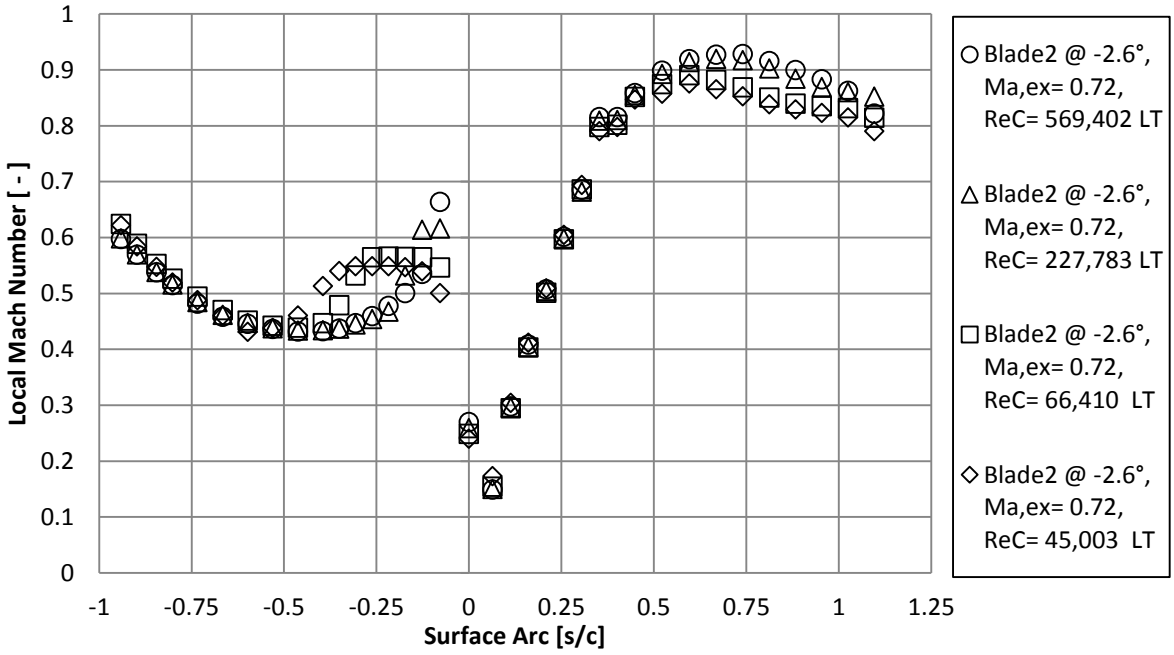

Figure 22: Low turbulence isentropic Mach distribution for Blade 2 at -36.8° incidence.

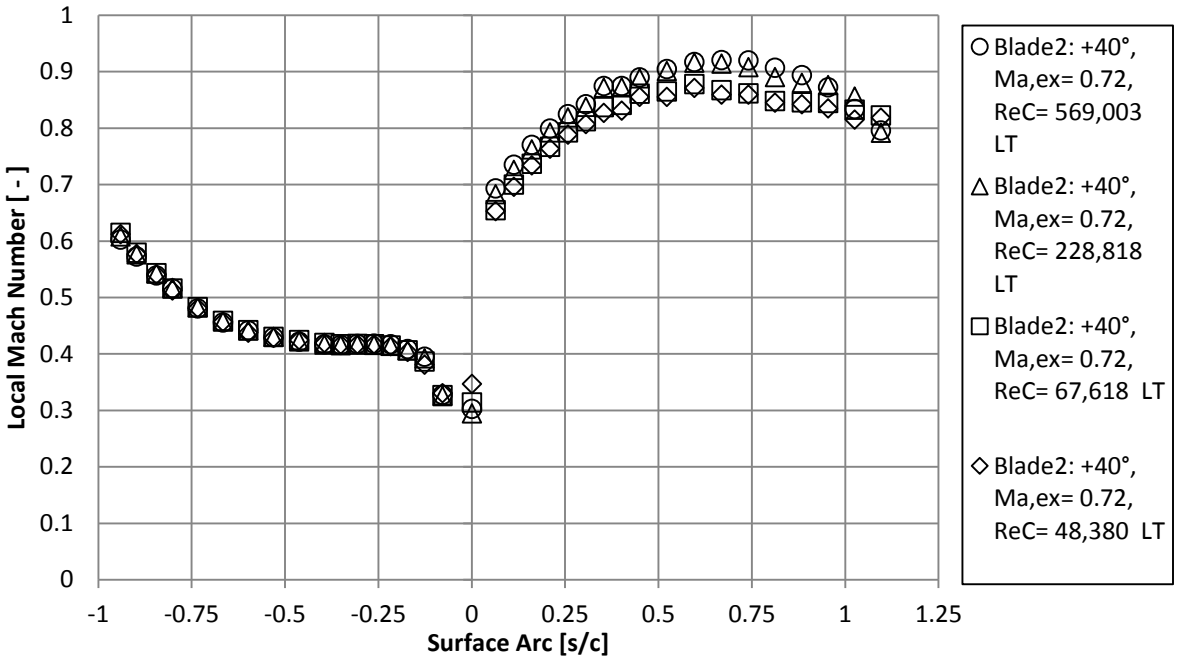

Figure 23: Low turbulence isentropic Mach distribution for Blade 2 at 5.8° incidence.

4.2.2 Incidence Angle Effect

The presented data clearly shows a strong dependence on incidence angle in addition to Reynolds number lapse. At the 5.8° incidence angle, the increased loading and mild favorable pressure gradient on the pressure surface of the blade helps keep the flow attached. Overall, the strength of the adverse pressure gradient along the pressure surface tends to increase as incidence angle is decreased. Separation near the trailing edge of the suction surface occurs consistently at the 50,000 and 66,000 Reynolds numbers for the three incident angles presented.

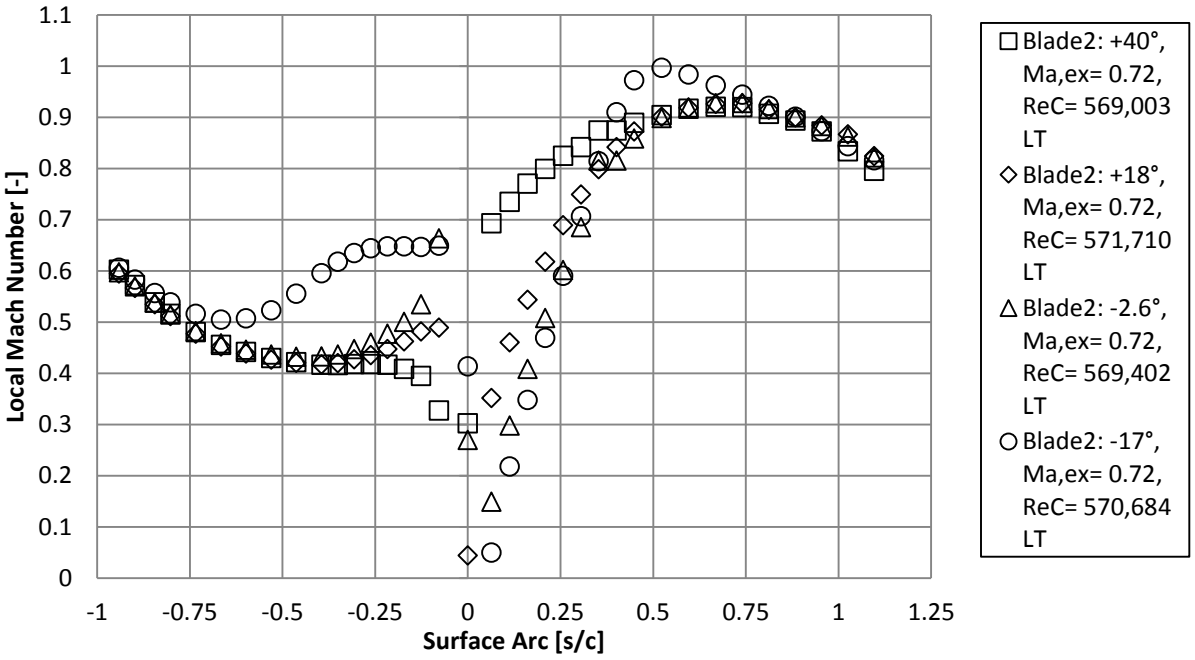

Figure 24: Effect of incidence angle on isentropic Mach distribution for Blade 2.

However, the onset of the separated flow moves downstream as incidence is increased from -51.2° to 5.8°, suggesting that the adverse pressure gradient decreases in strength with increasing incidence.

Figures Figure 24 Figure 25 show the effects of incidence variation on isentropic Mach distribution at 568,000 Reynolds number and 50,000 Reynolds number, respectively. Inlet angles of -17°, -2.6°, 18° and 40° are presented in each of the figures. The loading on the pressure surface and suction surface are clearly affected as the inlet angle is decreased from 40° to -17° for all Reynolds numbers. The trend shows that as incidence is decreased, the loading on the pressure surface is increased and the loading on the suction surface is also increased. Leading edge separation on the pressure surface is evident in Figure 24 at the -17° inlet angle, however it remains attached at the higher incidence angles in spite of the strong adverse pressure gradient seen at the 18° inlet angle. The stagnation region has also shifted upstream along the

leading edge of the suction surface from the origin of surface arc location at 40° to about 0.0635 at -17°. At the 50,000 Reynolds number in Figure 25, the flow characteristics around the leading edge of the pressure surface are strongly influenced by the incidence angle. The rapid deceleration after the overspeed region allowed a separation bubble to form at the -17°, -2.6° and possibly the 18° case as well. The location of the mean reattachment moved downstream as the blade incidence was decreased. A separation bubble also formed along the suction surface throughout the range of incidence angles seen in Figure 25. Reattachment of the separation bubble was again pushed downstream as incidence was decreased from 5.8° to -51.2°.

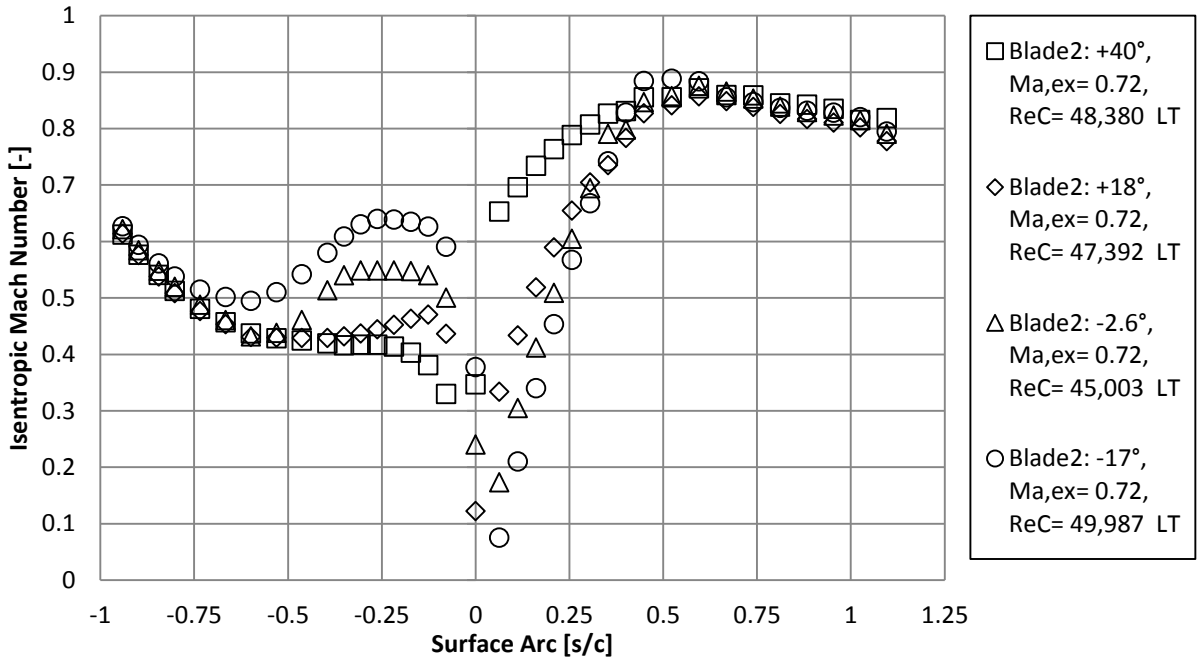

Figure 25: Effect of incidence angle on isentropic Mach distribution for Blade 2.

4.2.3 Effect of Free-stream Turbulence

The effect of free-stream turbulence has also been investigated in this study. The nominal turbulence intensity has been estimated to be about 4.0%, whose intensity is dependent on the free-stream velocity which varies with the inlet angle. Data in Figure 26 shows the effects

of free-stream turbulence on the isentropic Mach distributions at the incidence angle of 0°. There are no appreciable differences in the blade loading seen on either the pressure surface or the suction surface; a similar comparison can be seen in the 40° data presented in the Appendix. However, at the -36.8° incidence angle seen in Figure 27, significant affects can be seen on flow near the pressure surface. The separation bubble, which was present at the low turbulence intensity case, has been energized by the turbulence kinetic energy and mixed out. This acts to decrease the loading along the pressure surface, therefore improving the performance as the losses have been mitigated. Even more substantial changes in the flow are seen in the midspan Mach distributions at the -51.2° incidence angle in Figure 28. The separation bubble on the pressure surface was again suppressed via turbulent mixing at the leading edge.

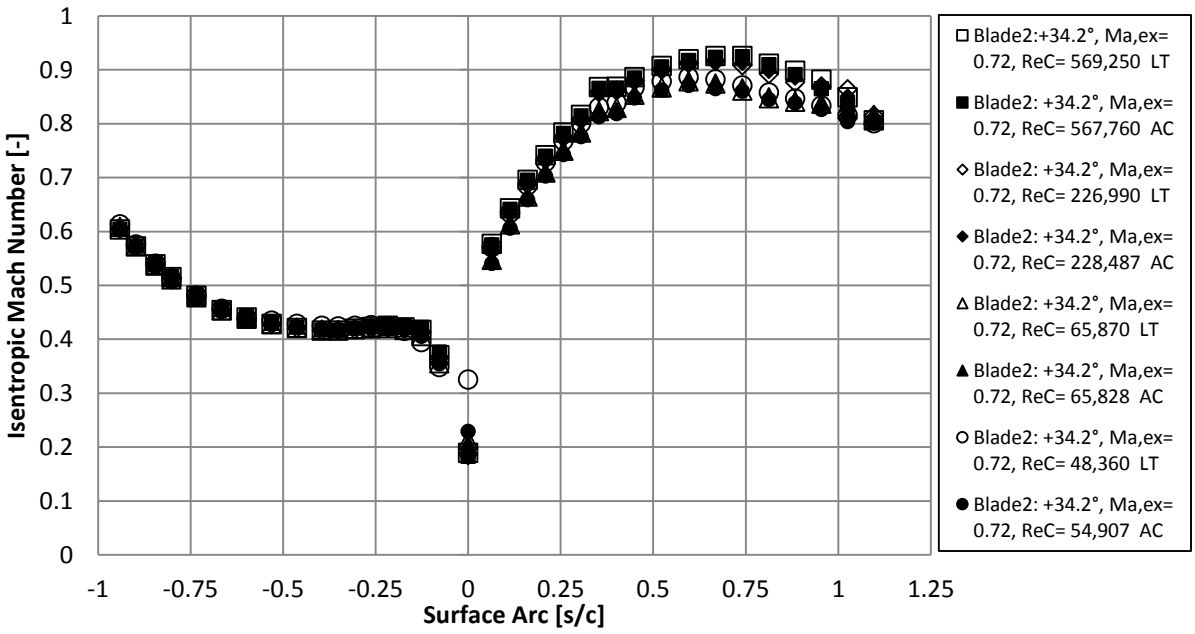

Figure 26: Effects of free-stream turbulence on midspan isentropic Mach distributions at 0° incidence.

The overspeed region near the suction surface has been affected by the free-stream turbulence as well, and the leading edge separation bubble has been mixed out. As a result, the favorable

pressure gradient is extended further along the suction surface at the 227,500 and 568,000 Reynolds numbers and the trailing edge separation bubble appears to have been weakened appreciably. Additionally, the presence of free-stream turbulence significantly weakened the suction surface separation bubble at the 50,000 and 66,000 Reynolds numbers.

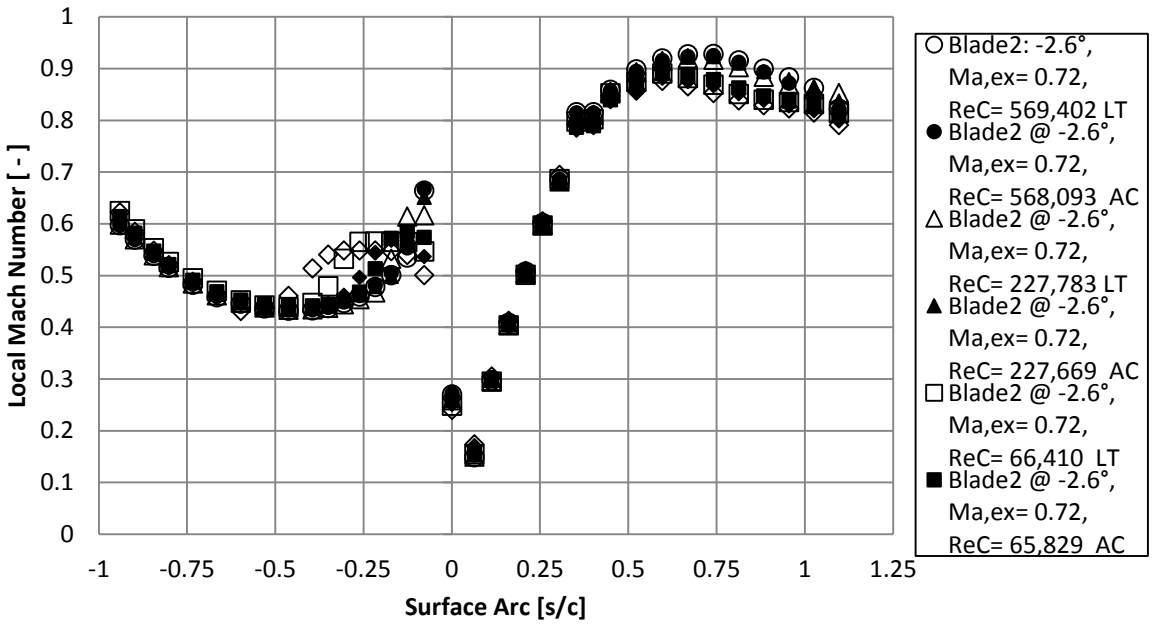

Figure 27: Effects of free-stream turbulence on midspan isentropic Mach distributions at -36.8° incidence.

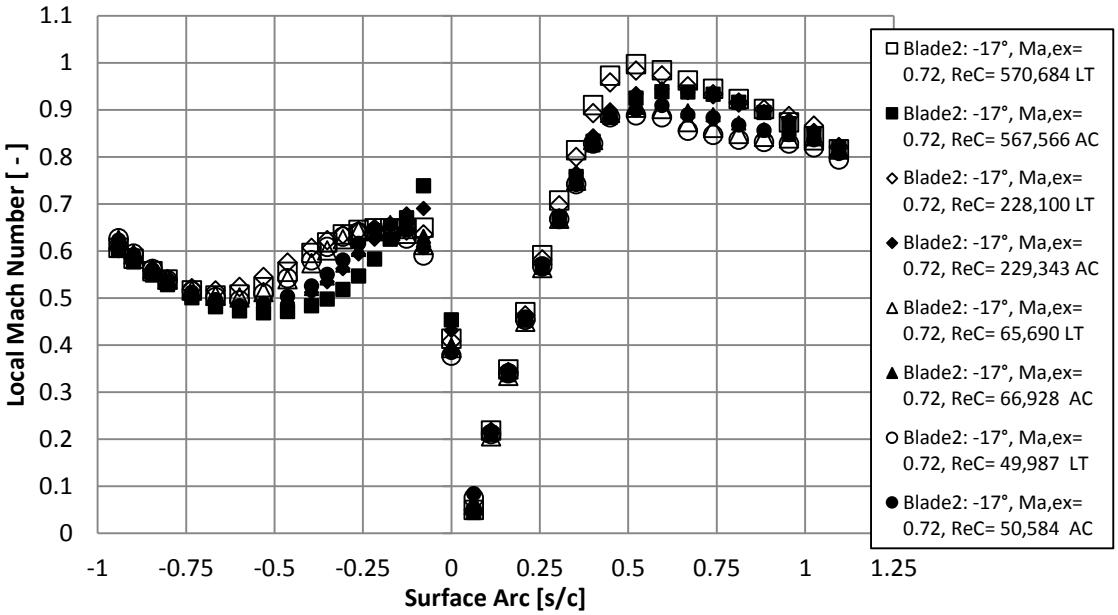

Figure 28: Effects of free-stream turbulence on midspan isentropic Mach distributions at -51.2° incidence.

4.2.4 Thwaite's Analysis of the Blades

Thwaite's Analysis was performed on Blade 2 using the isentropic Mach number data for the 34.2° and -12° inlet angles to estimate the location of separation of the boundary layer. The effects of Reynolds number on acceleration can also be seen in Figure 29 at the -34.2° inlet angle under low turbulence where the influence of the resulting acceleration on transition will be explained. The figure shows the acceleration parameter, K, plotted as a function of surface arc over the range of Reynolds numbers. Note, the data near the leading edge has been truncated to enhance the resolution of the pressure surface and suction surface. The acceleration parameter is defined in Equation (9) as,

$$K = \frac{v}{u_\infty^2}\frac{du_\infty}{dx} \qquad (9)$$

where ν is the kinematic viscosity, u_∞ is the local surface velocity, du_∞ is the differential change in surface velocity and dx is the differential change in surface length. Relaminarization of the

turbulent boundary layer is said to have occurred when the acceleration parameter exceeds $3 \cdot 10^{-6}$. There is a clear Reynolds number dependence on the acceleration parameter as the flow is more highly accelerated along the pressure surface at the 50,000 and 66,000 Reynolds numbers. Conversely, the flow is highly decelerated near the suction surface trailing edge where K falls below zero, indicating that the flow is susceptible to separating. This data supports the conclusions that were drawn from the isentropic Mach distributions from Figure 26.

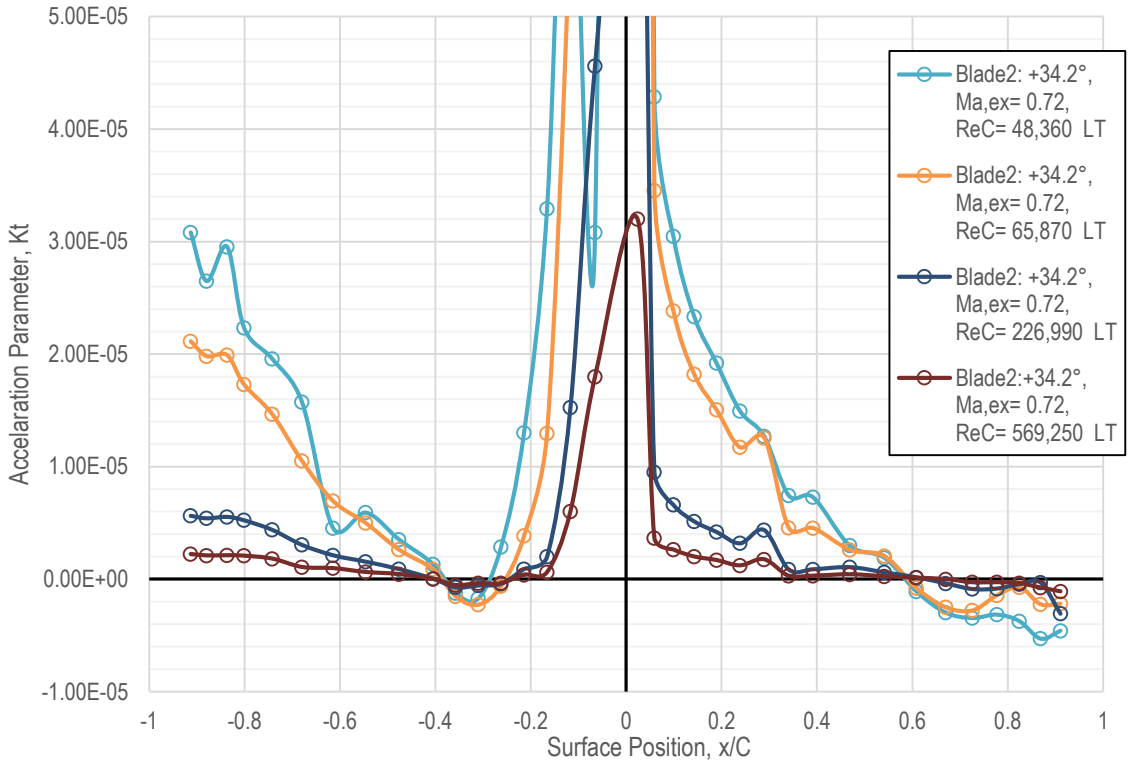

Figure 29: Acceleration parameter as a function of Reynolds number for 34.2° inlet angle under low turbulence.

A closer look of the transition process for this condition can be seen in Figure 30 which depicts the separation and transition criterion along the suction surface of the blade. The data represents the conditions at the 34.2° inlet angle under high turbulence over the range of Reynolds numbers. The pressure surface was omitted given the uniform pressure distribution over the

range of Reynolds numbers. The transition criterion from Mayle [24] was used to calculate the onset of transition based off the momentum thickness Reynolds number which can seen in Equation (10):

$$Re_{\theta Tr} = 400\, Tu^{-\frac{5}{8}} \tag{10}$$

where Tu is the turbulence kinetic energy in percentage.

Thwaite's acceleration parameter, λ, was used to calculate the onset of separation, as seen in Equation (11):

$$\lambda = \frac{\theta^2}{v}\frac{dU}{dx} \tag{11}$$

where θ is the momentum thickness, υ is the kinematic viscosity and $\frac{dU}{dx}$ is the local velocity gradient about the surface of the blade. The flow is said to have separated when λ falls below -0.086.

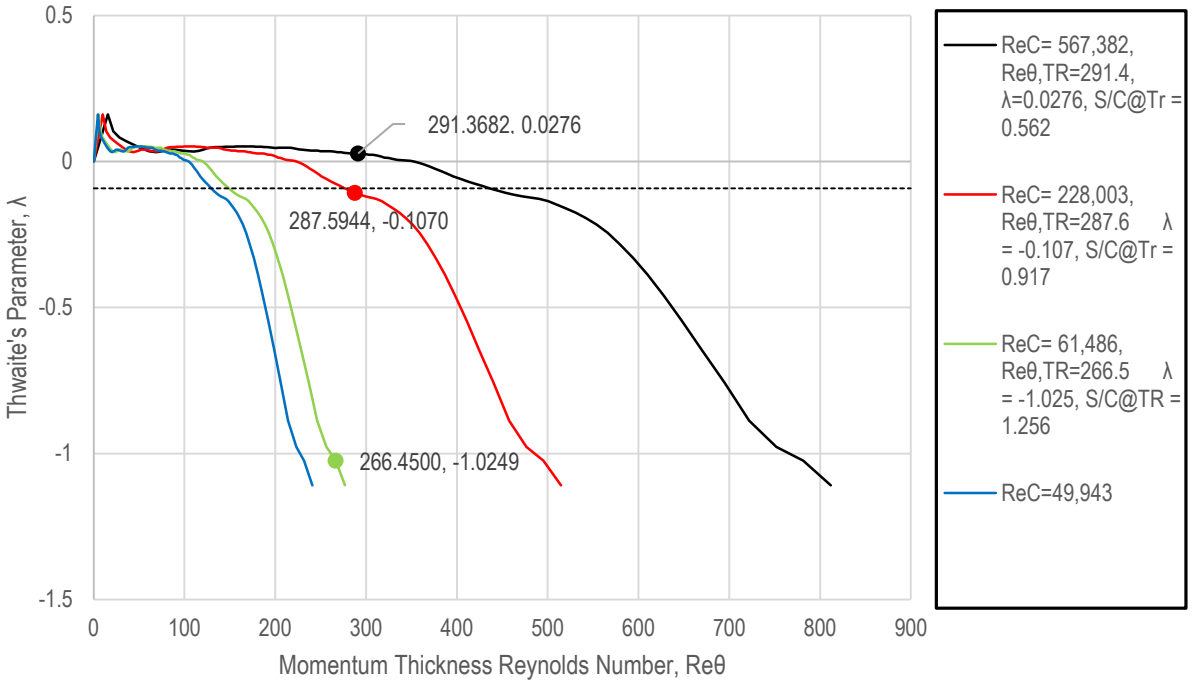

Figure 30: Separation and transition criterion as a function of Thwaites parameter and momentum thickness Reynolds number.

The filled in symbols in Figure 30 indicates the onset of transition, as defined by Equation 10. The dashed line represents the threshold for separation at $\lambda = -0.086$. At the 568,000 Reynolds number, the flow is transitional before the point of separation. At the 227,000 Reynolds number, transition is shown to occur just after the point of separation. This would suggest that a short laminar separation bubble exists at a surface arc location (S/C) of 0.917. However, at the lowest Reynolds numbers, 50,000 and 66,000, the data would suggest the flow for much of the suction surface is separated and transition is unlikely to occur. The data also suggests that the 4.0% turbulence intensity produced by the mock aero-combustor does not produce enough turbulence to affect the onset of transition, with the exception of the 568,000 Reynolds number case. A wake generator may be a means to increase the free-stream turbulence intensity in this facility. This increased levels of turbulence would enhance the rate of spot production which could potentially induce transition before transition.

4.3 Inlet Boundary Layer Measurements

The boundary layers were measured over the full range of Reynolds numbers to determine their influence on the overall losses in the cascade. Out of the four boundary layer rakes, two were used in the analysis and were positioned at the ½ passage location at ¼ axial chord upstream of Blades 2 and 3. Thwaite's analysis was used to develop an estimate of the momentum thickness Reynolds number and shape factor. The analysis was based off the entry length for the given inlet nozzle and the velocity distribution was calculated from the known inlet and outlet mass flow rates. The local acceleration parameters, Equation (11), were derived from the velocity distribution to determine the local skin friction values, Equations (12) and (13).

$$T(\lambda) = (\lambda + .0863)^{0.62} \tag{12}$$

$$\frac{Cf}{2} = \frac{T(\lambda)}{Re_{\theta}} \tag{13}$$

The estimate for skin friction in (13) was developed from the velocity gradient away from the wall with the assumption that the boundary layers were laminar. The accuracy of the skin friction estimates are expected to be within 10% at the 50,000 and 66,000 Reynolds numbers, however the accuracy falls off significantly at the 227,500 and 568,000 Reynolds numbers. The skin friction estimate for the moderate and high Reynolds numbers were estimated by fitting the data along log law region.

The effects of Reynolds number on the boundary layer, momentum thickness and shape factor are presented in Figure 31, which includes chord Reynolds numbers ranging from 50,000 to 568,000 at an exit Mach number of 0.72 for low turbulence at an inlet angle of 40°. The data were fitted to a log law correlation and Spalding's correlation [60]. As expected, the data

presented in Figure 31 indicates that the boundary layer thickness is significantly reduced at the higher Reynolds numbers. It is difficult to directly measure the thickness of the boundary layers with the five port boundary layer rakes used in this experiment, therefore they are characterized by their respective shape factors, momentum thickness Reynolds numbers and skin friction. By inspection, the boundary layers are especially thin at 227,500 and 568,000 chord Reynolds numbers, given that only the pressure tube positioned nearest to the endwall at a centerline distance of 0.516 mm from the endwall has been shown to measure the outer portion of the boundary layer. The strong acceleration of the flow in the reduction area inlet nozzles is likely responsible for the very thin boundary layers. Whereas, at the two lowest chord Reynolds numbers, 50,000 and 66,000, the rakes captured a much larger portion of the boundary layer just outside of the near wall region.

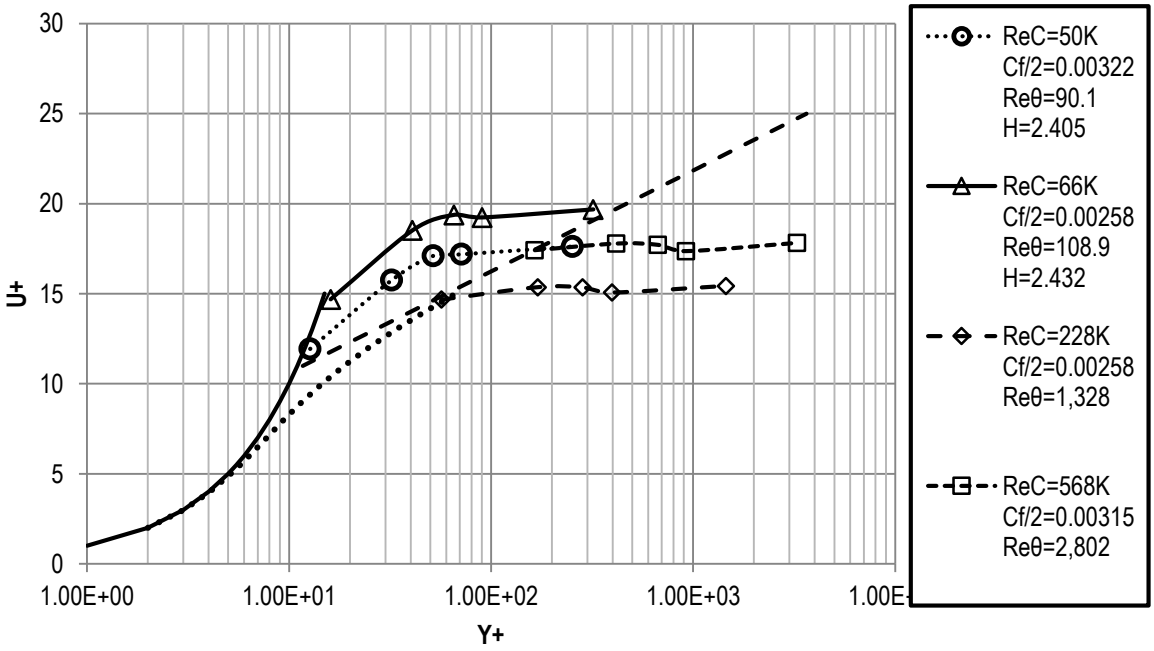

Figure 31: Boundary layer profiles at Mach 0.72, β_1 =40°, and low turbulence.

The data above suggests that the inlet boundary layers for the 50,000 and 66,000 Reynolds numbers are laminar. The shape factors (H) seen in

Table 4 for the low Reynolds numbers implies that the boundary layer is laminar given that it fits within the range of $2.3 < H < 3.70$ for typical laminar shape factors as defined by Schlichting [43]. The boundary layers appear to transition to a turbulent state at the 227,500 and 568,000 Reynolds numbers given the sharp rise in the skin friction coefficient estimate. White [33] provides a graphical representation of the skin friction coefficient plotted against Reynolds number for a flat plate with no acceleration in Figure 32. Generally, the figure shows that a sharp rise in skin friction for a given Reynolds number would indicate that the boundary layer flow is either in a transitional or turbulent state which is qualitatively in agreement with the data in

Table 4.

Table 4: Shape factor, skin friction and momentum thickness Reynolds number estimates for 40° inlet angle under low turbulence.

Re	50,000	66,000	227,500	568,000
H	2.499769	2.517308	-	-
Cf/2	0.002641	2.13E-03	0.0031	0.0028
ReTheta	94.04725	113.1506	1420.549	3047.876

Table 5: Shape factor, skin friction and momentum thickness Reynolds number estimates for 40° inlet angle under low turbulence.

Re	50,000	66,000	227,500	568,000
H	2.367	2.358	-	-
Cf/2	0.00382	0.00307	0.0033	0.00238
ReTheta	87.9	99.1	1,365	2,947

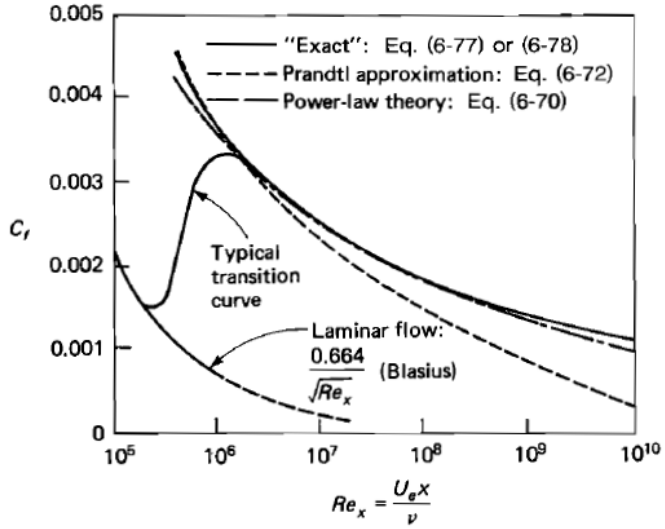

Figure 32: Local skin friction approximations on a smooth flat plate for laminar and turbulent flow [61]

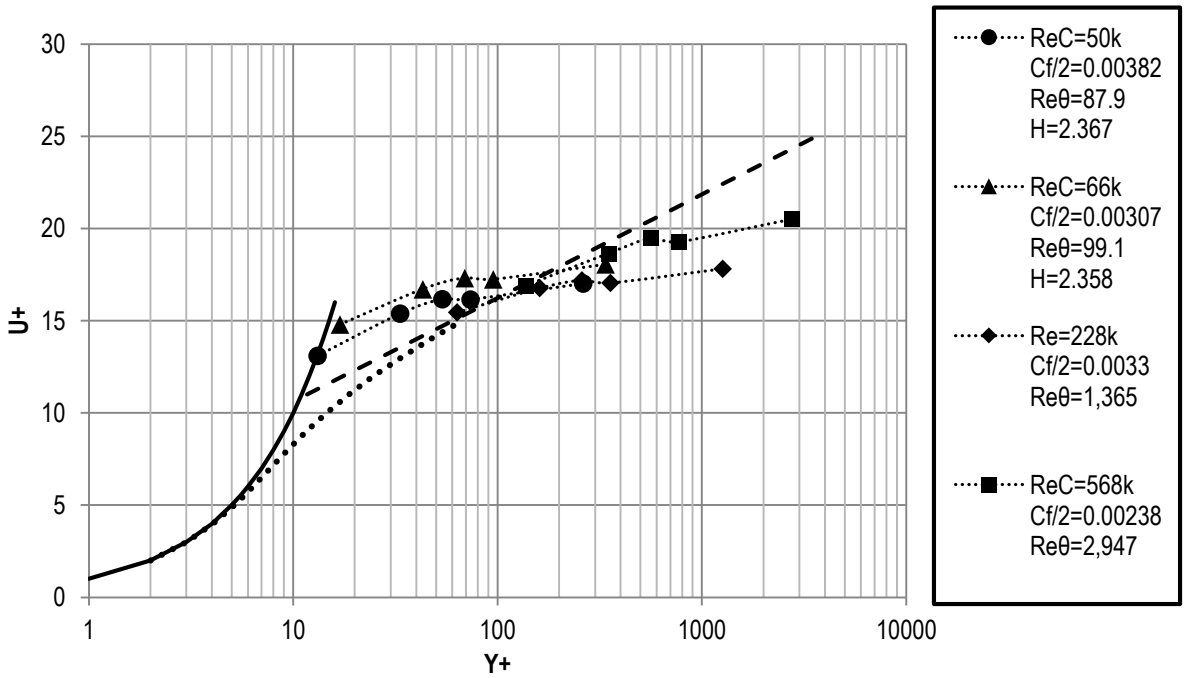

Figure 33: Boundary layer profiles at Mach 0.72, β_1 =40°, and aero-combustor turbulence level.

The boundary layers have been shown to increase in thickness at the AC turbulence condition at the 40° inlet angle. The momentum thickness Reynolds number (Re_θ) is shown to increase with Reynolds number in Figure 33. The estimated Re_θ for the low turbulence case at the 40° inlet angle increases from 87.9 at Re_C of 50,000 to 2,947 at 568,000 Reynolds number. This increase is a result of the higher momentum losses within the boundary layer with respect to the free stream at the high Reynolds number. The same process holds true for the high turbulence case where the momentum losses were very similar to the low turbulence condition.

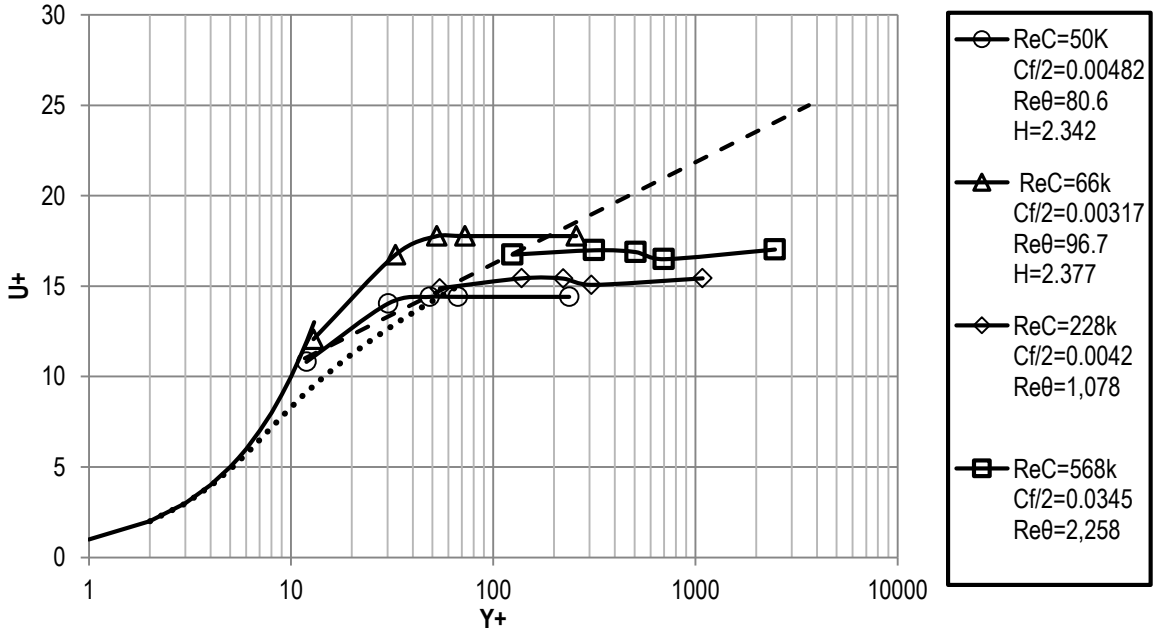

Figure 34: Boundary layer profiles at Mach 0.72, β_1 =-2.6°, and low turbulence.

As the incidence angle was decreased to -36.8° (-2.6° inlet angle), the inlet boundary layers were shown to increase in thickness from the 5.8° incidence (40° inlet) angle. Figure 34 presents the inlet boundary layer profiles as a function of Reynolds number and the profiles have shifted closer to the near wall region. This thickening was likely due to the lower bulk

velocity at the inlet of the cascade for the -2.6° inlet angle which is supported by the data presented in Figure 20. The boundary layer data seen in Figure 35 for the -2.6° inlet under high turbulence show similar trends. The boundary layers at the 50,000 and 66,000 have been shown to increase in thickness due to the enhanced mixing with the near wall fluid. The exact state of the boundary layers were difficult to determine, however the estimated skin friction values suggest either a laminar or transitional state.

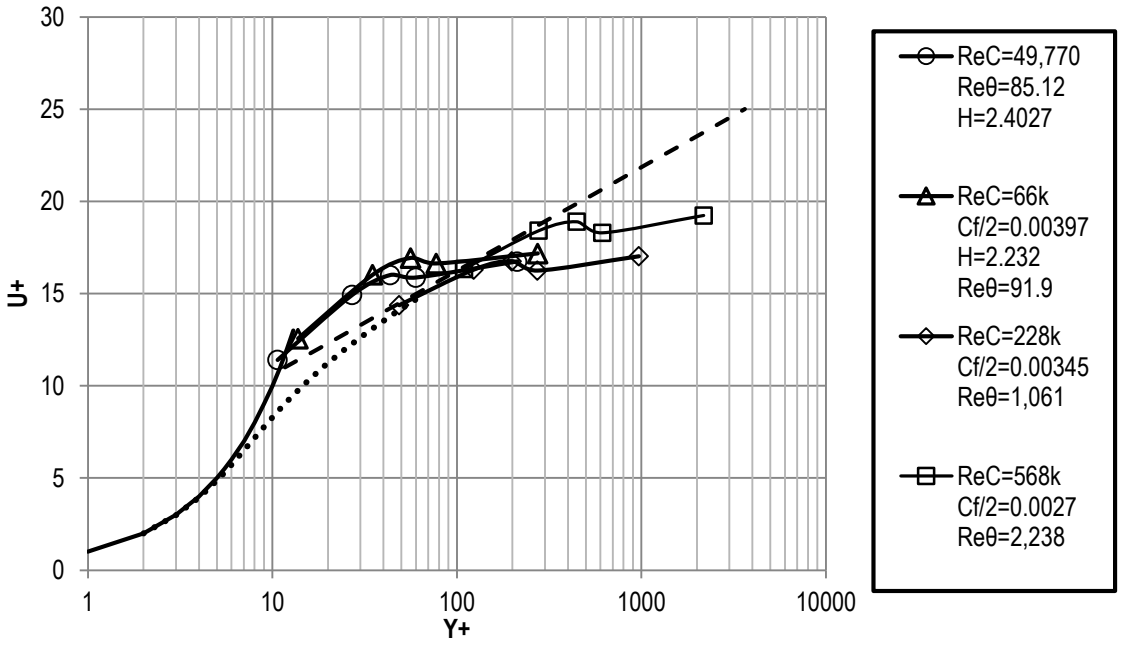

Figure 35: Boundary layer profiles vs. ReC for -2.6 at Mach 0.72 and aero-combustor turbulence level

4.4 Five-Hole Cone Probe Calibration Results

Calibrations were performed on the five-hole cone probe to develop relations of yaw and pitch sensitivities as a function of exit Mach number. The Reynolds number conditions and Mach number conditions were carefully simulated throughout this procedure to achieve the best results. Coefficients of yaw sensitivity are presented in Figure 36 for the exit Mach 0.7 condition

at a chord Reynolds number of 50,000. Overall, there is very good agreement between the experimental data and the predicted values. A third order "odd" function was used to fit a polynomial to the experimental data, as seen in Equation (12). The coefficients developed from these models were then used to formulate an approximation of for yaw sensitivity as a function of Mach number.

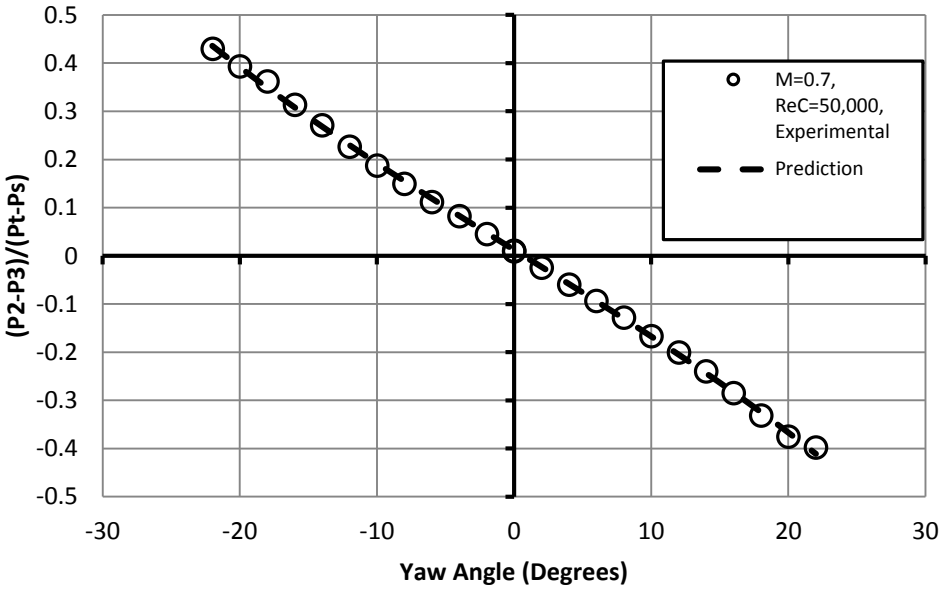

Figure 36: Yaw sensitivity coefficients at exit chord Reynolds number of 50,000

$$Cp_{yaw} = C_1 + C_2\beta + C_3\beta^3 \qquad (1)$$

Where C_1, C_2, C_3 are the calibration coefficients and β is the yaw angle of the probe. The accuracy of the polynomial fit begins to deviate from the experimental data near the outer bands of the calibration range at yaw angles of +/- 14°, especially at the lowest Mach number. A separation bubble may exist near Ports 4 and 5 (lower and upper locations), causing the flow to accelerate as it reattaches near the trailing edge of the probe; this effect will increase the pressure differential as the backside sees a lower pressure. Whereas, the leading edge port approaches a stagnation pressure as it becomes aligned with the direction of the flow. At negative angles,

Port 2 moves towards the direction of the flow as the yaw angle is increased with respect the free stream, therefore the pressure differential between Port 1 is decreased. Alternatively, Port 3 is at the trailing edge of the probe and reads a larger pressure differential due to the accelerated flow. As anticipated, this effect reverses as yaw is adjusted for positive angles.

The effects of changing Mach number can also be seen in the data, as presented in Figure 37 and 38 for the 50,000 and 568,000 chord Reynolds numbers. For all cases, the Mach numbers for which the probe was calibrated were all referenced to the design static pressure that would be seen during the exit surveys. Compressible flow relations were used at the design Mach number of 0.72 at the 50,000 Reynolds number condition to determine the approximate static pressure which was approximately 4050 Pa. This pressure was held constant for the range of Mach numbers during the calibration at the 50,000 Reynolds number. From the data in Figure 37, sensitivity with respect to Mach number appears to increase as the Mach number is decreased below 0.5. The increasing sensitivity may be attributed to, in part, by Reynolds number effects as the probe Reynolds number is reduced by 50% from the design operating condition; the probe Reynolds number seen at Mach 0.4 is 1150, whereas at the design point is at 2070. Experimental studies at these Reynolds numbers are rare and exceedingly so in the compressible flow regime. Lee and Jun [62] examined the effects of Reynolds numbers ranging from 6,600 to 31,700 at Mach 0.33 using non-nulling calibration techniques on a five-hole cone probe. They found significant Reynolds number effects on both yaw and pitch angle coefficients for angles less than 20°. However, the intent in their study was to avoid the effects of compressibility to isolate probe Reynolds number as the only variable, as the limit for incompressible flows are at free-stream Mach numbers less than 0.3-0.5 [63]. Mach numbers near the compressible and incompressible flow regime were examined in this study; the effects

of which are seen at the low Reynolds numbers. At the low probe Reynolds numbers, the effects of compressibility at Mach 0.4 and Mach 0.5 is another contributing factor for the increased sensitivity as seen in Figure 37. At Mach numbers from 0.6 to 0.8, the slopes of the sensitivities are nearly identical and generally linear with only slight variations at the higher yaw angles beyond +/- 12°.

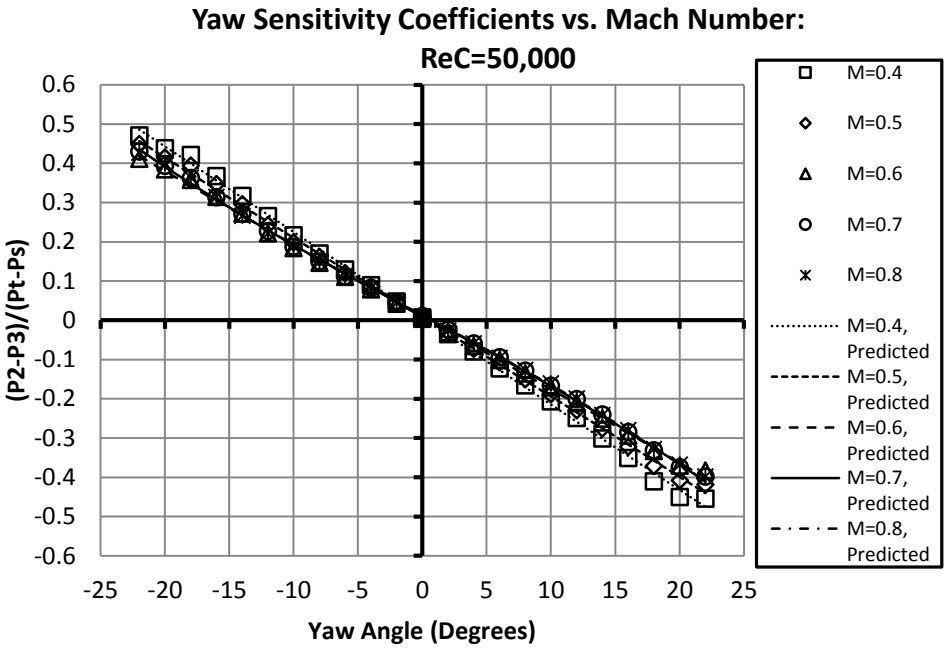

Figure 37: Coefficients of yaw angle sensitivity versus Mach number at exit Reynolds number of 50,000

Moving on to Figure 38, there is a much more consistent trends in the data over the range of Mach numbers than what was seen in Figure 37. At the higher Reynolds number of 568,000, it is shown that the effects of Mach number are greatly reduced as the flow is compressible throughout the measured range. The coefficients for yaw sensitivity are linear in nature for +/- 10°, after which the sensitivity increases with yaw. The most likely culprit for this are Reynolds number effects around the probe seen at higher yaw angles. The effects are much more pronounced at the 568,000 Reynolds number than they were at 50,000. This suggests that

the rate of acceleration around the trailing edge of the probe is greater for the highest Reynolds number than it was for the lowest Reynolds number.

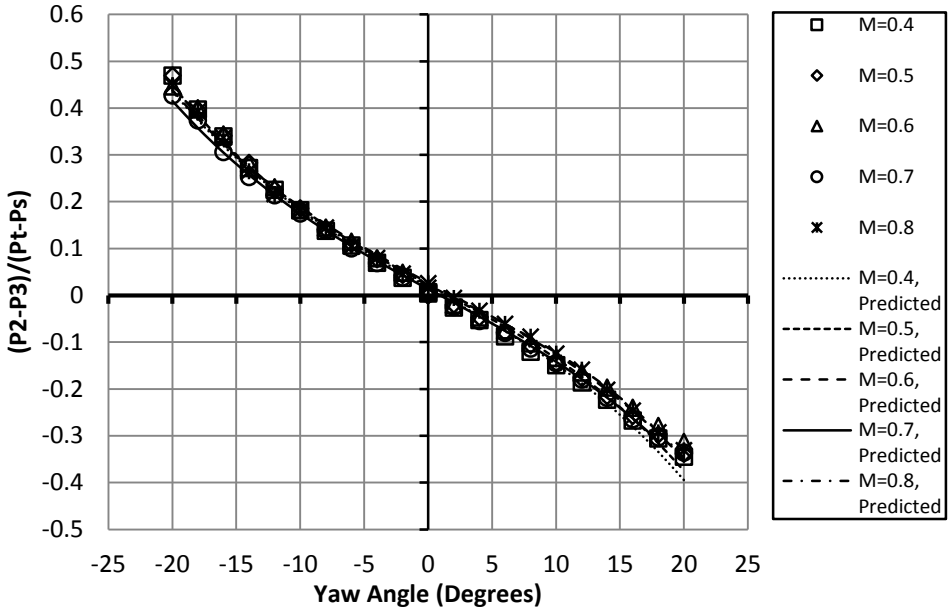

Figure 38: Coefficients of Yaw angle sensitivity versus Mach number at exit chord Reynolds number of 568,000

Figure 40 show the effects of Reynolds number for the calibrations at Mach 0.4 and 0.7, respectively. The Reynolds number effects are seen in Figure 39 show a wide degree of variation, especially at the higher positive yaw angles. Misalignment of the probe during calibration is likely responsible for the slight offset from the origin in the data for the Reynolds numbers at 227,500 and 568,000. A trend of increasing sensitivity with decreasing Reynolds number is present for both Mach conditions, however the differences are much more pronounced at Mach 0.4. The sensitivity coefficients are clearly affected as Reynolds number is decreased from 568,000 to 50,000 at Mach 0.4. A combination of both Reynolds number effects and Mach number effects are responsible for the data seen at the 50,000 and 66,000 Reynolds numbers in Figure 39. In Figure 40, the Reynolds number also appears to have an

influence on the yaw sensitivities at Mach 0.7. The data in the figure illustrated the necessity to account for the varying flow effects seen by probe in order to improve the accuracy of the aerodynamic loss measurements.

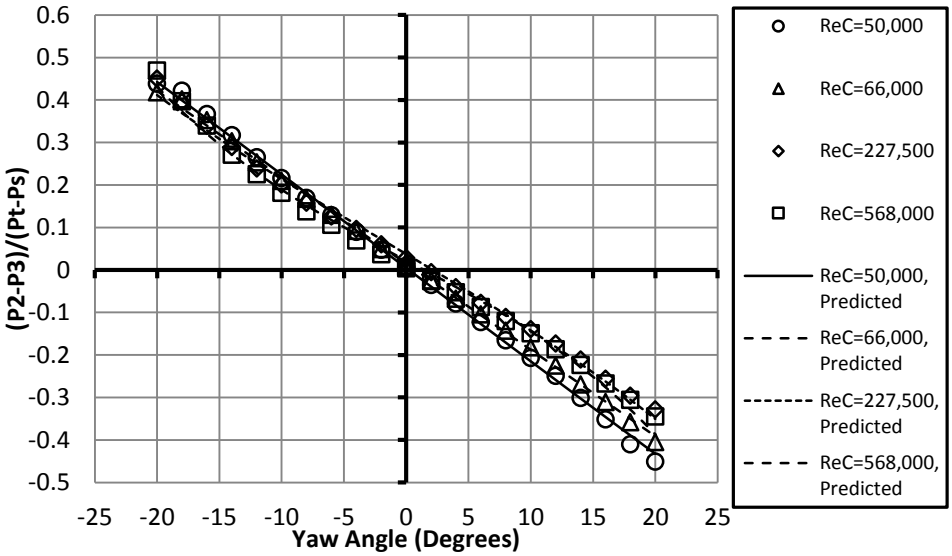

Figure 39: Coefficients of yaw sensitivity vs. Reynolds number at Mach 0.4

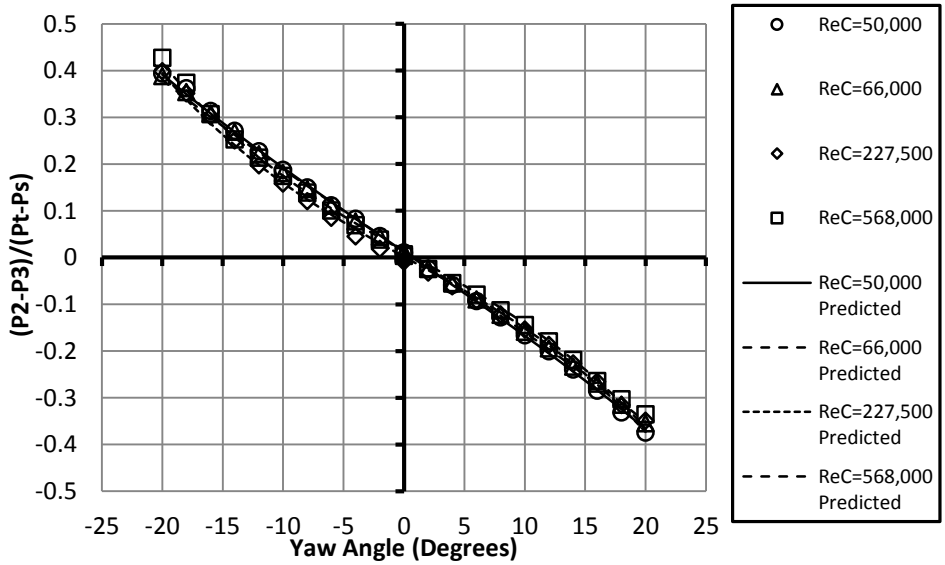

Figure 40: Coefficients of yaw sensitivity vs. Reynolds number at Mach 0.7

Coefficients of total pressure recovery as a function of Mach number were acquired from the calibrations and are presented in Figure 41 and Figure 42 for the 50,000 and 568,000 Reynolds numbers. The data in these figures exhibit good symmetry about the y-axis with a 1.5° yaw offset which will be accounted for within the exit survey analysis in Section 4.5. In Figure 41, there is clear influence of compressibility as Mach number is decreased to 0.4 at the 50,000 Reynolds number. A narrowing of the total pressure recovery loss bucket with decreasing Mach number suggests the probe loses its ability to recover the total pressure as yaw angles are increased beyond +/- 6° due to flow effects around the probe. Similarly, the same process is evident at the highest chord Reynolds number of 568,000 in Figure 42. As expected, the degree of which the Mach number has an effect on the flow at is reduced. The probe recovers the total pressure more effectively at the higher yaw angle, as evidenced by the reduction in total pressure correction. Interestingly, the coefficients appear to be much more symmetric and the offset has shifted from nominally 1.5° to about -0.8°; this may be related to the alignment of the probe during calibration.

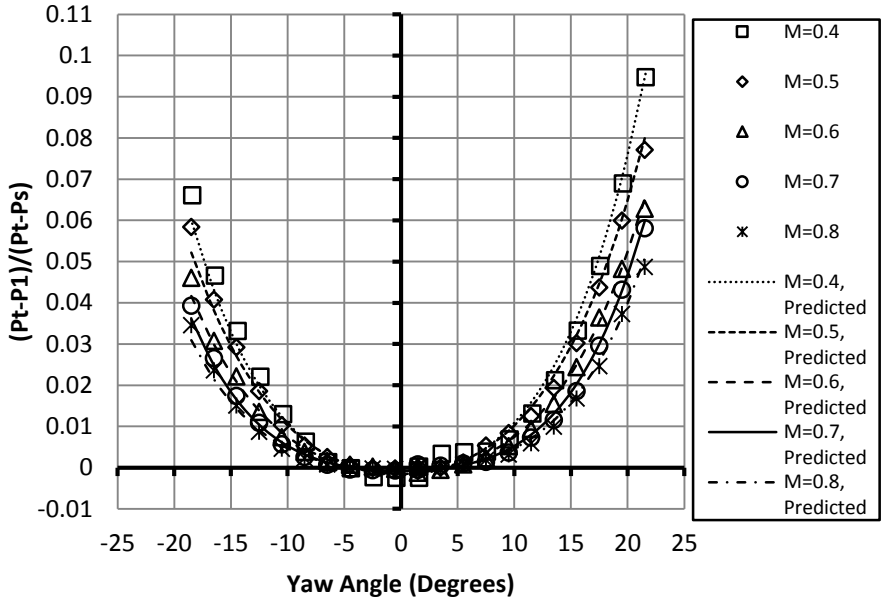

Figure 41: Coefficients of total pressure recovery vs. Mach number at ReC=50,000

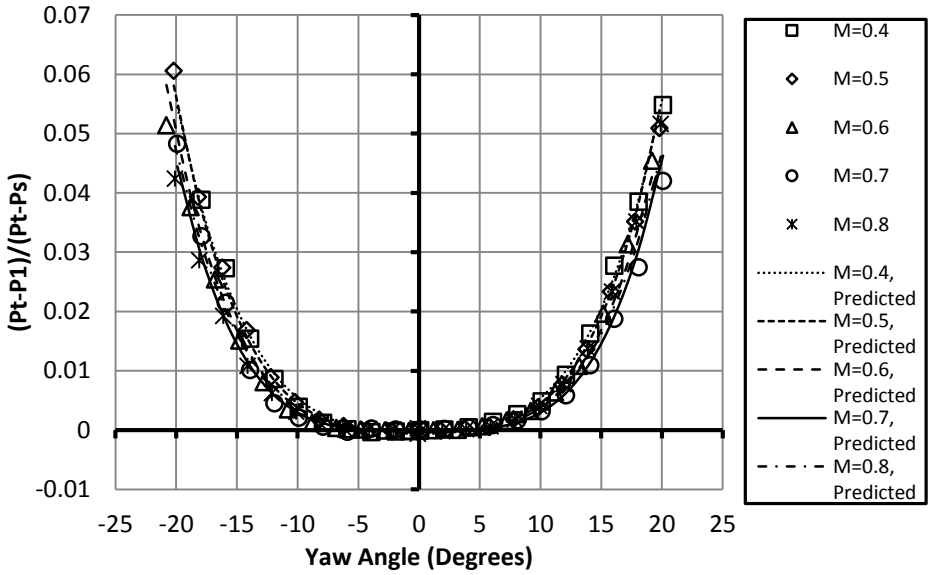

Figure 42: Coefficients of total pressure recovery vs. Mach number at ReC=568,000

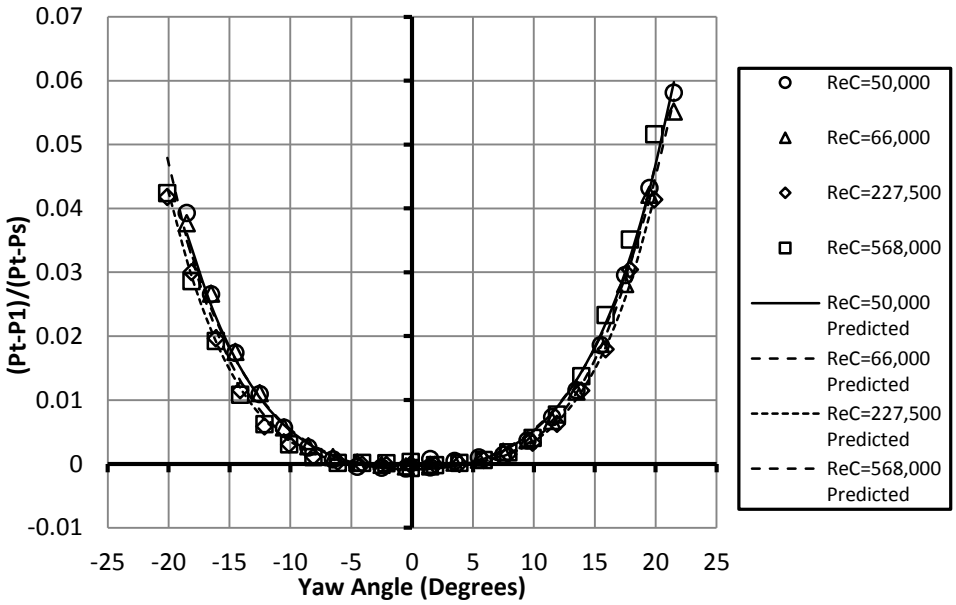

Figure 43: Total pressure recovery coefficients versus Reynolds number at Mach 0.7

The effects of Reynolds number on the total pressure recovery coefficients at Mach 0.7 are presented in 43. From the figure, it appears that the Reynolds number influence is not as significant as Mach number. The total pressure recovery is very consistent over the range of Reynolds numbers with only a slight offset which was due to the probe's alignment during calibration.

The static pressure sensitivity coefficients appear to be affected by Reynolds number and Mach number. Figure 44 shows the response of the static pressure port sensitivity over the range of Reynolds numbers at a constant Mach number of 0.7. Strong Reynolds number effects are seen in the data, especially at the 50,000 and 66,000 Reynolds numbers where separation along the tip of the probe is likely to occur. The data seen in Figure 45 at the 568,000 Reynolds number shows an influence of compressibility and Reynolds number. Overall, the data across the span of Mach numbers exhibit a smooth parabolic trend with some skewness which was influenced by the probe alignment. The sensitivity appears to increase as the Mach number

decreases with noticeable Reynolds number effects occurring at Mach 0.4 due to leading edge separation.

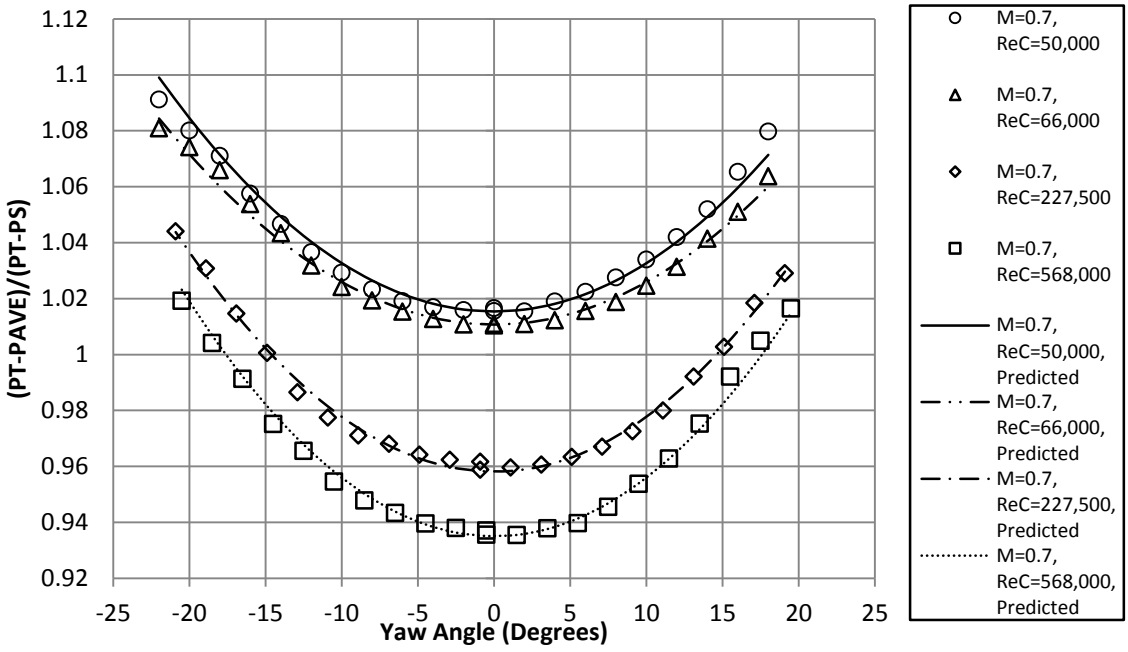

Figure 44: Pressure port sensitivity coefficients versus Reynolds number at Mach 0.7

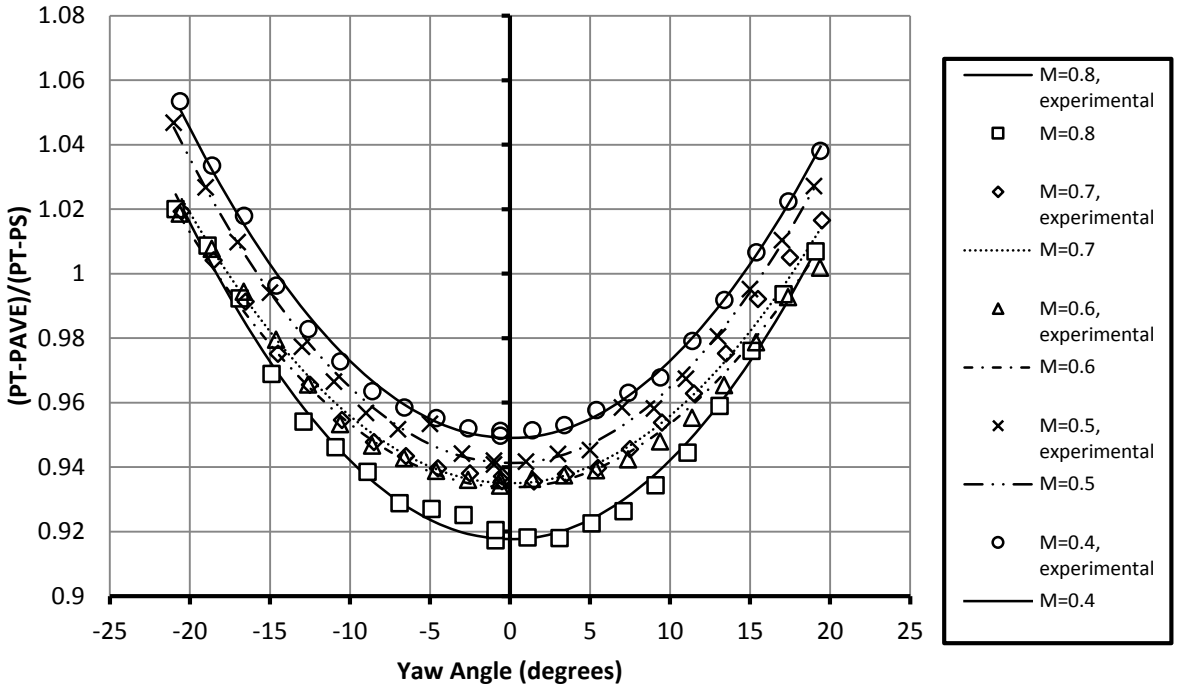

Figure 45: Pressure port sensitivity coefficients versus Mach number at Re_C=568,000

4.5 Aerodynamic Wake Analysis: An overview

The preceding boundary layer analysis, Section 4.3, was initially done to help paint a picture of the history effects of the flow field. The thin inlet boundary layers that were previously measured further enforced the validity of this high speed, compressible flow, wind tunnel facility. The experimental results in this section will be presented in two parts: first, the effects of Reynolds number lapse will be discussed for the low turbulence and high turbulence conditions and the second part will investigate the influence of incidence angle on the aerodynamic losses. The three design incidence angles will be presented in terms of inlet angle, -2.6°, 34.2° and 40°, and the worst case scenario at -17° will also be included in this discussion. The data for each inlet angle are presented in terms of the midspan total pressure loss, area weighted total pressure loss, exit turning angle and contours of total pressure loss. A summary of pertinent data will also be provided for each inlet angle. The conclusion of this section will

include total pressure loss buckets for each Reynolds number which will provide critical performance data over the entire range of incidence angles.

The exit survey analysis was completed in Excel in which the calibration coefficients, derived from the process described in Section 4.4, were implemented for a given Reynolds number and Mach number. A 2nd order polynomial fit was used for the coefficients of yaw angle sensitivity and total pressure loss as a function of Mach number in order to make the appropriate total pressure loss corrections for turning angles beyond +/- 6°. Increased turning is expected in the high loss regions, especially at the low Reynolds numbers, where the local Mach number has been reduced significantly with respect to the free-stream. However, it is expected that 100% of the total pressure is to be recovered for roughly +/- 6° range of turning, which can be seen in Figure 41. Therefore, beyond this range of flow angles, corrections in total pressure need to be made in order to improve the accuracy of the analysis. Equation (13) was used to determine the total pressure loss coefficient.

$$\Omega_{P_T} = \frac{P_t - P_1}{P_{Ave} + (P_t - P_1)} \tag{13}$$

$$P_{Ave} = \frac{(P_1 - P_2) + (P_1 - P_3) + (P_1 - P_4) + (P_1 - P_5)}{4} \tag{14}$$

$$V_\beta = U_\infty \sin(\beta) \tag{15}$$

$$V_\alpha = U_\infty \sin(\alpha) \tag{16}$$

The average differential pressure in Equation (14), P_{Ave}, was calculated from the pressure differentials between the total pressure port, P_1, and the circumferential pressure ports. Equations (15) and (16) were used to calculate the secondary flow velocities for yaw and pitch.

Where β is the yaw angle and α is the pitch angle of the flow and U_∞ is the free stream velocity. These values were then compiled into a 21 by 21 array which were then overlaid on the total pressure loss data in the contour plots using MATLAB. An example can be seen in Figure 46 from which the data was captured at $\beta_1 = 8°$ at the 50,000 Reynolds number condition at low turbulence. The secondary velocity vectors coincide with the main loss vortex system and as well as the secondary loss systems. The color bar on the right of the figure, titled Omega, represents the total pressure loss coefficients with the low loss regions represented in blue and the higher loss regions in red. Figure 46 is used only as an example to illustrate the analysis and a full description of the flow phenomena will be discussed later.

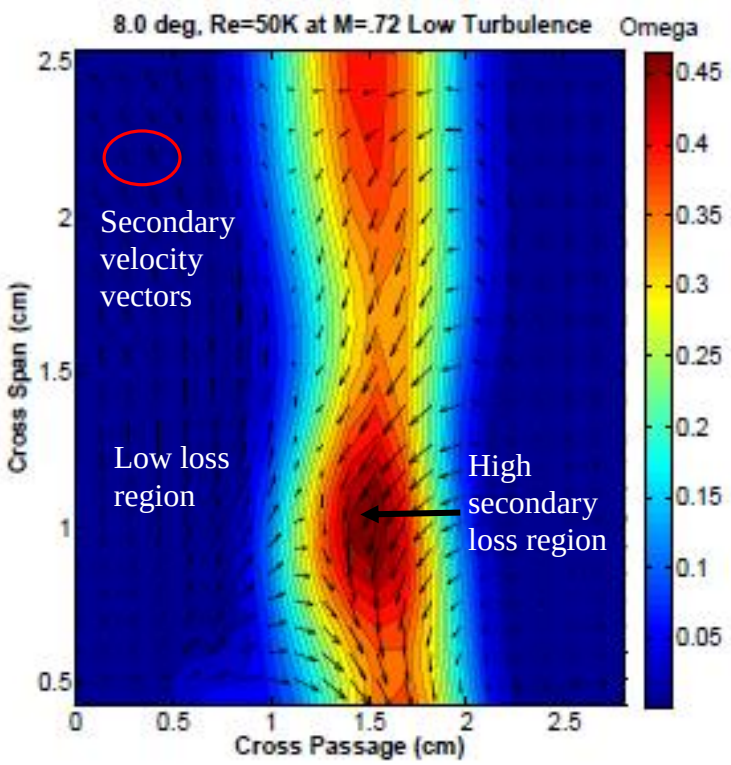

Figure 46: Example of contours of total pressure loss at the 8° inlet angle at the 50,000 Reynolds number under low turbulence.

An alternate method in presenting the loss data is in terms of the kinetic energy loss coefficient, as seen in Equation (17). This equation is a function of the measured kinetic energy versus the ideal kinetic energy. This relation is particularly useful to assess performance for stator vanes and as well as rotor applications as the axial velocity, V, can be easily substituted with the relative velocity. The kinetic energy loss contours and total pressure loss contours are qualitatively similar and an example can be seen in Figure 47 for the 8° inlet angle.

$$\zeta = 1 - \frac{V_{ex,\ actual}^2}{V_{ex,\ ideal}^2} \tag{17}$$

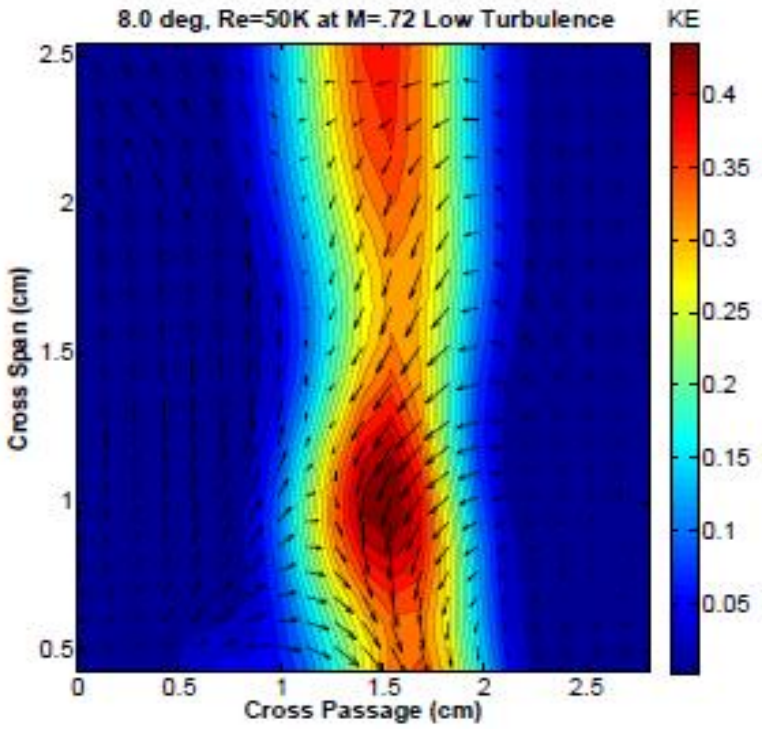

Figure 47: Example of contours of kinetic energy loss at the 8° inlet angle at the 50,000 Reynolds number under low turbulence.

The figure illustrates the similarities between the two methods for calculating the losses. The kinetic energy losses are qualitatively the same as the total pressure losses, however they differ

only in magnitude. More examples of the kinetic energy contour plots are presented in Appendix E.

4.5.1 Reynolds Number and Incidence Angle Effect: Midspan Losses

The midspan total pressure loss data for the low turbulence condition is presented in Figure 48 for the -2.6° inlet angle at low and high turbulence. The left side of the peak seen in the figure represents the suction surface of the blade and the right side depicts the losses from the pressure surface. The open symbols in the figure represent the low turbulence data and the closed symbols represent the high turbulence condition. The width and velocity deficit of the wake is highly dependent on Reynolds number. At the -2.6° inlet angle for the low turbulence condition, the midspan total pressure loss peaks at about 0.443 at the 50,000 Reynolds number and falls to about 0.205 at the 568,000 Reynolds number. As the Reynolds number decreases, friction on the blade surface is increased as the boundary layers thicken, which will cause the flow to decelerate, augment adverse pressure gradients, and make the flow susceptible to separation. The thicker boundary layers at the low Reynolds number will induce blockages and increase the overall velocity deficit, thus broadening the wake. When free-stream turbulence (FST) is introduced, the losses at the midspan have been shown to decease with a slight increase in the wake near the base. The high FST data also shows the presence of background losses along the endwall which may attributed to turbulent mixing with the cross-passage velocity gradient.

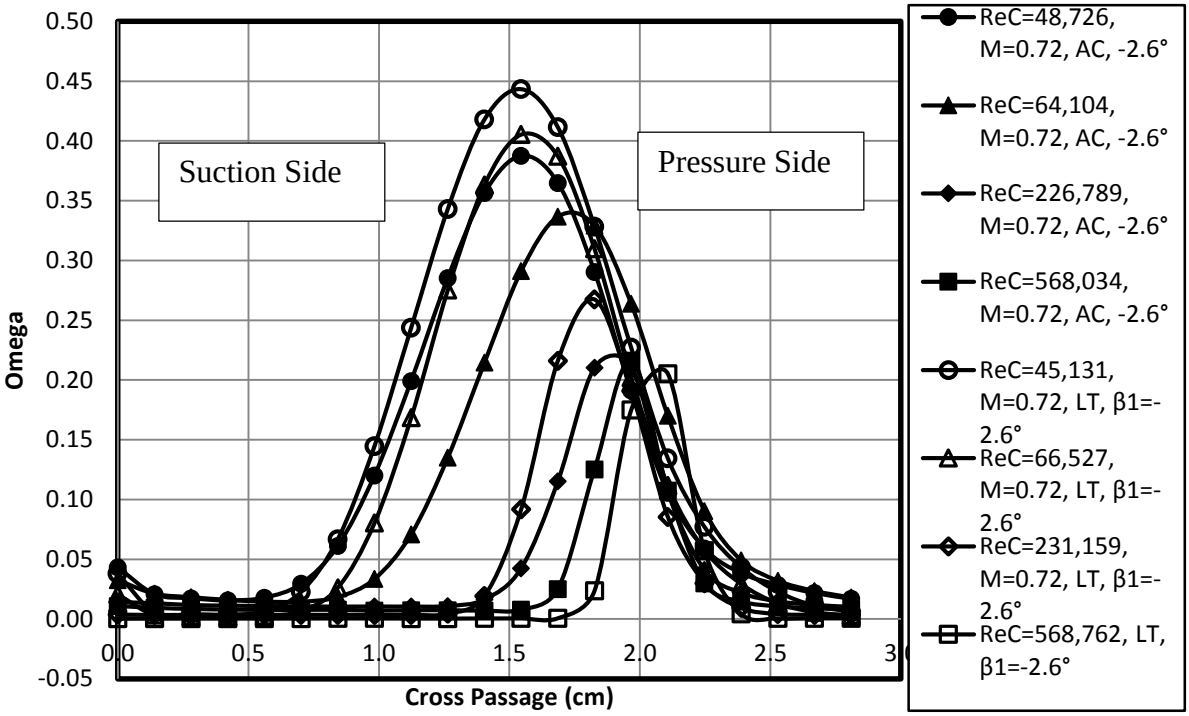

Figure 48: Cross passage total pressure loss vs. ReC at low turbulence and aero-combustor turbulence levels for β_1=-2.6°

Another key aspect of this study was to examine the role of incidence angle variation. The trend in the data in Figure 49 shows that the midspan total pressure losses generally decrease with inlet angle until -2.6° where the losses increase slightly at -17°. At -17° the flow along the pressure surface has clearly separated resulting in a massive loss region which is clearly visible in the figure. The wake from Blade 3 at the -17° inlet angle is also seen in the figure and may be the result of the massive leading edge separation. However, due to facility limitations, the wake from Blade 3 was not measured. Generally, with the exception of the extreme negative incidence angles, the thickness of the wakes decreases with decreasing blade incidence. This may indicate that the secondary loss cores shift towards the endwall at the lower inlet angles.

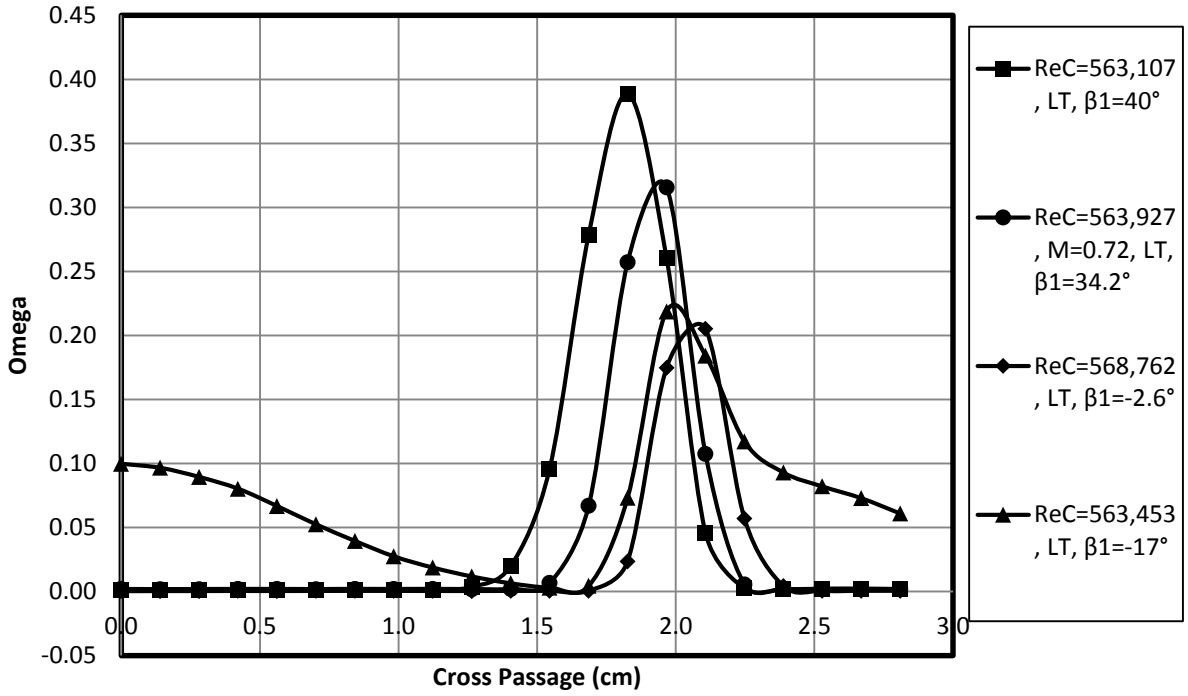

Figure 49: Midspan total pressure loss vs. inlet angle at Mach 0.72, and ReC =568,000

-2.6° Inlet Angle: Low Turbulence

Aerodynamic loss data at ¼ axial chord behind the trailing edge of Blade 2 have been acquired to investigate the effects of Reynolds number lapse over the 57° range of incidence angles at two levels of turbulence intensity, approximately 0.5% and 4.5%. The low turbulence data will be discussed first for the -2.6° inlet angle which lead into the discussion of the high turbulence condition. The most telling visual descriptions of the losses at the -2.6° inlet angle are seen in the total pressure loss contour plots in Figure 50 through Figure 53. Vectors of secondary velocities, which were calculated from Equations (14) and (15) have been overlaid on top of the total pressure losses, Ω, to show the influences of the main passage vortex on the secondary losses as well as other sources of loss. Additionally, the locations of the suction side (SS), pressure side (PS) and passage vortex (PV) have been overlaid on the contour plot in Figure 50.

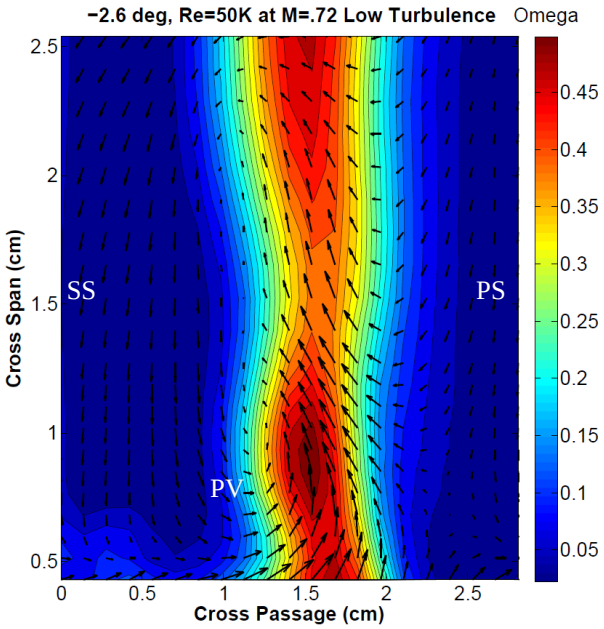

Figure 50: Contours of total pressure loss for Re_C= 50,000 at low turbulence and β_1=-2.6

The figure shows the total pressure loss contours at a chord Reynolds number of 50,000 at an exit Mach of 0.72. At approximately 1 cm off the endwall and 1.2 cm into the passage is location of the main passage vortex core. The peak losses in the passage vortex indicates regions of mixing with the secondary flows. An endwall vortex is also present at this condition, possibly arising from the pressure side corner vortex from the adjacent blade. Another corner vortex may lie near the endwall at 1.9 cm into the passage, given the strong losses. The strong pressure losses near the midspan of the blade would indicate that the flow has separated along the suction surface. This assumption is supported by the isentropic Mach distributions previously seen in Figure 22. Similar results can be seen as the Reynolds number was increased to 66,000 in Figure 51. At this Reynolds number the main loss vortex has upwards towards the midspan of the blade. The intensity of the main losses have shown to decrease and the same holds true for the secondary losses. Although difficult to see, the width of the wake has decreased which supports what was seen in Figure 48.

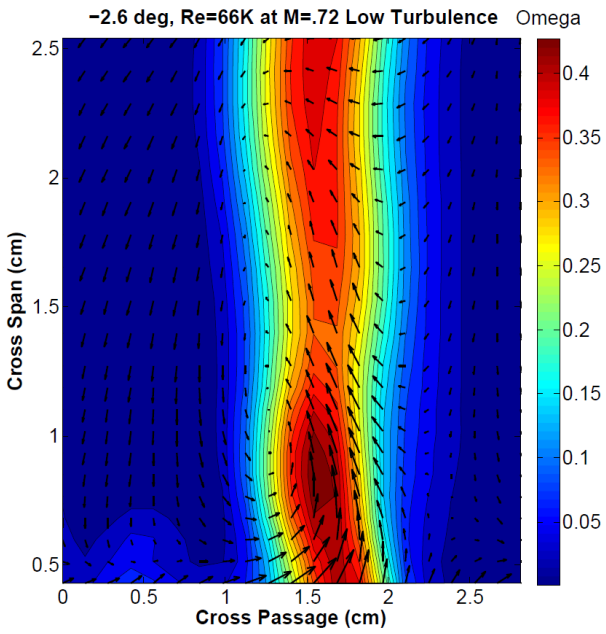

Figure 51: Contours of total pressure loss for Re_C= 66,000 at low turbulence and β_1=-2.6

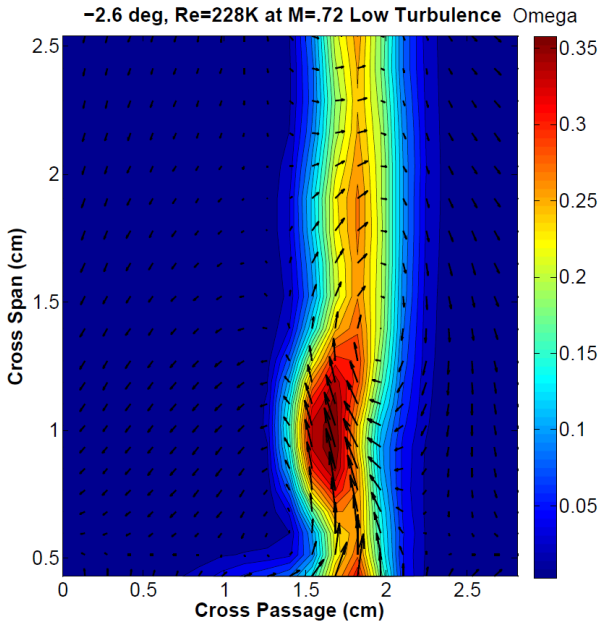

Figure 52: Contours of total pressure loss for Re_C= 227,500 at low turbulence and β_1=-2.6

Significant changes occur in the structure of the wake as Reynolds number is increased to 227,500. The main passage vortex has been shifted towards the endwall to roughly 0.6 cm off the wall as its advancement towards the midspan is suppressed by the thinner boundary

layers. The corner vortex near the endwall is now clearly visible at about 1.8 cm into the passage. In agreement with Figure 22, the flow appears to have separated along the suction surface at the midspan location given that the flow shows three-dimensional behavior in the figure, above. The overall width of the wake has also decreased significantly from the lowest Reynolds numbers and exhibits near two-dimensional behavior.

At the maximum Reynolds number condition at 568,000, the losses have been reduced even further. In Figure 53, the core of the main loss and secondary loss vortices has been shifted towards the endwall. The intensities of the main losses are similar as they were at the 227,500 Reynolds number and the wake is highly two-dimensional above the main loss core. As one should expect, there is a clear Reynolds number effect on the aerodynamic performance of this blade. The reduced losses at this incidence angle and Reynolds number is highly favorable for the takeoff condition as the Reynolds number is expected to relatively high when compared to the cruising conditions.

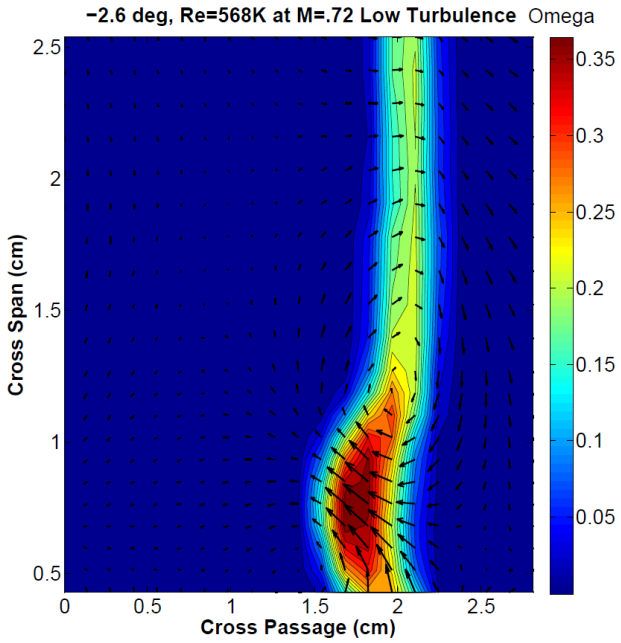

Figure 53: Contours of total pressure loss for Re_C= 568,000 at low turbulence and β_1=-2.6

Spanwise Turning Angle and Total Pressure Loss Coefficients: -2.6° Low Turbulence

Reynolds number can also affect the exit flow turning angle as they are dependent on the magnitude of the primary and secondary losses. The nominal turning angle of the blade is approximately 54.88° and the data in Figure 54 shows overturning near the endwall for all Reynolds numbers. However, they vary significantly with the strongest overturning occurring at the two lowest Reynolds numbers at approximately 50,000 and 66,000. The high degree of overturning is likely due to the cross passage pressure gradient acting on the low momentum endwall boundary layer fluid. Away from the endwall, the overturning reduces around the location of the main loss core. The earlier falloff in overturning at the 227,500 and 568,000 Reynolds numbers implies that the main loss cores have shifted towards the endwall. Overall, the trends show an increase in turning near the midspan as Reynolds number is increased. The

small degree of overturning near the midspan at the 50,000 and 66,000 Reynolds numbers is indicative of the secondary loss core.

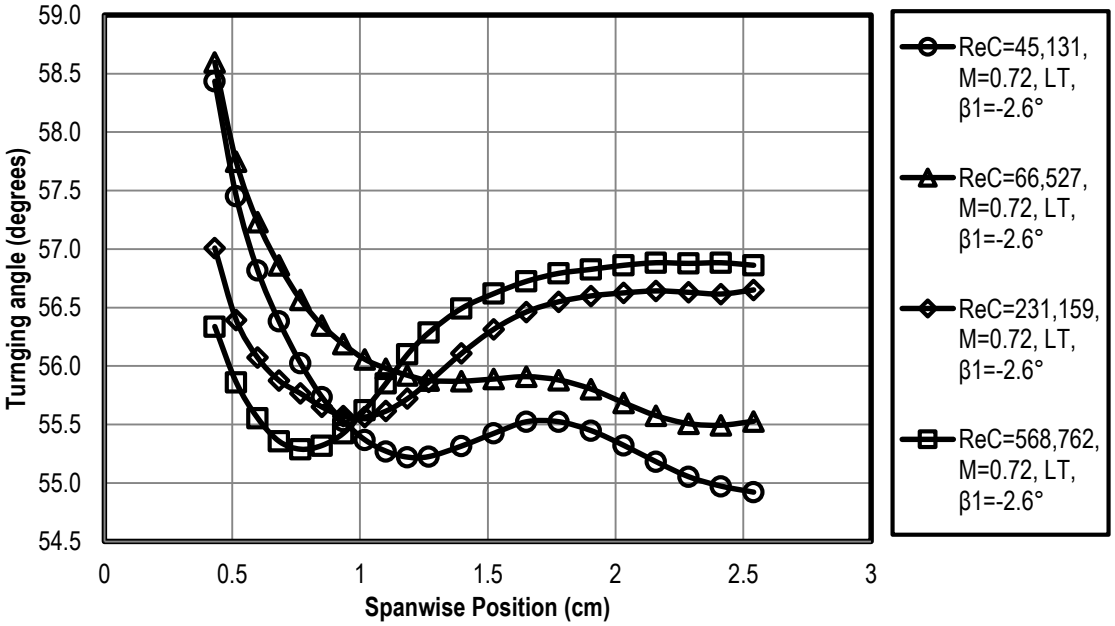

Figure 54: Spanwise turning angle versus ReC at low turbulence for β_1=-2.6°

The spanwise weighted total pressure loss coefficients are presented in Figure 55. In congruence with turning angle plot in Figure 54, the peaks seen near the endwall signifies the presence of a secondary flow vortex near the midspan of suction surface, and possible evidence of a corner vortex at the locations nearest to the endwall. At about 1.4 cm off the endwall for the two lowest Reynolds numbers, the total pressure losses begin to increase and reaches a maximum value of 0.135 at 50,000 Reynolds number and 0.112 at the 66,000 Reynolds number at the midspan. A separation bubble near the suction surface trailing edge is likely responsible for the increased total pressure losses near the midspan. As one should expect, the weighted total pressure losses decrease with increasing Reynolds numbers as they tend to reduce the

boundary layer thickness, suppress separation bubbles and dampen the strengths of secondary flows.

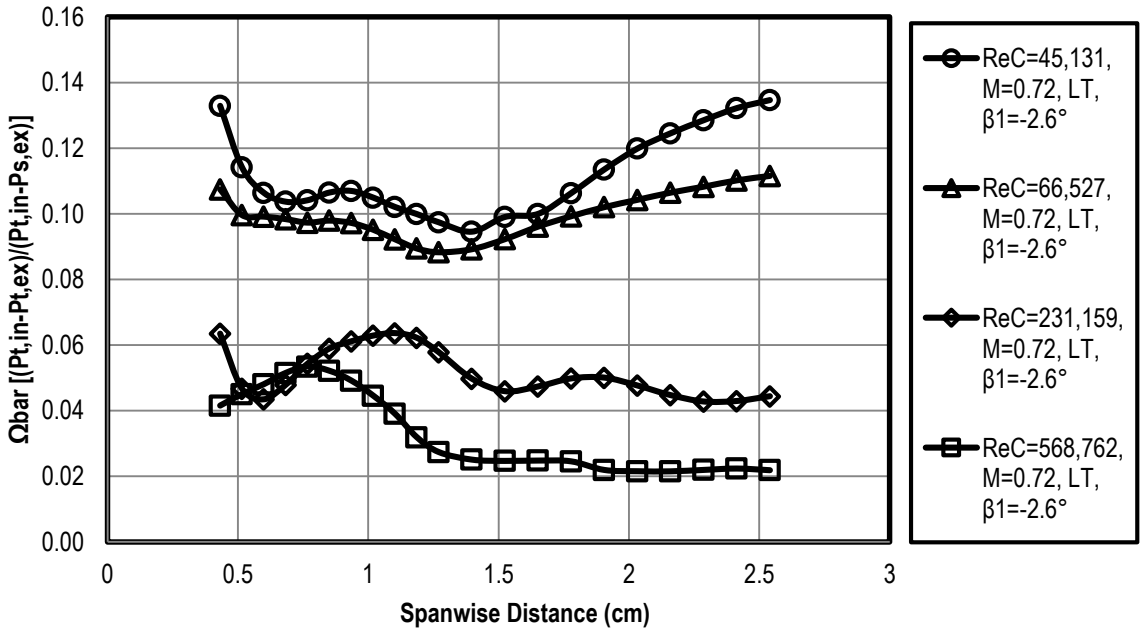

Figure 55: Spanwise weighted total pressure loss coefficients versus ReC at low turbulence for β_1=-2.6°

At the 227,500 Reynolds number condition, the losses are reduced significantly from the lowest Reynolds numbers and the separated flow region appears to have weakened considerable to 0.044. Losses at the 568,000 Reynolds number condition are reduced even further to 0.022, which is highly favorable for the takeoff condition. There is evidence of a weak secondary loss core near the endwall, likely a corner vortex, and the losses diminish quickly in the spanwise direction away from the wall and there are no visible signs of separated flow along the suction surface. The main passage vortex also appears to have shifted towards the endwall with the core centered near 0.77 cm.

-2.6° Inlet Angle: Aero-combustor Turbulence

Remarkable changes occurred as the free-stream turbulence intensity was increased to about 4.5% with the addition of the mock aero-combustor turbulence generator. The weighted total pressure losses, Ω, increased as a result of free-stream turbulence, which saw a ΔΩ of 0.29% at the 50,000 Reynolds number and a ΔΩ of 0.77% at the 568,000 Reynolds number due to the turbulent mixing of the secondary flows. However, the midspan total pressure losses have been shown to decrease with increasing turbulence levels as the secondary flows are mixed out by the passage vortex.

Contours of total pressure loss are presented in Figure 56 and 57 at the 50,000 and 66,000 Reynolds numbers; the wake has broadened from the low turbulence case due to turbulent mixing and the losses appear to be two-dimensional approaching the midspan. Whereas, at the low turbulence condition the flow was highly three-dimensional with the strong secondary flows. While the peak losses have decreased at the higher turbulence level, the overall pressure loss coefficient increased due to the broadening of the wake, resulting from the entrainment of more fluid from the free-stream into the wake flow and also due to the increased skin friction. The main loss core has shifted towards the midspan of the blade where it has effectively mixed out the horseshoe vortex. Losses near the endwall have also shown to increase and are attributed to turbulent mixing across the pitchwise pressure gradient. Another source of loss is introduced at the high free-stream turbulence level is known as the "background loss" whose role in the total pressure losses near the endwall is significant. The velocity vectors near the endwall shows the transport of fluid across the velocity gradient, from the pressure surface of Blade 3 to the suction surface of Blade 2, where it feeds into a strong corner vortex near the pressure surface. These results are in agreement with Ames and Plesniak [6] where they found

that 33-50% of the "background losses" are attributed to turbulent mixing while under the assumption that the production of turbulence is balanced by dissipation. The origins of such losses are believed to be due to turbulence mixing across inertial velocity gradients. Additionally, the apparent background losses are believed to be a result of turbulent redistribution of the endwall losses.

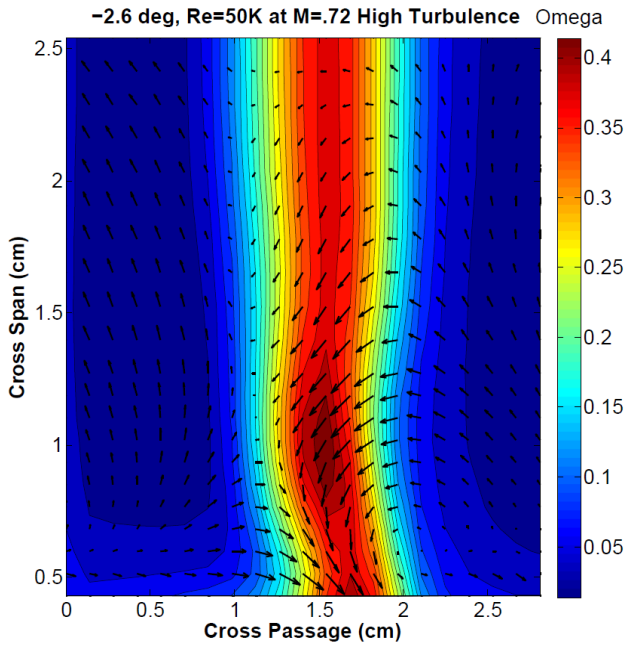

Figure 56: Contours of total pressure loss for Re_C= 50,000 at high turbulence and β_1=-2.6

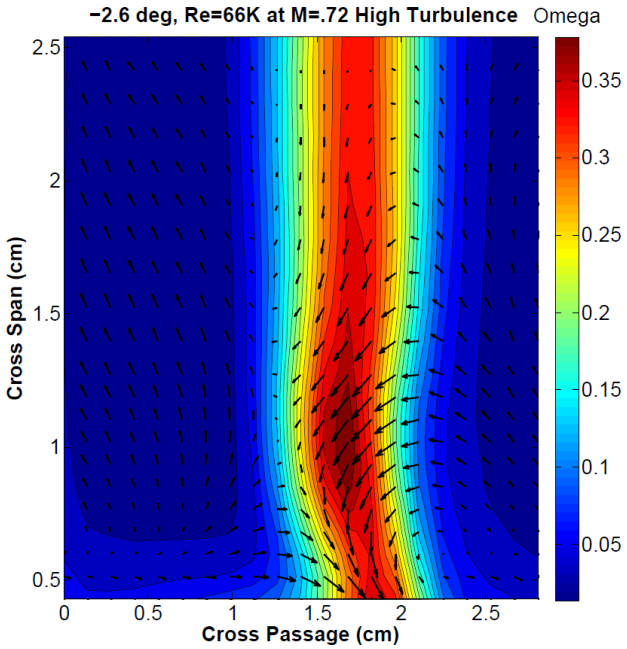

Figure 57: Contours of total pressure loss for Re_C= 66,000 at high turbulence and β_1=-2.6

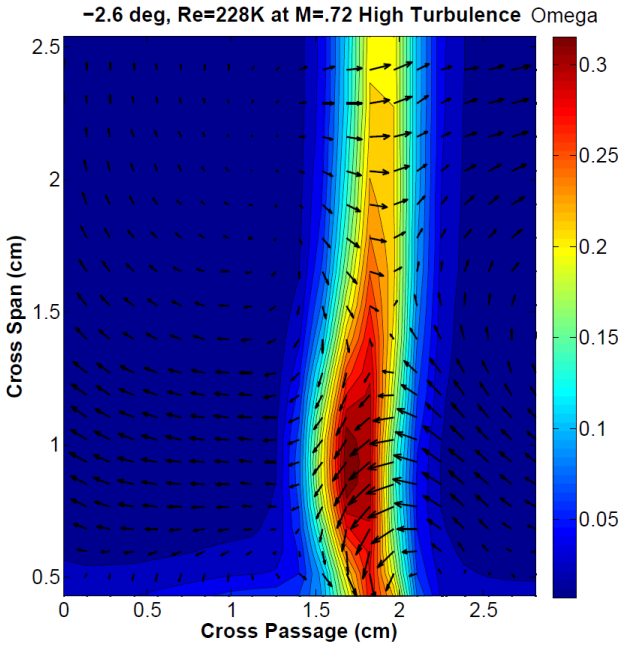

Figure 58: Contours of total pressure loss for Re_C= 228,000 at high turbulence and β_1=-2.6

At the 227,500 and 568,000 Reynolds numbers, and, the main loss core has moved towards the suction surface where it has decreased in size and intensity from the 50,000 Reynolds number. The wake is also thinner due to reduced separation loss on the suction and

pressure surfaces and is in agreement with the trends spotted in Figure 48. The total pressure losses at the 568,000 Reynolds number have been shown to decrease by a $\Delta\Omega$ of 6.3% from the 50,000 Reynolds number as the main core losses have weakened, thereby reducing the size of the wake.

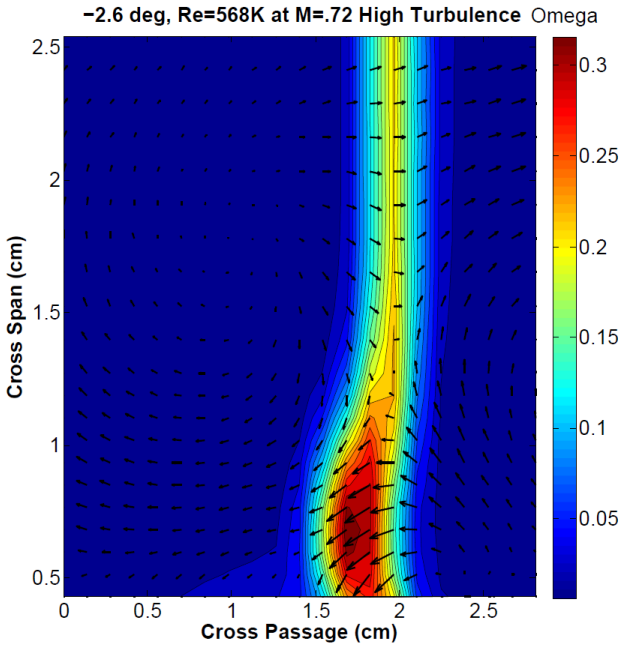

Figure 59: Contours of total pressure loss for Re_C= 568,000 at high turbulence and β_1=-2.6

Spanwise Turning Angle and Pressure Losses: -2.6° Aero-Combustor Turbulence

The spanwise turning at the aero-combustor (AC) turbulence condition from Figure 60 shows an increase in overturning near the endwall. This overturning is likely related to the increased skin friction due to the high turbulence case. In agreement with the low turbulence case, the data also shows the main loss vortex shifts closer to the endwall as Reynolds number increases. The increase in free-stream turbulence has also smoothed out the curves at the low Reynolds numbers and shows much more two-dimensional behavior at the midspan. Turning has also increased at the midspan location for the low Reynolds numbers indicating reduced midspan loading.

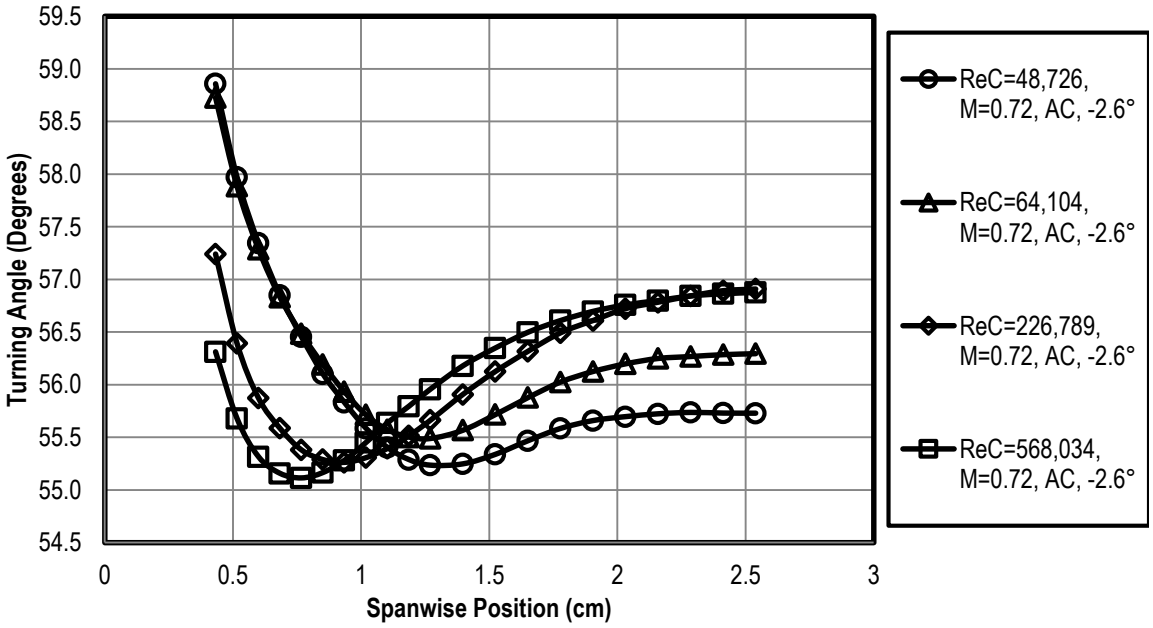

Figure 60: Spanwise turning angle versus ReC at high turbulence for β_1=-2.6°

The aero-combustor turbulence has had a significant effect on the total pressure loss coefficients in Figure 61. The two-dimensional flow near the midspan for all Reynolds numbers are in close agreement with the conclusions derived from Figure 60. The main loss and secondary loss peaks have been effectively smoothed out due the increase in turbulence mixing. The increased total pressure losses near the endwall also show the effects of the background losses. The wind tunnel conditions, aerodynamic losses and turning data are presented in Table 6. The average midspan loss coefficients, Ω_M, were typically lower for the AC turbulence condition than they were for the low turbulence case with the exception of the 568,000 Reynolds number. As expected, the overall mass averaged total pressure losses are shown to increase from the low turbulence condition.

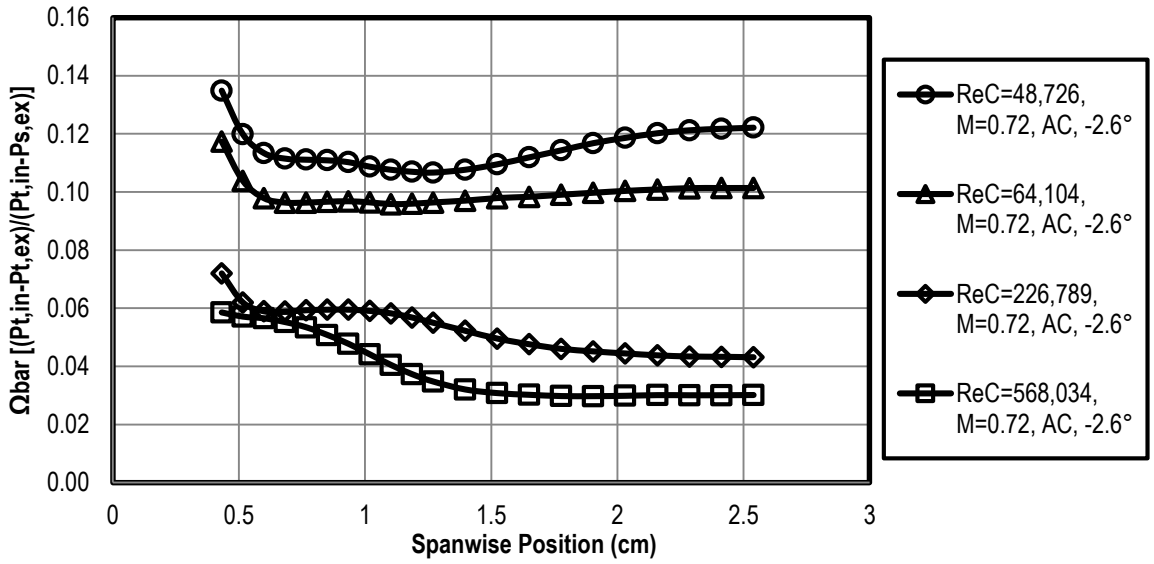

Figure 61: Spanwise wieghted total pressure loss versus ReC at high turbulence for β_1=-2.6°

Table 6: Wind tunnel conditions, mass averaged loss and turning angle for ¼ axial chord exit surveys at -36.7° incidence with aero-combustor and low turbulence conditions as a function of Reynolds number.

-2.6	**High Turbulence**				**Low Turbulence**			
Re_C	48,726	64,105	226,790	568,034	45,131	66,528	231,160	568,763
T_T (K)	325	325	324	326	320	316	311	315
P_T (Pa)	5,848	7,722	27,223	68,777	5,286	7,722	26,354	65,941
V_{ex}	249	248	247	247	249	245	243	243
M_{ex}	0.72	0.72	0.72	0.72	0.73	0.72	0.72	0.72
Ω_M	0.1221	0.1013	0.0413	0.0301	0.1347	0.1116	0.0444	0.0219
Ω_{Ave}	0.1176	0.1018	0.05448	0.0408	0.1147	0.1007	0.0524	0.0331
KE	0.1071	0.092	0.0488	0.0364	0.1043	0.0915	0.0472	0.0298
β_M	55.73	55.30	56.91	56.88	54.92	55.53	56.65	56.86
β_{Ave}	56.34	56.59	56.35	56.20	56.01	56.45	56.37	56.34

34.2° Inlet Angle: Low Turbulence

The effects of incidence angle can be seen as the inlet angle is increased to 34.2°. Figure 62 shows the total pressure loss contours at the 50,000 Reynolds number at the low turbulence condition at Mach 0.72. The main loss core, rotating in the counter clockwise direction, is easily discernable in the figure and is centered at about 1.2 cm off the endwall. The peak losses at this location are about Ω=0.50 where mixing with the secondary flows are maximum. A portion of the corner vortex is also clearly visible in the figure. Like the -2.6° inlet angle, the flow has separated near the trailing edge of the suction surface. As the loading along the pressure surface increased due to the higher incidence angle, a stronger adverse pressure gradient has resulted and thus augmented the size of the separated region. Similar results are presented in Figure 63 at the 66,000 Reynolds number, however the overall losses have decreased slightly.

Reynolds number effects can be seen by the notable reduction in the total pressure losses as the chord Reynolds number is increased to 227,500 and 568,000. At the 227,500 Reynolds number condition in Figure 64, the main passage vortex has lifted off the endwall and weakened considerably. A very pronounced secondary loss core is clearly visible and lies just above the main loss core. At the 568,000 Reynolds number in Figure 65, the main loss core and the secondary loss core appear to have merged closer to one another the losses have decreased. The wake is also thicker near the midspan location than it was for the -2.6° inlet angle as the main passage vortex has lifted off the endwall.

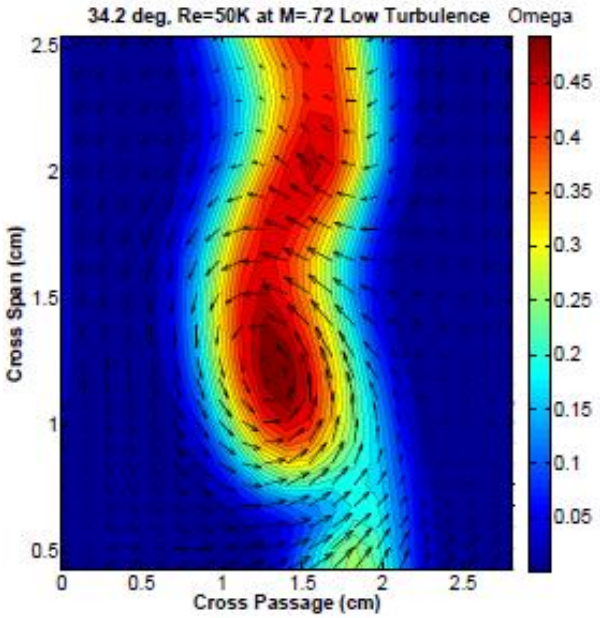

Figure 62: Contours of total pressure loss for Re_C= 50,000 at low turbulence and β_1=34.2°

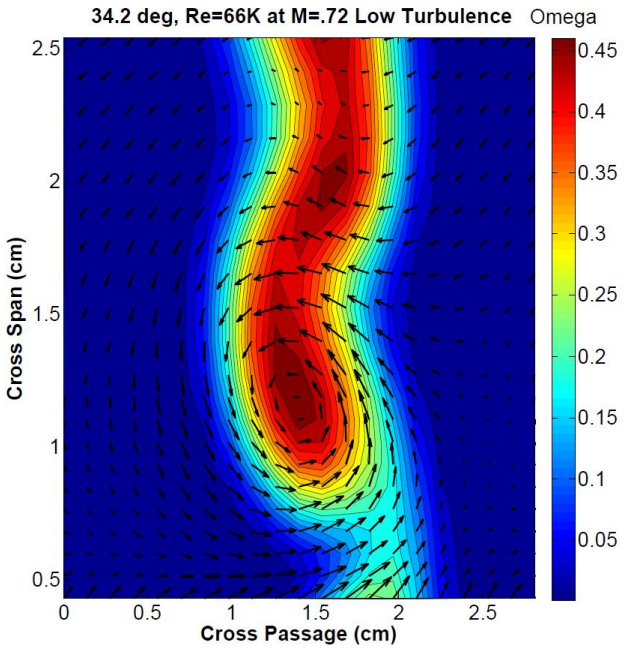

Figure 63: Contours of total pressure loss for Re_C= 66,000 at low turbulence and β_1=34.2°

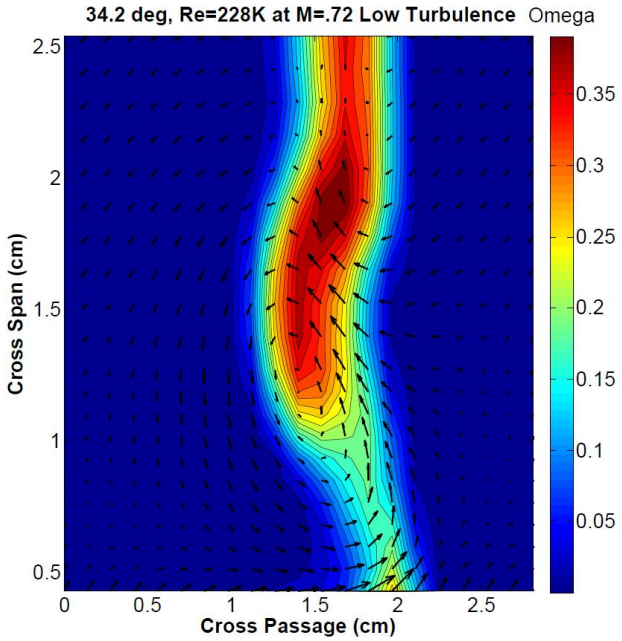

Figure 64: Contours of total pressure loss for Re_C= 227,500 at low turbulence and β_1=34.2°

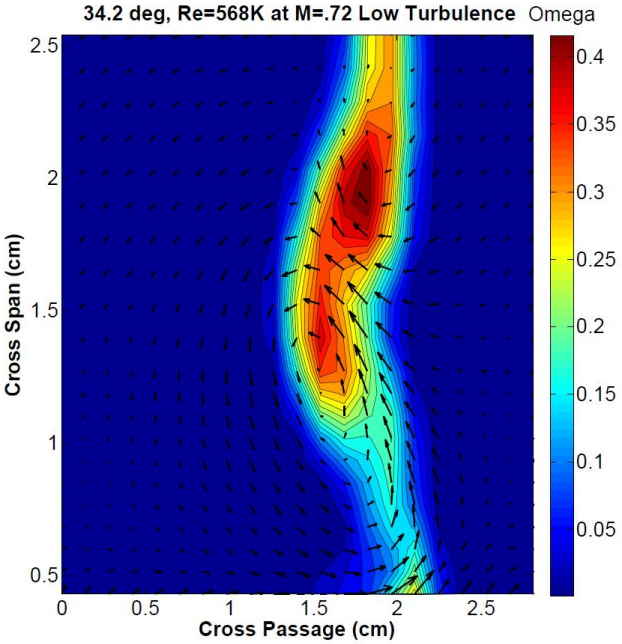

Figure 65: Contours of total pressure loss for Re_C= 568,000 at low turbulence and β_1=34.2°

Spanwise Turning Angle and Total Pressure Loss Coefficients: -34.2° Low Turbulence

Spanwise averaged turning angle data are presented in Figure 66 for the low turbulence condition at the 34.2° inlet angle. The data show much higher turning near the endwall

compared the -2.6° case due to the higher loading. Slight under turning is seen at about 1.65 cm off the endwall and may be attributed to the secondary loss core. As a whole, the flow is highly three-dimensional over the span of Reynolds numbers at this incidence angle when compared to the -2.6° inlet angle (-36.7° incidence). Figure 67 displays the spanwise weighted total pressure losses for the inlet angle of 34.2° (0° incidence). Overall, the losses have increased when compared to the -2.6° inlet angle which is a result of strong secondary losses and detached flow along the suction surface of the blade. Distinct peaks in the data can be seen in the figure, which are likely associated with the spanwise core locations of the secondary flow and passage vortex. The passage vortex is located near the blade's quarterspan location at 1.19 cm off the endwall and has displaced the secondary losses 1.91cm off the endwall for the 50,000 and 66,000 Reynolds numbers. The main loss core has migrated away from the endwall at the 227,500 and 568,000 Reynolds numbers. The secondary losses also appear to have moved closer to the main loss system as the intensity of each system lessened.

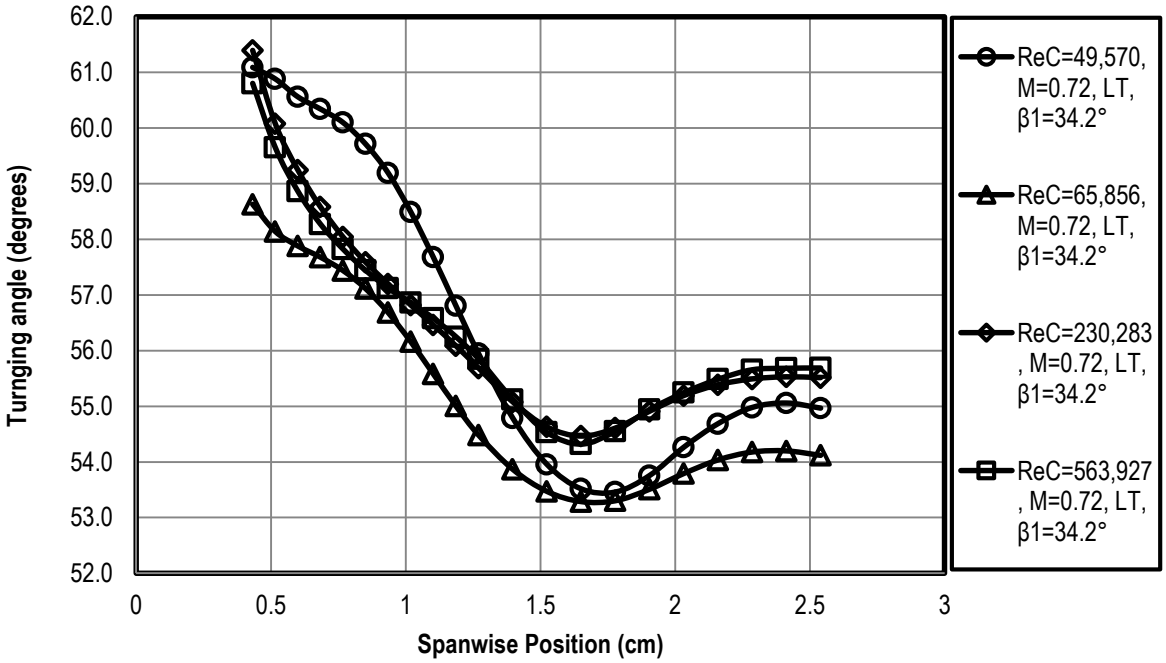

Figure 66: Spanwise turning angle versus ReC at low turbulence for β_1=34.2°

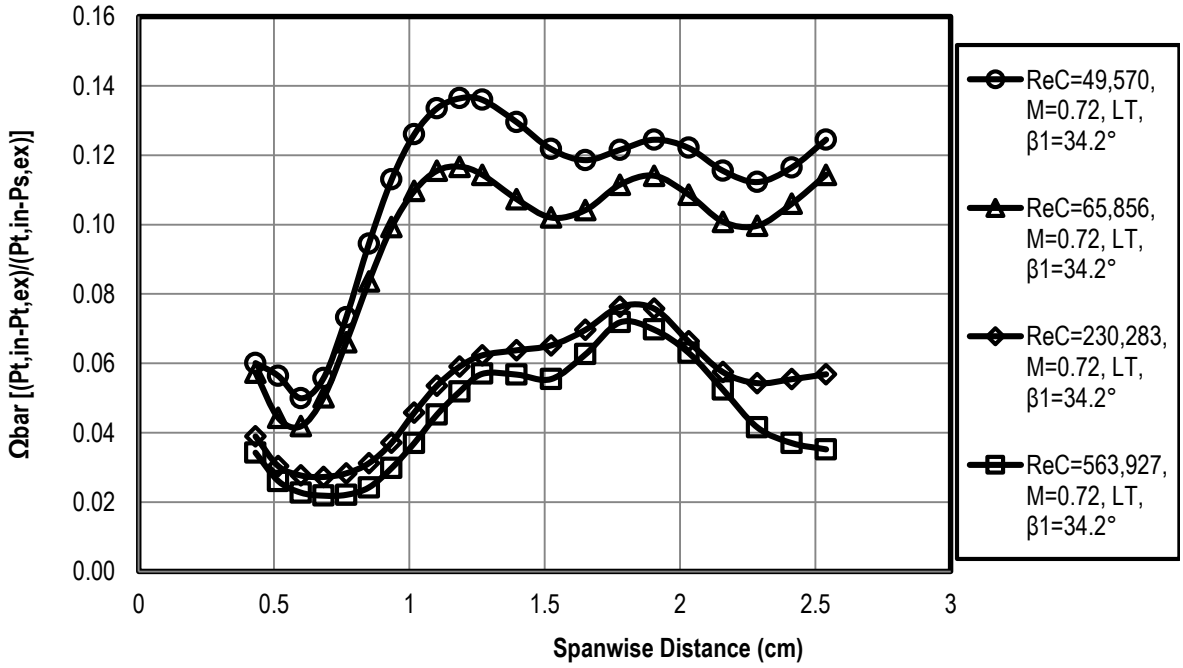

Figure 67: Spanwise total pressure loss versus ReC at low turbulence for β_1=34.2°

34.2° Inlet Angle: Aero-Combustor Turbulence

The effects of free-stream turbulence can be seen in the total pressure loss contour plots in Figures Figure 68 through 71 at the Mach 0.72 condition for the range of Reynolds numbers. The losses seen in Figure 68 and 69 for the 50,000 and 66,000 Reynolds numbers show a very strong main loss core mixing in with the secondary flows due to turbulent diffusion. The thicker suction surface boundary layers has also acted to increase the thickness of the wake. The overall losses have also increased by a $\Delta\Omega$ of 0.31% and 0.73% from the low turbulence condition for the 50,000 and 66,000 Reynolds numbers, respectively. As expected, the losses have decreased at the higher Reynolds numbers of 227,500 and 568,000 in Figures 64 and 65. The thickness of the wake at the midspan location is reduced significantly compared to the low Reynolds number cases. A comparison of the low and high turbulence conditions show that the overall losses have increased by a $\Delta\Omega$ of 1.62% for the 227,500 Reynolds number and a $\Delta\Omega$ of 0.73% for the 568,000 Reynolds number. The augmented losses are a result of the increased diffusion of the main and secondary losses due to free-stream turbulence and unsteadiness.

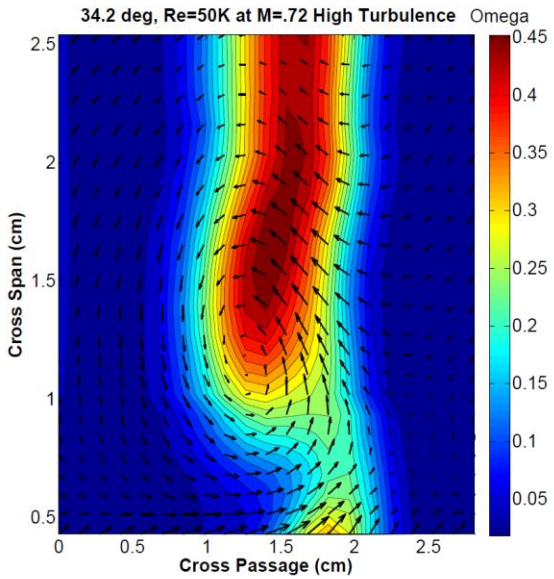

Figure 68: Contours of total pressure loss for Re_C= 50,000 at high turbulence at β_1=34.2°

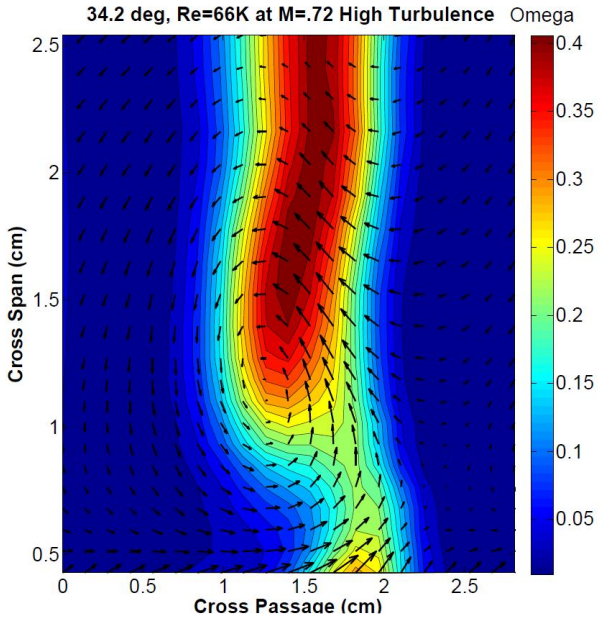

Figure 69: Contours of total pressure loss for Re_C= 66,000 at high turbulence at β_1=34.2°

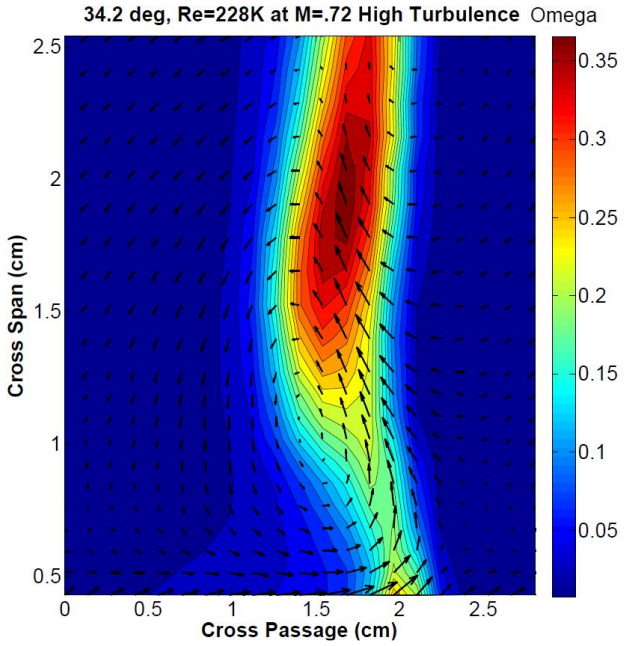

Figure 70: Contours of total pressure loss for Re_C= 227,500 at high turbulence at β_1=34.2°

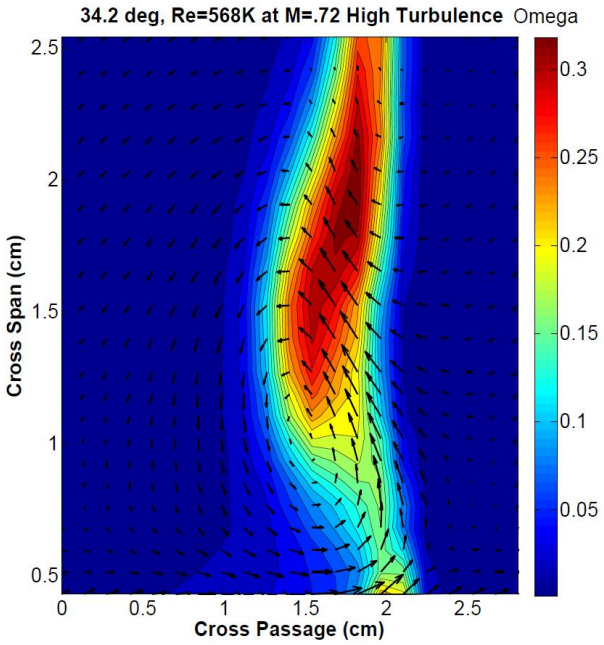

Figure 71: Contours of total pressure loss for Re_C= 568,000 at high turbulence at β_1=34.2°

Spanwise Turning Angle and Total Pressure Loss Coefficients: 34.2° Aero-Combustor Turbulence

Turning near the endwall in Figure 72 has increased slightly from the data in Figure 66 due to turbulent mixing of the main loss vortex with the secondary losses. Mixing within the flow was enhanced due to the high free-stream turbulence levels. The turning angle data at the midspan location in Table 7 show only a slight increase from the low turbulence case. The behavior for all four Reynolds numbers are very similar to one another and show slight underturning at 1.4 cm in the crosspan distance which is also the approximate center of the main loss vortex. The data in Figure 73 shows the effects of the AC turbulence on the average total pressure losses. The distinct peaks from Figure 67 have been smoothed out as the main loss vortex system mixed in with the secondary losses. In contrast to the midspan loss data in Table 6 for the -2.6° inlet angle, the data in Table 7 also show that average midspan losses have a increased with turbulence intensity at the 34.2° inlet angle.

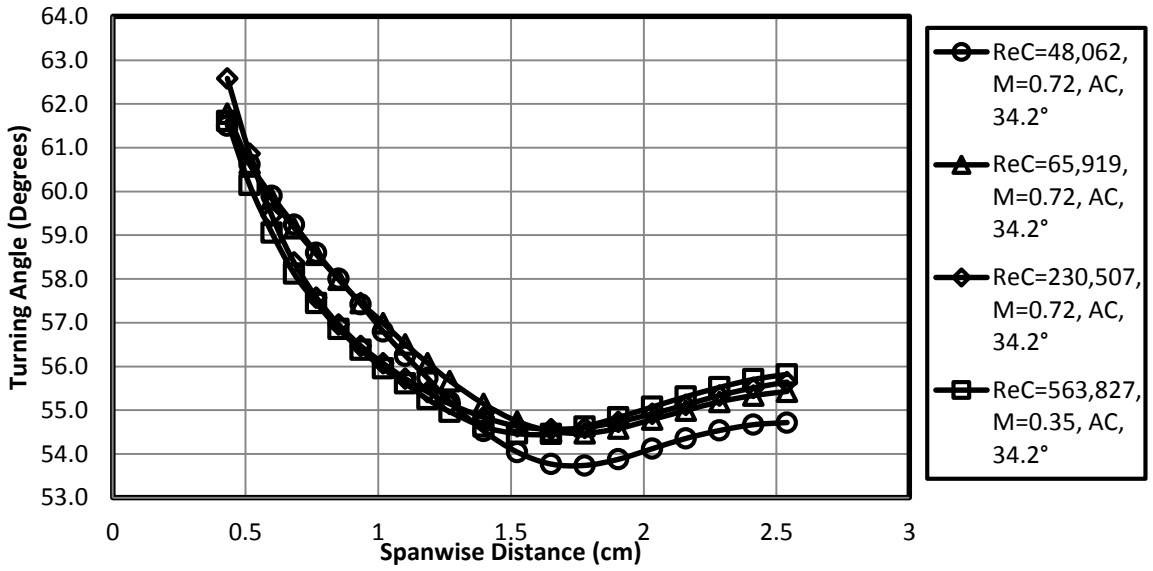

Figure 72: Spanwise turning angle versus ReC at aero-combustor turbulence for β_1=34.2°

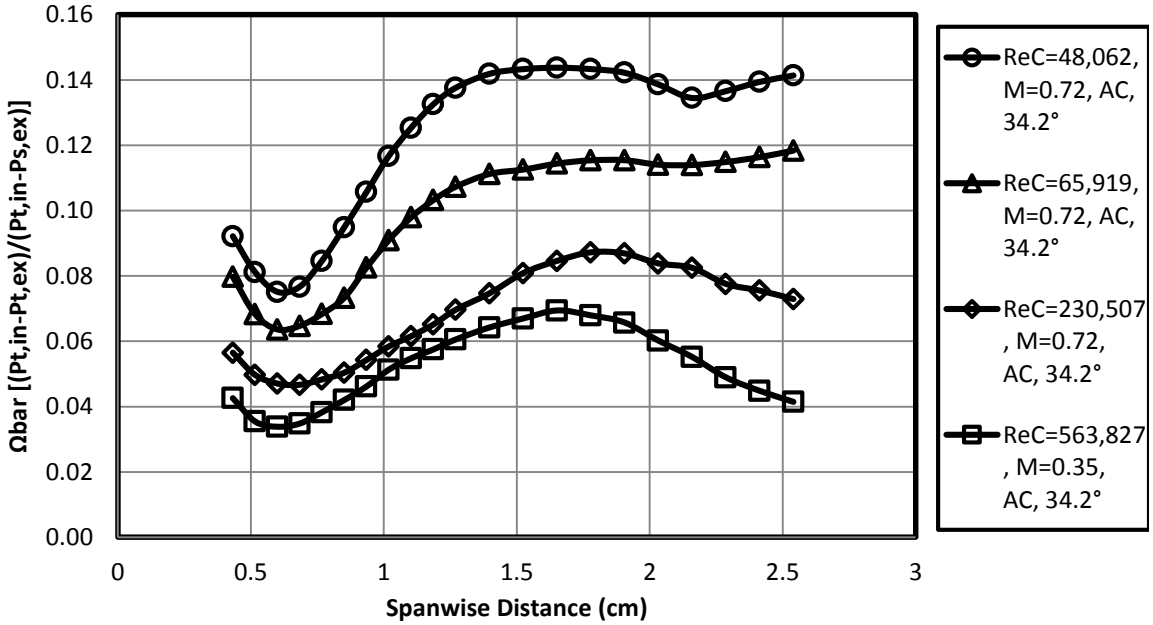

Figure 73: Span-averaged total pressure loss as a funciton of Reynolds number at β_1=34.2° under high turbulence.

Table 7: Wind tunnel conditions, mass averaged loss and turning angle for ¼ axial chord exit surveys at 0° incidence with aero-combustor and low turbulence conditions as a function of Reynolds number.

	High Turbulence				Low Turbulence			
Re_C	50,009	65,919	230,508	563,827	49,570	65,857	230,284	563,928
T_T (K)	314	322	320	324	313	312	309	313
P_T (Pa)	5,596	7,832	27,220	67,893	5,674	7,513	25,935	64,849
V_{ex}	247	248	245	246	244	244	242	243
M_{ex}	0.73	0.72	0.72	0.72	0.72	0.73	0.72	0.72
Ω_M	0.1414	0.1182	0.0729	0.0415	0.1456	0.1143	0.0569	0.0352
Ω_{Ave}	0.1053	0.0978	0.068	0.0514	0.1022	0.0905	0.0518	0.0441
KE	0.0946	0.0887	0.0612	0.0461	0.0917	0.0828	0.0469	0.0398
β_M	54.7166	55.5526	55.6426	55.8212	54.5812	54.1186	55.5135	55.6896
β_{Ave}	56.6785	57.0847	57.0219	56.8099	56.9122	57.0868	56.9925	56.8787

40° Inlet Angle: Low and Aero-Combustor Turbulence

The 40° inlet angle, or 5.8° incidence, represents the cruising condition for this blade design. Therefore, optimal aerodynamic performance at the low chord Reynolds numbers is critical since the majority of the engine's operation will be spent at cruising altitude. Many similarities are shared between the 0° and 5.8° incidence angles as seen in Figure 62 and Figure 74. For this reason, the data for the low and high turbulence have been combined into one section. On average, the losses are about 0.5% higher for the 5.8° incidence angle at low turbulence due to higher profile and secondary losses from the increased turning. The low turbulence contour plot on the left in Figure 74 shows the location of the passage vortex at about 1.25 cm in the cross span direction. A very strong secondary loss peak is above the passage vortex at about 2.2 cm in the cross span direction and is possibly the suction leg of the horseshoe

vortex. By inspection, the peak losses of secondary losses were greater than it was for the 0° incidence angle. Traces of the corner vortex is also apparent in the figure near the endwall location at 1.75 cm in the cross passage direction. However, due to the facility limitations of the traversing mechanism, it is not 100% clear if this a corner vortex. Increasing the Reynolds number from 50,000 to 66,000 in Figure 75, the losses have reduced by a $\Delta\Omega$ of -0.47% at the high turbulence condition and by -1.26% at the low turbulence condition which was due to the reduced profile and secondary losses.

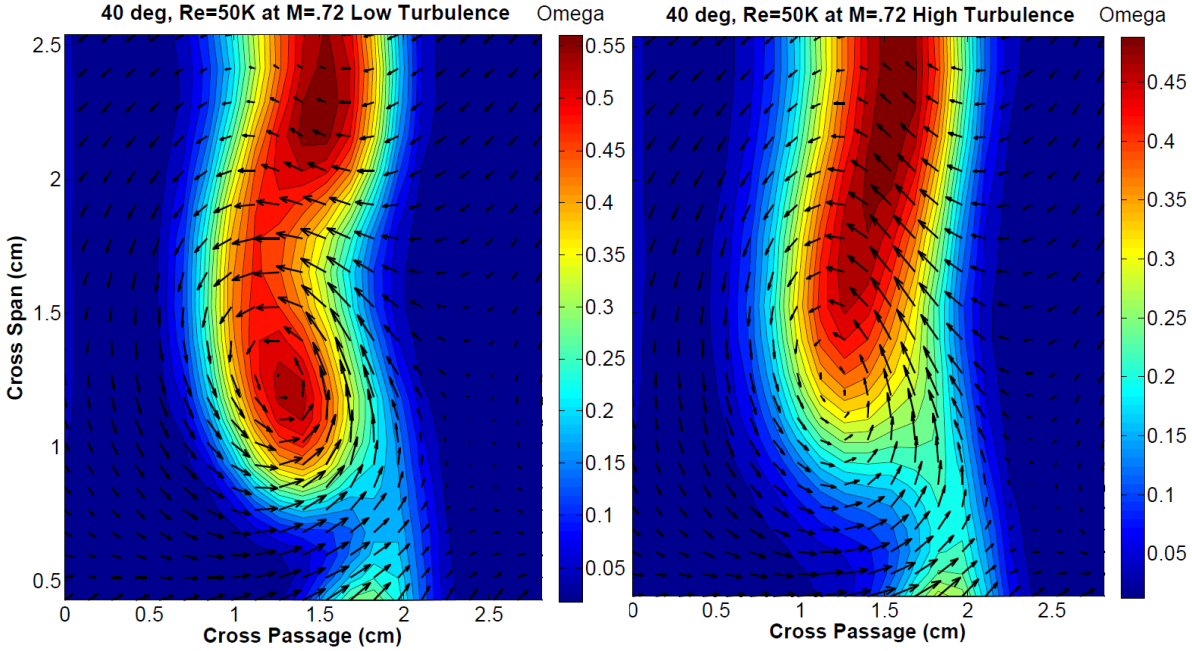

Figure 74: Contours of total pressure loss for Re_C= 50,000 at low turbulence (Left) and AC Turbulence (Right) at β_1=40.0°

The images on the right in Figure 74 and 75 show the total pressure losses at the aero-combustor turbulence (AC) condition. The effects of free-stream turbulence are clearly seen as the core of the main loss vortex has been displaced further away from the endwall in the cross span direction. The secondary losses also mixed in with the main losses due to turbulent mixing

of the flow. The overall width of the wake has also increased significantly due to increased profile losses and secondary losses.

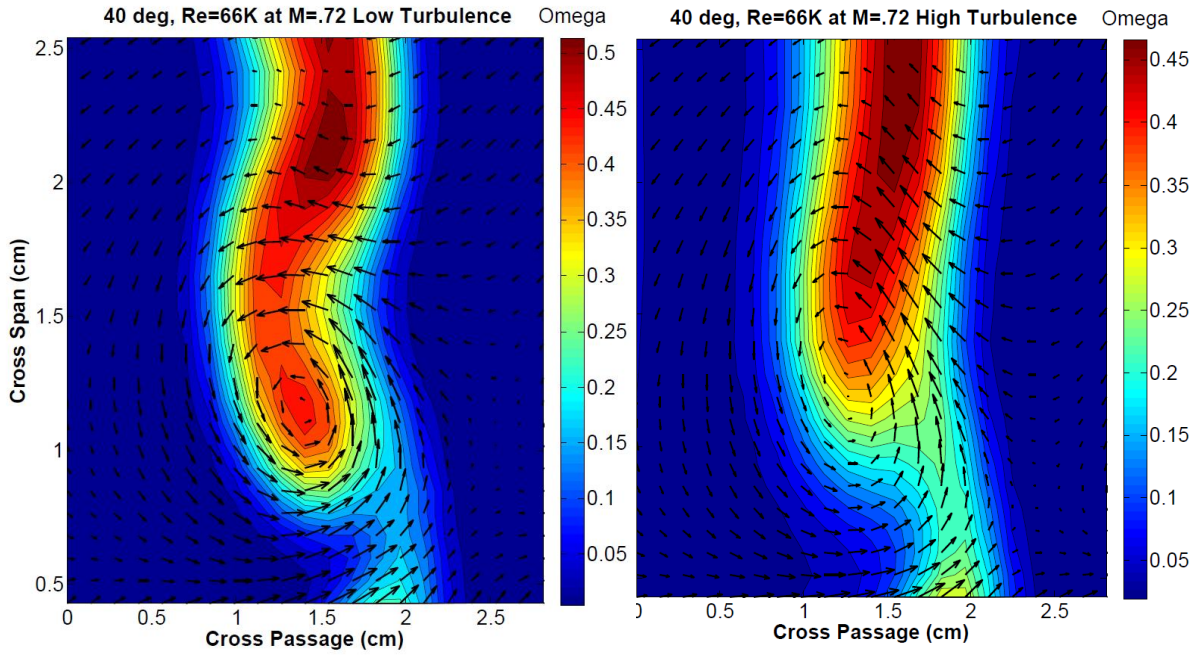

Figure 75: Contours of total pressure loss for Re_C= 66,000 at low turbulence (Left) and AC Turbulence (Right) at β_1=40.0°

As the chord Reynolds number is increased to 227,500, the flow appears to be highly three-dimensional in Figure 76. The main loss vortex has migrated to a cross span location of 1.4 cm. The magnitudes of the secondary losses are shown to be higher than the losses about the main passage vortex. Similar trends are seen at the 568,000 Reynolds number case in Figure 77. In agreement with the 0° incidence angle, the thickness of the wake has been shown to decrease with increasing Reynolds number.

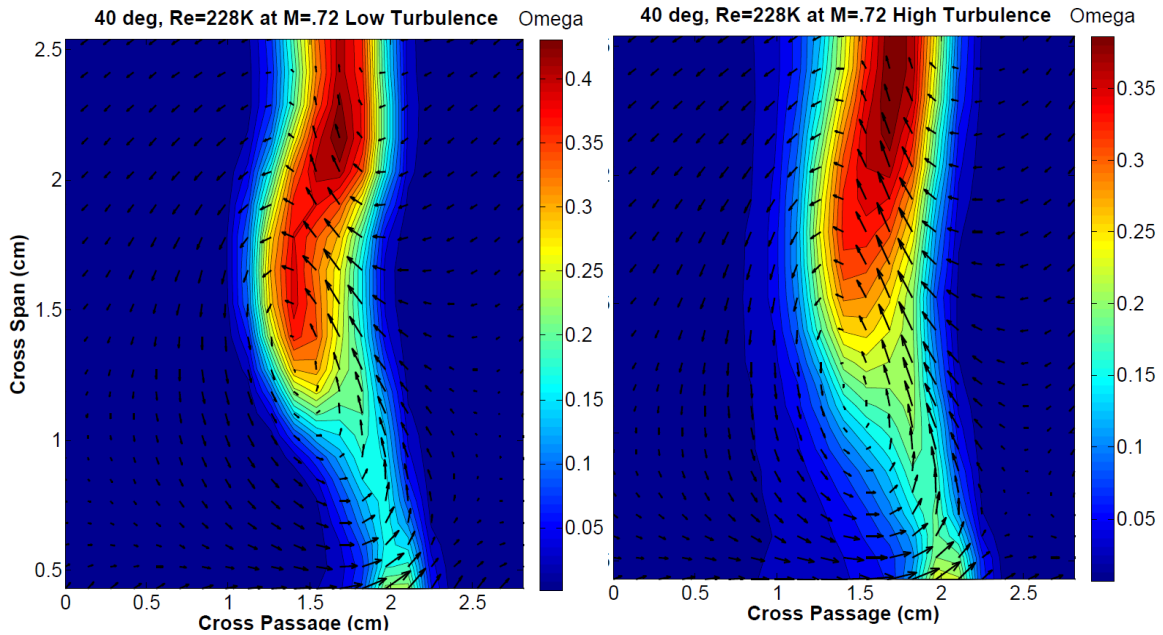

Figure 76: Contours of total pressure loss for Re_C= 227,500 at low turbulence (Left) and AC turbulence (Right) at β_1=40.0°

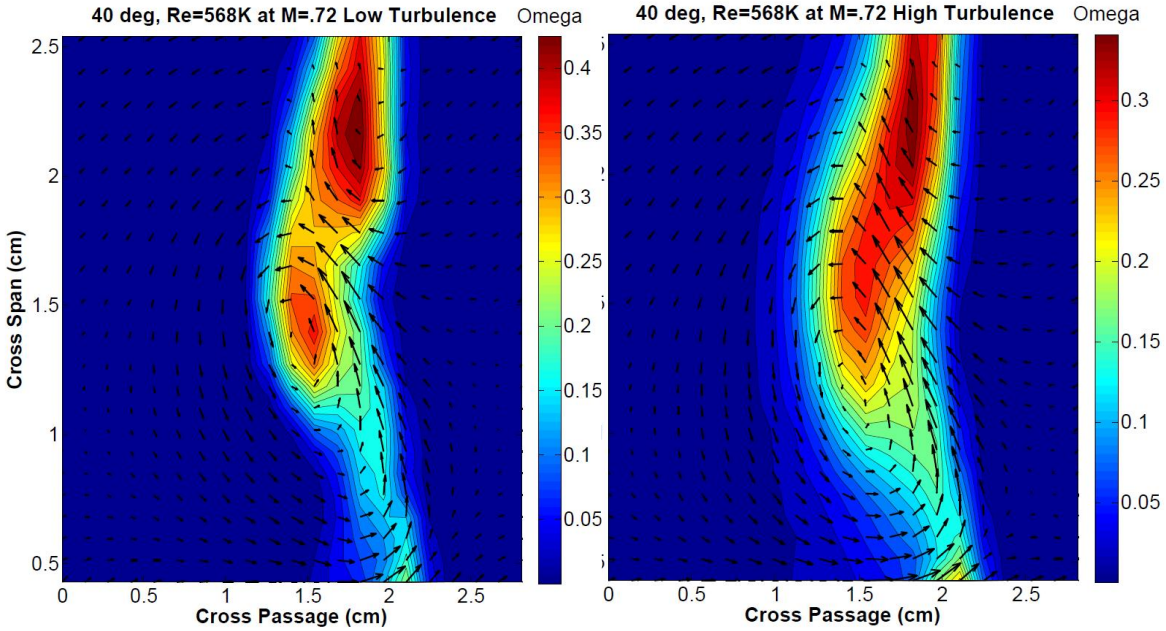

Figure 77: Contours of total pressure loss for Re_C= 568,000 at low turbulence (Left) and AC turbulence (Right) at β_1=40.0°

At the AC turbulence condition for the 227,500 and 568,000 Reynolds numbers, the primary loss and secondary loss systems are much less distinct as the increased turbulence

kinetic energy enhanced the mixing of these flows within the wake. The increased mixing in the flow has also increased the extent of the loss region near the midspan towards the endwall.

Spanwise Turning Angle and Total Pressure Loss Coefficients: 40°

The discharge flow turning angle data are presented in Figure 78 for the 5.8° incidence angle as a function of Reynolds number and turbulence intensity. The open symbols in the figure represent the low turbulence condition and the closed symbols represent the AC turbulence condition. The data, which is similar to the trends seen in Figure 66 for the 0° incidence angle, shows higher overturning near the endwall due to the strong cross-passage pressure gradient. The regions of underturning in the data shows the approximate locations of the secondary losses cores for each Reynolds number and turbulence condition.

The aero-combustor data are also presented in Figure 78 and show less erratic behavior from the main losses. The data are much more uniform compared to the low turbulence condition showing the effects of high free-stream turbulence. Similar to the low turbulence case, there is slight underturning around 1.8 cm into the span near the location of the secondary loss core. The data in Table 8 shows the tabulated average midspan turning angle and the span averaged turning for both turbulence conditions.

The span averaged total pressure losses at the 50,000 and 568,000 Reynolds numbers at low and AC turbulence are presented in Figure 79. The data clearly show an in increase in the average total pressure losses along the span of the blade and the span averaged data in Table 8 supports this conclusion. At the 50,000 Reynolds number for the AC turbulence condition, the flow appears to be two-dimensional.

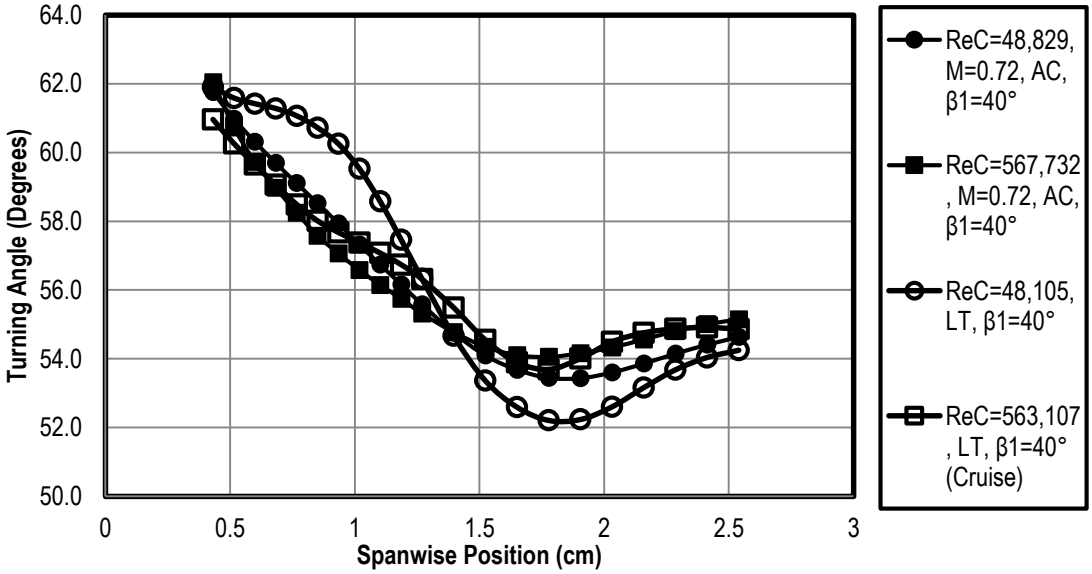

Figure 78: Spanwise turning angle versus ReC at low and AC turbulence for β_1=40°

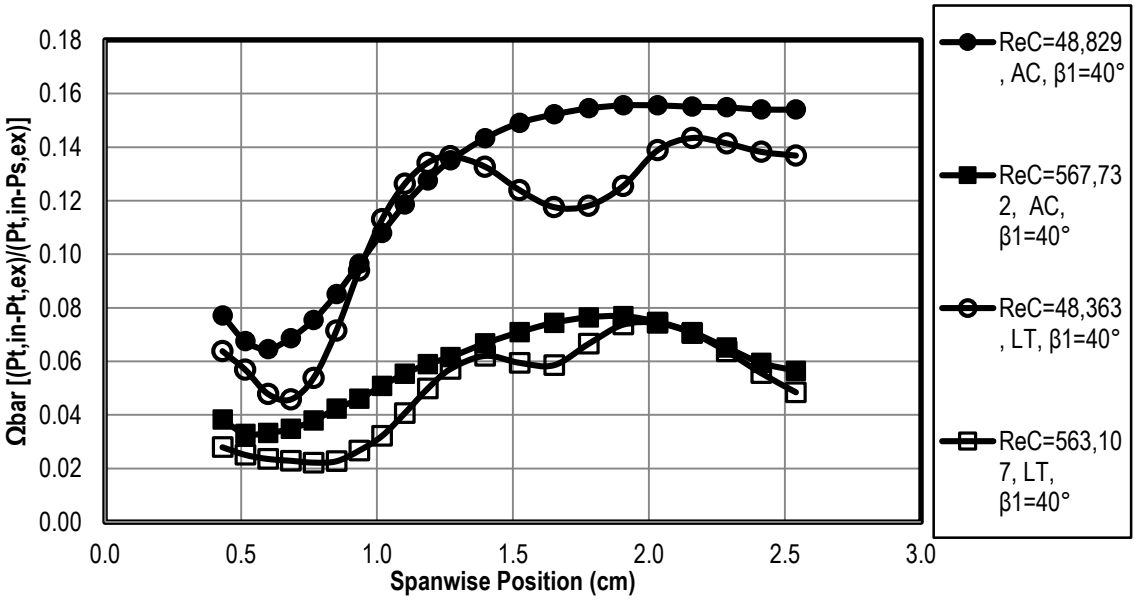

Figure 79: Spanwise total pressure loss versus ReC at low and AC turbulence for β_1=40°

Table 8: Wind tunnel conditions, mass averaged loss and turning angle for ¼ axial chord exit surveys at 5.8° incidence with aero-combustor and low turbulence conditions as a function of Reynolds number.

	High Turbulence				Low Turbulence			
Re_C	48,829	65,353	229,710	567,733	48,106	66,310	230,380	563,107
T_T (K)	318.5	319.5	316.0	320.3	309.4	308.1	307.2	306.8
P_T (Pa)	5,712	7,690	26,665	67,040	5,421	7,444	25,859	63,082
V_{ex}	246.7	246.2	244.7	246.5	243.2	242.1	240.3	240.3
M_{ex}	0.72	0.72	0.72	0.72	0.73	0.72	0.72	0.72
Ω_M	0.1541	0.1487	0.0967	0.0565	0.1574	0.1303	0.0727	0.0485
Ω_{Ave}	0.1199	0.1152	0.0726	0.0560	0.1095	0.0969	0.0564	0.0468
KE	0.1099	0.1051	0.0653	0.0501	0.1008	0.0885	0.0511	0.0423
β_M	54.6354	54.8893	54.9821	55.1456	54.2489	54.7179	54.8600	54.8672
β_{Ave}	56.7903	56.9976	57.2256	56.8437	56.9954	57.2509	56.9774	56.8280

-17° Inlet Angle: Low Turbulence

The losses increased dramatically at the -51.2° incidence angle (-17° inlet angle) which was the worst case scenario of this study. The total pressure losses at the 50,000 and 66,000 Reynolds numbers, Figure 80 and 81, shows a highly three-dimensional flow-field caused by the massive leading edge separation on the pressure surface and the separation along the suction surface. The main passage vortex has been displaced out of the sensing plane of the five-hole cone probe. A strong, counter-rotating, secondary vortex near the pressure surface appears to be displacing the passage vortex away from the endwall. An endwall vortex near the suction surface is also present and is possibly the suction surface corner vortex. A counter rotating corner vortex is also visible along the pressure surface for all Reynolds numbers except for the 568,000 case where it is out of the sensing plane. The losses have been shown to decrease significantly by a $\Delta\Omega$ of 1.8% as the Reynolds number was increased from 50,000 to 66,000.

The reduced losses were likely caused by weaker secondary losses as the laminar separation regions weakened in size and intensity.

Interestingly, the flow begins to show two-dimensional behavior as the Reynolds number increased to 227,500 and 568,000, as seen in Figure 82 andFigure 83. The increased momentum in the flow at the high Reynolds number suppresses the pressure surface leading edge and trailing edge separation bubbles. The leading edge separation bubble is still present at the 568,000 Reynolds number but has been weakened significantly from the 50,000 Reynolds number. At the 227,500 Reynolds number the passage vortex has shifted towards the endwall and is located at about 35% span. Very little of the passage vortex is visible as the Reynolds number was increased to 568,000. As the counter-rotating secondary vortex weakened, it allowed the main loss vortex to migrate closer to the endwall and further into the passage. An additional loss component is also present at the elevated Reynolds numbers as losses due to the pressure surface leading edge separation bubble from the adjacent blade are clearly visible. The location of the pressure surface separation bubble from Blade 3 is highlighted in Figure 82.

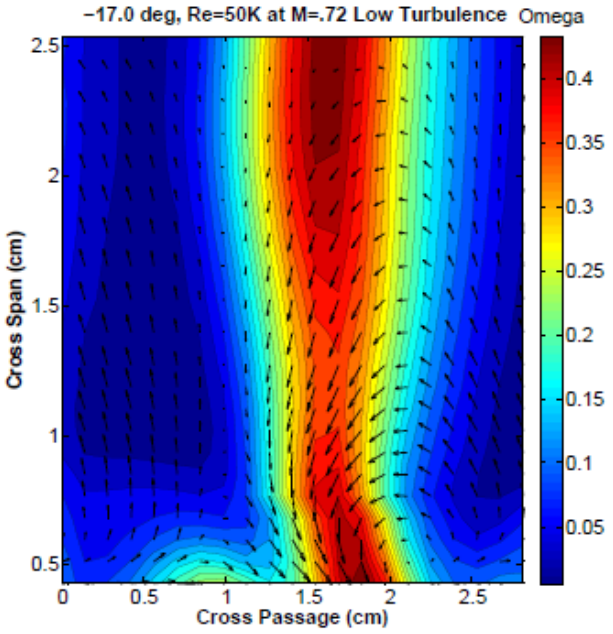

Figure 80: Contours of total pressure loss at Re_C=50,000 at low turbulence for β_1=-17°

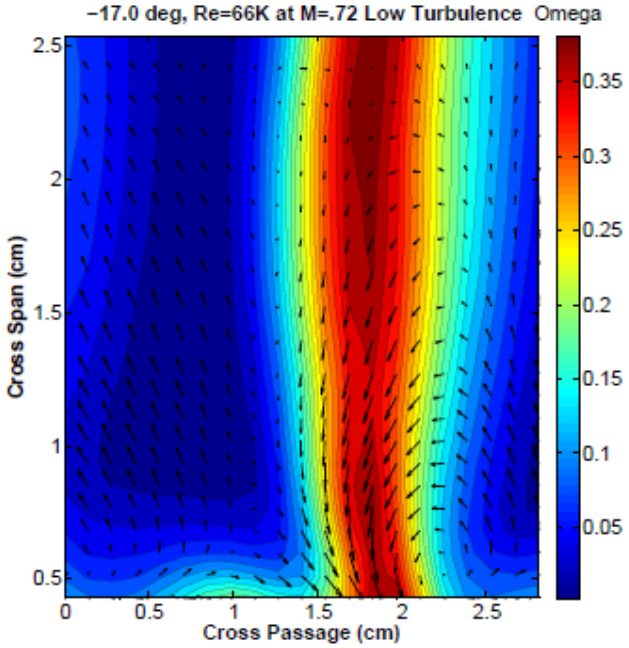

Figure 81: Contours of total pressure loss at Re_C=66,000 at low turbulence for β_1=-17°

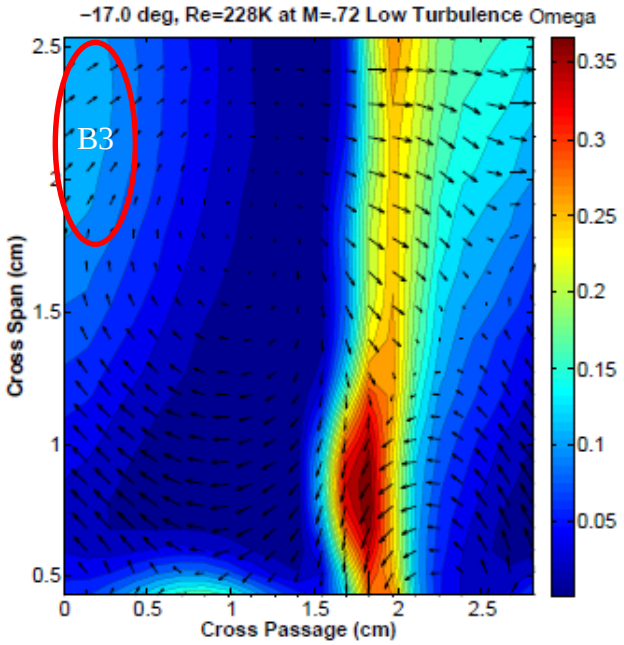

Figure 82: Contours of total pressure loss at Re_C=227,500 at low turbulence for β_1=-17°

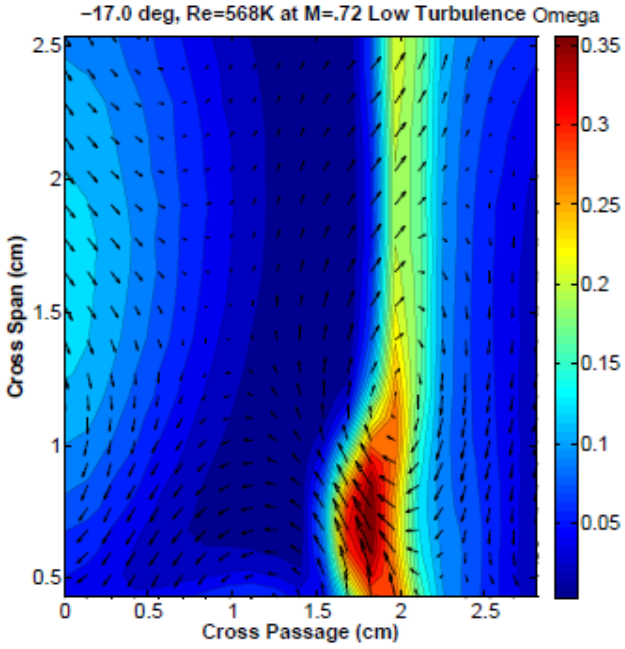

Figure 83: Contours of total pressure loss at Re_C=568,000 at low turbulence for β_1=-17°

Spanwise Turning Angle and Pressure Losses: -17° Low Turbulence

The passage averaged losses versus span for each Reynolds number at Mach 0.72 are shown in Figure 84. The peak losses occur near the endwall for the range of Reynolds numbers as expected. The losses are highest at the 50,000 and 66,000 Reynolds number. The rise in total pressure loss approaching the midspan shows the extent of the separation bubble which increases in size as Reynolds number was reduced. Two-dimensional behavior at the 568,000 Reynolds number is also seen in the figure which supports the data in Figure 83. Turning data are presented in Figure 85 for the -51.2° incidence angle. The data for all Reynolds numbers show concentrated overturning near the endwall, coinciding with the location of the corner vortex. The overturning is stronger at the 50,000 and 66,000 Reynolds which implies the corner vortex has intensified.

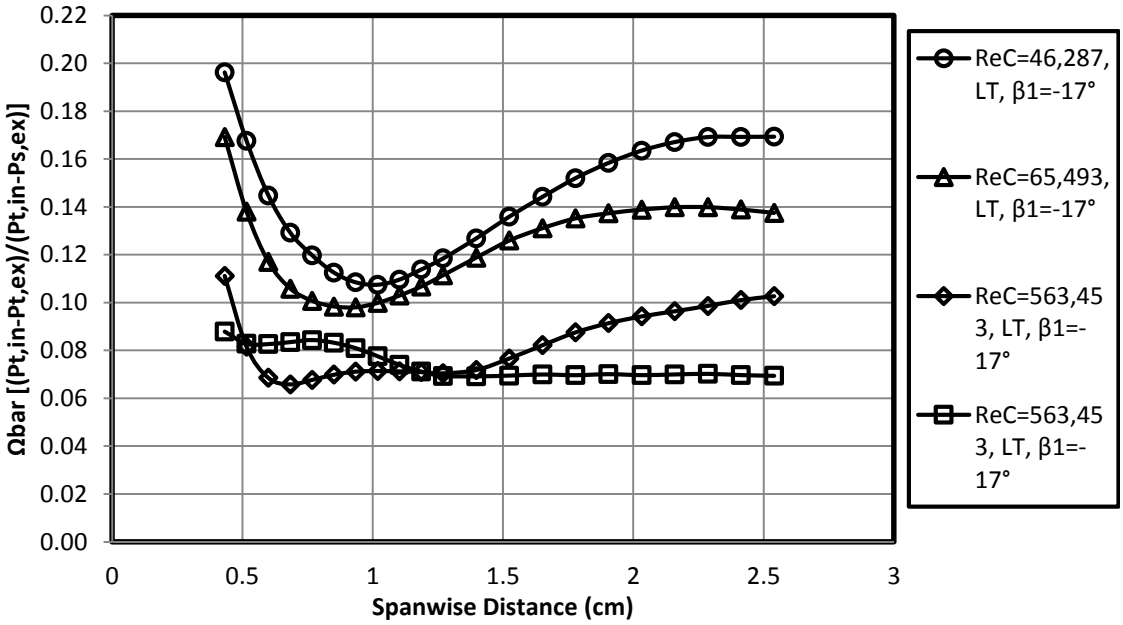

Figure 84: Passage averaged total pressure loss versus Reynolds number at β_1=-17° under low turbulence condition.

However, the secondary losses are significantly reduced as the blockages from the separated flow along the leading edge suppresses formation of the secondary flows. Additionally, the total turning angle is only about 40° which causes less cross-passage pressure gradient. Interesting behavior is seen at the 227,500 Reynolds number as the turning increases from the quarterspan location towards the midspan of the blade and is possibly due to unsteadiness.

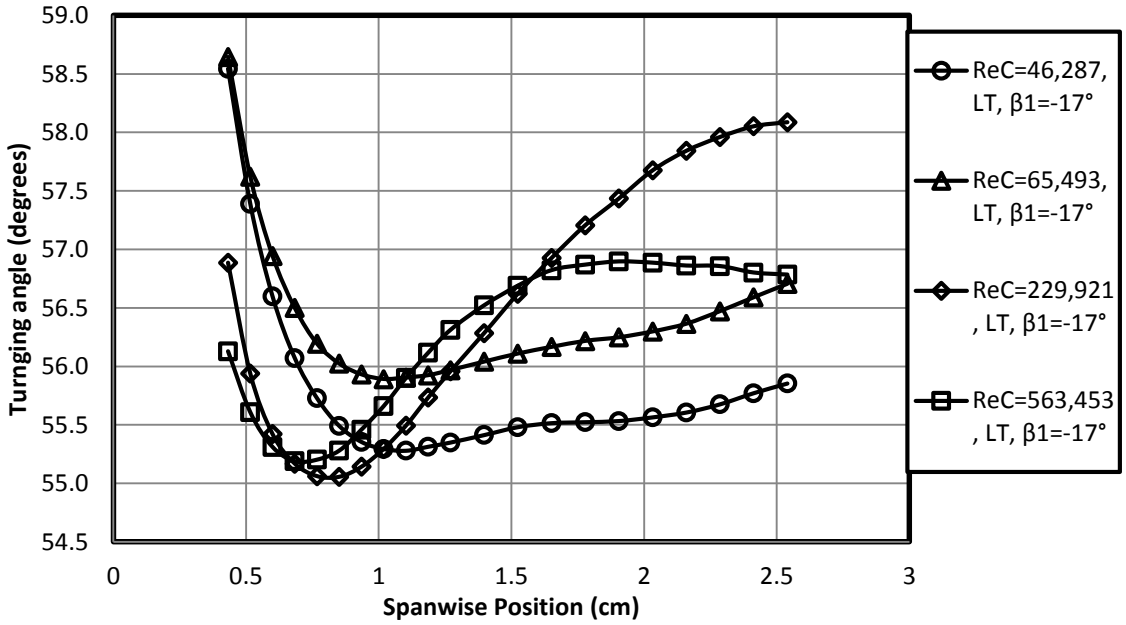

Figure 85: Turning angle versus Reynolds number at β_1=-17° under low turbulence condition.

-17° Inlet Angle: Aero-Combustor Turbulence

The effects of free-stream turbulence and Reynolds number are presented in Figure 86 through 88 at the -17° inlet angle. The losses at the 50,000 and 66,000 Reynolds numbers have been shown to increase only slightly from the low free-stream turbulence (FST) conditions. The pressure surface leading separation bubble seen at the low turbulence case in the isentropic Mach distributions in Section 4.2 has been suppressed as a result of the increased turbulent mixing. The increased spot production rate at the high FST condition energized the leading edge

boundary layer and allowed for a much quicker reattachment. The midspan loss coefficients at the 50,000 and 66,000 in Figure 86 and 87 have reduced as a result of the quick reattachment of the laminar separation bubble. The wall vortex near the suction side has been effectively mixed out by the strong endwall flow. The high loss regions encompass a much broader portion of the span and the main loss core has shifted towards the endwall when compared to the 40° inlet angle. The wake flow at the 227,500 and 568,000 Reynolds numbers appear to be much more two-dimensional with the secondary losses concentrated near the endwall. Even at the highest Reynolds number the wake encompasses the majority blade-to-blade passage owing to the highly negative incidence. Interestingly, the overall total pressure losses at the 568,000 Reynolds number decreased by a $\Delta\Omega$ of -0.67% from the low FST condition.

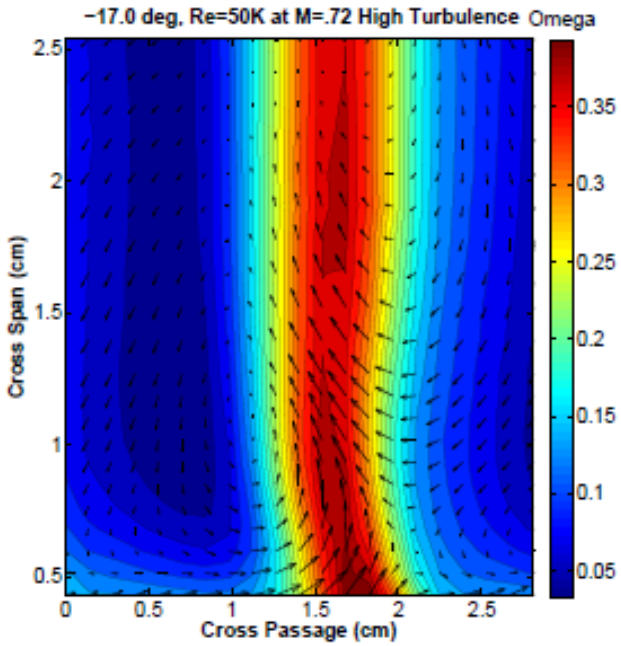

Figure 86: Contours of total pressure loss at Re_C=50,000 at high turbulence for β_1=-17°

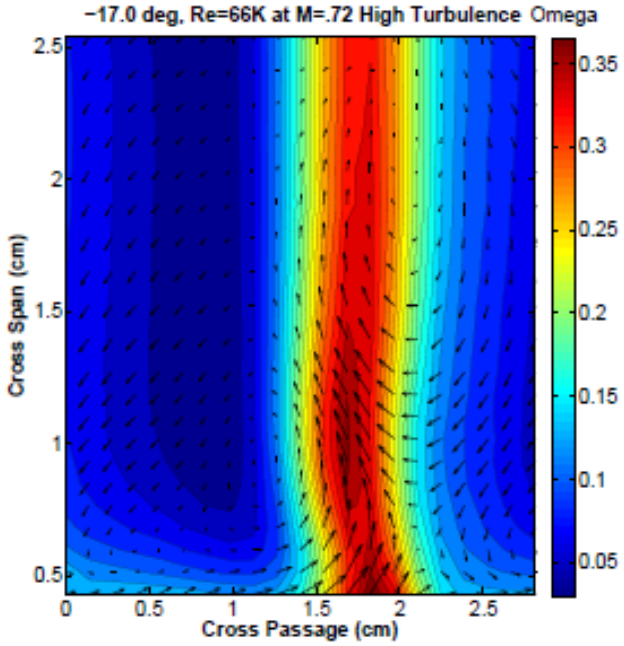

Figure 87: Contours of total pressure loss at Re_C=66,000 at high turbulence for β_1=-17°

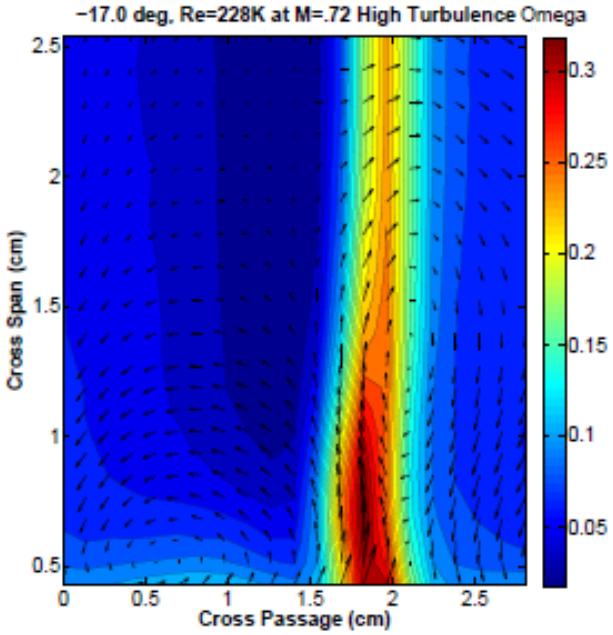

Figure 88: Contours of total pressure loss at Re_C=227,500 at high turbulence for β_1=-17°

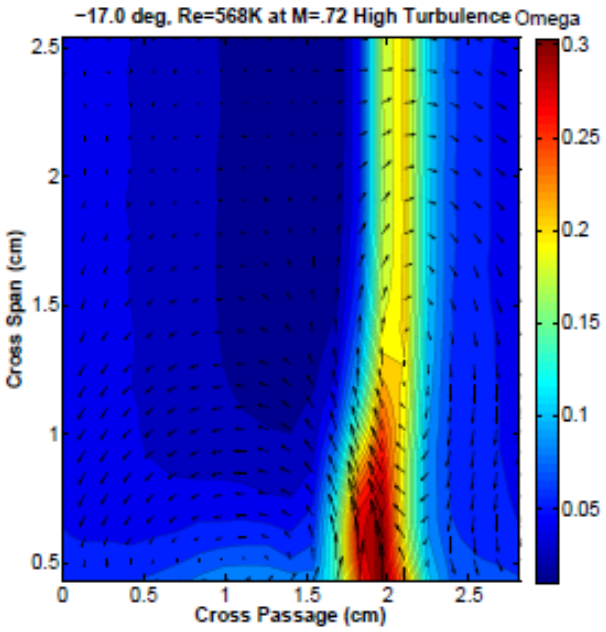

Figure 89: Contours of total pressure loss at Re_C=568,000 at high turbulence for β_1=-17°

Spanwise Turning Angle and Pressure Losses: -17° Aero-Combustor Turbulence

Spanwise total pressure loss and turning are presented in Figure 90 and 91 for the high turbulence condition at -17° inlet angle. The losses along the span have been shown to increase, particularly near the quarter-span location. The increased mixing with the secondary flows is a likely cause of the higher losses seen in the data. Turning data, as seen in Figure 91, shows a much smoother distribution when compared to the low turbulence case in Figure 85. The midspan turning has remained relatively constant with the exception of the 50,000 Reynolds number where the turning has reduced by about 1.3° at the high turbulence level. Pertinent wind tunnel conditions and loss data are presented in

Table 9 for this case. The total pressure losses are generally higher for the elevated turbulence condition with the exception of the 568,000 Reynolds number. The losses decreased at the 568,000 Reynolds number as the leading edge separation bubble seen at the lower turbulence condition from Blade 3 was suppressed due to the increase in turbulent mixing.

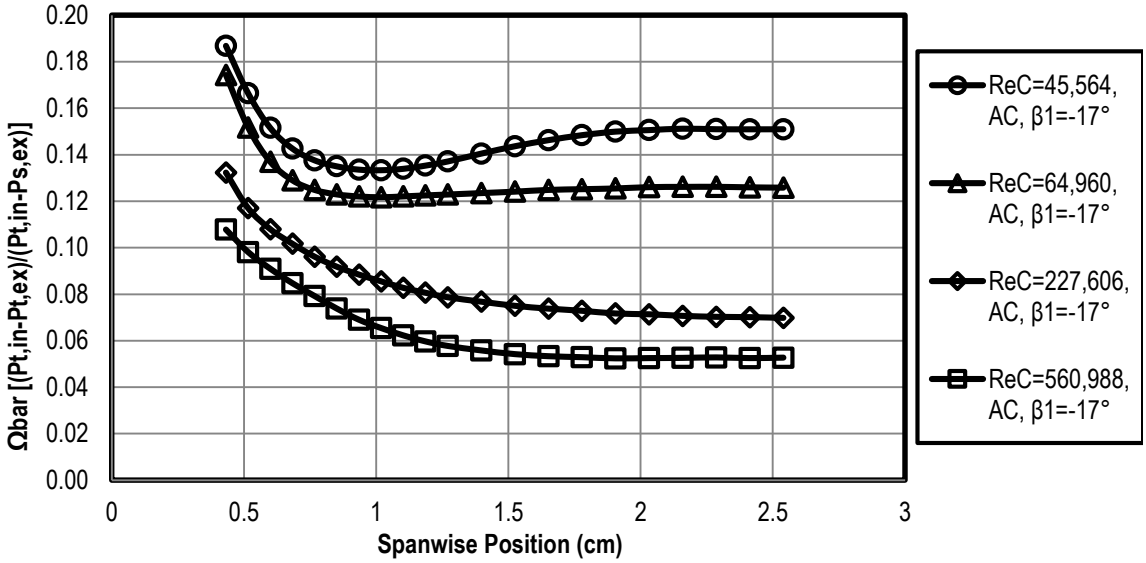

Figure 90: Passage averaged total pressure loss versus Reynolds number at β_1=-17° under high turbulence condition.

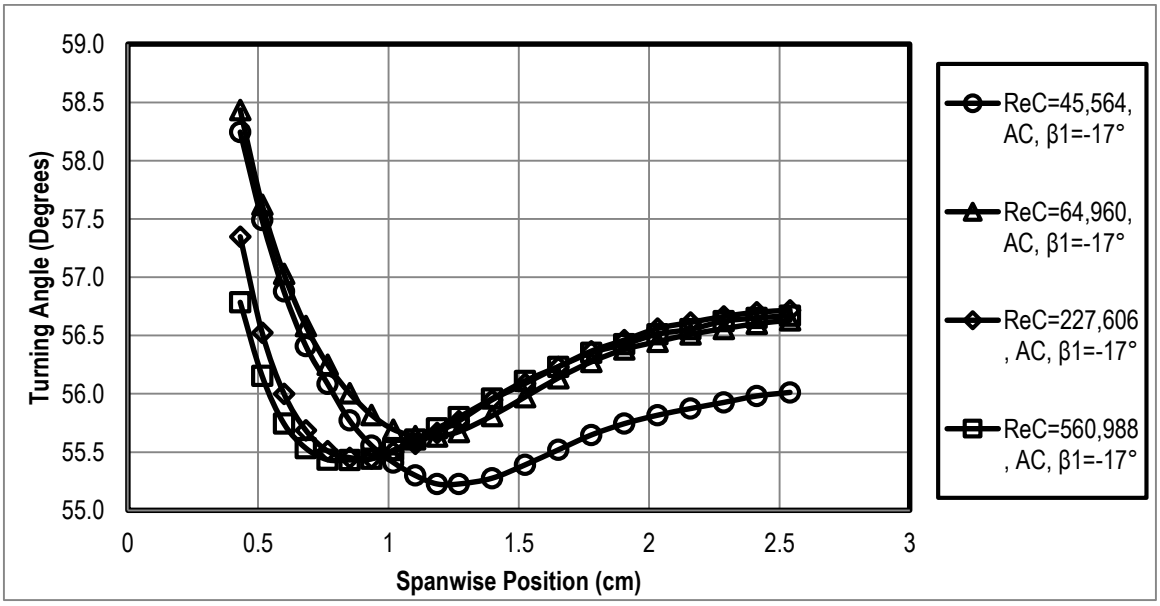

Figure 91: Turning angle versus Reynolds number at β_1=-17° under high turbulence condition.

Table 9: Wind tunnel conditions, mass averaged loss and turning angle for ¼ axial chord exit surveys at -51.2° incidence with aero-combustor and low turbulence conditions as a function of Reynolds number.

	High Turbulence				Low Turbulence			
Re_C	45,564	64,960	227,607	560,988	46,288	65,493	229,922	563,454

T_T (K)	329	330	329	329	323	323	319	317
P_T (Pa)	5,532	7,968	27,829	68,756	5,523	7,826	27,006	65,663
V_{ex} (m/s)	253	250	249	248	248	247	246	244
M_{ex}	0.73	0.72	0.72	0.72	0.72	0.72	0.72	0.72
Ω_M	0.1509	0.1259	0.0698	0.0527	0.1693	0.1375	0.1027	0.0694
Ω_{Ave}	0.1522	0.1342	0.089	0.0691	0.1513	0.1313	0.0873	0.0758
KE	0.1378	0.1212	0.0796	0.0615	0.1378	0.1189	0.0783	0.0677
β_M	56.0116	56.6302	56.7169	56.6705	55.854	56.7054	58.0886	56.7838
β_{Ave}	56.2123	56.6343	56.3482	56.2172	56.1148	56.696	56.6623	56.293

4.5.1 Effects of Inlet Angle

The effects of incidence angle, or inlet angle, can clearly be seen in the total pressure loss contour plots in Figure 92 (A-F) for the 50,000 Reynolds number at the low turbulence condition. Most noticeably, the figures clearly show the migration of the main loss vortex from the quarterspan location at the 40° inlet angle towards the endwall at the -12° inlet angle. As the main loss core moves towards the endwall with decreasing blade incidence, the overall total pressure losses decreases until about 8°. The pressure surface leading edge separation bubble also becomes more discernable as incidence is reduced beyond the -2.6° inlet angle. At the extreme negative inlet angles, the wake becomes much thicker due to blockages from the pressure surface leading edge separation bubble. The wake at the extreme negative incidence angles encompass the majority of the blade-to-blade passages which was in agreement with McVetta [10].

At the 568,000 Reynolds number in Figure 93, the midspan losses are highly three-dimensional at the 40° and 28° inlet angles given the location of the passage and secondary loss vortex systems. Like the low Reynolds number case, as incidence is reduced the secondary losses stay

closer to the endwall. The flow becomes much more two-dimensional along the span of the blade, even at the extreme negative incidence angles.

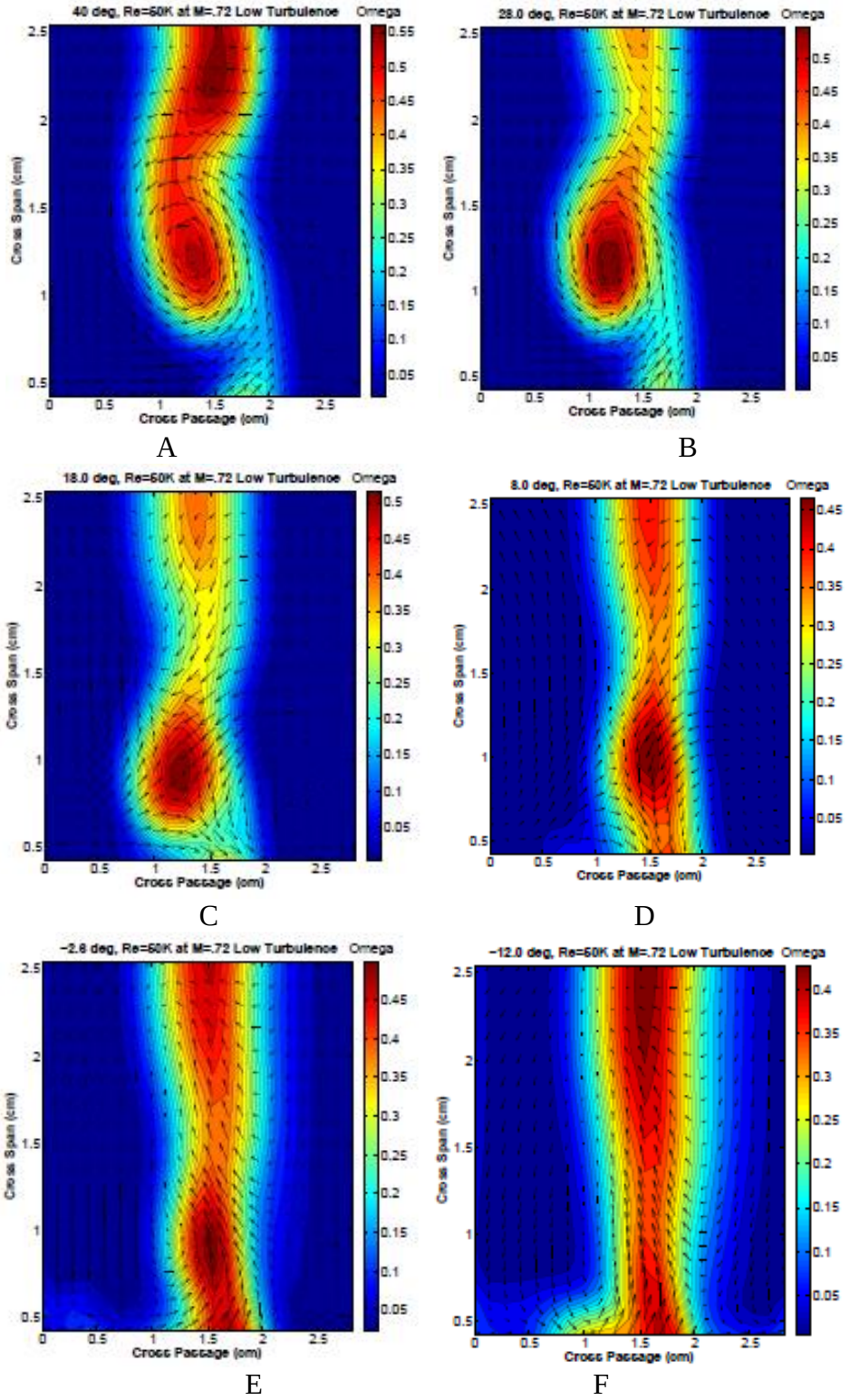

Figure 92 (A-F): Contours of total pressure loss at A) 40°, B) 28°, C) 18°, D) 8°, E) -2.6°, F) -12° inlet angles at ReC=50,000 at low turbulence.

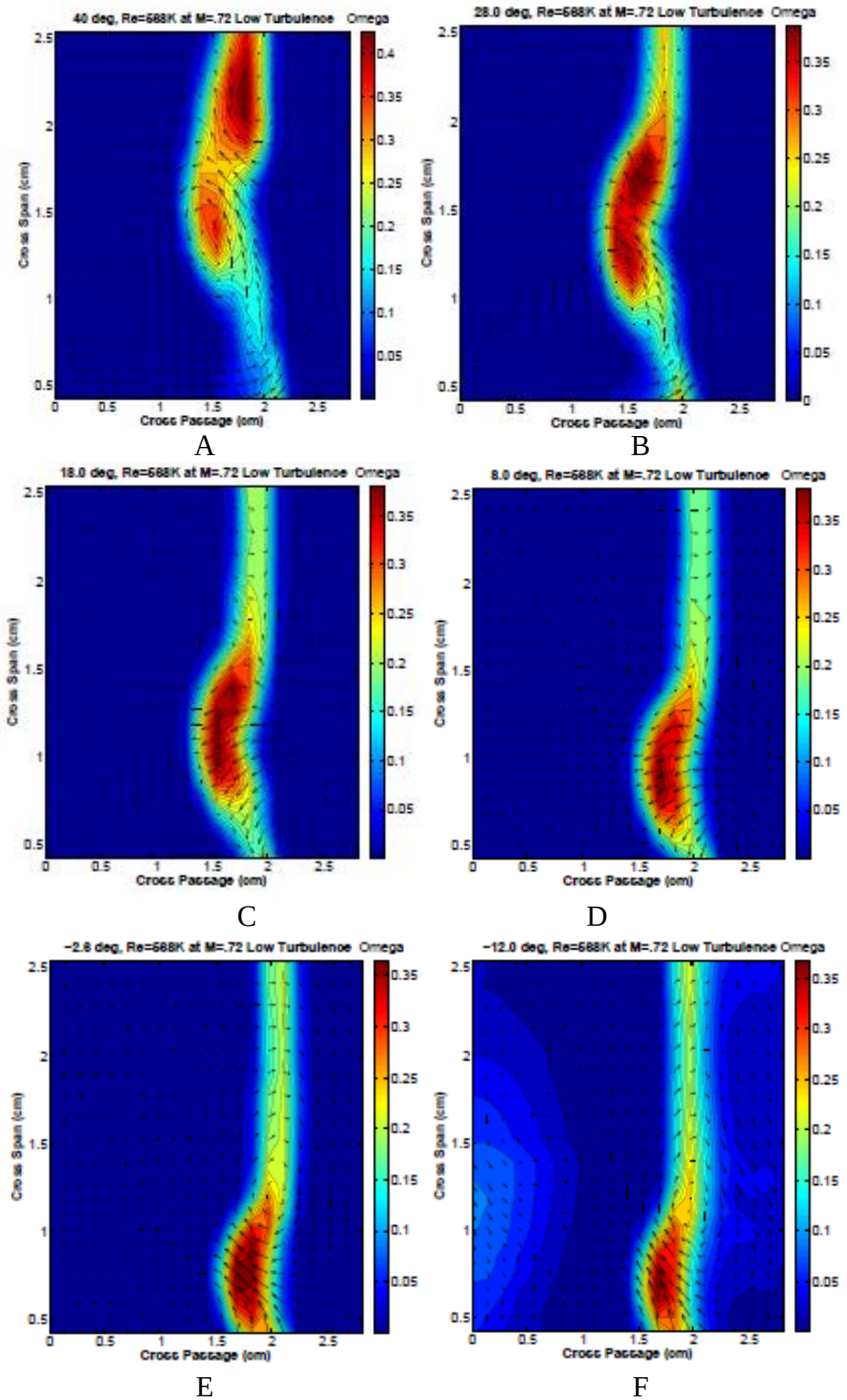

Figure 93(A-F): Contours of total pressure loss at A) 40°, B) 28°, C) 18°, D) 8°, E) -2.6°, F) -12° inlet angles at ReC=50,000 at low turbulence.

Weighted Total Pressure Losses

The ultimate goal of this study was to provide a detailed documentation of the total pressure losses over the 57° range of incidence. Thus far, this analysis has shown the detailed flow effects on the aerodynamic losses for the selected design conditions. The purpose of this section is to present the overall aerodynamic loss buckets to illustrate the performance of the blade design through the entire range of incidence. The mass weighted loss coefficients for each incidence angle and Reynolds number are presented in Figure 94 and 95 for the low and high turbulence conditions, respectively. The effects of incidence angle on the loss coefficients are clearly evident. Generally, the losses increase as incidence angle decreases from -6.2° incidence (+28° inlet angle) for the 50,000 and 66,000 Reynolds numbers. At the 227,500 and 568,000 Reynolds numbers, the loss coefficients show a very good operating range between -6.2° and -36.7° incidence and remain relatively constant. The loss coefficients generally increase significantly at the exceedingly negative incidence angles as the flow is massively separated at the pressure surface leading edge. The total pressure losses increase form the -6.2° incidence angle to 5.8° which is likely due to stronger secondary losses and laminar separation along the aft portion of the suction surface. Clear Reynolds number effects are seen in the data, as well. The losses are maximum at the 50,000 Reynolds number due to strong profile and secondary losses typically seen at very low Reynolds numbers. The losses decrease significantly towards the 568,000 Reynolds number as the high Reynolds number fluid suppressed the extent of the separation bubbles/

Figure 95 shows the effects of high free-stream turbulence intensity. The behavior is very similar to the low turbulence case but the losses have generally increased with the exception of the extreme negative incidence angles. The wakes broadened as a result of the

increased turbulent mixing with the secondary flows but the overall losses at the midspan were reduced. The background losses along the passage endwall also contributed to the overall losses which were present only at the aero-combustor turbulence levels. Additionally, the turbulent mixing suppressed the suction surface laminar separation bubble and likely forced an earlier reattachment allowing for increased loading along the blade. The increased turbulence levels significantly improved the performance at the extreme negative incidence angles by forcing an earlier transition and reattachment of the pressure surface separation bubble along the leading edge.

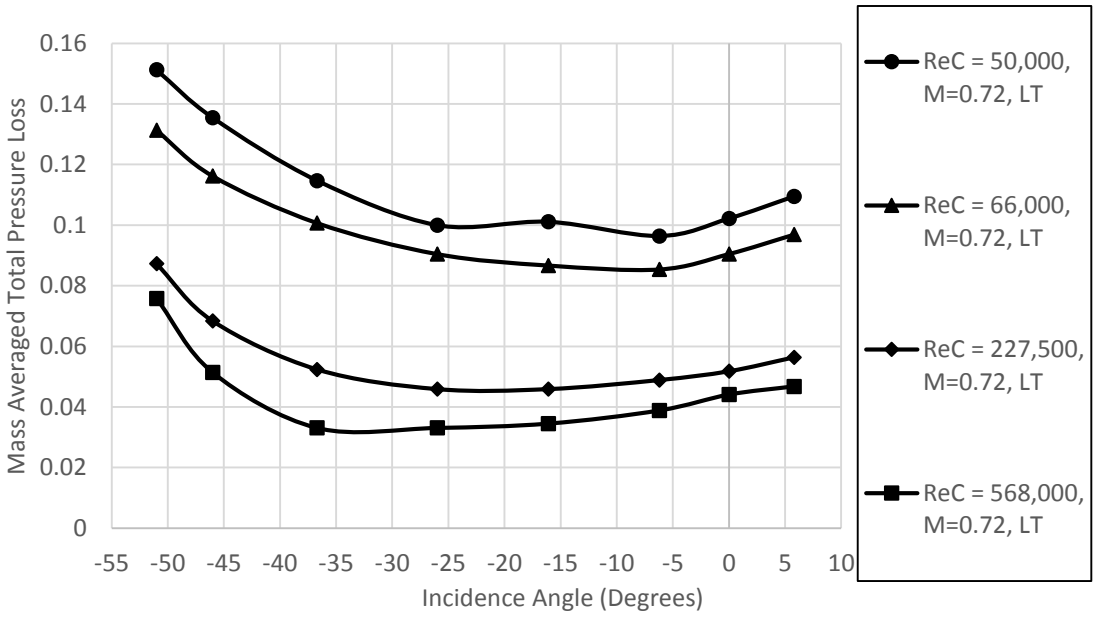

Figure 94: Mass averaged total pressure loss buckets as a function of Reynolds number and incidence angle under low turbulence.

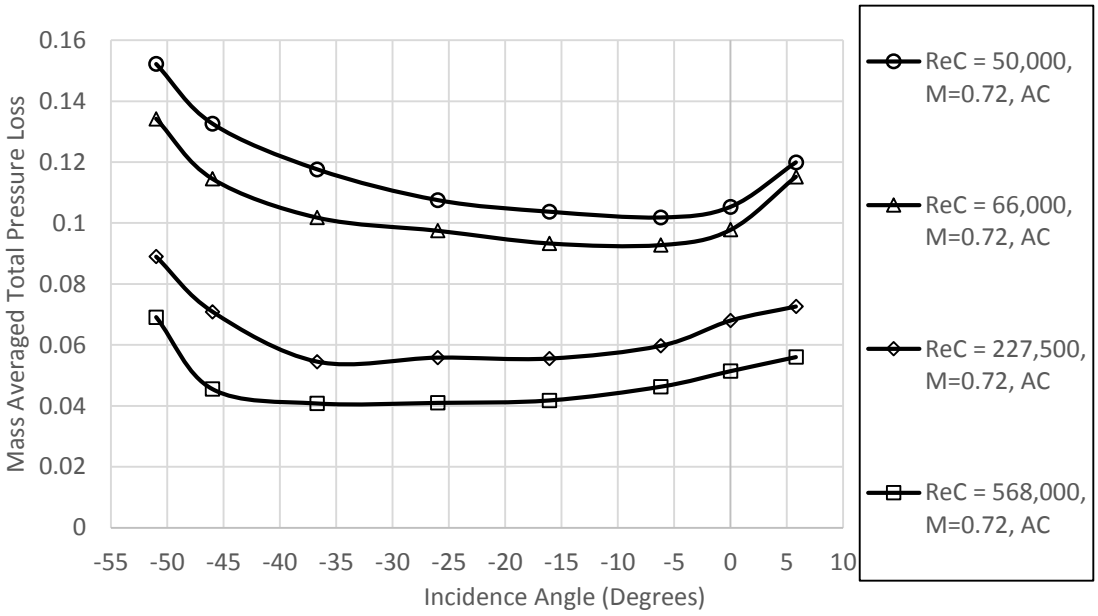

Figure 95: Mass averaged total pressure loss buckets as a function of Reynolds number and incidence angle under high turbulence.

CHAPTER V:

CONCLUSIONS

UND's high speed compressible flow wind tunnel facility has been reconfigured to experimentally investigate the aerodynamic losses of NASA's variable speed incident tolerant low pressure turbine blade. The facility was configured to acquire aerodynamic data for eight discrete incidence angles which ranged from -51.2° to 5.8°. The tests were conducted in the closed circuit wind tunnel over a span of chord Reynolds numbers based off exit conditions from 50,000 to 568,000 at two levels of turbulence intensity, 0.5% and 4.5%, at Mach 0.72. Compressibility effects were also studied at Mach 0.35 at the 227,500 and 568,000 Reynolds numbers at the design incidence angles, 5.8°, 0° and -36.8°, to match data from NASA Glenn Research Center. To perform this investigation, eight inlet nozzles were fabricated with the appropriate inlet angle. A four blade linear cascade insert was also fabricated for this study which was instrumented with midspan and quarterspan static pressure taps to determine the loading profile. Exit survey measurements were conducted to investigate the effects of incidence variation, Reynolds number lapse, and turbulence intensity. The measurements were compiled into mass weighted total pressure loss buckets as a function of incidence angle and Reynolds number to provide valuable information of the blade's performance.

Inlet and exit static pressure measurements were conducted to determine the quality of the flow throughout the test section. The endwall measurements were acquired at the

¼ axial chord location upstream of the leading edge and downstream of the trailing edge. The inlet static pressure measurements showed Reynolds number effects as the blockages downstream restricted the flow through the cascade at the 50,000 and 66,000 Reynolds numbers. Reynolds number was shown to have the most significant effect on the inlet flow distribution with turbulence having only a minor effect. Exit flow uniformity was achieved but showed slight variations in the cross passage direction.

Blade loading measurements conducted at the -51.2°, -36.8°, -0° and 5.8° incidence angles showed the effects of Reynolds number, incidence variation and turbulence intensity. The conclusions from the surface pressure measurements are as follows.

- A laminar separation bubble existed along the suction surface trailing edge at the 50,000 and 66,000 Reynolds numbers for all incidence angles and was a large contributing factor in the overall losses. Thwaite's analysis for separation at the high Reynolds number condition suggested the flow had separated.
- It was also found that much of the flow along the surface of this blade was transitional and earlier transition was seen as Reynolds number was increased and was likely due to higher spot production rates.
- A leading edge pressure surface separation bubble was prominent at the extreme negative incidence angles due to the strong adverse pressure gradient just aft of the overspeed region of the blade. The high turbulence intensity condition was not shown to have strong effect on the loading for incidence angles higher than -36.8°. However at the extreme negative angles, separation has causes reduced loading on the blade and the suction surface must compensate for the lost loading. This was shown by the increased loading on the suction surface leading edge.

- The quarterspan measurements conducted on Blade #3 did not show the effects of endwall vortices and were in close agreement with the midspan measurements.

The inlet boundary layers at the nozzle/cascade interface were measured using two custom built boundary layer rakes. The rakes consisted of five 0.794 mm diameter tubes and were positioned upstream of the passages between Blades 1 & 2 and Blades 2 & 3 and were equipped with piezoresistive pressure sensors to acquire the measurements. The findings are summarized below:

- The measurements showed a strong Reynolds number dependence for all incidence angles. The rakes captured much of the boundary layer at the 50,000 and 66,000 Reynolds numbers and the shape factor estimates suggested the boundary layer was laminar.
- The boundary layer likely transitioned to a turbulent boundary layer at the 227,500 and 568,000 Reynolds numbers and were especially thin as only the pressure port nearest to the endwall captured a portion of the boundary layer flow. Skin friction increased dramatically at these Reynolds numbers which implied the boundary layer was turbulent.
- The high free-stream turbulence condition was shown to increase the thickness of the inlet boundary layer.

The exit survey measurements was the key component of this investigation. Few studies have been conducted to the author's knowledge that have encompassed such wide range of incidence angles over a wide span of Reynolds numbers. The effects of incidence, Reynolds

number and turbulence cannot be understated and the results of this investigation are summarized as follows:

- Incidence angle was found to have a significant impact on nature of the wake. As the blade incidence was decreased from 5.8° to -51.2°, the main passage vortex had migrated from the quarterspan location towards the endwall due to reduced turning and the resulting interactions from the secondary flows.
- The pressure losses were maximum at the -51.2° incidence angle due to massive blockages from the leading edge separation on the pressure surface. The mass averaged losses were as high as 15% at the 50,000 Reynolds number at the low turbulence condition.
- The total pressure losses improved for the moderate incidence angles but generally increased at the 0° and 5.8° incidence angles. At the high Reynolds numbers, the losses were relatively constant between -36.8° and -6.2° incidence angles.
- The losses increased dramatically as Reynolds number decreased due to profile losses and stronger secondary loss cores.
- Turbulence was a major factor as it diffused the losses within the wake. The increased turbulence intensity also caused the suction leg of the horseshoe vortex to get mixed out by the passage vortex.
- The mass averaged losses were generally higher for the aero-combustor case as a result the increased levels of boundary layer skin friction and turbulent mixing across velocity gradients in the flow.

APPENDICES

APPENDIX A: Inlet and Exit Endwall Mach Distributions

Inlet and exit endwall isentropic Mach distributions are presented for the cases that were not included in Chapter IV of this document.

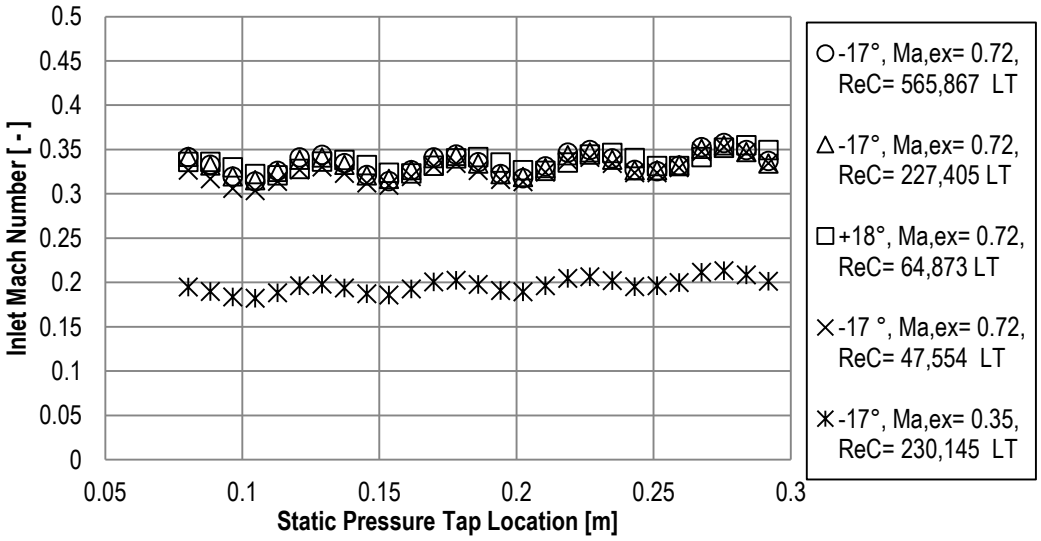

Figure 96: Inlet isentropic Mach distributions as a function of Reynolds number at -17° inlet angle under low turbulence.

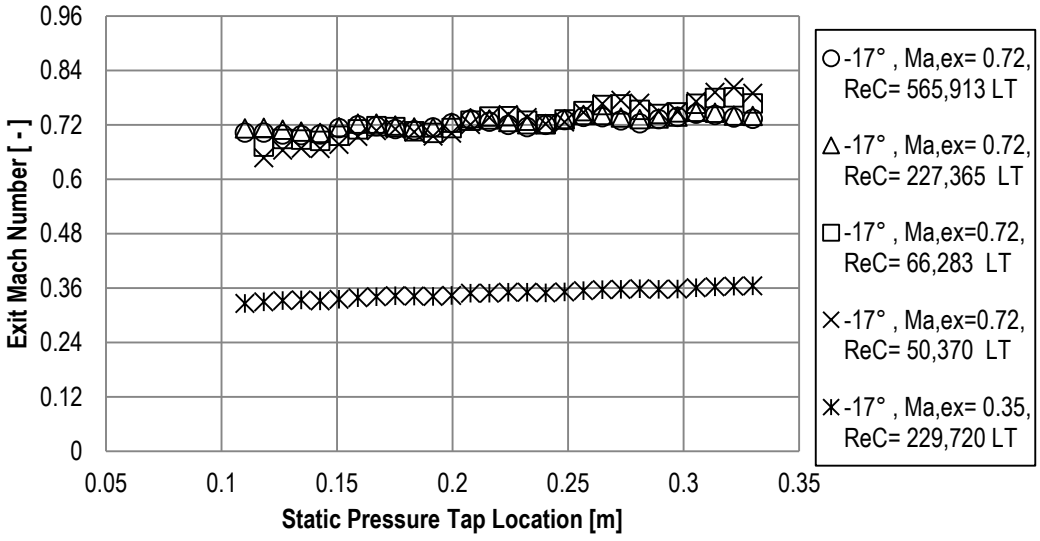

Figure 97: Exit isentropic Mach distributions as a function of Reynolds number at -17° inlet angle under low turbulence.

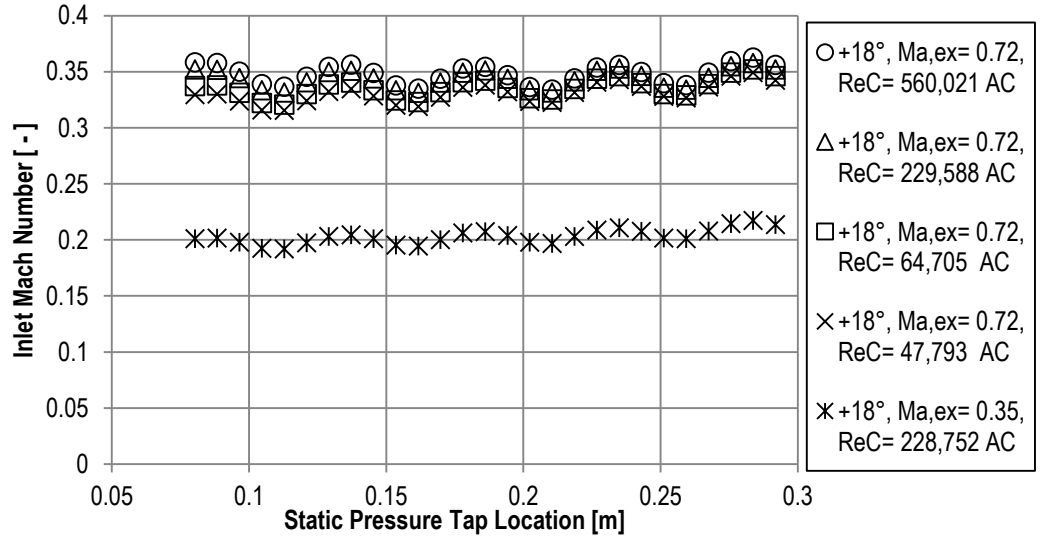

Figure 98: Inlet isentropic Mach distributions as a function of Reynolds number at -17° inlet angle under high turbulence.

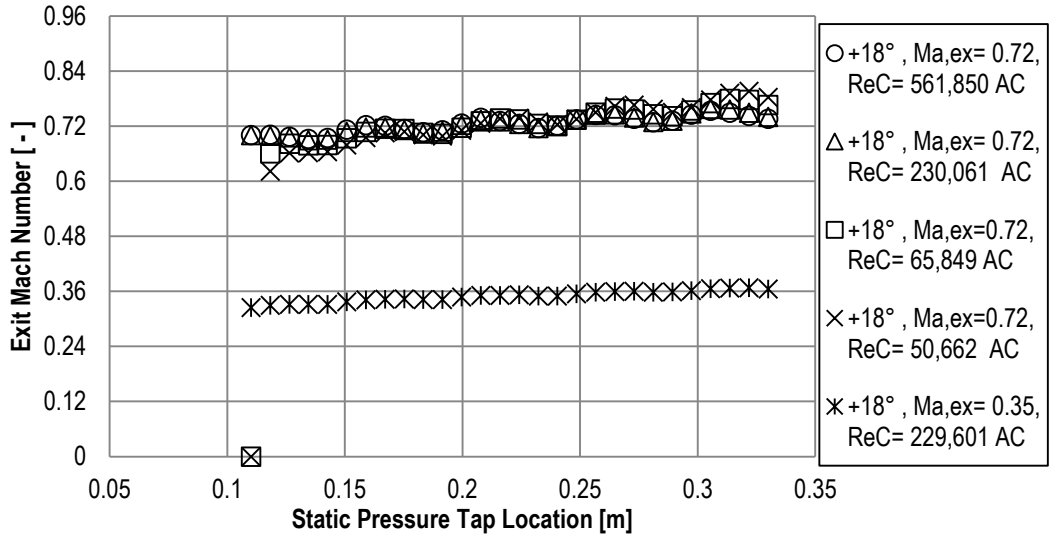

Figure 99: Exit isentropic Mach distributions as a function of Reynolds number at -17° inlet angle under low turbulence.

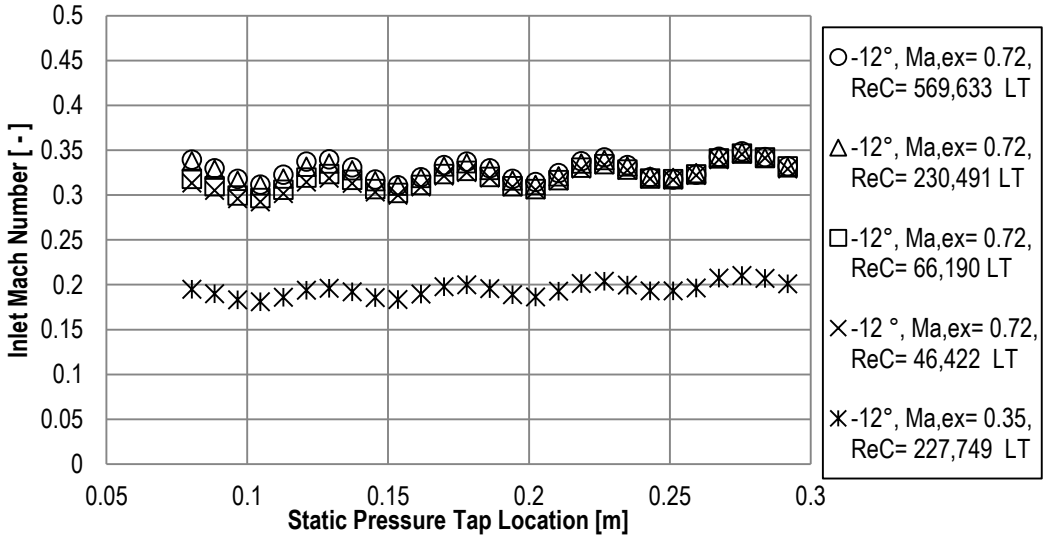

Figure 100: Inlet isentropic Mach distributions as a function of Reynolds number at -12° inlet angle under low turbulence.

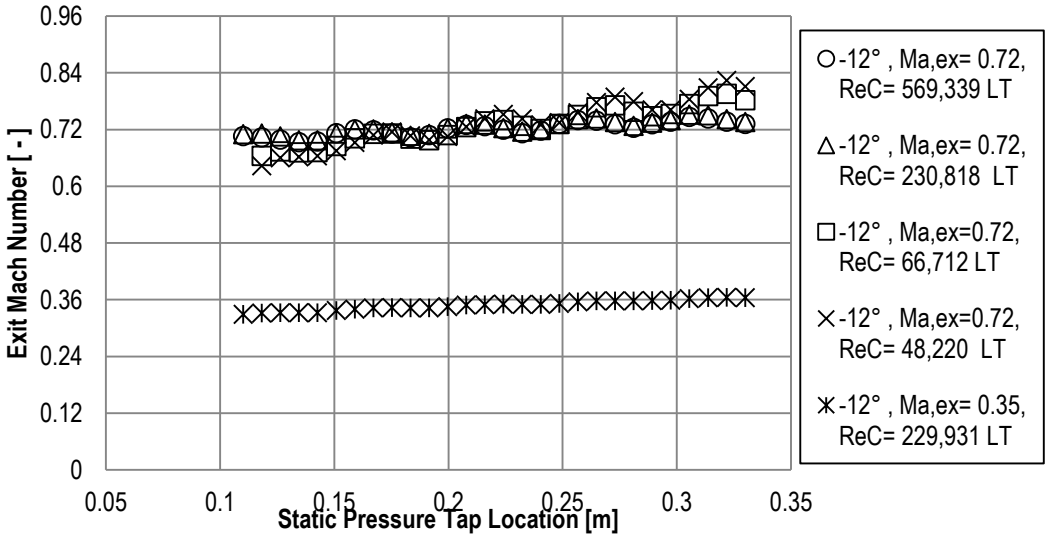

Figure 101: Exit isentropic Mach distributions as a function of Reynolds number at -12° inlet angle under low turbulence.

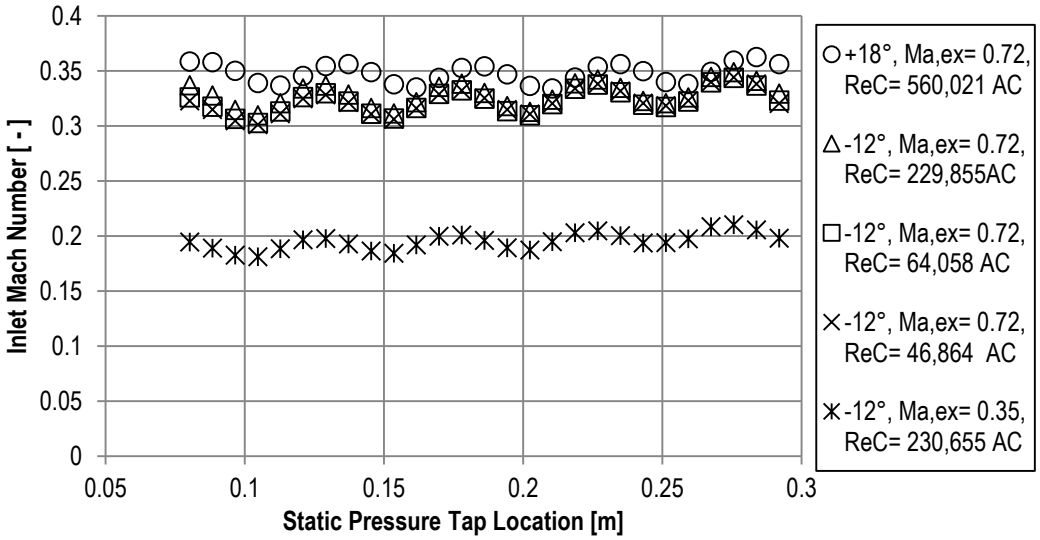

Figure 102: Inlet isentropic Mach distributions as a function of Reynolds number at -12° inlet angle under high turbulence.

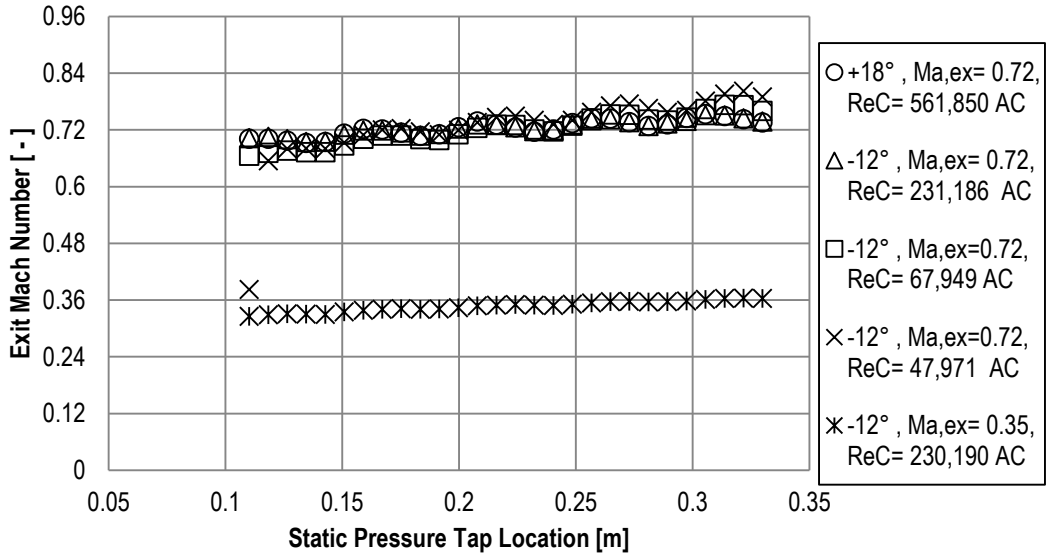

Figure 103: Exit isentropic Mach distributions as a function of Reynolds number at -12° inlet angle under high turbulence.

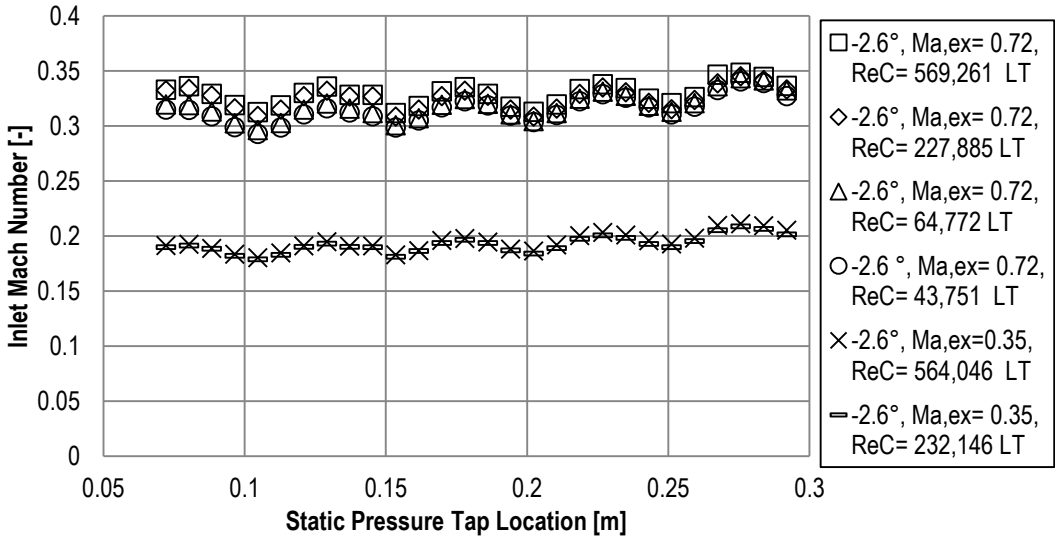

Figure 104: Inlet isentropic Mach distributions as a function of Reynolds number at -2.6° inlet angle under low turbulence.

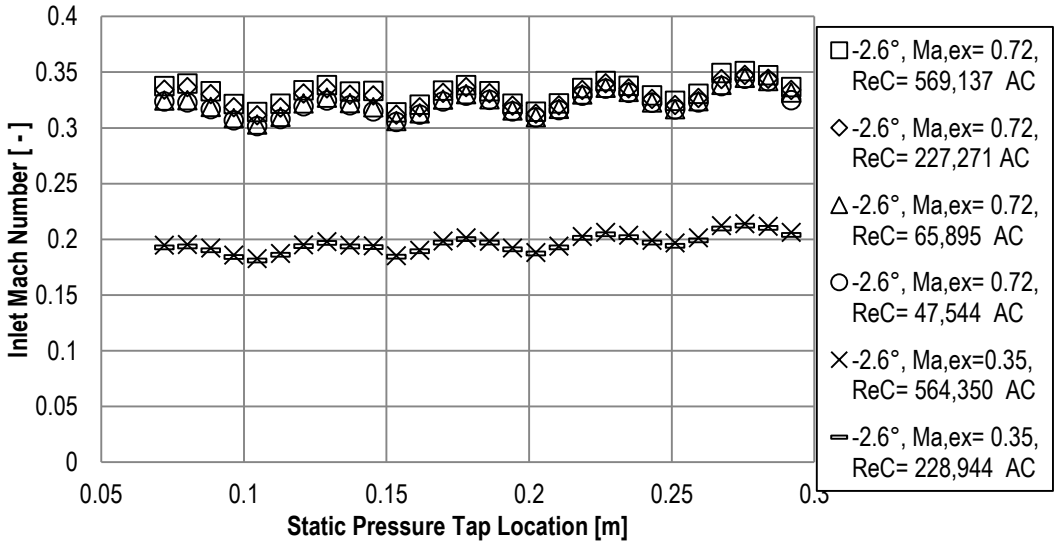

Figure 105: Exit isentropic Mach distributions as a function of Reynolds number at -2.6° inlet angle under high turbulence.

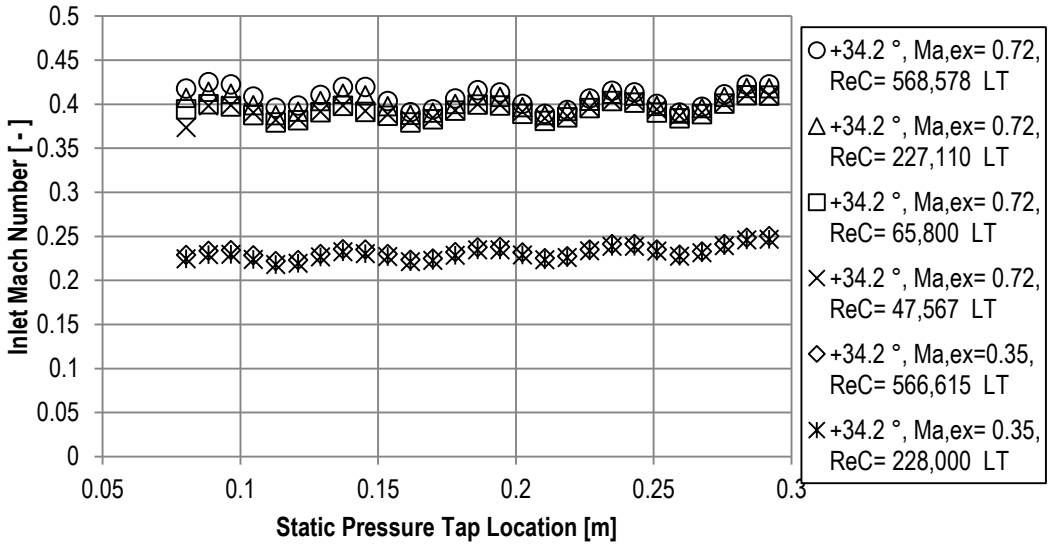

Figure 106: Inlet isentropic Mach distributions as a function of Reynolds number at 34.2° inlet angle under low turbulence.

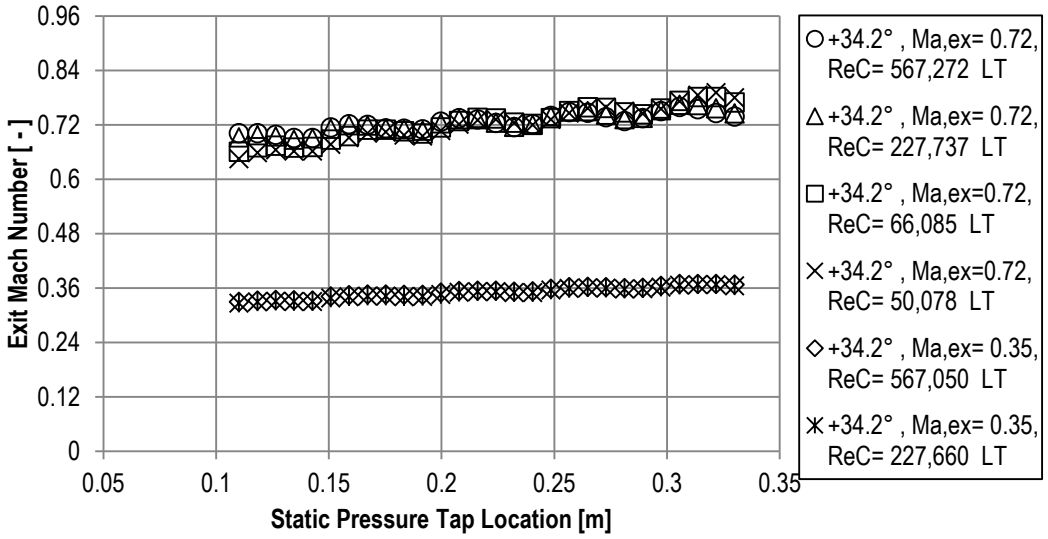

Figure 107: Exit isentropic Mach distributions as a function of Reynolds number at 34.2° inlet angle under low turbulence.

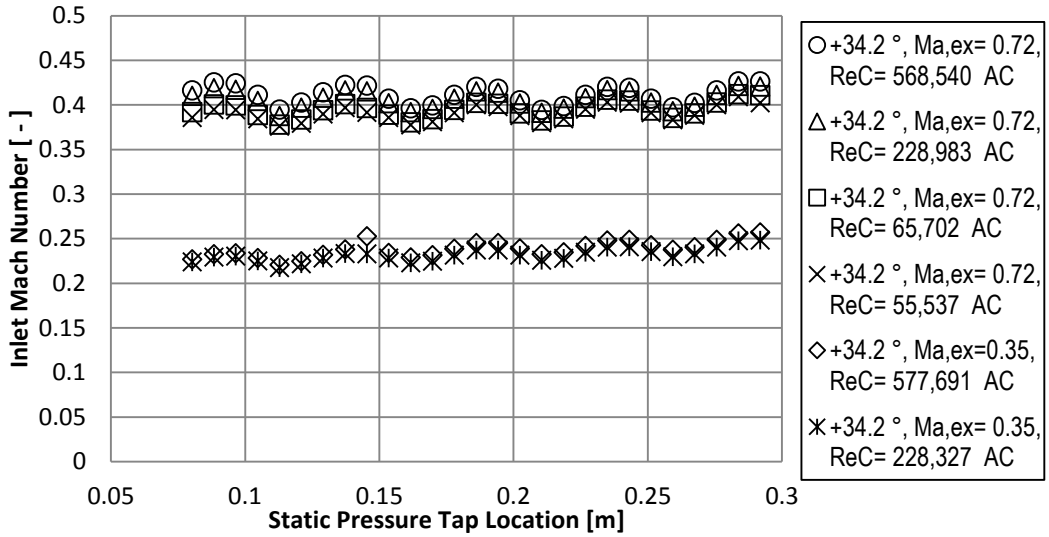

Figure 108: Inlet isentropic Mach distributions as a function of Reynolds number at 34.2° inlet angle under high turbulence.

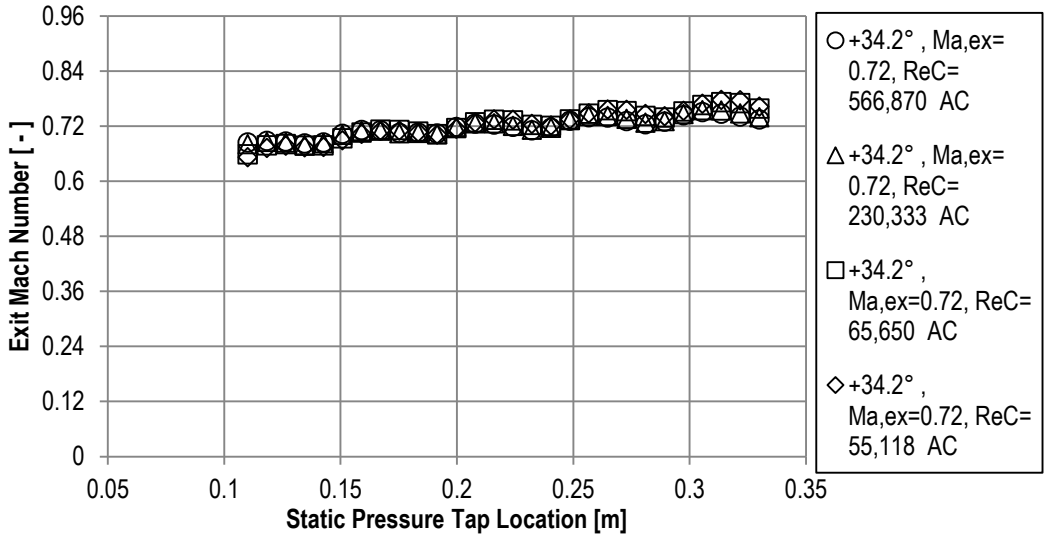

Figure 109: Inlet isentropic Mach distributions as a function of Reynolds number at 34.2° inlet angle under high turbulence.

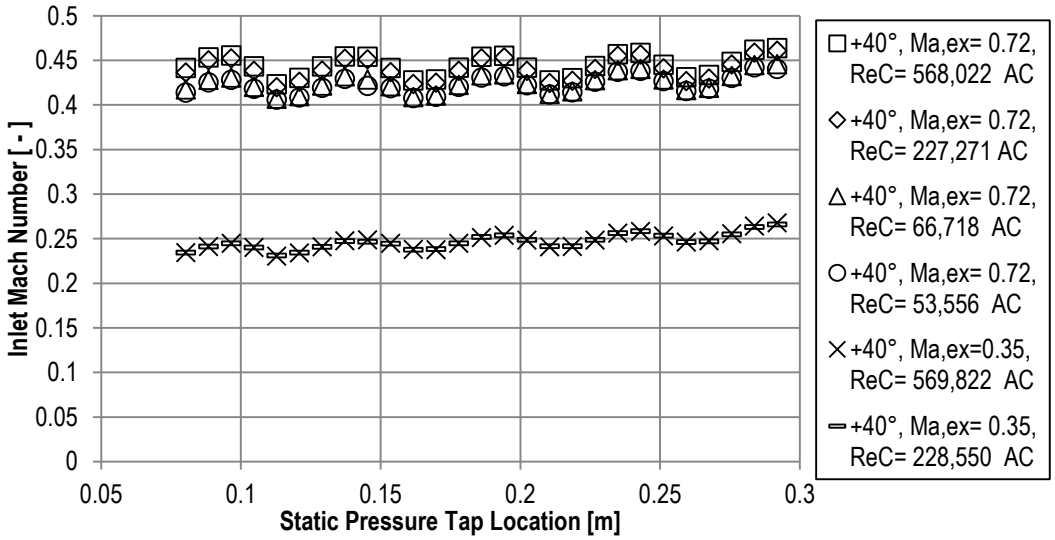

Figure 110: Inlet isentropic Mach distributions as a function of Reynolds number at 40° inlet angle under high turbulence.

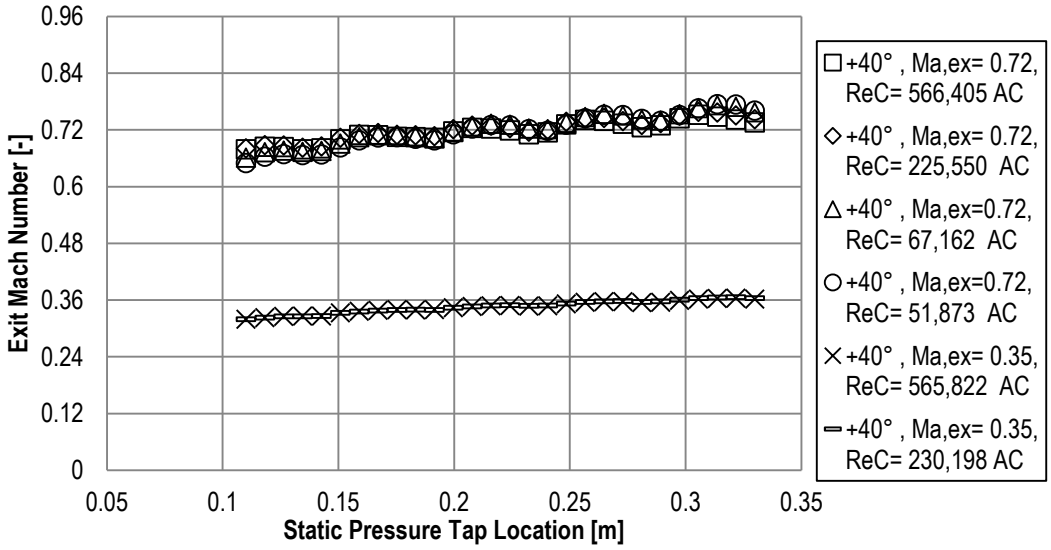

Figure 111: Exit isentropic Mach distributions as a function of Reynolds number at 40° inlet angle under high turbulence.

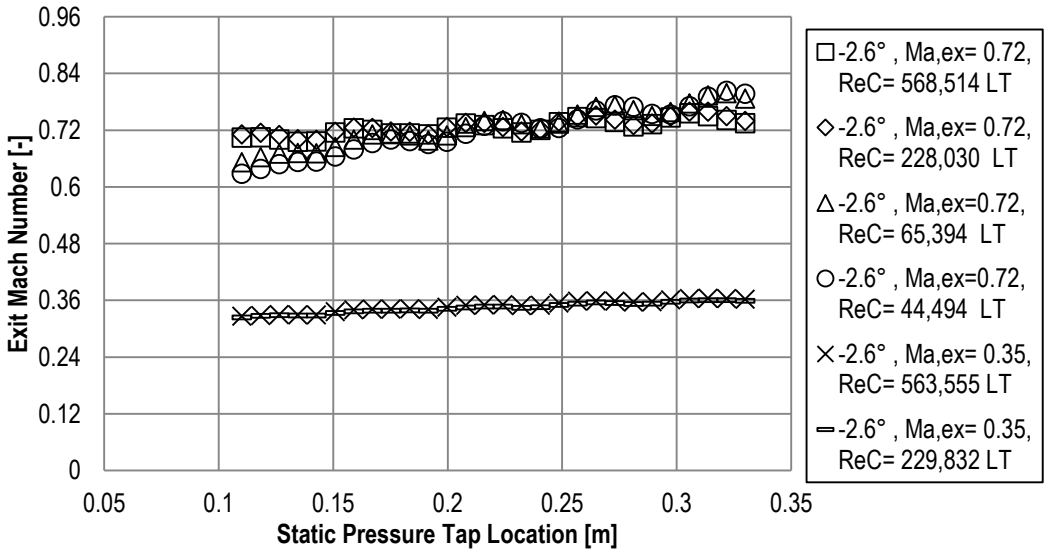

Figure 112: Exit isentropic Mach distributions as a function of Reynolds number at -2.6° inlet angle under low turbulence.

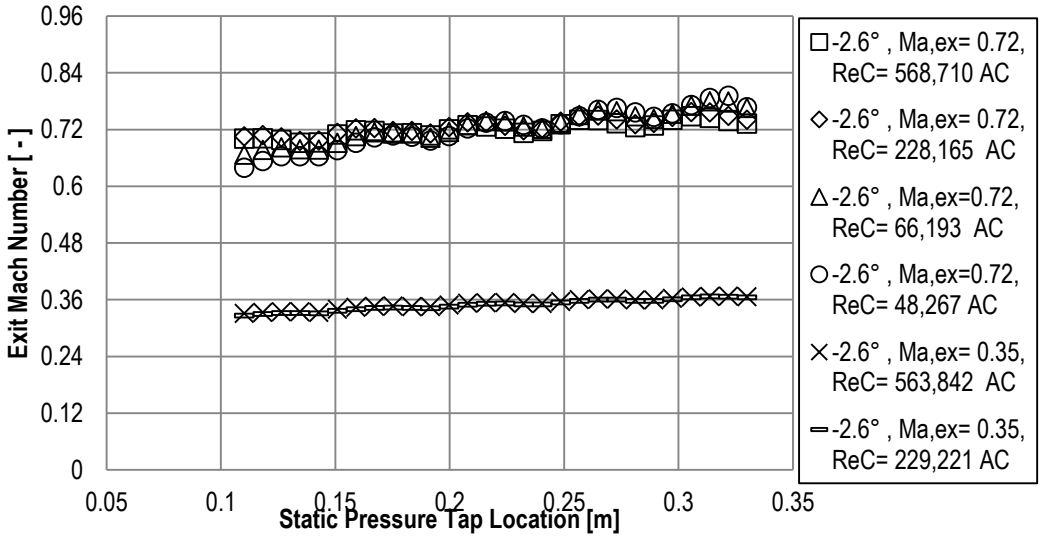

Figure 113: Exit isentropic Mach distributions as a function of Reynolds number at -2.6° inlet angle under high turbulence.

APPENDIX B: Midspan and Quarterspan Pressure Distributions

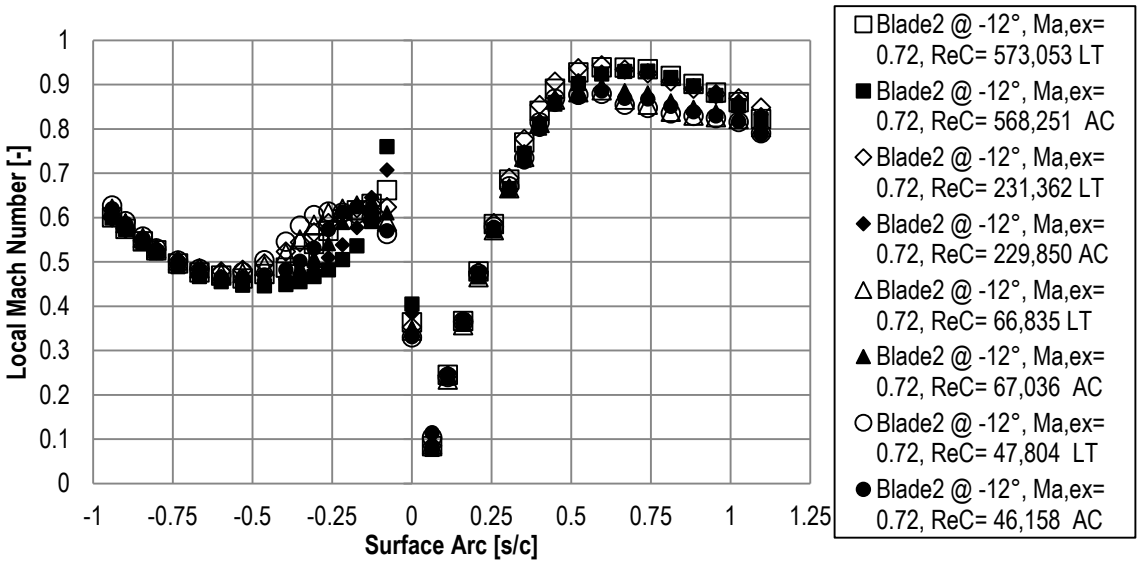

Figure 114: Midspan isentropic Mach distribution as a function of Reynolds number and turbulence intensity at -12° inlet angle.

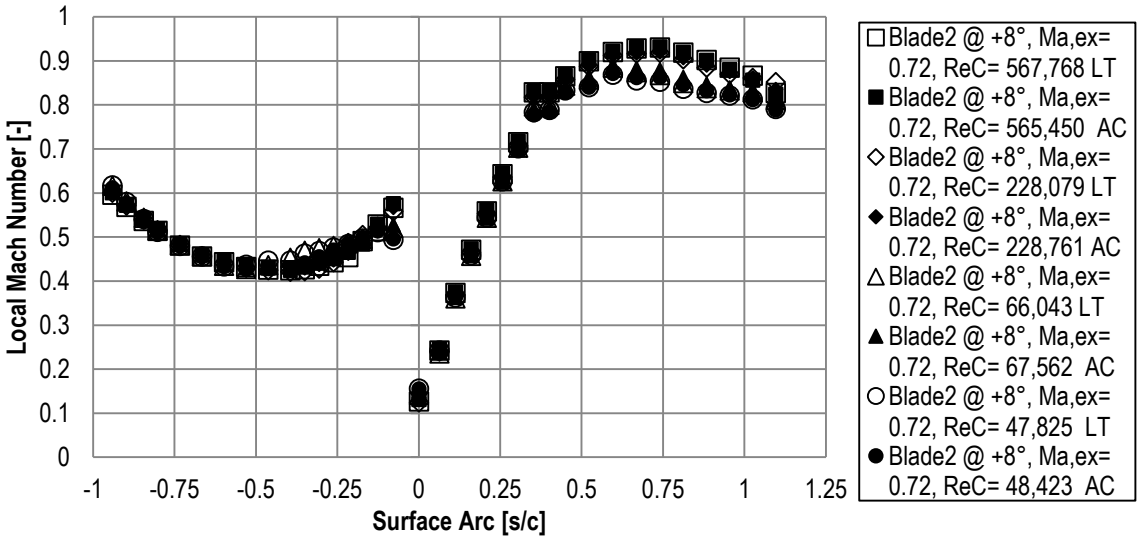

Figure 115: Midspan isentropic Mach distribution as a function of Reynolds number and turbulence intensity at 8° inlet angle.

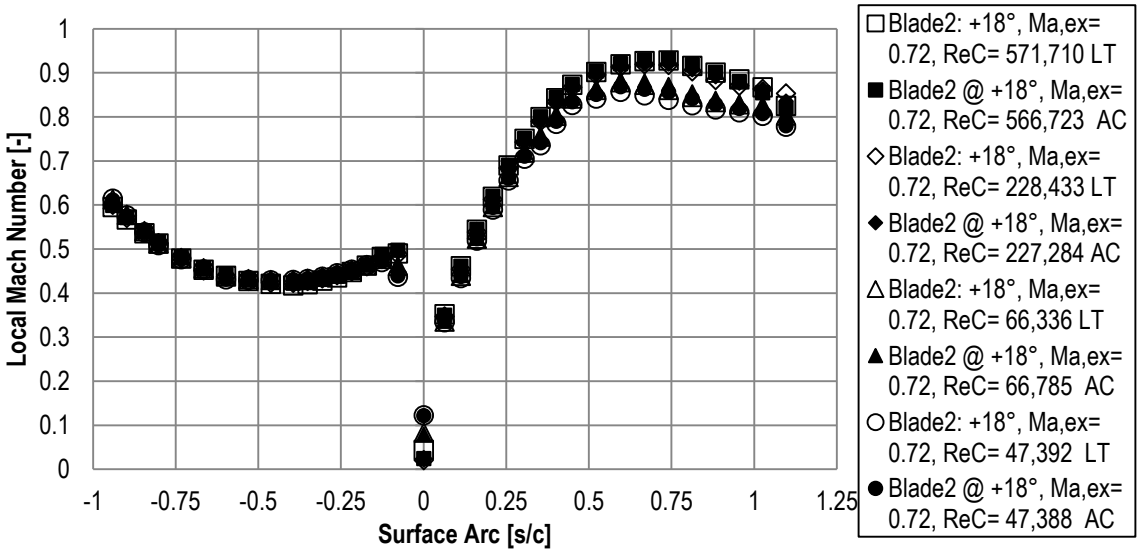

Figure 116: Midspan isentropic Mach distribution as a function of Reynolds number and turbulence intensity at 18° inlet angle.

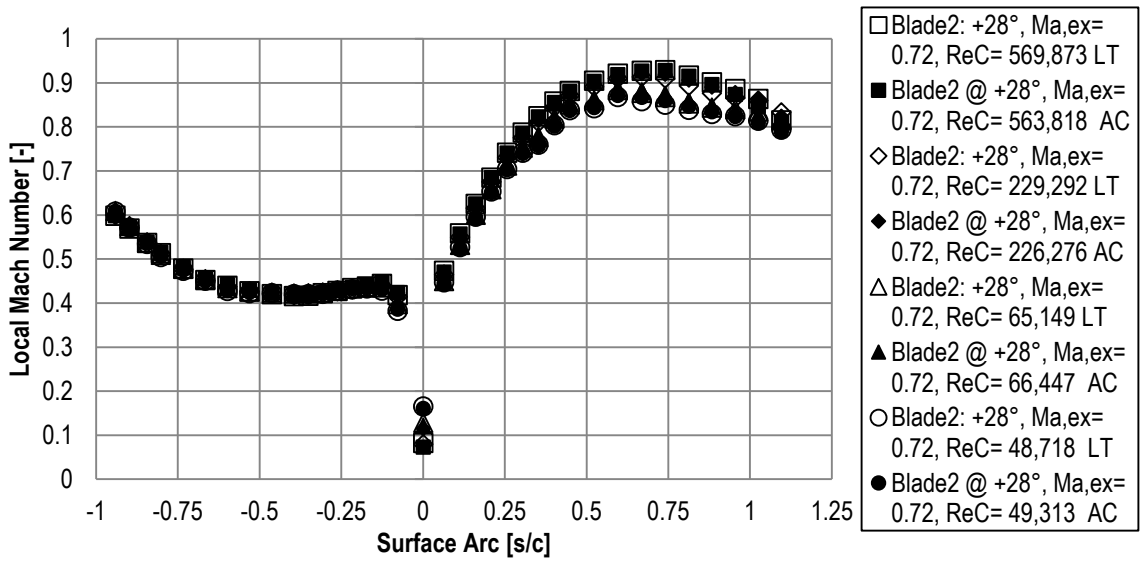

Figure 117: Midspan isentropic Mach distribution as a function of Reynolds number and turbulence intensity at 28° inlet angle.

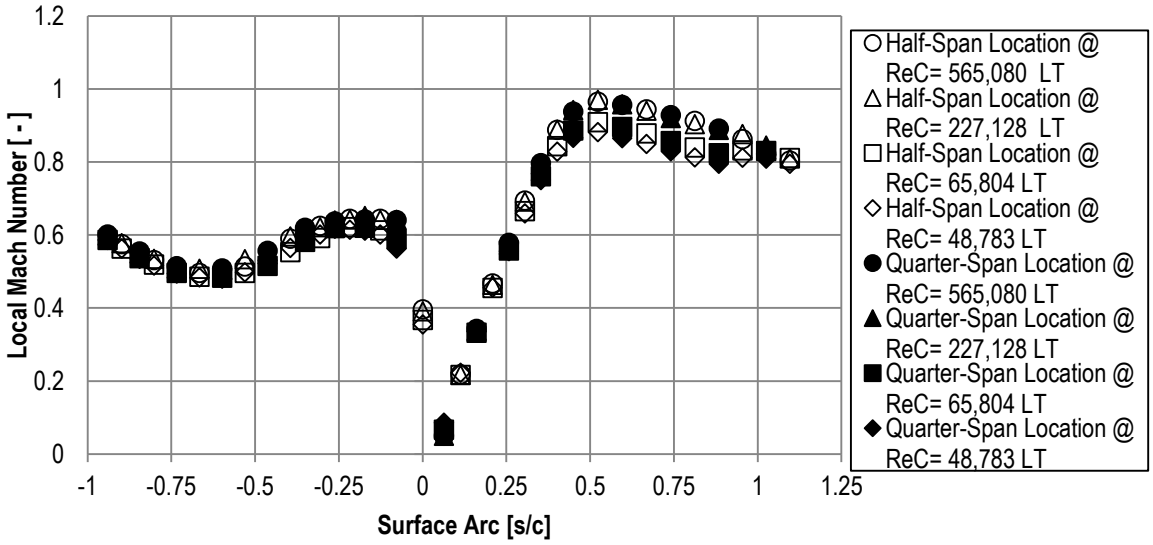

Figure 118: Midspan and quarterspan isentropic Mach distribution as a function of Reynolds number at -12° inlet angle for Blade 3 under low turbulence.

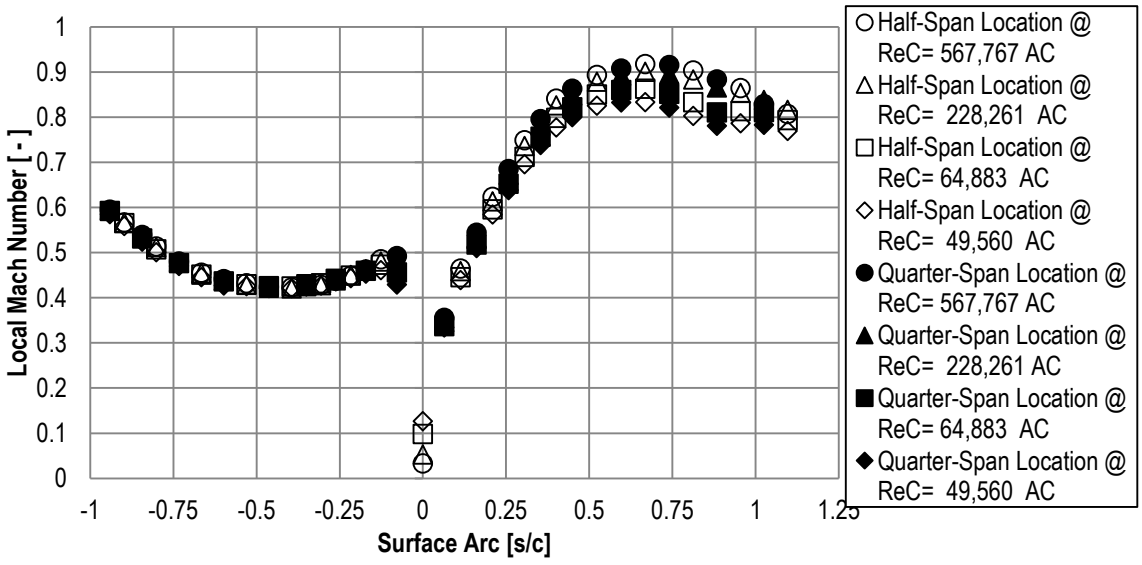

Figure 119 Midspan and quarterspan isentropic Mach distribution as a function of Reynolds number and turbulence intensity at -17° inlet angle for Blade 3.

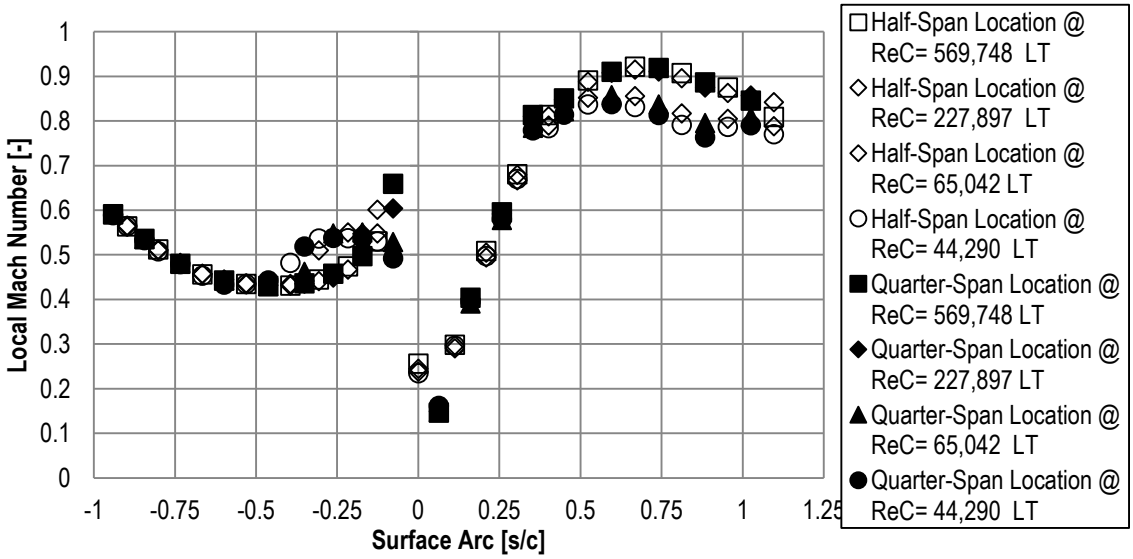

Figure 120: Midspan and quarterspan isentropic Mach distribution as a function of Reynolds number at -2.6° inlet angle for Blade 3 under low turbulence.

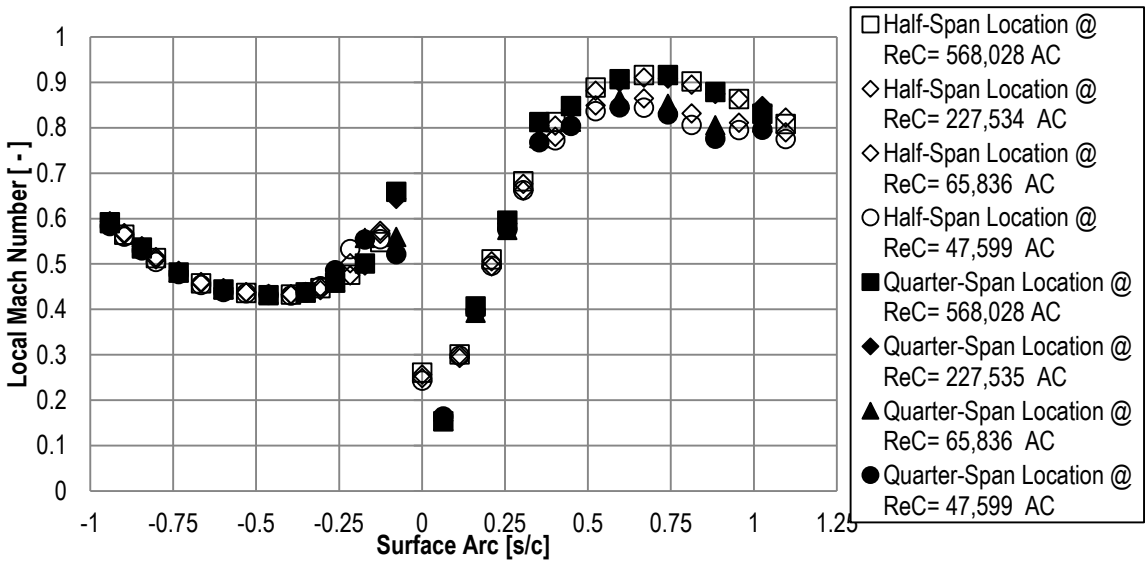

Figure 121: Midspan and quarterspan isentropic Mach distribution as a function of Reynolds number at -2.6° inlet angle for Blade 3 under high turbulence

APPENDIX C: Boundary Layer Distributions

Thwaite's Analysis was used for the determination of skin friction, shape factor and momentum thickness Reynolds number for each inlet angle.

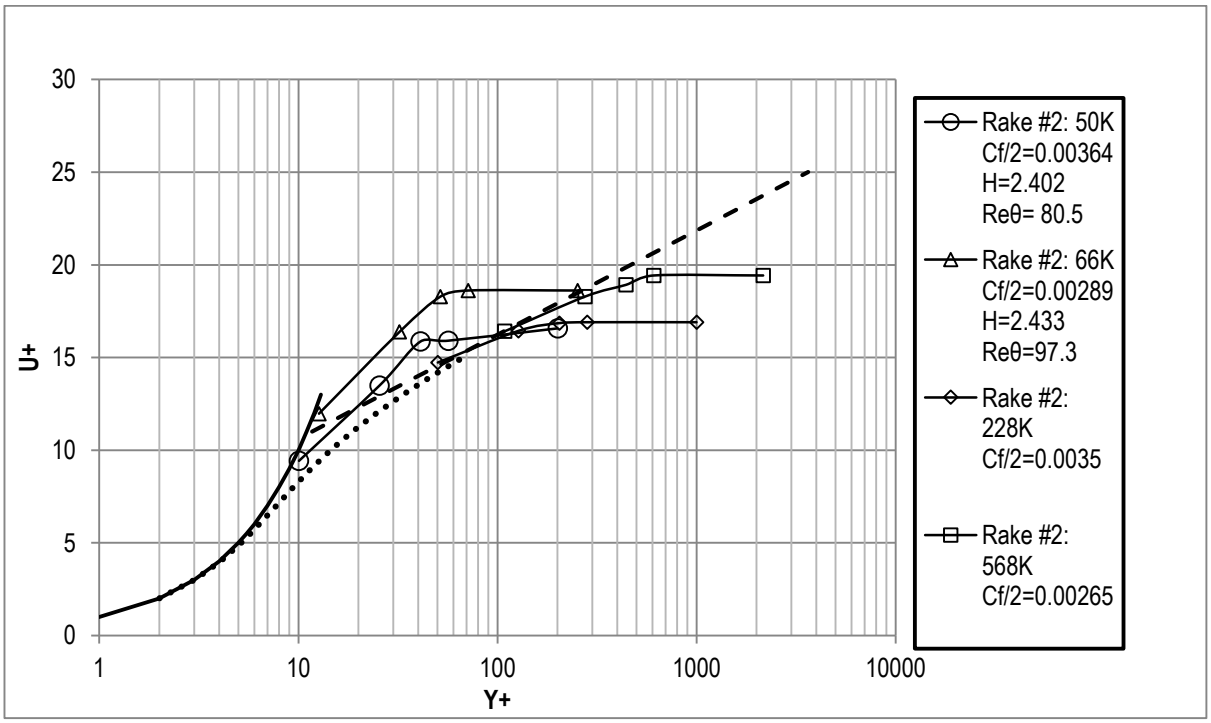

Figure 122: Boundary layer distributions as a function of Reynolds number at -12° under low turbulence.

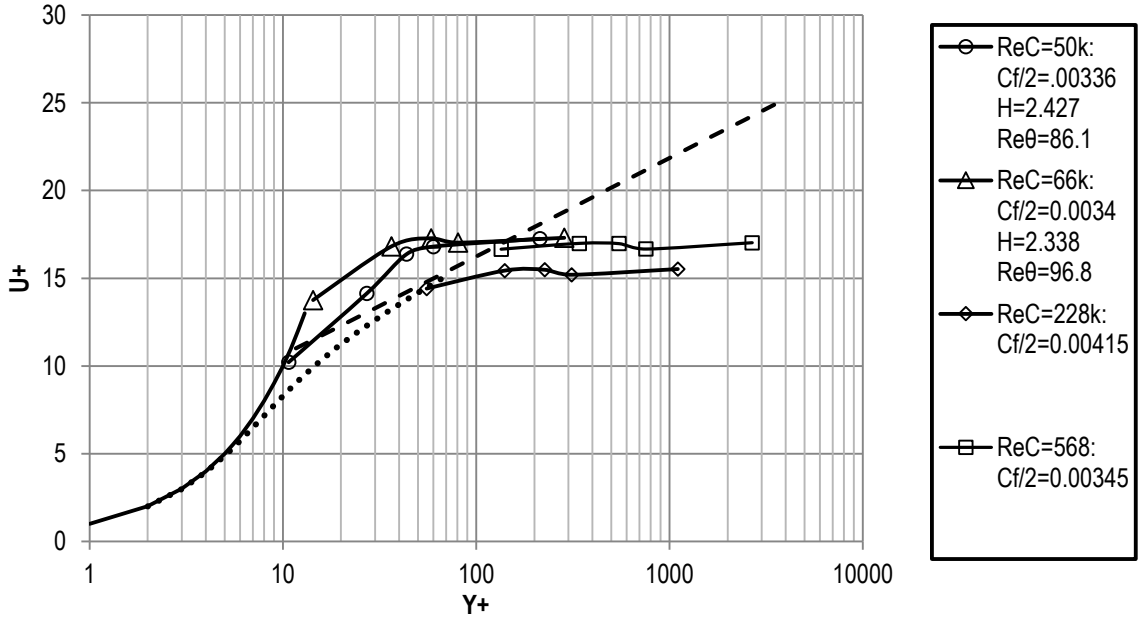

Figure 123: Boundary layer distributions as a function of Reynolds number at 18° under low turbulence.

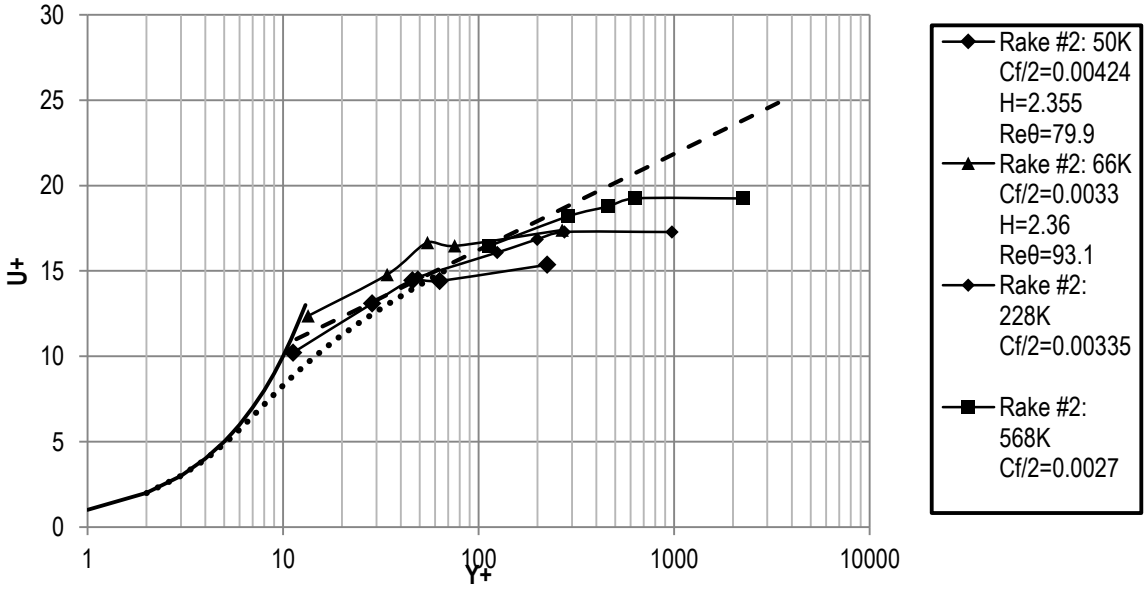

Figure 124: Boundary layer distributions as a function of Reynolds number at -12° under high turbulence.

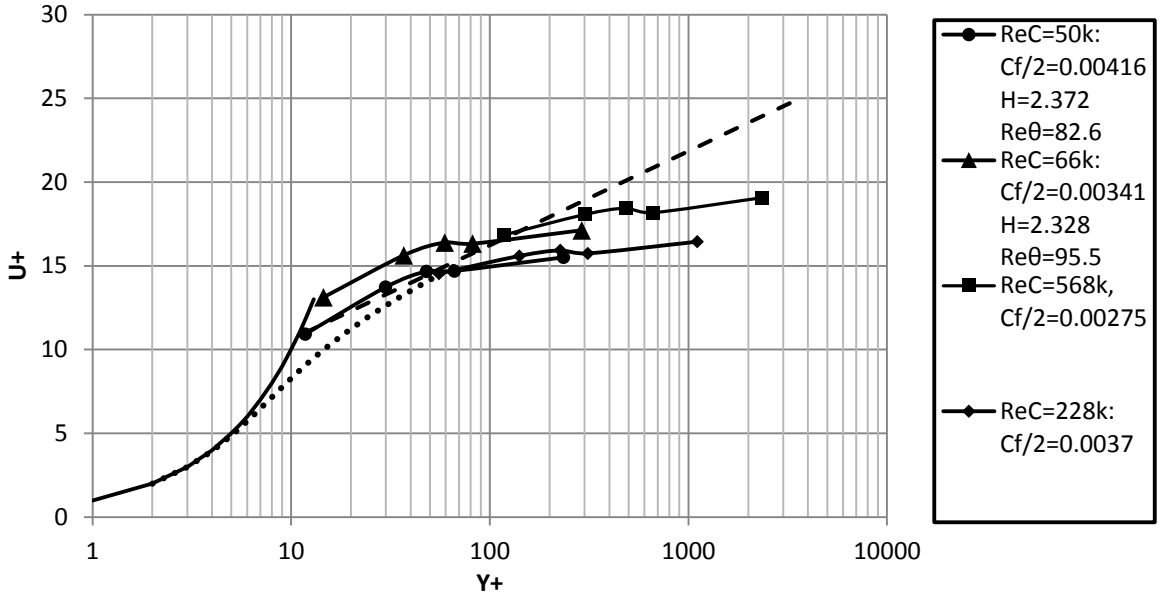

Figure 125: Boundary layer distributions as a function of Reynolds number at 18° under high turbulence.

APPENDIX D: Cone Probe Calibration Methodology and Results

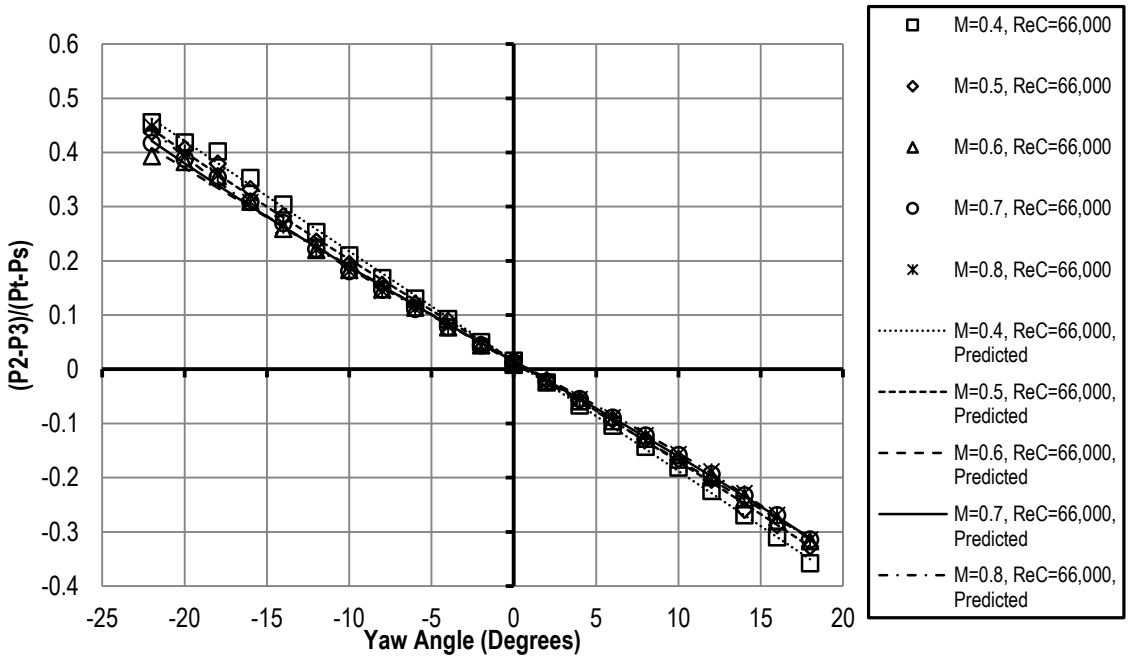

Figure 126: Coefficients of yaw sensitivity as a function of Mach number at ReC=66k showing predicted and experimental values.

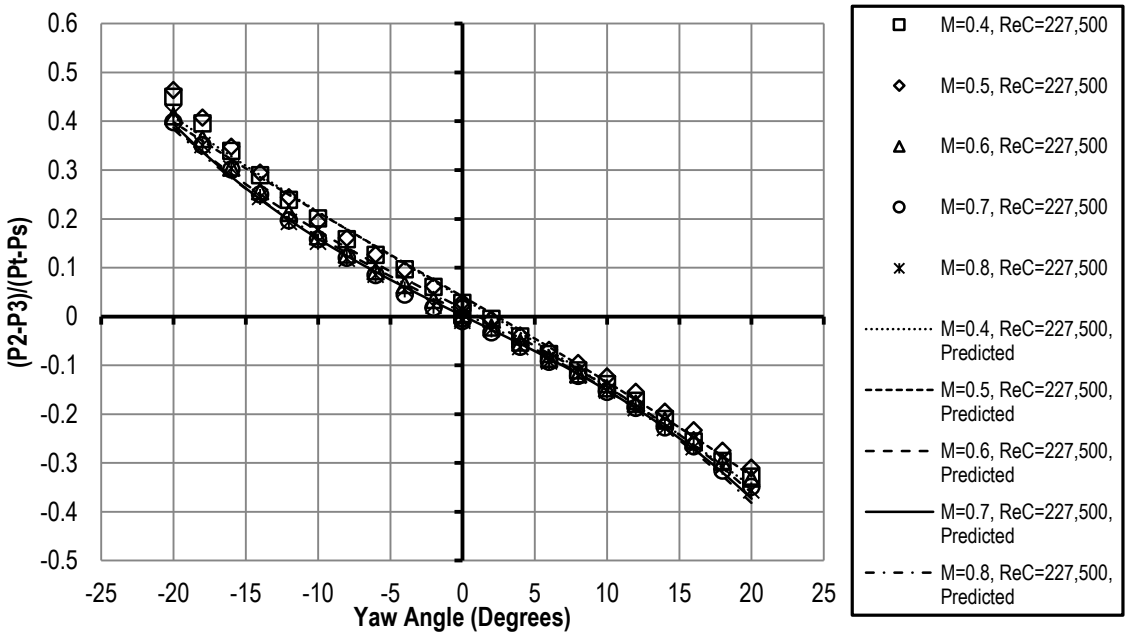

Figure 127: Coefficients of yaw sensitivity as a function of Mach number at ReC=227.5k showing predicted and experimental values.

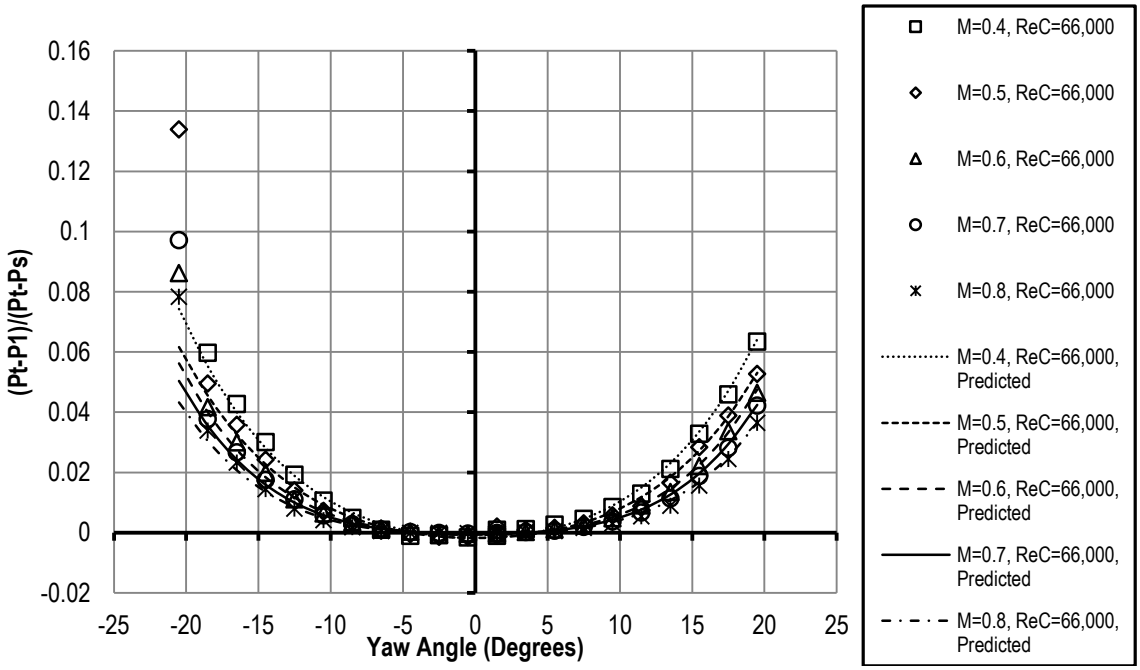

Figure 128: Coefficients of total pressure sensitivity as a function of Mach number at ReC=66k showing predicted and experimental values.

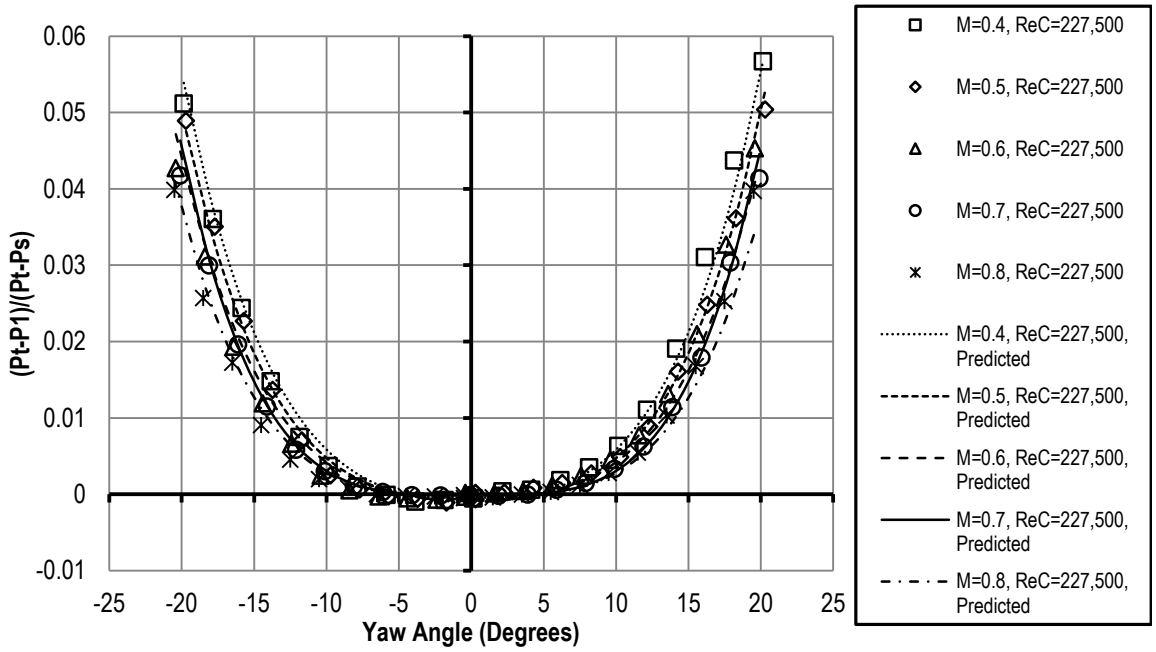

Figure 129: Coefficients of total pressure sensitivity as a function of Mach number at ReC=227.5k showing predicted and experimental values.

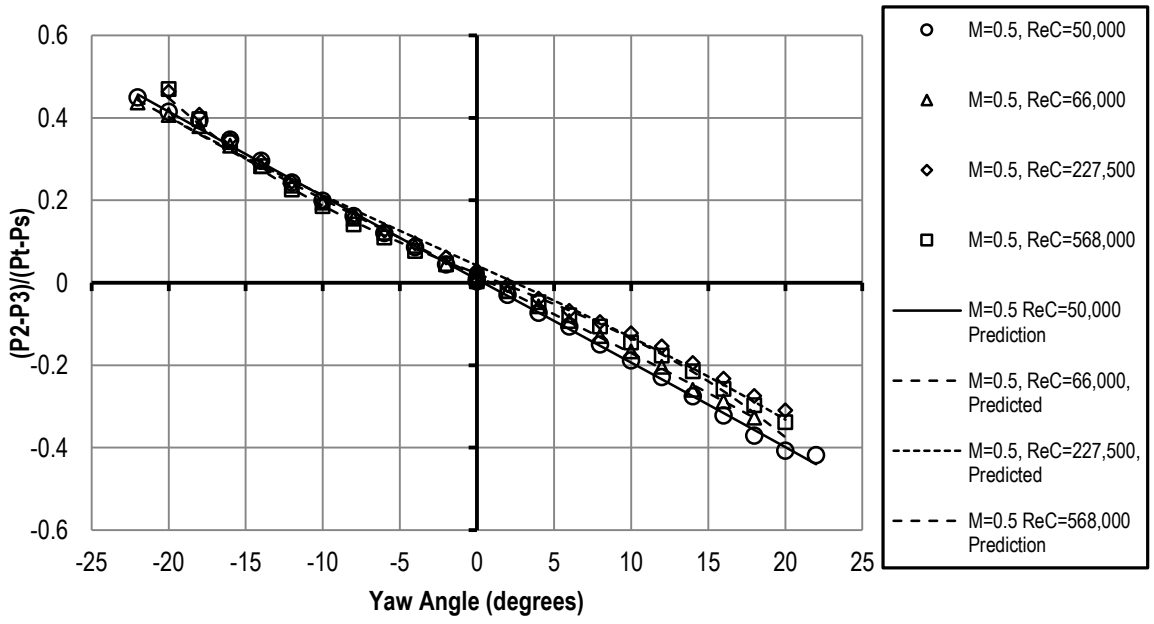

Figure 130: Coefficients of yaw sensitivity as a function of Reynolds number at M=0.5 showing predicted and experimental values.

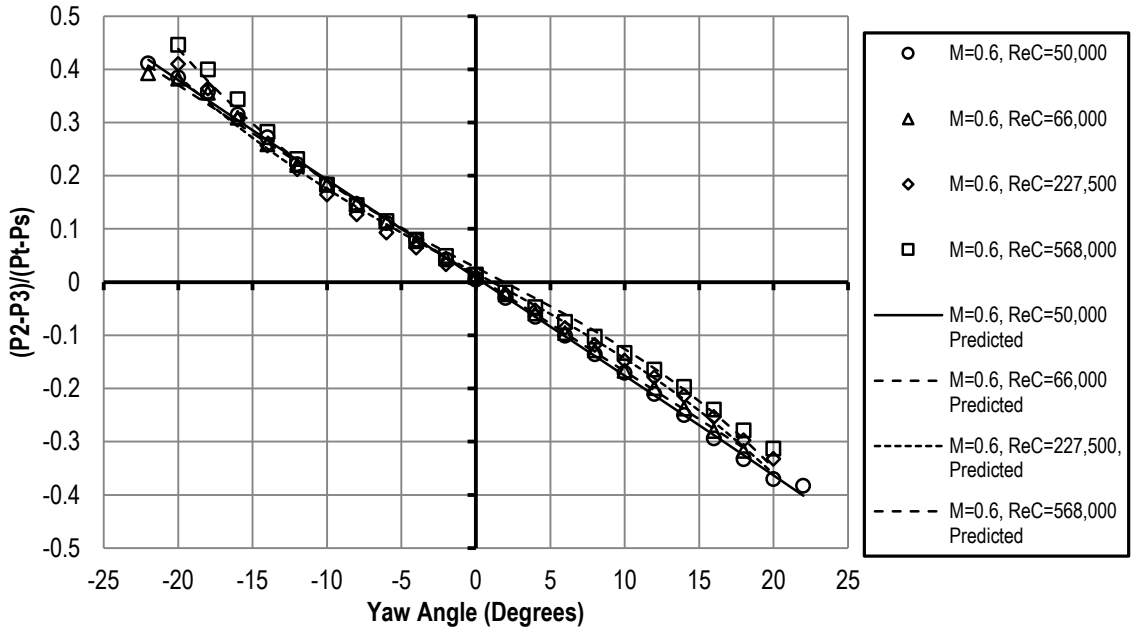

Figure 131: Coefficients of yaw sensitivity as a function of Reynolds number at M=0.6 showing predicted and experimental values.

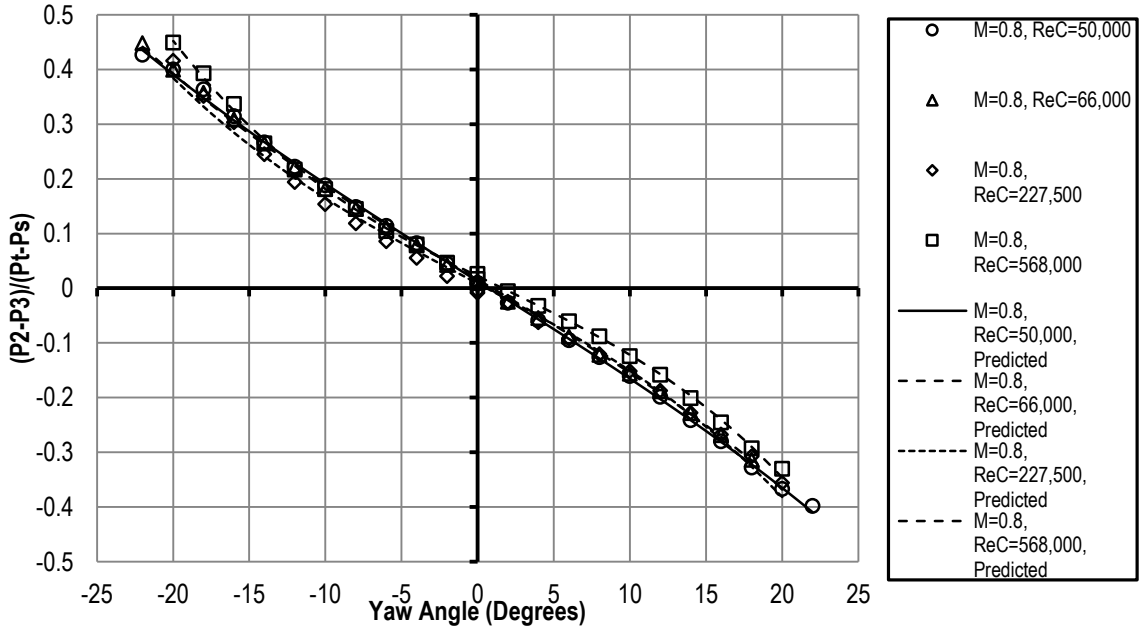

Figure 132: Coefficients of yaw sensitivity as a function of Reynolds number at M=0.8 showing predicted and experimental values.

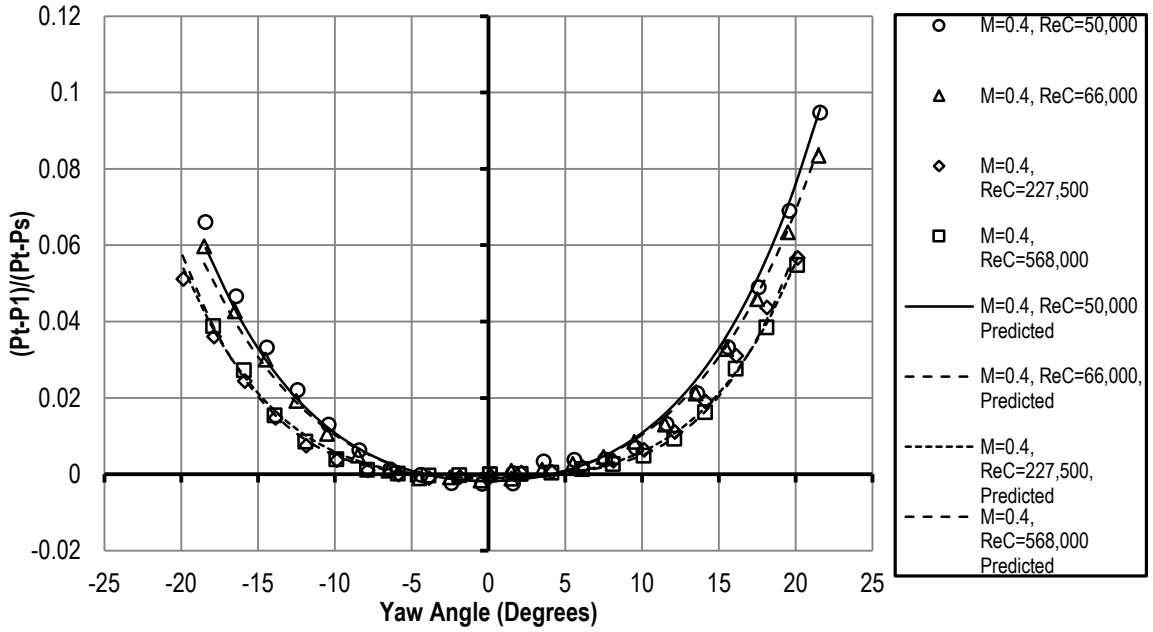

Figure 133: Coefficients of total pressure recovery as a function of Reynolds number at M=0.4 showing predicted and experimental values.

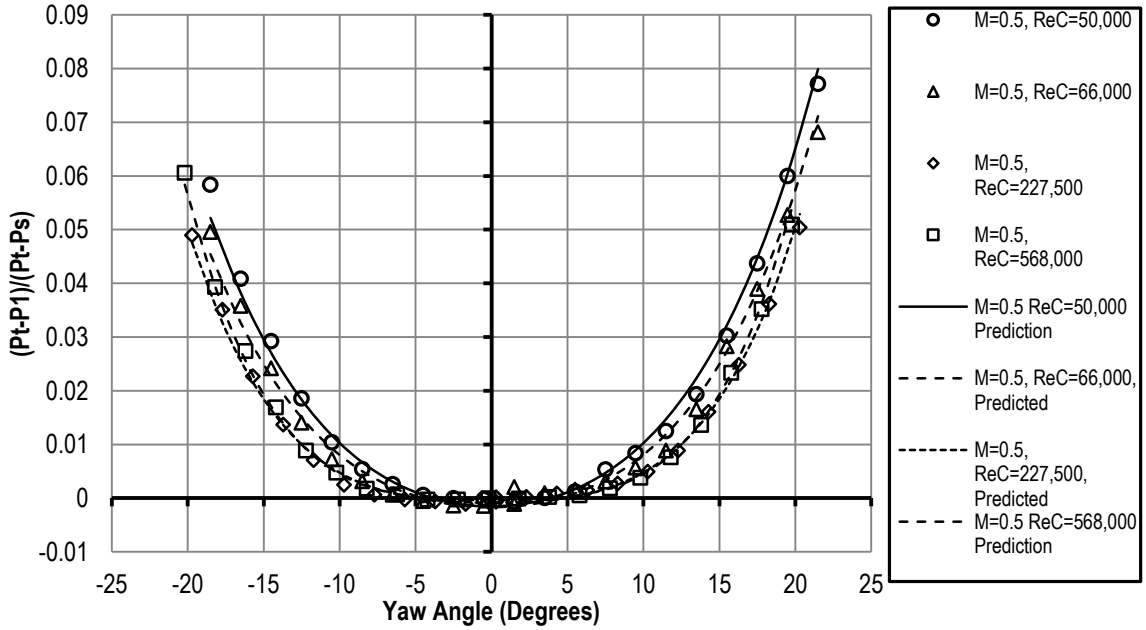

Figure 134: Coefficients of total pressure recovery as a function of Reynolds number at M=0.5 showing predicted and experimental values.

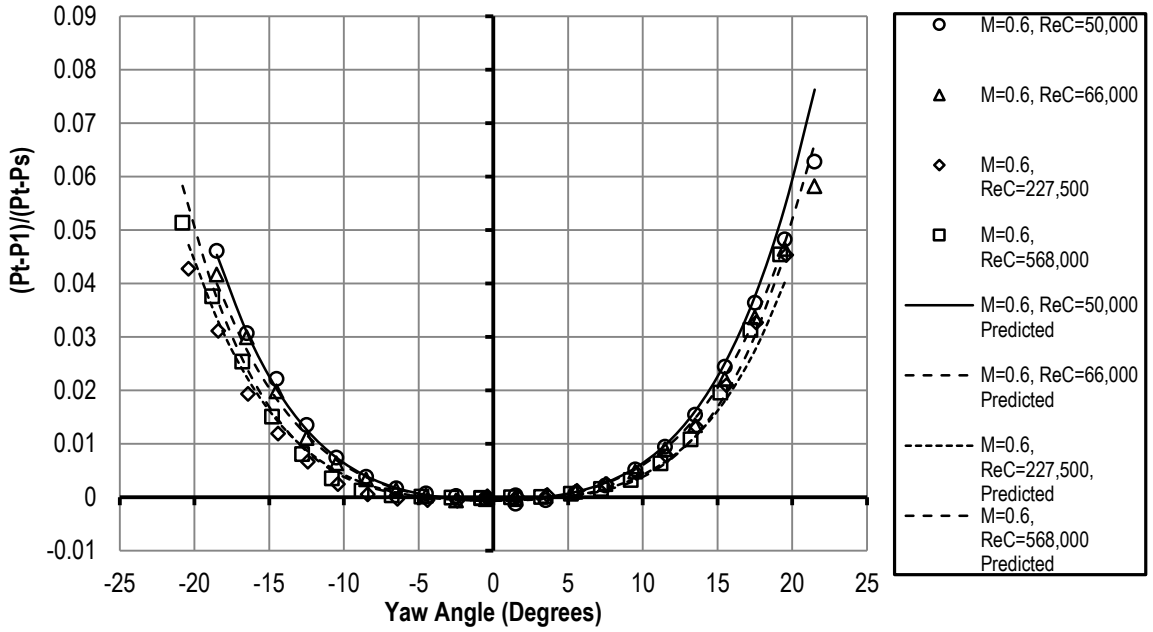

Figure 135: Coefficients of total pressure recovery as a function of Reynolds number at M=0.6 showing predicted and experimental values.

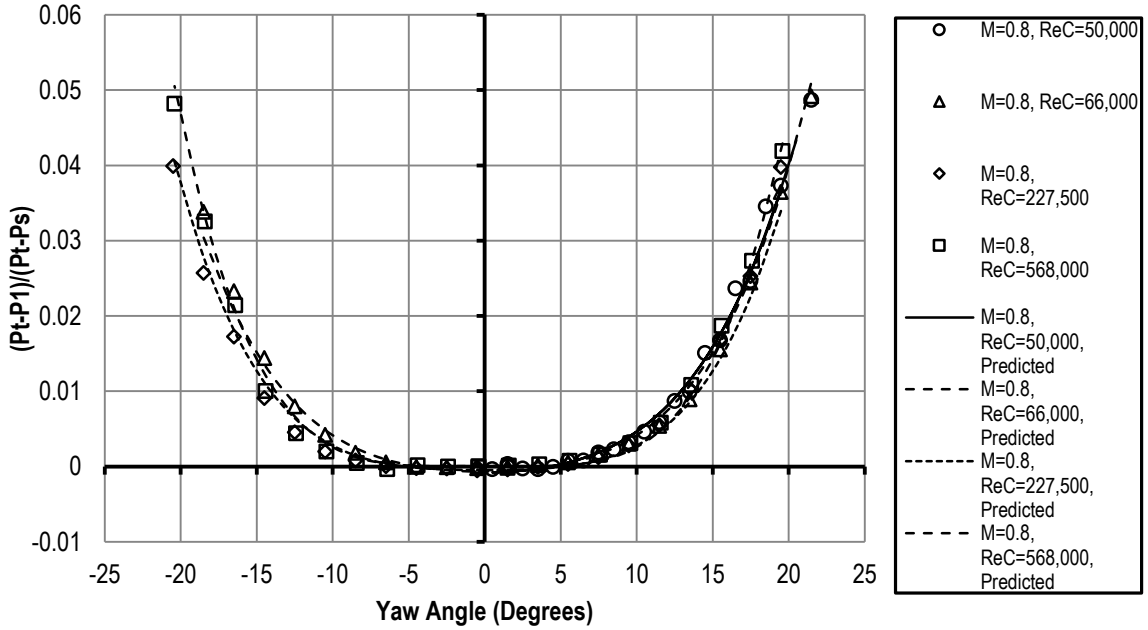

Figure 136: Coefficients of total pressure recovery as a function of Reynolds number at M=0.8 showing predicted and experimental values.

APPENDIX E: Aerodynamic Losses Results

Table 10: Wind tunnel conditions, mass averaged loss and turning angle for ¼ axial chord exit surveys at -26.2° incidence with aero-combustor and low turbulence conditions as a function of Reynolds number.

	High Turbulence				Low Turbulence			
Re_C	50,353	64,025	230,567	563,281	49,094	66,543	228,724	564,423
T_T (K)	327	327	324	327	319	318	317	317
P_T (Pa)	6,103	7,722	27,643	68,726	5,743	7,792	26,666	65,837
V_{ex}	250	251	248	246	248	246	245	244
M_{ex}	0.72	0.73	0.72	0.71	0.73	0.72	0.72	0.72
Ω_M	0.1165	0.1104	0.0447	0.0288	0.1115	0.1053	0.0411	0.0223
Ω_{Ave}	0.1075	0.1045	0.0558	0.041	0.09999	0.09047	0.0459	0.0331
KE	0.0977	0.0947	0.0499	0.0366	0.091	0.0822	0.0413	0.0297
β_M	55.6925	56.318	56.7376	56.7149	55.0386	55.3792	56.567	56.8005
β_{Ave}	56.44	56.869	56.4193	56.2515	56.1386	56.4374	56.4238	56.3804

Table 11: Wind tunnel conditions, mass averaged loss and turning angle for ¼ axial chord exit surveys at -16.2° incidence with aero-combustor and low turbulence conditions as a function of Reynolds number

	High Turbulence				Low Turbulence			
Re_C	49,193	64,965	228,098	564,358	48,298	65,761	228,684	563,014
T_T (K)	328	329	329	331	319	318	314	313
P_T (Pa)	5,953	7,936	27,880	69,619	5,634	7,713	26,285	64,757
V_{ex}	251.7	250.0	248.9	248.9	247.8	244.8	244.1	243.2
M_{ex}	0.73	0.72	0.72	0.72	0.73	0.72	0.72	0.72
Ω_M	0.1183	0.1042	0.0466	0.0292	0.1152	0.1002	0.0441	0.0239
Ω_{Ave}	0.1037	0.0933	0.0555	0.0418	0.1011	0.0867	0.0459	0.0345
KE	0.0944	0.0846	0.0498	0.0374	0.0923	0.0788	0.0414	0.0311
β_M	55.7273	56.0378	56.6027	56.6265	54.9683	55.4448	56.2964	56.6649
β_{Ave}	56.5855	56.6798	56.5919	56.2611	56.3600	56.5745	56.4784	56.4268

Table 12: Wind tunnel conditions, mass averaged loss and turning angle for ¼ axial chord exit surveys at -6.2° incidence with aero-combustor and low turbulence conditions as a function of Reynolds number

	High Turbulence				Low Turbulence			
Re_C	48,725	64,793	222,576	559,218	48,526	66,786	229,974	564,422
T_T (K)	322	321	323	328	319	318	316	316
P_T (Pa)	5,741	7,693	26,497	68,210	5,675	7,835	26,651	65,747
V_{ex}	251	247	248	248	247	245	245	244
M_{ex}	0.73	0.72	0.72	0.72	0.73	0.72	0.72	0.72
Ω_M	0.1202	0.1087	0.0563	0.0331	0.1096	0.1006	0.0494	0.0266
Ω_{Ave}	0.1018	0.0928	0.0597	0.0463	0.0964	0.0854	0.0489	0.03886
KE	0.0923	0.0843	0.0537	0.0415	0.0881	0.0779	0.0442	0.0351
β_M	55.6602	55.9694	56.0864	56.5142	55.0402	55.7025	56.3448	56.4978
β_{Ave}	57.0141	57.2356	56.9147	56.9977	56.7694	57.2938	57.18365	57.0169

Table 13: Wind tunnel conditions, mass averaged loss and turning angle for ¼ axial chord exit surveys at -46.2° incidence with aero-combustor and low turbulence conditions as a function of Reynolds number

	High Turbulence				Low Turbulence			
Re_C	51,068	66,546	224,474	562,689	50,763	66,672	228,098	565,055
T_T (K)	329	329	326	329	323	322	314	319
P_T (Pa)	6,231	8,120	27,048	69,351	6,030	7,876	26,288	66,565
V_{ex}	251	250	249	247	249	249	244	245
M_{ex}	0.73	0.72	0.72	0.71	0.73	0.73	0.72	0.72
Ω_M	0.1326	0.1112	0.0558	0.0337	0.149	0.1227	0.0782	0.038
Ω_{Ave}	0.1326	0.1145	0.0709	0.0455	0.1355	0.1162	0.0684	0.0514
KE	0.1205	0.1033	0.0634	0.406	0.1236	0.1051	0.0613	0.0459
β_M	56.0654	56.6061	56.6779	56.7779	55.4683	56.1404	57.3866	56.6862
β_{Ave}	56.2204	56.5798	56.1519	56.1425	55.8716	56.3307	56.4611	56.3732

Total Pressure Loss Contours: Low and AC Turbulence at Mach 0.35

The contour plots presented in this section encompass tunnel conditions at the design points, -2.6, 34.2 and 40. These figures represent the match points between the tests conducted at NASA Glenn Research Center.

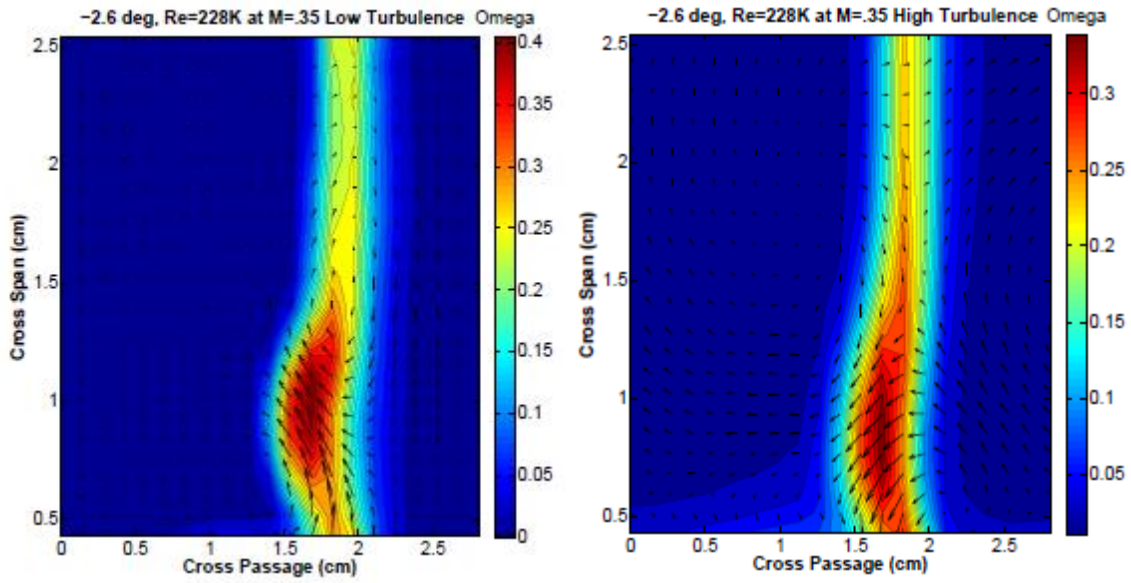

A B

Figure 137: Total pressure loss contours at β_1=-2.6°, ReC=227,500, M=0.35 under low (A) and high (B) turbulence conditions.

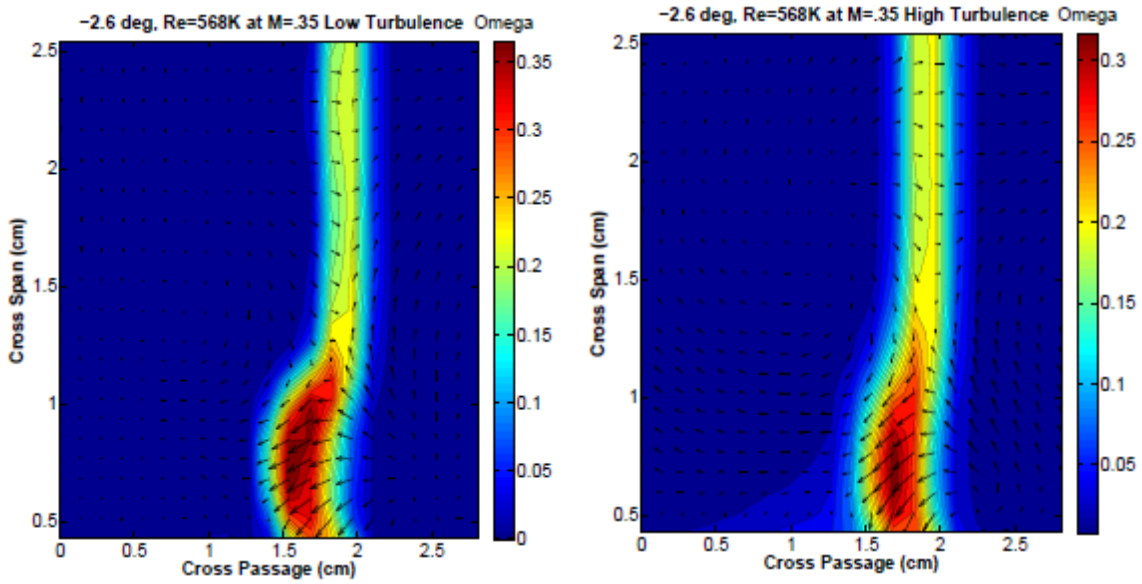

A B

Figure 138: Total pressure loss contours at β_1=-2.6°, ReC=568,000, M=0.35 under low (A) and high (B) turbulence conditions.

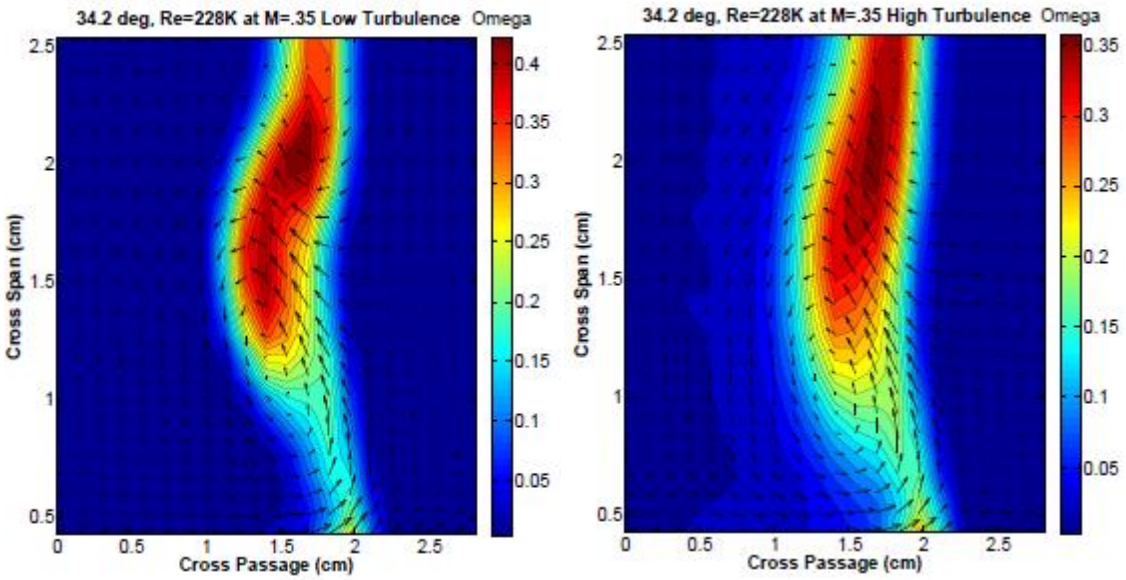

A B

Figure 139: Total pressure loss contours at β_1=34.2°, ReC=227,500, M=0.35 under low (A) and high (B) turbulence conditions.

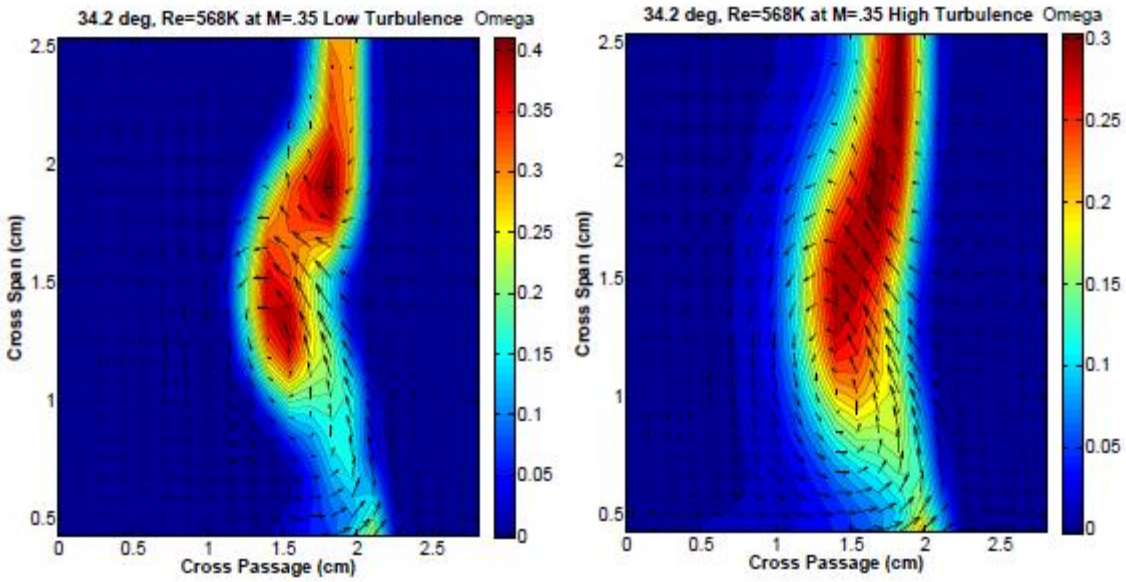

A B

Figure 140: Total pressure loss contours at β_1=34.2°, ReC=568,000, M=0.35 under low (A) and high (B) turbulence conditions.

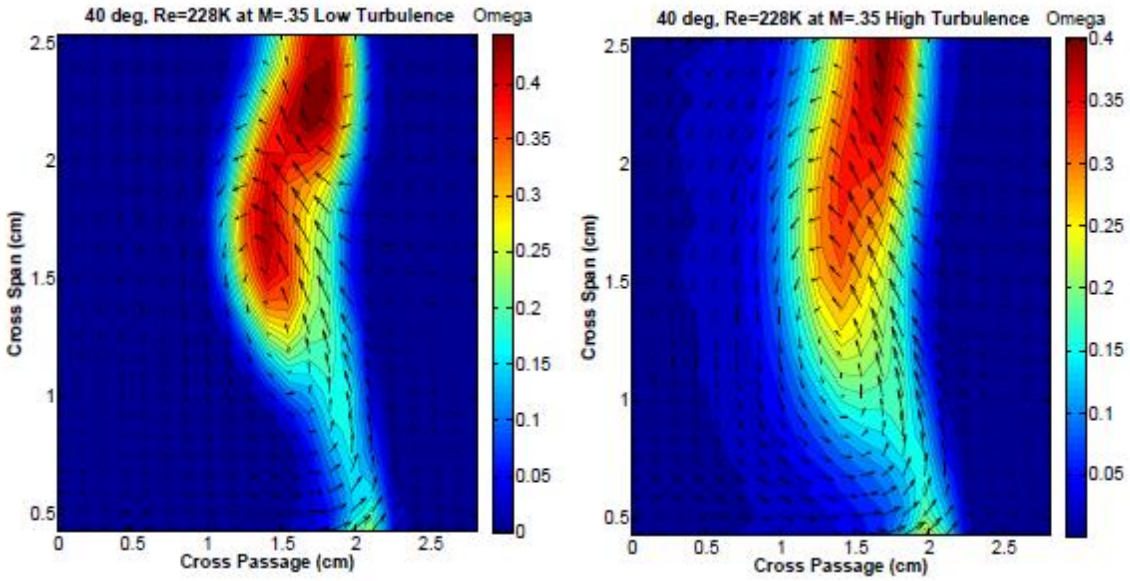

A B

Figure 141: Total pressure loss contours at β_1=40°, ReC=227,500, M=0.35 under low (A) and high (B) turbulence conditions.

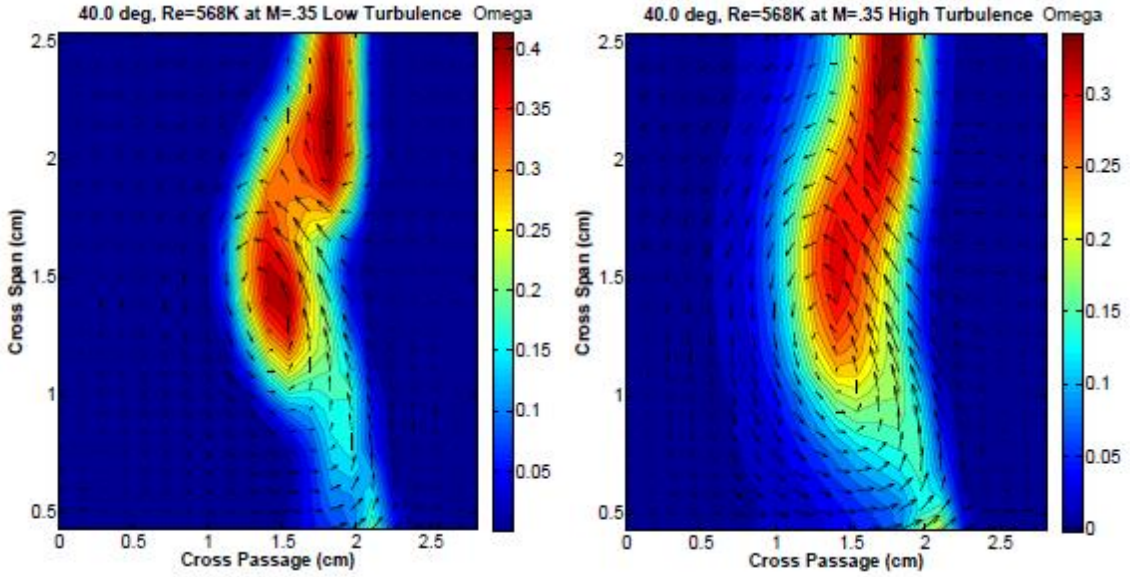

A B

Figure 142: Total pressure loss contours at β_1=40°, ReC=568,000, M=0.35 under low (A) and high (B) turbulence conditions.

-12° Total Pressure Loss Contours: Low and AC Turbulence

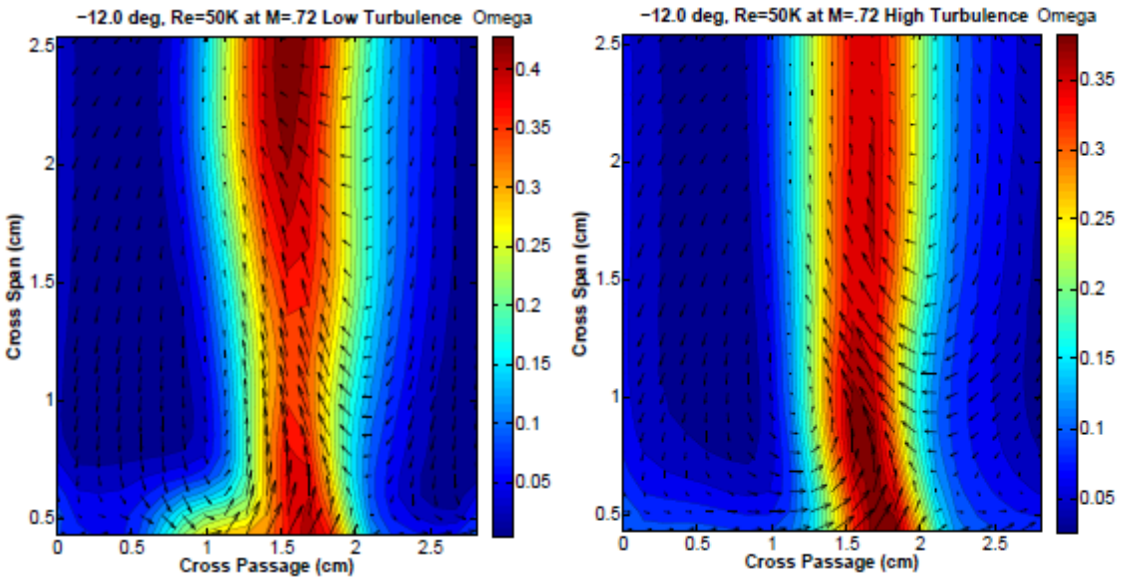

A B

Figure 143: Total pressure loss contours at β_1=-12°, ReC=50,000, M=0.72 under low (A) and high (B) turbulence conditions.

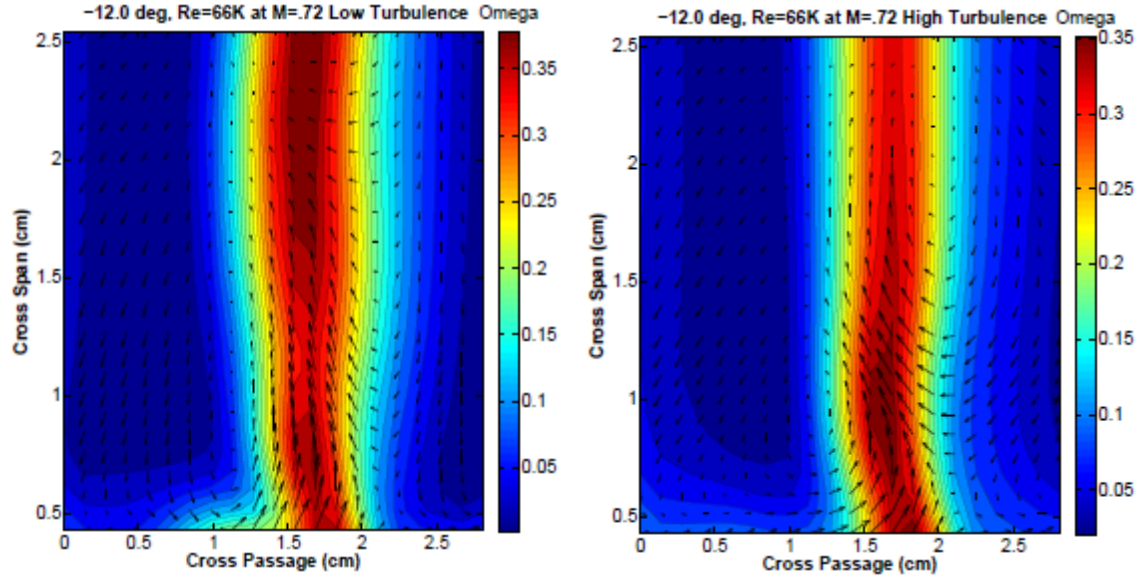

A B

Figure 144: Total pressure loss contours at β_1=-12°, ReC=66,000, M=0.72 under low (A) and high (B) turbulence conditions.

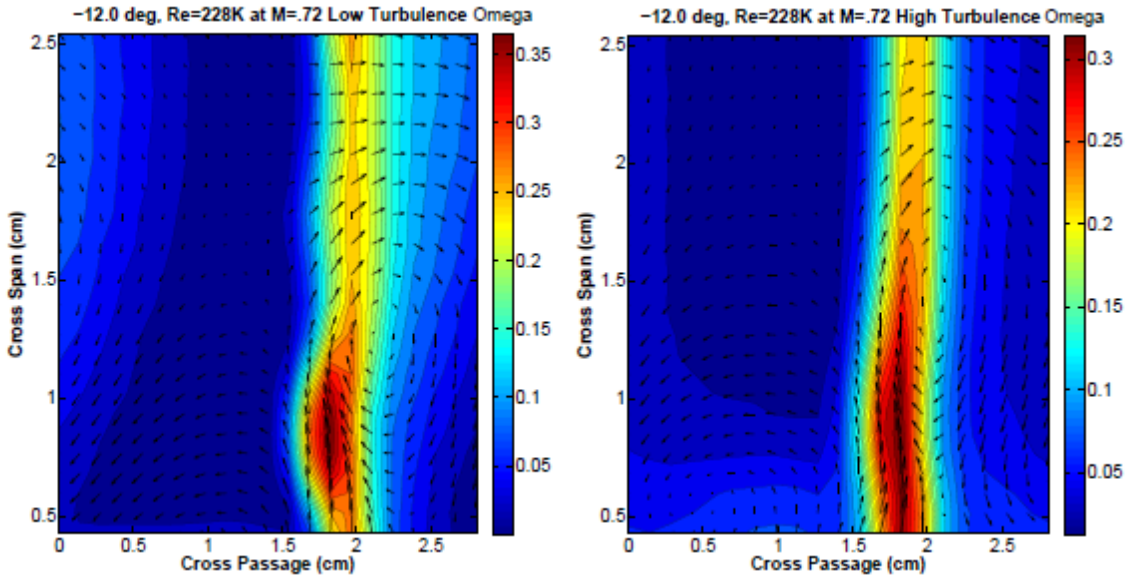

A B

Figure 145: Total pressure loss contours at β_1=-12°, ReC=227,500, M=0.72 under low (A) and high (B) turbulence conditions.

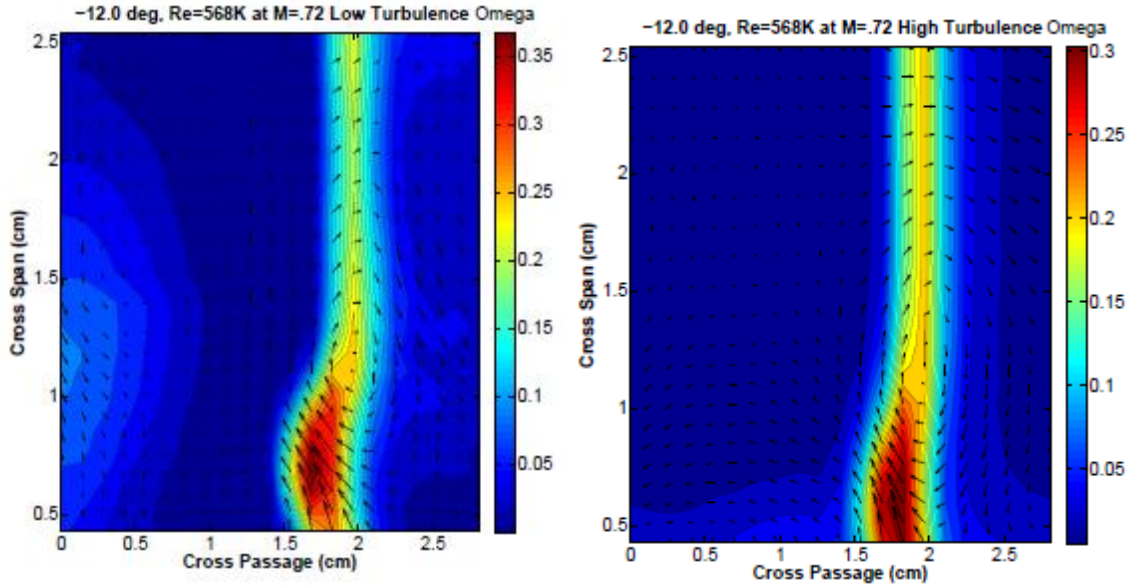

A B

Figure 146: Total pressure loss contours at β_1=-12°, ReC=568,000, M=0.72 under low (A) and high (B) turbulence conditions.

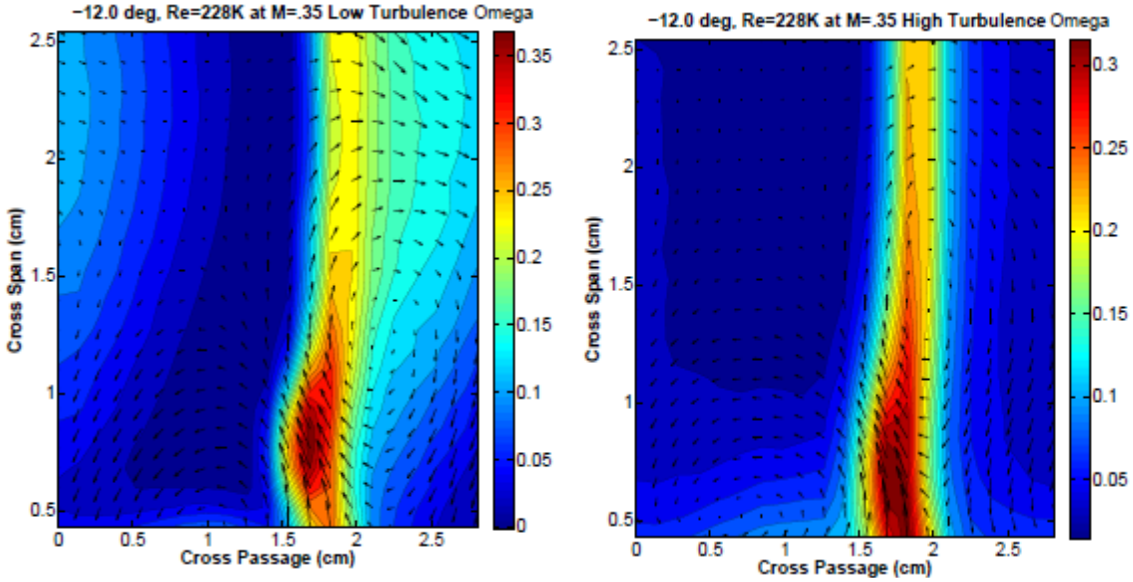

A B

Figure 147: Total pressure loss contours at β_1=-12°, ReC=227,500, M=0.35 under low (A) and high (B) turbulence conditions.

8° Total Pressure Loss Contours: Low and AC Turbulence

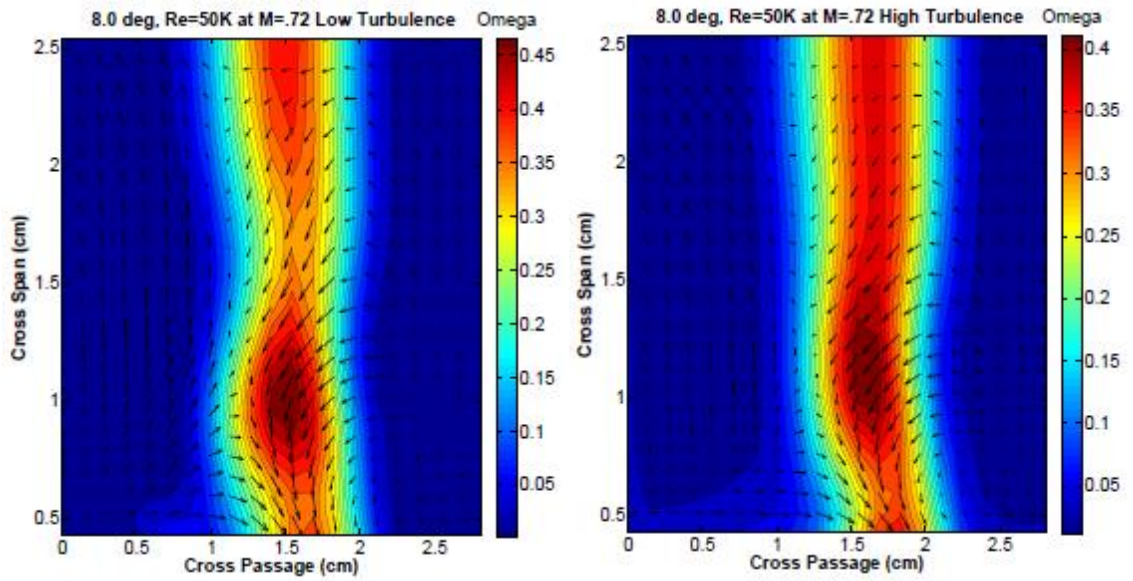

A B

Figure 148: Total pressure loss contours at β_1=8°, ReC=50,000, M=0.72 under low (A) and high (B) turbulence conditions.

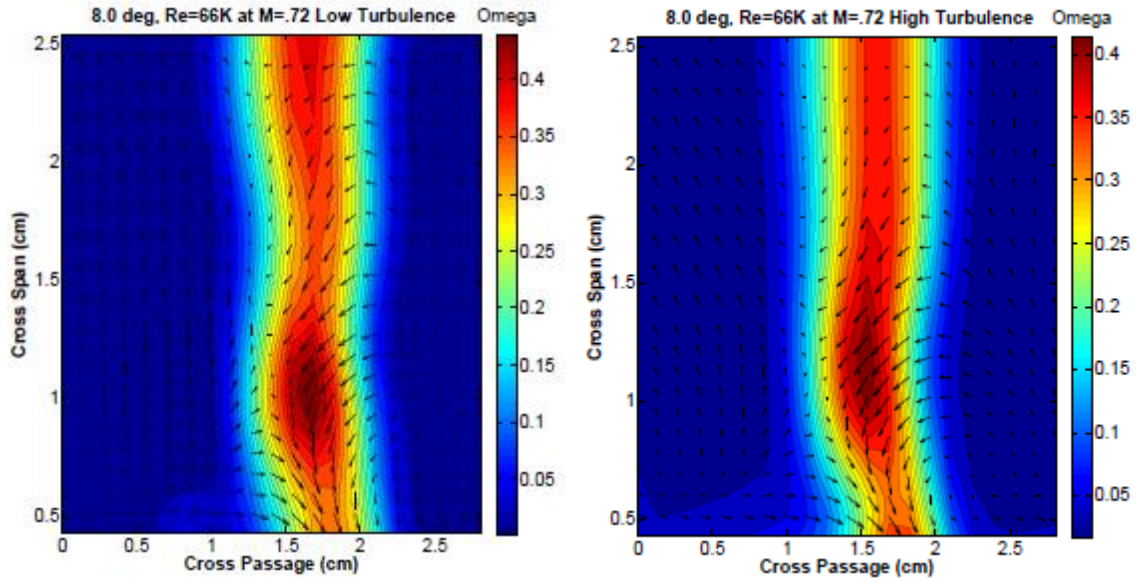

A B

Figure 149: Total pressure loss contours at β_1=8°, ReC=66,000, M=0.72 under low (A) and high (B) turbulence conditions.

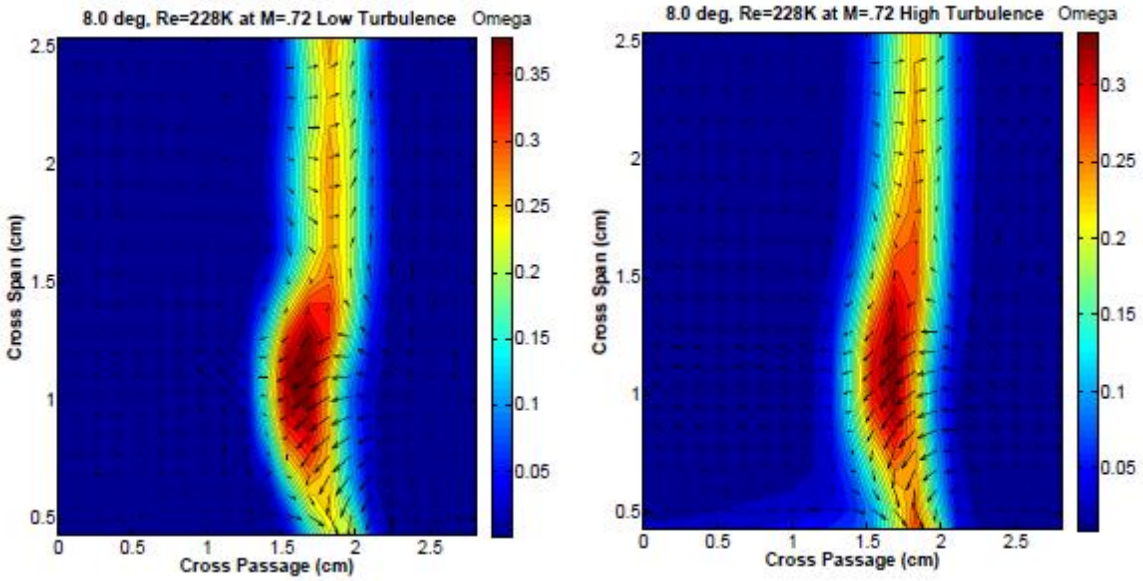

A B

Figure 150: Total pressure loss contours at β_1=8°, ReC=227,500, M=0.72 under low (A) and high (B) turbulence conditions.

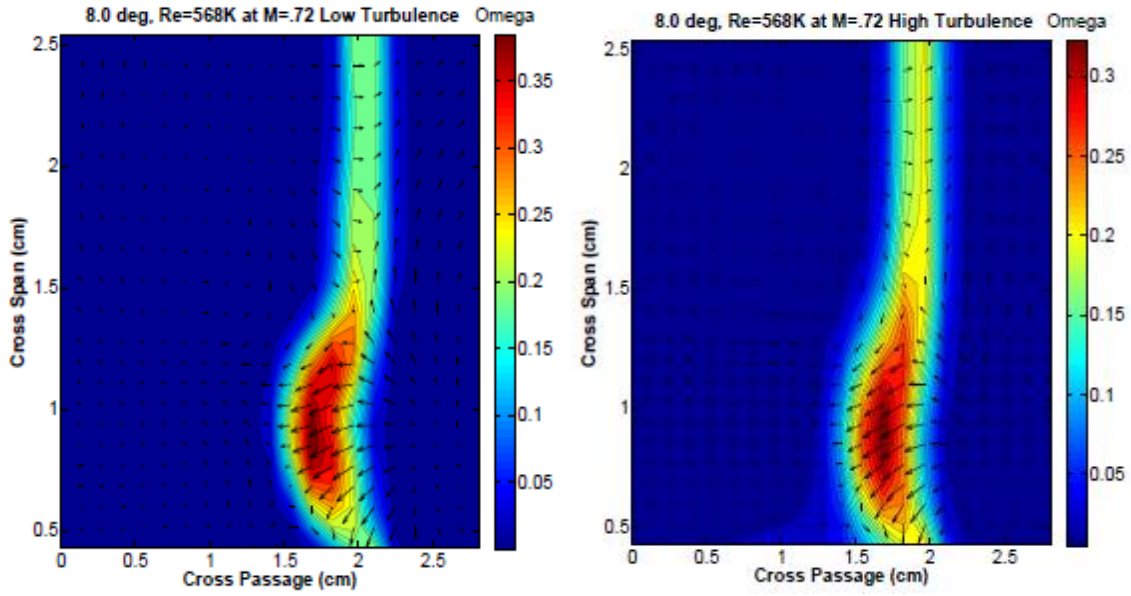

A B

Figure 151: Total pressure loss contours at β_1=8°, ReC=568,000, M=0.72 under low (A) and high (B) turbulence conditions.

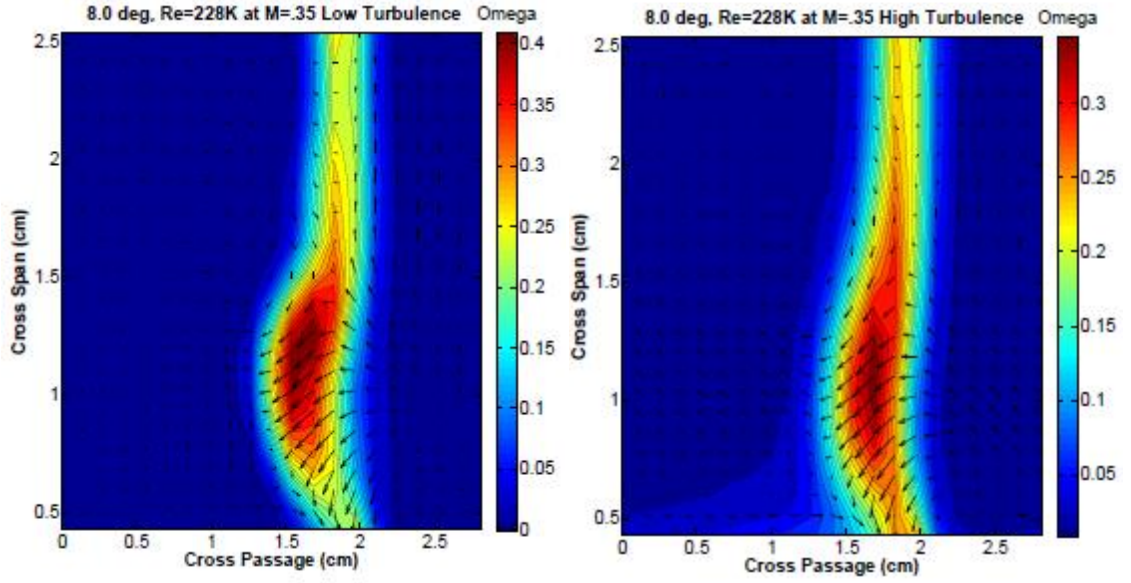

A B

Figure 152: Total pressure loss contours at β_1=8°, ReC=227,500, M=0.35 under low (A) and high (B) turbulence conditions.

18° Total Pressure Loss Contours: Low and AC Turbulence

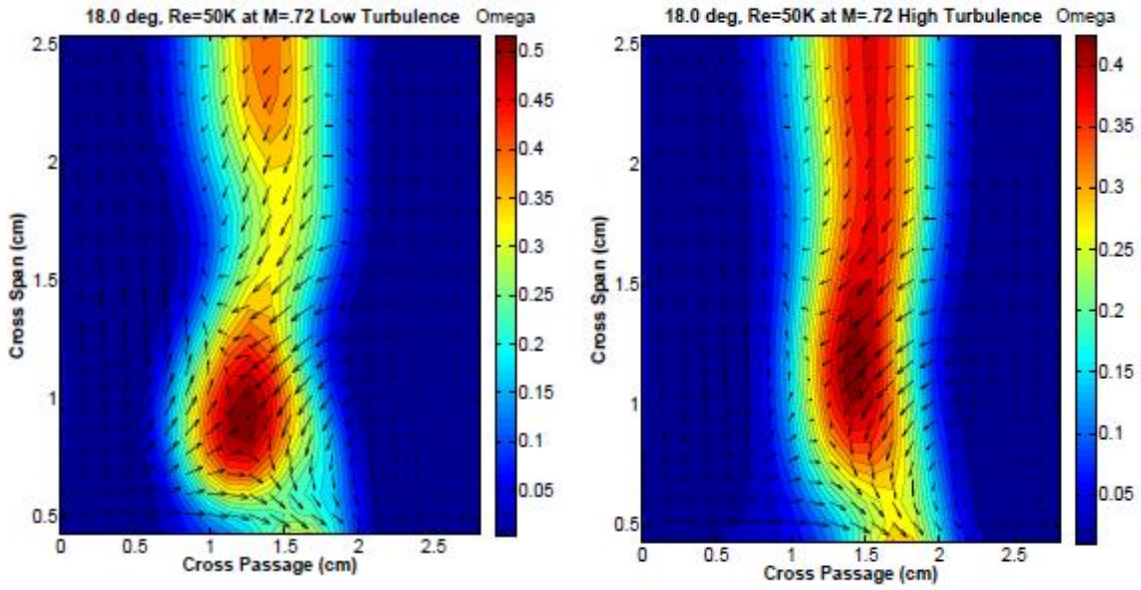

A B

Figure 153: Total pressure loss contours at β_1=18°, ReC=50,000, M=0.72 under low (A) and high (B) turbulence conditions.

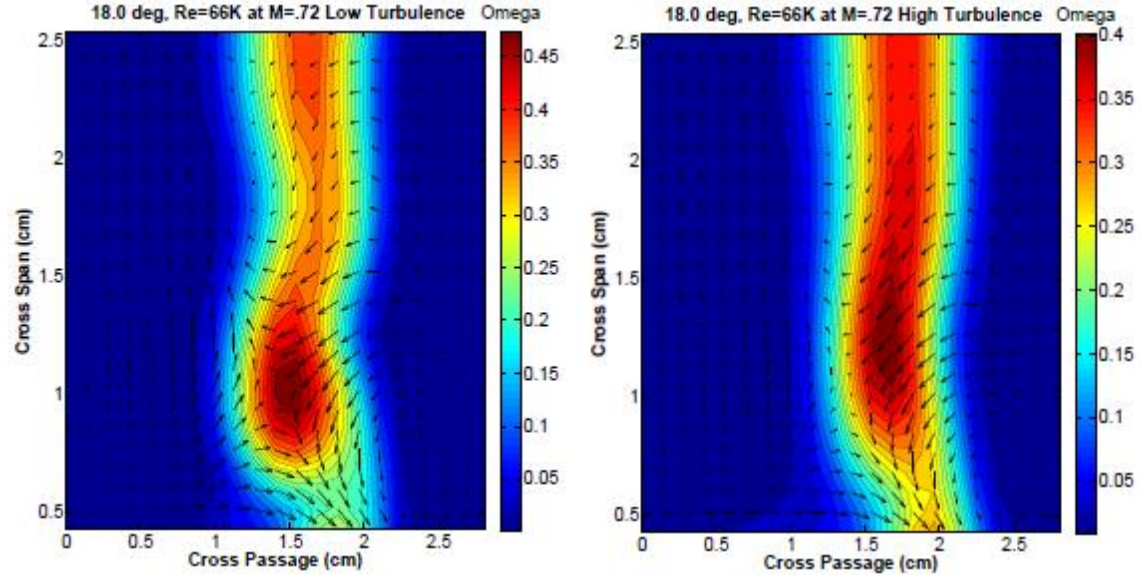

A B

Figure 154: Total pressure loss contours at β_1=18°, ReC=66,000, M=0.72 under low (A) and high (B) turbulence conditions.

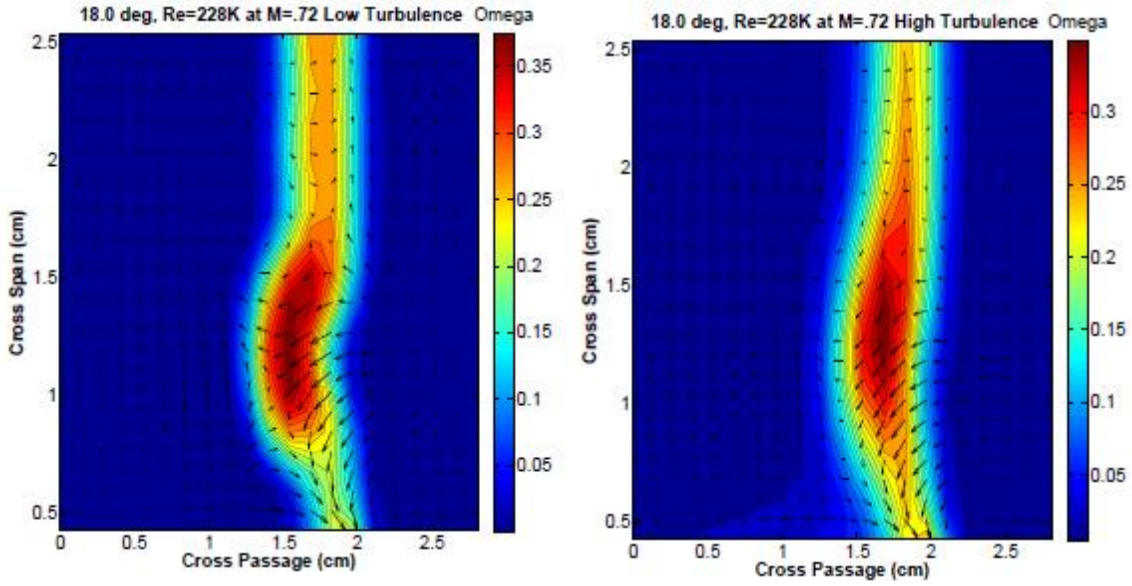

A B

Figure 155: Total pressure loss contours at β_1=18°, ReC=227,500, M=0.72 under low (A) and high (B) turbulence conditions.

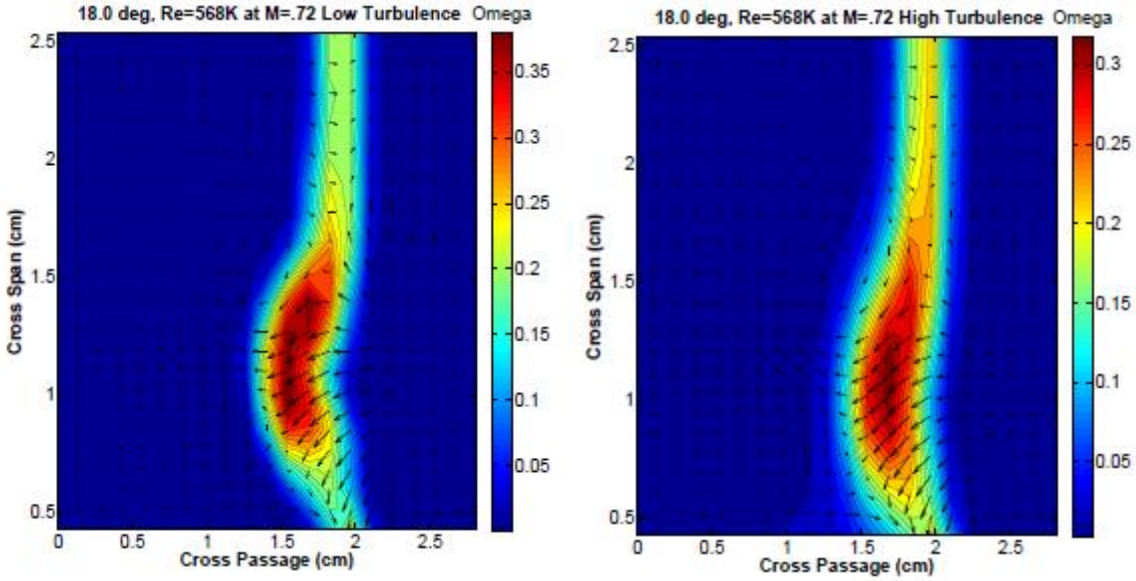

A B

Figure 156: Total pressure loss contours at β_1=18°, ReC=568,000, M=0.72 under low (A) and high (B) turbulence conditions.

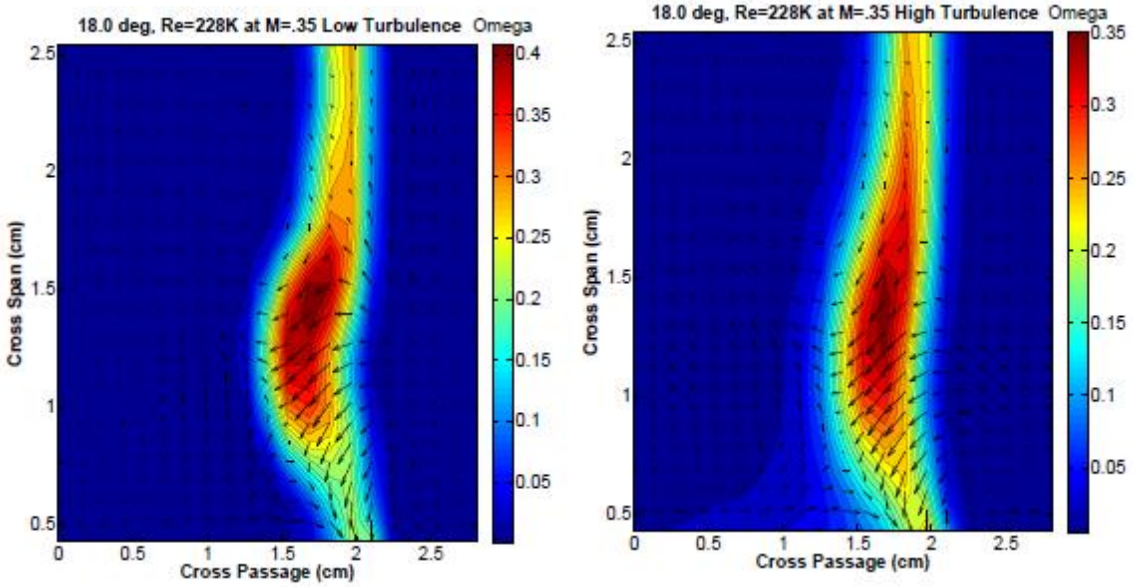

A B

Figure 157: Total pressure loss contours at β_1=18°, ReC=227,500, M=0.35 under low (A) and high (B) turbulence conditions.

28° Total Pressure Loss Contours: Low and AC Turbulence

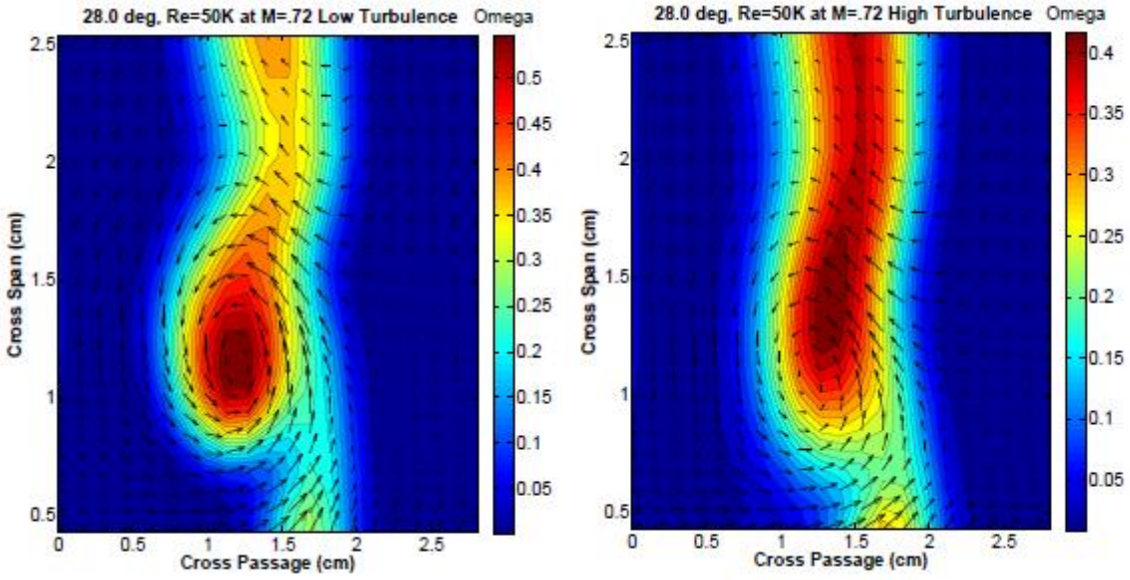

A B

Figure 158: Total pressure loss contours at β_1=28°, ReC=50,000, M=0.72 under low (A) and high (B) turbulence conditions.

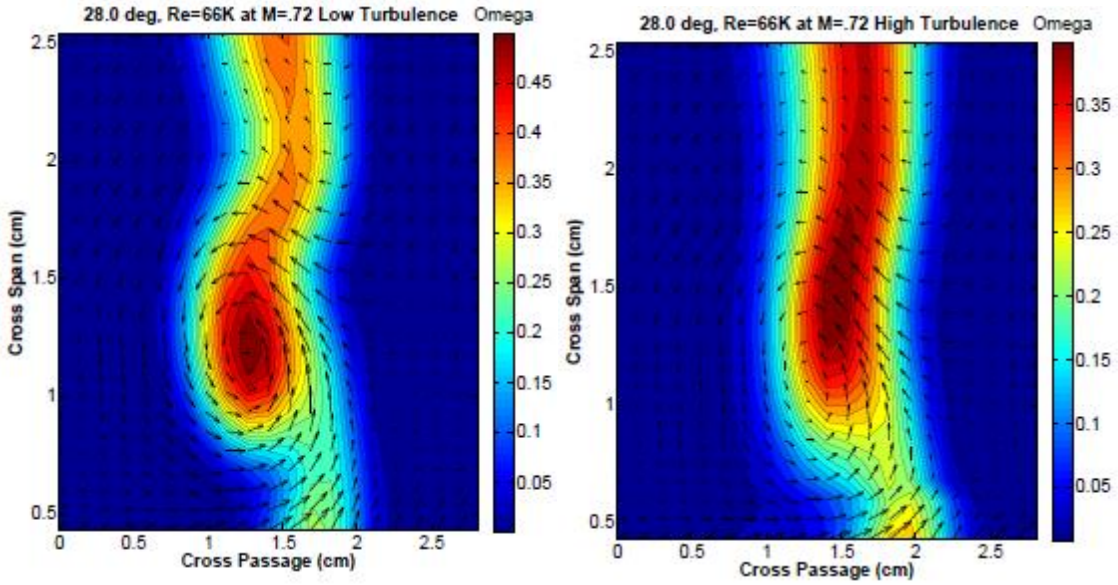

A B

Figure 159: Total pressure loss contours at β_1=28°, ReC=66,000, M=0.72 under low (A) and high (B) turbulence conditions.

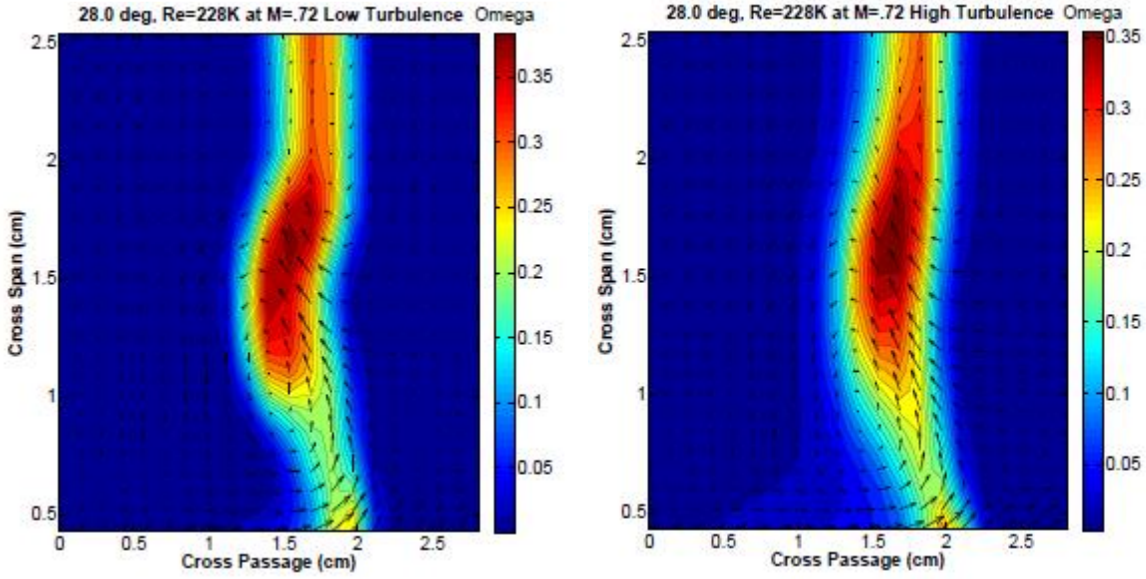

A B

Figure 160: Total pressure loss contours at β_1=28°, ReC=227,500, M=0.72 under low (A) and high (B) turbulence conditions.

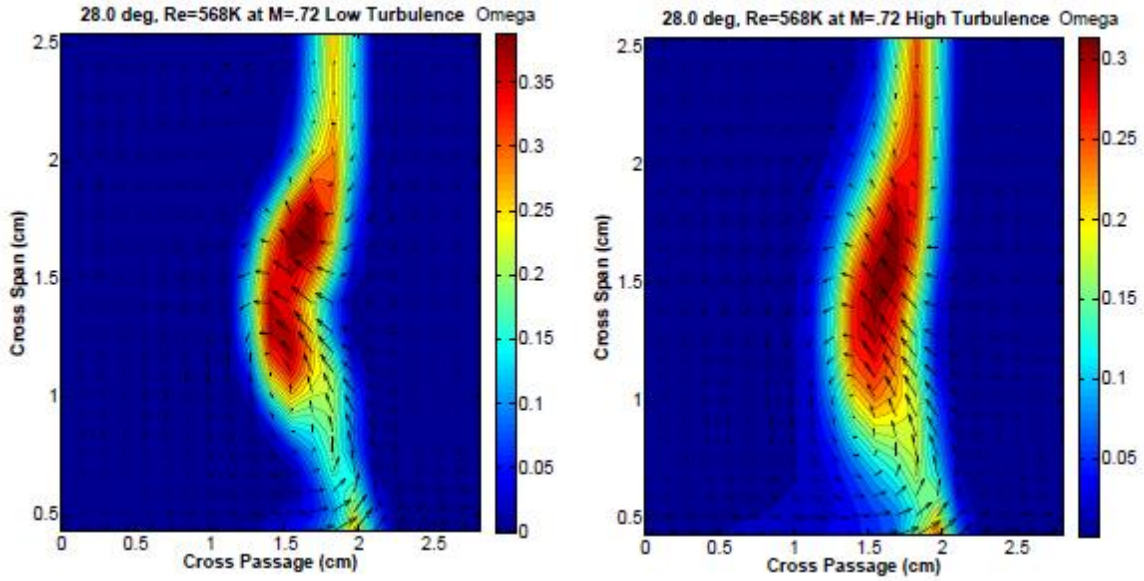

A B

Figure 161: Total pressure loss contours at β_1=28°, ReC=568,000, M=0.72 under low (A) and high (B) turbulence conditions.

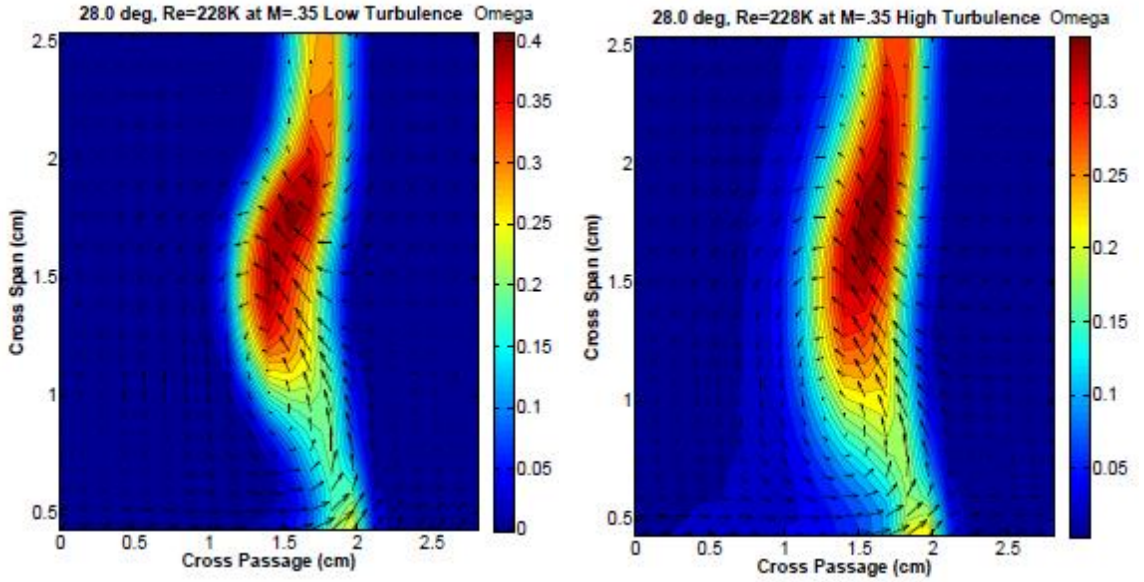

A B

Figure 162: Total pressure loss contours at β_1=28°, ReC=227,500, M=0.35 under low (A) and high (B) turbulence conditions.

Kinetic Energy Loss Contours

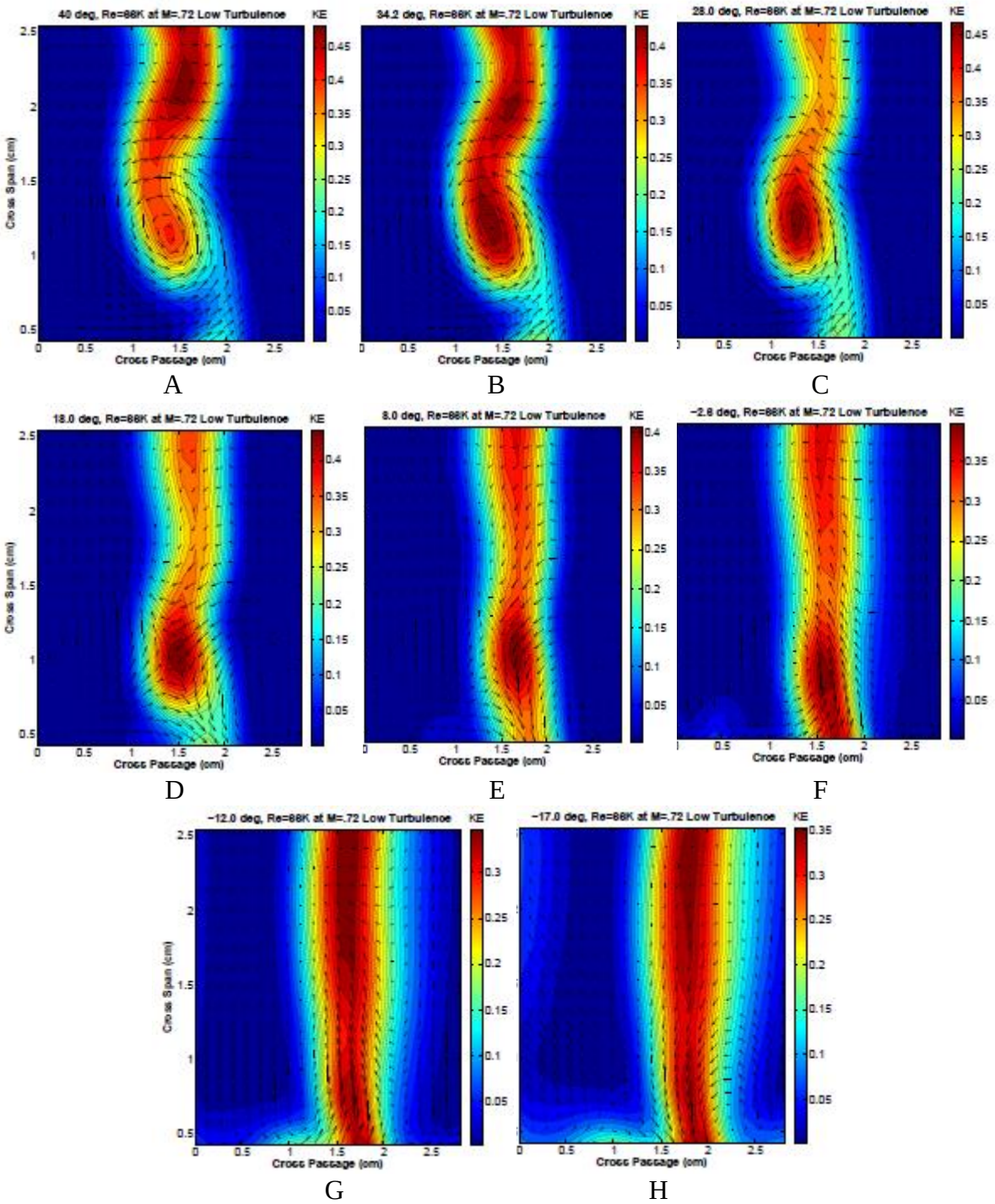

Figure 163: Kinetic energy loss contours at ReC=66,000 vs. inlet angle: (A) 40°, (B) 34.2°, (C) 28°, (D) 18°, (E) 8°, (F) -2.6°, (G) -12° and (H) -17°

Bibliography

[1] A. Glassman, "Turbine Design and Application, Vols. 1-3," NASA SP-290, 1973.

[2] H. P. Hodson and J. D. Coull, "Predicting the Profile Loss of High-Lift Low Pressure Turbines," *Journal of Turbomachinery,* vol. 134, March 2012.

[3] D. Halstead, D. Wisler, T. Okiishi, G. Walker, H. Hodson and H.-W. Shin, "Boundary Layer Development in Axial Compressors and Turbines: Part 3 of 4 - LP Turbines," *Journal of Turbomachinery,* vol. 119, pp. 225-237, April 1997.

[4] H. P. Hodson and R. J. Howell, "Bladerow Interactions, Transition and High-Lift Aerofoils in Low-Pressure Turbines," *Annual Review of Fluid Mechanics,* vol. 37, pp. 71-98, 2005.

[5] R. Mayle, "A Theory for Predicting the Turbulent-Spot Production Rate," *Journal of Turbomachinery,* vol. 121, pp. 588-593, 1999.

[6] F. Ames and M. Plesniak, "The Influence of Large-Scale High-Intensity Turbulence on Vane Aerodynamic Losses, Wake Growth, and the Exit Turbulence Parameters," *Journal of Turbomachinery,* vol. 119, pp. 182-192, April 1997.

[7] J. Dunham, "A Review of Cascade Data on Secondary Losses in Turbines," vol. 12, 1970.

[8] M. Schobeiri and Ozturk, "Experimental Study of the Effect of Periodic Unsteady Wake Flow on Boundary Layer Development, Separation and Reattachment Along the Surface of a Low Pressure Turbine Blade," *Journal of Turbomachinery,* vol. 126, pp. 66-676, October 2004.

[9] J. Gier, K. Engel, M. Kuerner, G. A. Reichstein, D. Schrack, M. G. Rose and S. Staudacher, "Low Pressure Turbine Secondary Vortices: Reynolds Lapse," *Journal of Turbomachinery,* vol. 134, November 2012.

[10] A. B. McVetta, P. W. Geil and G. E. Welch, "Aerodynamic Measurements of a Variable-Speed Power-Turbine Blade Section in a Transonic Turbine Cascade at Low Inlet Turbulence," June 2013.

[11] H. Hodson, I. Huntsman and A. Steele, "An Investigation of Boundary layer Development in a Multistage LP Turbine," *Journal of Turbomachinery,* vol. 116, pp. 375-383, 1994.

[12] R. Howell, H. Hodson, V. Schulte, R. S. H.-P. Stieger, F. Haselbach and N. Harvey, "Boundary Layer Development in the BR170 and BR715 LP Turbines-The Implementation of High-Lift and Ultra-High-Lift Concepts," *Journal of Turbomachinery,* vol. 124, no. 3, pp. 385-392, July 10, 2002.

[13] J. Gler, M. Franke, N. Hubner and T. Schroder, "Designing LP Turbines for Optimized Airfoil Lift," *Journal of Turbomachinery,* vol. 132, no. 3, March 25, 2010.

[14] L. Langston, "Secondary Flows in Axial Turbines - A Review," *Heat Transfer in Gas Turbine Systems,* vol. 934, pp. 11-26, 2001.

[15] C. Sieverding, "Recent Progress in the Understanding of Basic Aspects of Secondary Flows in Turbine Blade Passages," *Journal of Turbomachinery,* vol. 107, pp. 248-257, 1985.

[16] O. Sharma and T. Butler, "Predictions of Endwall Losses and Secondary Flows in Axial Flow Turbine Cascades," *Journal of Turbomachinery,* vol. 109, no. 2, pp. 229-236, April 1, 1987.

[17] M. P.H. and C. Sieverding, "Secondary Flows Within Turbomachinery Bladings," *AGARD-CP-24 Secondary Flows in Turbomachines,* vol. 11, 1977.

[18] H. Wang, S. Olson, R. Goldstein and E. Eckert, "Flow Visualizations in a Linear Turbine Cascade of High Performance Turbine Blades," *Journal of Turbomachinery,* vol. 119, pp. 1-8, 1997.

[19] C. Prakash, D. G. Cherry, H. W. Shin, J. Machnaim, L. Dailey, R. Beacock, D. Halstead, A. R. Wadia, S. Guillot and W. F. Ng, "Effect of Loading Level and Distribution on LPT Losses," *Journal of Turbomachinery,* Vols. No. GT2008-50052, pp. 917-925, 2008.

[20] P. Lampart, "Investigation of Endwall Flows and Losses in Axial Turbines. Part I. Formation of Endwall Flows and Losses," *Journal of Theoretical and Applied Mechanics*, vol. 72, no. 2, pp. 321-342, 2009.

[21] S. Sjolander and D. Corriveau, "Influence on Loading Distribution on the Performance of High Pressure Turbine Blades," *ASME Proceedings: Axial Flow Turbine Aerodynamics,* Vols. No. GT2006-90849, pp. 809-820, 2006.

[22] Q. Zhang, S. W. Lee and P. M. Ligrani, "Effects of Surface Roughness and Turbulence Intensity on the Aerodynamic Losses Produced by the Suction Surface of a Simulated Turbine Airfoil," *Journal of Fluids Engineering,* vol. 126, pp. 257-265, March 2004.

[23] R. J. Volino, "Separated flow measurements on a highly loaded low-pressure turbine airfoil," vol. 132, no. 1, 2009.

[24] R. E. Mayle, "The Role of Laminar-Turbulent Transition in Gas Turbine Engines," *Journal of Turbomachinery,* p. 27 Pages, September 1991.

[25] H. Emmons, "The laminar-turbulent transition in a boundary layer. Part I," *Journal of Aerodynamics and Science,* vol. 18, pp. 490-498, 1951.

[26] J. Elder, "An experimental investigation of turbulent spots and breakdown to turbulence," *Journal of Fluid Mechanics,* vol. 9, pp. 235-246, 1960.

[27] T. A. Zaki and D. Kyriazis, "Bypass transition to turbulence and teh anatomy of turbulent spots," Imperial College London, July 2010.

[28] T. Zaki, R. J. Wissink and P. Durbin, "Direct numerical simulation of transition in a compressor cascade: The influence of free-stream turbulence," *Journal of Fluid Mechanics,* vol. 665, pp. 57-98, December 2010.

[29] G. Schubauer and P. Klebanoff, "Contribution to the Mechanism of Boundary-Layer Transition," NACA TN 3489, 1955.

[30] B. Abu-Ghannam and R. Shaw, "Natural Transisiton of Boundary Layers - The Effects of Turbulence, Pressure Gradient and Flow History," *Journal of Mechanical Engineering Science,* vol. 22, pp. 213-228, 1980.

[31] M. Acharya, "Pressure Gradient and Free-Stream Turbulence Effects on Boundary-Layer Transition," in *Forschungsbericht KLR 85-127*, Baden, Switzerland, 1985.

[32] C. Kuan and T. Wang, "Some Intermittent Behavior of Transitional Boundary Layer," *AIAA,* no. AIAA Paper 89-1890, 1989.

[33] F. M. White, "Transition to Turbulence," in *Viscous Fluid Flow*, McGraw-Hill, Inc., 1991, pp. 369-375.

[34] F. M. White, "Figure 5-28 Description of the boundary-layer transition process: (a) idealized sketch of flat-plate flow.," in *Viscous Fluid Flow*, McGraw-Hill, Inc., 1991, p. 376.

[35] P. Klebanoff, K. Tidstrom and L. Sargent, "The three-dimensional nature of boundary-layer instability," National Bureau of Standards, Washington, DC, 5 June 1961.

[36] P. Andersson, M. Berggren and D. S. Henningson, "Optimal disturbances and bypass transition in boundary layers," *Physics of Fluids,* vol. II, no. 1, pp. 134-150, 29 September 1998.

[37] T. A. Zaki and D. Kyriazis, "Figure 1. A boundary layer undergoing bypass transition due to free-stream turbulence.," Imperial London College, London, UK, July 2010.

[38] J. Hourmouziadis, "Aerodynamic Design of Low Pressure Turbines," in *AGARD Lecture Series 167,* Toronto, Canada, 1989.

[39] E. Malkiel and R. Mayle, "Transition in a Separation Bubble," *Journal of Turbomachinery,* vol. 118, no. 4, p. 8 pages, Oct 01, 1996.

[40] J. A. Redford and M. W. Johnson, "Predicting Transitional Separation Bubbles," *Journal of Turbomachinery,* vol. 127, pp. 497-501, July 2005.

[41] A. Hatman and T. Wang, "A Prediction Model for Separated-Flow Transition," *Journal of Turbomachinery,* vol. 121, pp. 594-602, July 1999.

[42] F. White, Viscous Fluid Flow, Singapore: McGraw-Hill, 1991.

[43] H. Schlicting, Boundary Layer Theory, New York : McGraw-Hill Book Company, 1979.

[44] J. Denton, "Loss Mechanisms in Turbomachines," *Journal of Turbomachinery*, vol. 115, pp. 621-656, October, 1993.

[45] B. S. M. Ozturk and D. E. Ashpis, "Intermittent Behavior of the Separated Boundary Layer alond the Suction Surface of a Low Pressure Turbine Blade under Periodic Unsteady Flow Conditions," *Proceedings of GT2005,* Vols. ASME Turbo Expo 2005; Power for Land, Sea and Air, no. GT2005-68603, pp. 1-17, June 2005.

[46] P. Chakka and M. Schobeiri, "Modeling Unsteady Boundary Layer Transition on a curved Plate Under periodic Unsteady Flow Conditions: Aerodynamic and Heat Transfer Investigations," *Journal of Turbomachinery,* vol. 121, pp. 88-97, January 1999.

[47] M. Schobeiri, B. Ozturk and D. E. Ashpis, "Effect of Reynolds Number and Perdiodic Unsteady Wake Flow Condition on Boundary Layer Develpment, Separation and Intermittency Behavior Along the Suction Surface of a Low Pressure Turbine Blade," *Journal of Turbomachinery,* vol. 129, no. 1, pp. 92-107, Feb. 01, 2005.

[48] P. Kupferschmied, P. Koppel and W. Gizzi, "Time-resolved flow measurments with fast-response aerodynamic probes in turbines," *Meas. Sci. Technol.,* vol. 11, pp. 1036-1054, 2000.

[49] C. Sieverding, T. Arts, R. Denos and J.-F. Brouckaert, "Measurement Techniques for Unsteady Flows in Turbomachines," *Experiments in Fluids,* vol. 28, pp. 285-321, 2000.

[50] T. J. Dudzinski and L. N. Krause, "Flow-Direction Measurement with Fised-Position Probes," NASA Technical Memorandum, Washington D.C., October 1969.

[51] D. Bohn and T. Schnittfelt, "The Dynamic Response of Capillary tubes for use in Miniature Pressure Probes," in *Proceedings of 11th Symposium on "Measuring Techniques for Transonic and Supersonic Flow in Cascades and Turbomachines."*, Universitat der Bundeswehr Munchen, 1992.

[52] G. Dibelius and G. Minten, "Measurement of Unsteady Pressure Fluctuations using Capillary Tubes," in *Proceedings of 7th Symposium on "Measureing Techniques for Transonic and Supersonic Flow in Cascades and Turbomachines"*, RWTH Aachen, 1983.

[53] M. P. Mihelish, "HEAT TRANSFER, TRANSITION, AND AERODYNAMIC LOSS IN A LINEAR VANE CASCADE AT LOW REYNOLDS NUMBERS IN HIGH SPEED FLOWS," University of North Dakota, Grand Forks, ND, May 2012.

[54] M. Mihelish and F. Ames, "THE DEVELOPMENT OF A CLOSED LOOP HIGH SPEED CASCADE WIND TUNNEL FOR AERODYNAMIC AND HEAT TRANSFER TESTING AT MODERATE TO LOW REYNOLDS NUMBERS," vol. 3C, 2013.

[55] L. P. G. Moualeu, "Heat Transfer Measurements on a Incidence-Tolerant Low Pressure Turbine Blade in a High Speed Linear Cascade at Low to Moderate Reynolds Numbers," A Thesis Submitted to the University of North Dakota, Grand Forks, ND, December 2013.

[56] M. Mihelish and F. Ames, "Aerodynamic Loss Measurements in a Compressible Flow Vane Cascade Showing the Influence of Reynolds Number Lapse," vol. 6A, no. GT-2013-95052, 2013.

[57] A. Treaster and A. Yocum, "The Calibration and Application of Five-Hole Probes," *ISA Transactions,* vol. 18, pp. 23-34, 1979.

[58] G. E. Welch, A. B. McVetta, M. A. Stevens, S. A. Howard, P. W. Giel, A. A. Ameri, W. To, D. R. Thurman and G. J. Skoch, "Variable-Speed Power-Turbine Research at Glenn Research Center," National Aeronautics and Space Administration, Clevelend, Ohio, July 2012.

[59] R. J. Moffat, "Describing the Uncertainties in Experimental Results," *Experimental Thermal and Fluid Science,* pp. 3-17, 1988.

[60] D. Spalding, "A single formula for the law of the wall," *ASME: Journal of Applied Mechanics,* no. 28, pp. 455-458, 1961.

[61] F. M. White, *Figure 6-20 Local skin friction on a smooth flat plate for turbulent flow, showing several theories,* New York, NY: McGraw-Hill Inc., 1991.

[62] S. W. Lee and S. B. Jun, "Reynolds Number Effects on the Non-Nulling Calibration of a Cone-Type Five-Hole Probe for Turbomachinery Applications," *journal of Mechanical Science and Technology,* vol. 19, no. 8, pp. 1632-1648, 2005.

[63] J. J. Bertin and R. M. Cummings, Aerodynamics for Engineers, 5th ed., Upper Saddle River, NJ: Pearson Prentice Hall, 2009.

[64] F. Ames, *Laminar to Turbulent Transition,* Lecture conducted from University of North Dakota, Grand Forks, March 2012.

[65] F. Haselbach, H.-P. Schiffler, M. Horsman, S. Dressen, N. Harvey and S. Read , "The Application of Ultra High Lift Blading in the BR715 LP Turbine," *Journal of Turbomachinery,* vol. 124, pp. 45-51, January 2002.

[66] C. H. Sieverding, D. Ottolia, C. Bagnera, A. Comadoro, J. Brouckaert and J.-M. Desse, "Unsteady Turbine Blade Wake Characteristics," *Journal of Turbomachinery,* vol. 129, pp. 551-559, October 2004.

[67] C. H. Sieverding, H. Richard and J. M. Desse, "Turbine Blade Trailing Edge Flow Characteristics at High Subsonic Outlet Mach Number," *Journal of Turbomachinery,* vol. 125, pp. 298-309, April 2003.

[68] F. N.J., J. Johnson and F. Ames, "Aerodynamics of a Letterbox Trailing Edge: Effects of Blowing Rate, Reynolds Number, and Turbulence on Aerodynamic Losses and Pressure Distribution," *Journal of Turbomachinery,* vol. 132, October 2010.

[69] R. Goldstein and R. Spores, "Turbulent Transport on the Endwall in the Region Between Adjacent Turbine Blades," *Journal of Heat Transfer,* vol. 110, pp. 862-869, 1988.